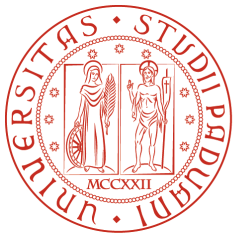

Università
degli Studi
di Padova

Sede amministrativa: Università degli Studi di Padova
Dipartimento di Fisica e Astronomia "Galileo Galilei"

Corsi di Dottorato di Ricerca in Astronomia
XXX ciclo

# THE MASS ASSEMBLY IN GALAXIES AND CLUSTERS:

## A new perspective from the luminosity profiles

**Direttore della Scuola:** Ch.mo Prof. Giampaolo Piotto
**Supervisore:** Ch.mo Prof. Mauro D'Onofrio
**Co-Supervisore:** Ch.mo Dott. Giovanni Fasano

**Dottorando:** Stefano Cariddi

# Contents


**1 Introduction** **3**

**2 The WINGS and Omega-WINGS surveys** **11**
2.1 The WINGS survey . . . . . 11
2.2 The Omega-WINGS survey . . . . . 14
2.3 Our data sample . . . . . 14

**3 The photometric profiles construction** **21**
3.1 The intensity profiles construction . . . . . 21
3.1.1 The completeness correction . . . . . 22
3.1.2 The galaxy fraction . . . . . 24
3.1.3 The field intensity . . . . . 24
3.2 The photometric profiles construction . . . . . 27
3.3 The faint objects correction . . . . . 27
3.4 The mass profiles construction . . . . . 28
3.5 The photometric and mass profiles . . . . . 30

**4 The photometric profiles analysis** **79**
4.1 The modeling of luminosity profiles . . . . . 79
4.1.1 The King model . . . . . 80
4.1.2 The standard $\beta$-model . . . . . 81
4.1.3 The Sérsic model . . . . . 81
4.2 The goodness-of-fit criterium choice . . . . . 82
4.3 The profile fitting procedure . . . . . 84
4.4 The fits . . . . . 87

**5 The structural parameters relations** **117**
5.1 General considerations . . . . . 117
5.2 The non-homology of galaxy clusters . . . . . 122
5.3 The CM diagram of galaxy clusters . . . . . 124
5.4 The main scaling relations of galaxy clusters . . . . . 126

**6 The Fundamental Plane** **137**
6.1 Introduction on the Fundamental Plane . . . . . 137
6.2 The Fundamental Plane problem . . . . . 140
6.3 The new proposed solution . . . . . 141
6.4 The observed projections of the FP . . . . . 147
6.5 The connection between $L$, SFR and $\sigma$ . . . . . 153
6.6 More on the FJ and PFJ planes . . . . . 155
6.7 The SF activity in galaxies . . . . . 159

**7 Conclusions** **165**
7.1 Summary and conclusions . . . . . 165
7.1.1 The photometric decomposition of galaxy clusters . . . 165
7.1.2 The Fundamental Plane . . . . . 166
7.2 Future prospects . . . . . 168
7.2.1 The BCG-cluster connection . . . . . 168
7.2.2 Comparison with numerical simulations . . . . . 170
7.2.3 A possible explanation . . . . . 174

**A A possible origin for the FJ relation** **179**
A.1 The case of single stars . . . . . 179
A.2 The case of galaxies . . . . . 182

**Bibliography** **186**

# Chapter 1

# Introduction

This thesis deals with the optical properties of galaxy clusters and aims at emphasize the similarities and the differences of these systems with respect to the less massive early-type galaxies (ETGs).

Galaxy clusters are the largest virialized structures observed in the Universe. They can be divided in two main categories: 1) rich clusters; 2) poor clusters. The division is made according to the number of galaxies brighter than $m_3$+2 (where $m_3$ is the magnitude of the third brightest cluster member) within a radius of $r \simeq 1.5\,h^{-1}$ Mpc from the cluster center. If this amount of galaxies is larger or equal 30 the cluster is defined "rich", otherwise it is "poor" (Abell 1958).

The galaxies in rich clusters move with random peculiar velocities of the order of $\sim 750$ km s$^{-1}$ (median line-of-sight velocity dispersion), which translates in a mass of the order of $\sim 5\times10^{14}\,h^{-1}$ M$_\odot$ within $r \simeq 1.5\,h^{-1}$ Mpc from the cluster center. Rich clusters provide also the best laboratory for studying the baryon fraction (i.e., the ratio of the baryonic mass to the total mass of the system) on Mpc scale. The mass of baryons in clusters is composed by two main components (Gonzalez et al. 2013): the hot intracluster medium and the matter condensed into stars. The temperature of the hot intracluster gas ranges from $\sim 2$ to $\sim 14$ keV, and is typically $\sim 5$; the central gas density is $\sim 10^{-3}$ $e^-$ cm$^{-3}$.

The hot plasma is detected through its X-ray emission, produced by thermal bremsstrahlung, with $L_X \sim 10^{44}$ erg s$^{-1}$. The X-ray luminosity well correlates with the velocity dispersion (Lubin and Bahcall 1993) and the observed correlation indicates that, on average, the energy per unit mass in the gas and in the galaxies is the same.

The typical iron abundance in the hot intracluster gas is $\sim 0.3 \pm 0.1$ (see e.g., Jones et al. 1992). A strong correlation between the total iron mass and the total luminosity of the ETGs is observed (Jones et al. 1992). It is likely

caused by the gas stripped out of the ETGs. The overall iron abundance decreases by a factor $\sim 2$ from $z = 0$ to $z \sim 1$ (Anderson et al. 2009).

Poor clusters have less ETGs and more late-type galaxies than rich clusters, and also a smaller amount of intra-cluster medium (ICM; see e.g., Sanderson et al. 2003). However, the metallicity of ICM is nearly the same $(0.3 \pm 0.1)$ over a wide range of cluster masses (see e.g., Songaila et al. 1990; Ciotti et al. 1991) and also the $\alpha$-elements content, which is compatible with that typical of the solar neighborhood (Ishimaru and Arimoto 1997).

According to the $\Lambda$-CDM model, our Universe is made of three different components: baryonic matter, accounting for about 5% of the total mass/energy budget; dark matter (DM), constituting the 25%; dark energy, which accounts for the 70% and is responsible for its accelerated expansion (Perlmutter et al. 1998; Riess et al. 1998). In this framework, galaxy clusters accrete their mass thanks to a hierarchical series of mergers, driven by the DM mass contribution and Einstein's General Relativity Theory gravity law, that build up more massive structures starting from less massive ones.

Zwicky (1933) was the first to use one of them (namely, the Coma cluster) for providing observational evidences for the presence of DM. Decades later, Hoessel et al. (1980) used clusters to derive an acceleration parameter consistent with the most recent findings. Later, the clustering properties were used to verify the gaussianity of random initial fluctuations predicted by the Cosmological Inflation theory (Bahcall and Soneira 1983). During the 1990s, galaxy clusters provided an invaluable contribution for deriving the baryonic matter density in the Universe (White et al. 1993) and for constraining the cosmological density parameter (Bahcall and Fan 1998; Donahue et al. 1998). Finally, with the new millennium there was a surge of studies aimed at characterizing the mass power spectrum (see e.g., Borgani et al. 2001; Reiprich and Böhringer 2002; Seljak 2002; Pierpaoli et al. 2003; Allen et al. 2003; Schuecker et al. 2003), the hot intra-cluster medium and the galaxy number counts (see e.g., Allen et al. 2011).

Nowadays, the increasing power of modern computing centers favoured the execution of complex N-body simulations (e.g., the Millennium Simulation; Springel et al. 2005) that allowed the establishment of a standard formation and evolution scenario. Consequently, many of the bulk properties of clusters are thought to be determined only by their initial conditions, DM properties and budget, and gravity law. Moreover, the nearly closed-box nature of their deep potential wells makes them ideal laboratories to study the galaxy formation processes and their effects on the surrounding intergalactic medium. Therefore, we understand the necessity of precisely characterizing the global cluster parameters (e.g., total luminosity, total mass, virial radius, velocity dispersion) in order to compare them with those ruling the galaxy

regime, and we understand also the importance of precisely characterizing the galaxy distribution within the clusters themselves (e.g., morphology-density relation; Fasano et al. 2015).

Up to now, the bulk of our empirical knowledge of galaxy clusters comes mainly from the X-ray observations of hot ICM. In fact, the X-ray studies permitted the first measurements of the baryonic mass within clusters and the first determination of the cluster virial radii. The mass measurements are based on the analysis of the surface brightness profile of hot ICM and on the precise knowledge of the background surface brightness levels (see e.g., Ettori et al. 2013; Maughan et al. 2016). Then, the data are fitted using a model involving the gas temperature as free parameter and the so-derived density profile is translated, by means of the ideal gas and the hydrostatic equilibrium laws, into a mass profile. The whole procedure is based on several assumptions: 1) the isothermality of ICM; 2) the hydrostatic equilibrium of hot ICM; 3) the spherical geometry of the system. In case of rich clusters and groups with a regular X-ray morphology the hydrostatic isothermal model (see e.g., Jones and Forman 1984) and its surface brightness counterpart (i.e., the standard beta model; Cavaliere and Fusco-Femiano 1976) are generally able to reproduce the density and surface brightness profiles. However, this is not true in case of, e.g., irregular groups or cool-core clusters. Nonetheless, in both cases the application of a double-component beta model has brought to a measurable improvement of the fit quality (see e.g., Mulchaey and Zabludoff 1998; Ettori 2000). In any case, the X-ray observations have two main limitations: they requires a good evaluation of the background surface brightness level (in order not to introduce a zero-point systematic error) and they do not allow to measure mass profiles up to large radii, as the gas is usually detectable only in the central cluster regions.

On the other hand, dynamical studies permitted the analysis of the DM component in clusters. The dynamical mass profiles (see e.g., Biviano et al. 2017) are based on two key assumptions: 1) that the cluster is in dynamical equilibrium (which is not true, e.g., in case of recent mergers); 2) that the mass follows the light (a condition without which the virial theorem cannot be used for calculating the total mass of the system; Sadat 1995). However, while several X-ray studies confirmed that the dark component is well traced by the luminous one (see e.g., Fabricant et al. 1986; Smail et al. 1995; Kneib et al. 2003; Umetsu et al. 2010; Medezinski et al. 2013; Grillo et al. 2015), the mutual connection seems to evade a straightforward explaination. For example, while Rines et al. (2000) and Medezinski et al. (2013) measured a decrease of the mass-to-light ratio outside the cluster core, Rines et al. (2004) found such decrease only outside the virial radius, here defined by $r_{200}$ (i.e., the radius enclosing an average overdensity 200 times larger than

the critical density of the Universe at a fix redshift); on the contrary, instead, Rines et al. (2001) measured a flat profile. Moreover, while Newman et al. (2013) determined an approximatively null amount of DM at the cluster center, identified with the brightest cluster galaxy (BCG), Grillo et al. (2015), by adopting a different center selection criterion, found a dominant DM contribution at the smallest clustercentric distances. In any case, the dynamical analysis requires the precise measurement, through the Doppler shift, of the radial velocities of at least several dozen cluster galaxies, possibly at least to $r_{200}$, and a subsequent correct modellization of the potential well of the cluster.

Another way of deriving the cluster mass profile is through the gravitational lensing (see e.g., Umetsu et al. 2014; Merten et al. 2015; Andreon 2015). With this method no prior assumption is needed to derive the cluster mass distribution. However, both the weak and the strong lensing cases are not free of issues. The strong lensing, in fact, is statistically unlikely to happen and in any case can provide information only about the central, densest cluster regions. Both the issues can be overcome by using, instead, the weak lensing, but in this case we need to face two main biases (Hoekstra et al. 2013): 1) the most suitable sources used to detect it are the most distant (i.e., the faintest ones), which is a huge obstacle in their redshift determination, and consequently in most cases the adopted sample is highly incomplete; 2) the lack of redshift information can result in a misclassification of cluster objects as "background objects", which leads to an underestimation of the cluster mass that varies with the clustercentric distance. Consequently, the mass derived this way is affected by much larger errors. The idea of combining the two methods has arised since the 1990s (see e.g., Bartelmann and Steinmetz 1996; Abdelsalam et al. 1998; Seitz et al. 1998), however its practical implementation continues to be technically challenging.

The use of simulations for reproducing the information coming from the previously-analyzed methods (see e.g., Navarro et al. 1995) allowed to prove that DM haloes are self-similar (i.e., homologous) structures (Navarro et al. 1996). The Navarro, Frenk & White model (Navarro et al. 1997) was the first one providing a correct representation of the data, and nowadays is still the most widespread, although subsequent simulations by Navarro et al. (2004), Graham et al. (2006), and Merritt et al. (2006) proved that the Einasto (1965) profile and similar models designed to reproduced the deprojection of the Sérsic profile (Merritt et al. 2006) can match more closely the observations. The Navarro, Frenk & White model is completely characterized by means of two parameters: the virial mass and the concentration parameter (i.e., the ratio between the virial radius and the scale radius of the DM halo). The two parameters are not independent, in fact the characteristic overdensity of

a halo is tightly related to the halo formation time (Navarro et al. 1997). In particular, haloes that form earlier are more concentrated and, at the same time, more likely characterized by smaller mass values. Consequently, the concentration parameter is expected to anti-correlate with the virial mass, albeit with significant scatter (see e.g., Macciò et al. 2007). Several models have been developed to parametrize the Concentration-Mass Relation. At the present, the most accurate one is that of Zhao et al. (2009).

Finally, also the optical analysis of clusters is not problem-free. The correct determination of the galactic extinction, the foreground and background galaxies contamination, the data completeness and the membership uncertainty are only some of the reasons that limited, together with the decades-long lack of large optical surveys, the number of studies in this field (see e.g., Oemler 1974; Dressler 1978; Adami et al. 1998; Carlberg et al. 1996; Girardi et al. 2000). Even more difficult with these data is the estimate of stellar masses and mass profiles, which have been derived, in most cases, by means of strong assumptions. For example, some authors neglected the contribution of the galaxies outside the red sequence or under a certain mass threshold, while others assumed a radial-independent luminosity function, therefore neglecting the well-known luminosity segregation effect (see e.g., Andreon 2002; Durret et al. 2002). Moreover, works based on the early releases of the *Two Micron All Sky Survey* (2MASS; Skrutskie et al. 2006) lack the light contribution coming from the outskirts of the measured galaxies, together with the detection of low-surface-brightness galaxies. Finally, the absence of a proper evaluation of the field objects number counts allowed only a partial background subtraction, when present, thus biasing the results. Consequently, discrepancies of a factor $2-3$ between the masses obtained through different methods have been reported (e.g., Wu and Fang 1997).

The modern surveys, producing huge amounts of high-quality data, are allowing to obtain much better results on the galaxy clusters study. For example, the *MAssive Cluster Survey* (MACS; Ebeling et al. 2001)[1], aimed at characterizing distant, X-ray luminous clusters, so far comprises 124 spectroscopically-confirmed objects at redshift $0.3 < z < 0.7$. Instead, other surveys, such as the *Two-Degree Field Galaxy Redshift Survey* (2dFGRS)[2], allowed the dynamical profiles determination for statistically-significant samples of objects (e.g., Biviano and Girardi 2003). Finally, to the lensing technique was dedicated the *Cluster Lensing And Supernova survey with Hubble* (CLASH; Postman et al. 2011)[3], which targeted 25 massive clusters with detected

[1]http://www.ifa.hawaii.edu/∼ebeling/clusters/MACS.html
[2]http://www.2dfgrs.net/
[3]http://www.stsci.edu/∼postman/CLASH/Home.html

strong lensing signatures and resulted so far in more than 100 pubblications. Along this vein is the WIde-field Nearby Galaxy-cluster Survey (WINGS), that will be discussed later on in this thesis. With these data the possibility of studying the stellar luminosity and mass profiles of galaxy clusters has finally become concrete.

The aim of this PhD project is twofold: first, to derive the optical galaxy clusters photometric profiles; second, to compare the main correlations found between the structural parameters of clusters with those of ETGs. In fact, from a dynamical point of view, galaxy clusters are similar to ETGs: both the systems are dominated by random motions of particles, they are virialized at $z = 0$ and, as we will show in this thesis, they also share many other properties. What can we deduce from the similarity of the light distribution and of the scaling relations of these systems, given the different spatial scales involved?

There are many scaling relations, involving the ETGs structural parameters, which we decided to test in the galaxy clusters regime in order to probe the mass assembly of cosmic structures at very different spatial scales. The first one is the color-magnitude relation (Baum 1959). It correlates the stellar population properties of galaxies, expressed by their colors, with their luminosity. In the color-magnitude space, ETGs show a very tight correlation, known as "red sequence", while late-type galaxies are more loosely distributed in what is named as the "blue cloud". The red sequence is characterized by two parameters: scatter and slope. Little evolution of the slope has been observed up to $z \sim 1.3$ (see e.g., van Dokkum et al. 2000; Mei et al. 2006). This fact, together with the small scatter of the correlation, puts strong constraints on galaxy formation models. In this thesis work we identified, for the first time ever, the existence of a red sequence also in the galaxy clusters color-magnitude diagram.

Moreover, we tested the predicted homology of galaxy clusters (i.e., the independence of their light distribution from other parameters, such as the effective radius) and we found that, contrairy to the theoretical predictions, galaxy clusters appear to be non-homologous structures, like ETGs.

The final relation that we want to mention is the Fundamental Plane (FP; Djorgovski and Davis 1987; Dressler et al. 1987). It connects the effective radius with the average intensity (or surface brightness) within it and the central velocity dispersion of ETGs. The physical mechanisms shaping this relation are still unclear and will be investigated later in this thesis. Here we limit ourselves to mention that it is connected with several other galaxy relations (e.g., the Kormendy relation; Kormendy 1977). In this thesis work we proposed a new explaination to its tilt, tightness and Zone of Exclusion.

The structure of this thesis is the following:

- in Chapter 2 we introduce the WINGS and Omega-WINGS surveys (Fasano et al. 2006; Cava et al. 2009; Gullieuszik et al. 2015; Moretti et al. 2015) from which we obtained the data for performing our work;
- in Chapter 3 we present the procedure that we used for building the luminosity and mass profiles;
- in Chapter 4 we discuss about the photometric decomposition performed on the photometric profiles;
- in Chapter 5 we present the detected relations among the structural parameters, among which the color-magnitude relation and the non-homology of clusters;
- in Chapter 6 we focus on the FP relation;
- in Chapter 7 we present the conclusions and future prospects of our work;
- in the Appendix, finally, we discuss some physical arguments that were skipped in Chapter 6 for sake of conciseness.

Throughout the work we have assumed a $\Lambda$-CDM universe, with $H_0 = 70$ km s$^{-1}$ Mpc$^{-1}$ and $\Omega_m = 0.3$.

# Chapter 2

# The WINGS and Omega-WINGS surveys

In this chapter we present the WINGS (Section 2.1) and the Omega-WINGS (Section 2.2) surveys and we give on overview of the data sample used during the whole project (Section 2.3).

## 2.1 The WINGS survey

The WIde-field Nearby Galaxy-cluster Survey (i.e., WINGS, Fasano et al. 2006) is a spectro-photometric survey aimed at creating a high-quality and statistically significant database of the properties of the nearby galaxy clusters and of their galaxies.

The clusters have been selected from the ROSAT X-ray-brightest Abell-type Cluster Sample Survey (Ebeling et al. 1996) and its extensions (Ebeling et al. 1998, 2000) according to two criteria:

- a redshift within the range $0.04 \lesssim z \lesssim 0.07$;
- a galactic latitude $|b| \geq 20^{\circ}$.

The core of the project is called WINGS-OPTical (WINGS-OPT; Fasano et al. 2006; Varela et al. 2009) and consists in $B$- and $V$-band observations collected with the Wide Field Camera at the Isaac Netwon (WFC@INT) for the northern emisphere and the Wide Field Imager at Max Planck Gesellschaft (WFI@MPG) for the southern one (see e.g., Figure 2.1).

The Isaac Newton Telescope (INT) is a 2.54-m optical telescope run, since 1984, by the Isaac Newton Group of Telescopes at Roque de los Muchachos Observatory on La Palma in the Canary Islands. Its mostly used instrument

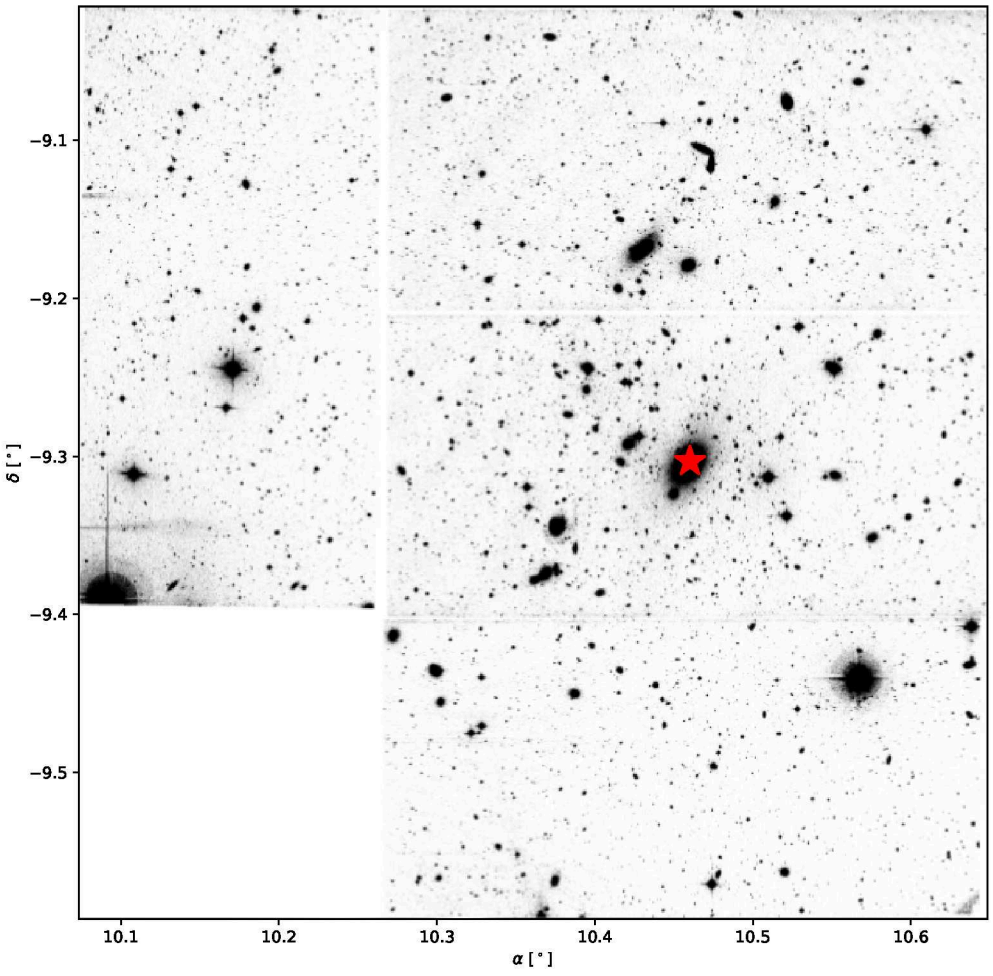


Figure 2.1: WINGS V-band image of A85. North is on the top, East on the right. The red star identifies the BCG position.

is the Wide Field Camera (WFC), a four CCD instrument with a $34' \times 34'$ field-of-view (FoV), which was commissioned in 1997. The WFC consists of 4 thinned EEV 2kx4k CCDs. The CCDs have a pixel size of 13.5 microns corresponding to 0.33 arcsec pixel$^{-1}$. Both broadband and Strömgren filter sets can be installed on the filter wheel, as well as a range of narrow band filters.

The Max Planck Gesellschaft (MPG), instead, is a 2.2-m telescope at the European Southern Observatory (ESO) in La Silla, Chile. MPG was built in 1984 too, and its telescope time is shared between the Max Planck Institute for Astronomy (MPIA) and Max Planck Institute for Extraterrestrial Physics (MPE) observing programmes, while the operation and maintenance an ESO responsibility. The Wide Field Imager (WFI) is a focal reducer-type camera permanently mounted on it. It has a $34' \times 33'$ FoV, a 0.238 arcsec pixel$^{-1}$ and an excellent sensitivity from the near ultraviolet to the near infra-red, with more than 40 filters simultaneously available.

In addition WINGS-OPT was enriched with the WINGS-SPEctroscopy project (WINGS-SPE; Cava et al. 2009), consisting in 6137 spectra obtained by the Wide-field Fibre Optic Spectrograph at the William Herschel Telescope (WYFFOS@WHT) and the Two Degree Field spectrograph at the Anglo-Australian Telescope (2dF@AAT), covering 51 out of the 76 photometrically-observed clusters.

The William Herschel Telescope (WHT) is a 4.2-m optical/near-infrared telescope located at Roque de los Muchachos Observatory, as a part of the Isaac Newton Group of Telescopes. WYFFOS is a multi-object, wide-field, fibre spectrograph containing 150 science fibres, each one of 1.6" diameter, and 10 fiducial bundles for acquisition and guiding. Its spectral range and dispersion are 3800–7000 Å and 3 Å for objects brighter than $m_V = 20$.

The Anglo-Australian Telescope (AAT) is a 3.9-m equatorial telescope operated by the Australian Astronomical Observatory and situated at the Siding Spring Observatory, Australia. It was commissioned in 1974 and in 2009 was ranked as the fifth highest-impact telescope of the world. The Two-degree Field instrument (2dF) installed at the primary focus permits the observation of a field of 2 degrees per pointing. The instrument possesses a spectrograph equipped with two banks each of 200 optical fibres, permitting the simultaneous measurement of 400 spectra. Its spectral range and dispersion are 3600–8000 Å and 9 Å for objects brighter than $m_V = 20$. Consequently, WINGS-SPE is 1.5 magnitudes deeper than the 2dF survey, and 2.0 magnitudes deeper than the SDSS.

Later, WINGS-OPT and WINGS-SPE were enriched with near infrared data thanks to the WINGS-Near Infra-Red project (WINGS-NIR; Valentinuzzi et al. 2009), which consists in $J$- (and $K$-band) images of 19 (and

27) clusters obtained with WFCAM@UKIRT. Moreover, ultra-violet $U$-band data of 17 galaxy clusters were collected from Omizzolo et al. (2014) by combining observations from three different instruments: 90prime@BOK, WFC@INT, and LBC@LBT.

Thanks to the vast amount of data collected, a large number of publications was created, covering a variety of topics, such as: the study of the fundamental plane (D'Onofrio et al. 2008, 2013), the properties of early-type galaxies (Vulcani et al. 2011b; Valentinuzzi et al. 2011), the characterization of superdense massive galaxies (Valentinuzzi et al. 2010; Poggianti et al. 2013) and of faint galaxies (Bettoni et al. 2011), the morphology of galaxies (Fasano et al. 2010, 2012) and its evolution with redshift (Poggianti et al. 2009), the connection of galaxy morphology with the stellar populations (D'Onofrio et al. 2011), the initial mass function of galaxies (Vulcani et al. 2011a) and their mass distribution (Vulcani et al. 2012), or the surface photometry of galaxies (D'Onofrio et al. 2014).

## 2.2 The Omega-WINGS survey

The WINGS project, despite being undoubtedly successfull from the scientific point of view, did not allow a proper study of the transition region between the cluster core and the surrounding environment. In fact, the $34' \times 34'$ WINGS field of view grants a radial coverage limited to $r \lesssim 0.6\, r_{200}$. This is an important limitation, in fact it has been widely demonstrated that the cluster properties vary with the clustercentric distance (see e.g., Lewis et al. 2002; Gómez et al. 2003). For example, Fasano et al. (2015) proved that the morphology-density relation (Dressler 1980) holds only within the cores of WINGS clusters.

To overcome this deficiency and allow a proper study of the property gradients, the Omega-WINGS project was born. Thanks to OmegaCAM@VST $B$- and $V$-band images of 46 WINGS clusters (see e.g., Figure 2.2), with a FoV of 1 square degree each, were obtained by Gullieuszik et al. (2015). Moreover, spectroscopic observations of 17985 objects from 33 of these clusters were carried on by Moretti et al. (2017) thanks to AAOmega@AAT, which spans the wavelenght interval between 3800 Å and 9000 Å.

## 2.3 Our data sample

The photometric and spectroscopic WINGS and Omega-WINGS catalogs are available in the Virtual Observatory thanks to the work of Moretti et al.

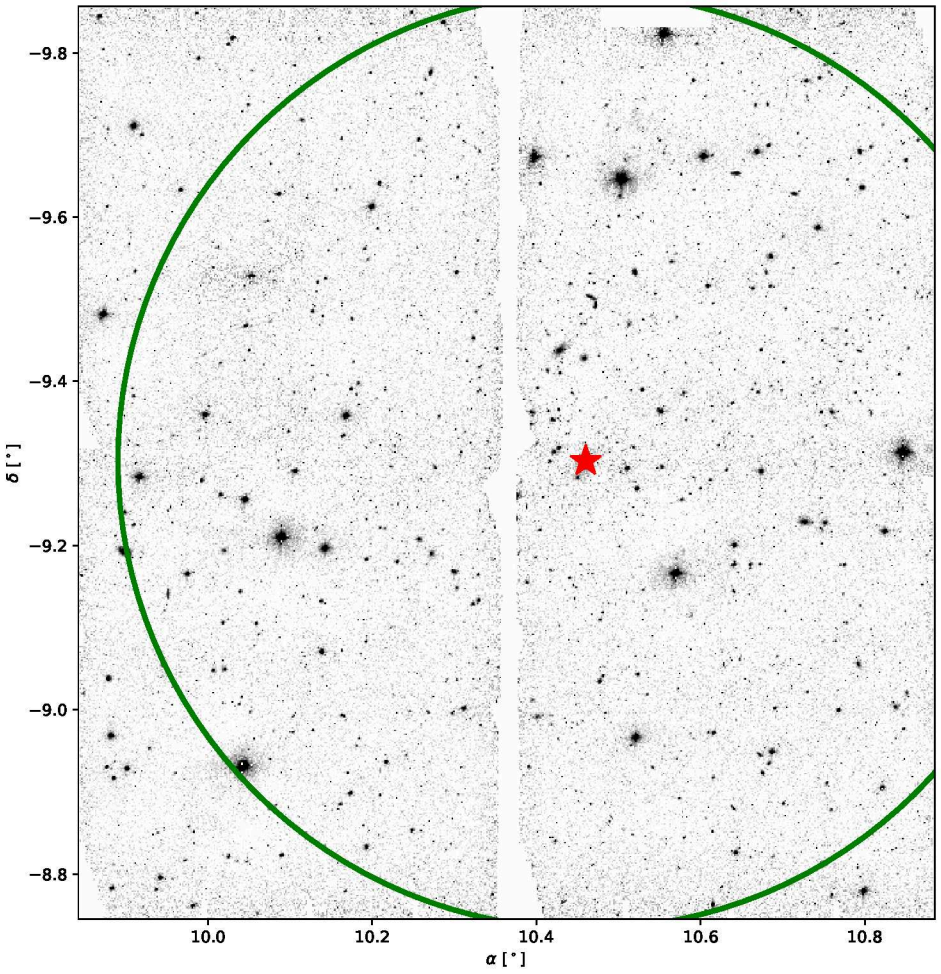


Figure 2.2: Omega-WINGS V-band image of A85. North is on the top, East on the right. The red star identifies the BCG, the green circle $r_{200}$.

(2014) and of Gullieuszik et al. (2015). These catalogs contain not only the magnitude and position of each galaxy, but also other important quantities, such as the effective parameters, the axial ratio, the morphological type, or the SED-derived mass (when available).

In this work we used the following data:

- WINGS and Omega-WINGS $B$- and $V$-band photometric data;
- WINGS and Omega-WINGS spectroscopic data.

The $B$- and $V$-band magnitudes used for each object are the SExtractor AUTO magnitudes (see Bertin and Arnouts 1996 for details), while the WINGS and the Omega-WINGS $V$-band completeness were calculated, respectively, by Varela et al. (2009) and Gullieuszik et al. (2015). The completeness is different from survey to survey, with WINGS being slightly deeper than Omega-WINGS (90% completeness treshold at magnitude $m_V \sim 21.7$ for the WINGS data versus $m_V \sim 21.2$ mag for the Omega-WINGS ones).

The objects in the photometric catalogs belong to three different categories: stars, galaxies, and unknown. This classification was performed according to the SExtractor *stellarity index* of each object and further refined by using different diagnostic diagrams (see Varela et al. 2009 and Gullieuszik et al. 2015 for details). The stars were useless to our purpose, so we focused on the galaxies and unknown objects.

The redshifts of the galaxies in the spectroscopic catalogs, the mean cluster redshifts and the rest-frame velocity dispersions were measured by using a semi-automatic method (Paccagnella et al. 2016). A galaxy was classified as "member" if its redshift was compatible with the cluster redshift with an error at most equal to $\pm 3$ root-mean-squares (RMS). $r_{200}$ was computed as in Poggianti et al. (2006) and used to express the distance from the cluster center (assumed to be the BCG).

In total, we had at our disposal spectroscopic data for 42 of the 46 Omega-WINGS galaxy clusters.

A recap of all the WINGS and Omega-WINGS observations at our disposal is shown in Table 2.1.

Table 2.1: Summary of all the WINGS and OmegaWINGS photometric and spectroscopic observations.

| WINGS cluster | Omega-WINGS photometry | WINGS spectroscopy | Omega-WINGS spectroscopy |
|---|---|---|---|
| A85 | yes | no | yes |
| A119 | yes | yes | no |
| A133 | no | no | no |
| A147 | yes | no | no |
| A151 | yes | yes | no |
| A160 | yes | yes | no |
| A168 | yes | no | yes |
| A193 | yes | yes | yes |
| A311 | no | no | no |
| A376 | no | yes | no |
| A500 | yes | yes | yes |
| A548b | no | no | no |
| A602 | no | no | no |
| A671 | no | yes | no |
| A754 | yes | yes | yes |
| A780 | no | no | no |
| A957 | yes | yes | yes |
| A970 | yes | yes | yes |
| A1069 | yes | yes | yes |
| A1291 | no | yes | no |
| A1631a | yes | yes | yes |
| A1644 | no | yes | no |
| A1688 | no | no | no |
| A1736 | no | no | no |
| A1795 | no | yes | no |
| A1831 | no | yes | no |
| A1983 | yes | yes | no |
| A1991 | yes | yes | no |
| A2107 | yes | yes | no |
| A2124 | no | yes | no |
| A2149 | no | no | no |
| A2169 | no | yes | no |
| A2256 | no | no | no |
| A2271 | no | no | no |
| A2382 | yes | yes | yes |

Table 2.1: Continued.

| WINGS cluster | Omega-WINGS photometry | WINGS spectroscopy | Omega-WINGS spectroscopy |
|---|---|---|---|
| A2399 | yes | yes | yes |
| A2415 | yes | yes | yes |
| A2457 | yes | yes | yes |
| A2572a | no | yes | no |
| A2589 | yes | yes | no |
| A2593 | yes | yes | no |
| A2622 | no | yes | no |
| A2626 | no | yes | no |
| A2657 | yes | no | no |
| A2665 | yes | no | no |
| A2717 | yes | no | yes |
| A2734 | yes | no | yes |
| A3128 | yes | yes | yes |
| A3158 | yes | yes | yes |
| A3164 | no | no | no |
| A3266 | yes | yes | yes |
| A3376 | yes | yes | yes |
| A3395 | yes | yes | yes |
| A3490 | no | yes | no |
| A3497 | no | yes | no |
| A3528a | yes | no | yes |
| A3528b | yes | no | yes |
| A3530 | yes | no | yes |
| A3532 | yes | no | yes |
| A3556 | yes | yes | yes |
| A3558 | yes | no | yes |
| A3560 | yes | yes | yes |
| A3562 | no | no | no |
| A3667 | yes | no | yes |
| A3716 | yes | no | yes |
| A3809 | yes | yes | yes |
| A3880 | yes | no | yes |
| A4059 | yes | no | yes |
| IIZW108 | yes | yes | yes |
| RX0058 | no | yes | no |
| RX1022 | no | yes | no |
| RX1740 | no | yes | no |

Table 2.1: Continued.

| WINGS cluster | Omega-WINGS photometry | WINGS spectroscopy | Omega-WINGS spectroscopy |
|---|---|---|---|
| MKW3s | yes | yes | no |
| Z1261 | no | no | no |
| Z2844 | no | yes | no |
| Z8338 | no | yes | no |
| Z8852 | yes | yes | no |

# Chapter 3

# Construction of the photometric and mass profiles

In this chapter we discuss the procedure that allowed us to build the photometric and mass profiles of Omega-WINGS galaxy clusters. In Section 3.1 we present the procedure that allowed us to build the cluster intensity profiles from which, in Section 3.2, we derived the photometric profiles. In Section 3.3 we quantify the correction associated to the objects fainter than our photometric cut, and in Section 3.4 we explain in which way we combined all the previous data for obtaining the stellar mass profiles of our clusters. Finally, in Section 3.5 we show and comment the photometric and mass profiles of our clusters.

## 3.1 The intensity profiles construction

The Omega-WINGS FoV is 4 times larger than the WINGS one, but it generally does not contain the central regions of the cluster. Moreover, WINGS data are tipically deeper than the corresponding Omega-WINGS ones. For these reasons, instead of working on the Omega-WINGS data alone, we chose to merge the two photometric catalogs. In case of disagreement in the source magnitude, we chose to use the WINGS value, as slightly more precise in most cases. All the objects classified as *stars* were rejected, so we kept only the galaxies and the unknown objects. We will now use the definition of *main photometric catalog* when referring to this catalog, which contains the position of each object, its $B$- and $V$-band magnitudes, and its classification as galaxy, star or unknown objects (see Section 3.1.2 for details).

Then we performed a cross-check with the spectroscopic catalog in order to move the known non-member galaxies (identified by the redshift measure-

ment) from the main photometric catalog to a non-members catalog.

Finally, all the objects in the main photometric catalog were sorted according to their distance from the BCG, which was taken as a reference for defining the cluster center, and we could calculate the intensity profiles starting from the following formula:

$$I(R_n) = \sum_{i=1}^{n} \left[ cc(m_i, R_i) \cdot gf(m_i) \cdot 10^{-0.4\, m_i} \right] - I_{field}, \tag{3.1}$$

where $R_n$ is the distance of the $n$-th source from the BCG computed in degrees (from now on, we will use the notation $R$ when referring to angular distances and $r$ for physical distances), $i \leq n$ is the index of a generic object within $R_n$, $m_i$ the magnitude of this generic object, $R_i$ its distance from the BCG and $cc(m_i, R_i)$ and $gf(m_i)$ its completeness and galaxy fraction corrections (see Sections 3.1.1 and 3.1.2), and $I_{field}$ (Section 3.1.3) is the integrated intensity of all the field objects within the considered area. In Section 3.1.1 we will deepen the completeness correction, in Section 3.1.2 the galaxy fraction correction, and in Section 3.1.3 the field intensity calculation.

### 3.1.1 The completeness correction

The detection probability of a source varies as a function of many parameters, the most important of which, in our case, are its magnitude $m_i$ and cluster-centric distance $R_i$. The completeness correction $cc(m_i, R_i)$ is the inverse of this detection probability. Under the hypothesis that the two parameters are uncorrelated (which is true, if we consider an average CCD sensibility curve by neglecting second-order variations connected to the flat-field of each image), we can express the completeness correction as the product of two mutually-independent terms:

$$cc(m_i, R_i) = c_{ph}(m_i) \cdot ac(R_i), \tag{3.2}$$

namely, the photometric completeness $c_{ph}(m_i)$, and the areal completeness $ac(R_i)$. Each of them will now be studied in detail, starting from $c_{ph}(m_i)$.

The detection rate of galaxies is far more complicated to parametrize than the detection rate of stars because galaxies are extended sources, so their light distribution is not only a function of their magnitude, but it depends also on many secondary parameters (e.g., morphological type, compactness, or inclination). The impact of each parameter on the detection rate could be quantified by running several Monte Carlo simulations meticulously tuned to reproduced the observed parameter distribution, however this approach would not only be time-consuming, but also affected by severe uncertainties.

For avoiding this problem, we decided to introduce a photometric cut where the detection rate is $\sim$ 100%, and to neglect the contribution of fainter sources. We will now discuss the details of our choice.

Moretti et al. (2017) demonstrated that the photometric sample is well represented by the spectroscopic one as long as $m_V \leq 20$ mag. For the WINGS survey the $V$-band detection rate of galaxies was calculated by Varela et al. (2009), who randomly added artificially-generated stars to the WINGS images and quantified the average detection rate as a function of the magnitude. Gullieuszik et al. (2015), instead, calculated the relative completeness of the two surveys by comparing the number of Omega-WINGS objects to the number of WINGS objects, after having applied a normalization to match the total number of sources with $V$-band magnitude 16 mag $< m_V <$ 21 mag, to correct the observations for the different sky coverage.

At $m_V = 20$ mag the WINGS detection rate is equal to 97%, and the relative completeness among the two surveys is 100%, plus the fraction of light given by the unknown objects is completely negligible, which means that SExtractor is able to properly classify the overwhelming majority of galaxies. All these considerations made us feel safe to choose $m_V = 20$ mag for applying the previously-mentioned photometric cut. In Section 3.3 we will demonstrate that this choice is legitimated also by the fact that the integrated contribution of the fainter sources to the cluster luminosity is negligible.

The $B$-band completeness correction, instead, was not evaluated for any of the two surveys. Therefore, being unable to determine the $B$-band 97% completeness treshold, we chose to build our photometric profiles by using only a $V$-band limited sample of objects, with $m_V \leq 20$ mag, and to assume $c_{ph} = 1$ also in the case of the $B$-band observations.

In order to determine whether these assumptions could lead us to introducing some bias, we considered the following facts:

- the equal number of sources in the $B$ and $V$ bands rules out the possibility of having drastically different $c_{ph}$ values between the two bands within the considered photometric range;
- the integrated intensity of all the sources of our catalogs with $m_B \leq 20$ exceeds of a factor larger than 10 the combined intensity of all the sources within the magnitude range: 20 mag $< m_B \leq 21$ mag;
- the introduction of a $B$-band photometric cut, whose difference with respect to the $V$-band photometric cut is tuned to reproduced the observed average cluster color (i.e., $\overline{(B-V)} \sim 0.8$), did not significantly modify the measured intensity and color profiles.

All these considerations made us feel safe in assuming only a $V$-band completeness treshold and a photometric completeness correction $c_{ph} = 1$ for both the photometric bands.

So the completeness correction was approximated with only the second term of Equation 3.2, namely the areal completeness correction $ac(R_i)$.

The detection rate of an object is a function of its position in the sky, here expressed thanks to the clustercentric distance $R_i$. In fact, due to the presence of gaps between the CCDs and to the fact that our FoV is not a circle centered on the BCG, when integrating on circular areas a fraction of each circle can lay outside the FoV. The areal completeness correction is used to account for this pixel loss, which reflects on a loss of sources too, therefore it is defined as the inverse of the fraction of the ring of mean radius $R_i$ and thickness 1 pixel that lies inside the merged WINGS and Omega-WINGS FoVs.

### 3.1.2 The galaxy fraction

Under the reasonable assumption that SExtractor did not misclassify any star as *galaxy*, at least in the considered photometric range, the galaxy fraction is 1 for all the sources classified as *galaxies*. However, it becomes smaller than 1 when we consider the unknown objects, because they can contain a certain fraction of stars. This galaxy fraction among the unknown was calculated by Varela et al. (2009) and is in good agreement with other values that can be found in literature at least up to $m_V = 24$ mag.

For objects brighter than 20 the expected percentage of galaxies among the unknown is 100%, while for fainter objects (observed only in the $B$ band) it goes down to 95%.

### 3.1.3 The field intensity

To quantify the intensity emitted by the field galaxies firstly we used the galaxy number counts provided by Berta et al. (2006), which were derived with the same WINGS instrumental setup, and secondly we corrected the derived quantity for the intensity associated to the already identified field objects. Therefore, the intensity associated to the field objects can be expressed according to the following formula:

$$I_{field}(R_n) = I_{Berta}(R_n) - I_{non\text{-}members}(R_n), \tag{3.3}$$

where $I_{Berta}(R_n)$ is the intensity calculated starting from the statistical number counts, and $I_{non\text{-}members}(R_n)$ is the intensity associated to the detected

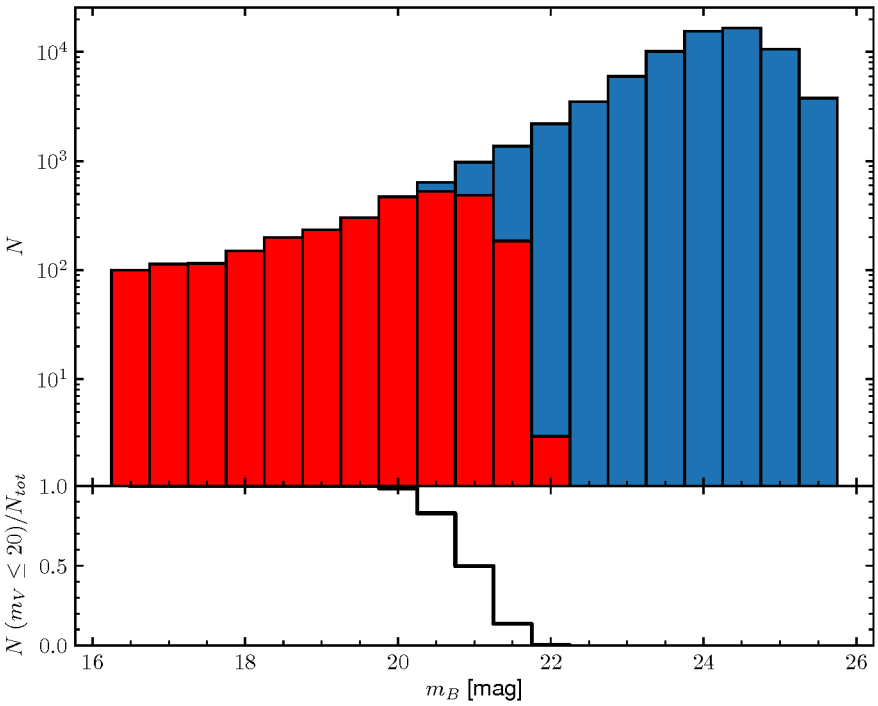


Figure 3.1: Upper panel: total number of galaxies in each $B$-band magnitude interval detected by Berta et al. (2006) (in blue), and fraction of them with $m_V \leq 20$ mag (in red). Lower panel: fraction $f_j$ of galaxies with $V$-band magnitude brighter than 20 as a function of their $B$-band magnitude.

non-member galaxies in the considered FoV and within the considered radius $R_n$. Now we will analyze each of the previous terms in detail, starting from the first one.

Berta et al. (2006) provide the $V$- and $B$-band galaxy number counts from magnitude 16 to 28 and normalized to a 1-square-degree FoV, with bins of width 0.5 mag. Therefore, we can define $I_{Berta}$ as:

$$I_{Berta}(R_n) = \pi\, R_n^2 \cdot \sum_{j=1}^{p} N_j \cdot f_j(m_V \leq 20) \cdot 10^{-0.4 m_j}, \tag{3.4}$$

where $j$ is the generic index associated to any magnitude bin, $p$ is the total number of bins, $N_j$ and $m_j$ are the number of counts and their average magnitude within the $j$-th bin, and $f_j(m_V \leq 20)$ is the fraction of galaxies in the considered magnitude bin with $m_V \leq 20$ mag.

For the $V$ band $f_j(m_V \leq 20)$ is a step function equal to 1 when $m_V \leq 20$ mag and equal to 0 when $m_V \geq 20$ mag, while for the $B$-band data, given that we are dealing with a $V$-band-limited sample, it is necessary to subtract only the field contribution given by objects brighter than $m_V = 20$ mag. To achieve this, we downloaded the Berta et al. (2006) original photometric data and we rebuilt the histogram of galaxy counts taking into account only these sources. In Figure 3.1 we show their trend (in red) versus the trend of the original sample (in blue). The trend of $f_j(m_V \leq 20)$ in fractional units, instead, is plotted in the bottom panel.

Now we will analyze the second term: $I_{non\text{-}members}(R_n)$. It is needed because, while $I_{Berta}$ can provide the intensity of the statistically-expected field sources, we already removed a certain amount of such object due to the membership check. So, in order to avoid the oversampling of the field objects contribution, we needed to introduce this term into the equation. Under the hypothesis of having detected $q$ field galaxies, $I_{non\text{-}members}$ is equal to:

$$I_{non\text{-}members} = \pi\, R_n^2 \cdot \sum_{k=1}^{q} \frac{10^{-0.4 m_k}}{\mathrm{FoV}}, \tag{3.5}$$

where $k$ is the index associated to the a generic detected field galaxy with magnitude $m_k$, and the FoV is expressed in square degrees. The lower magnitude limit for including an object in the sum corresponds to the bright end of Berta et al. (2006) number counts, while the upper one to our photometric cut.

## 3.2 The photometric profiles construction

Equation 3.1 allowed us to calculate the the integrated intensity value at the distance of every source from the BCG, which resulted in an oversampling of the profiles and in an irregular spacing between the points. In order to have equally-spaced points we rebinned our data through a weighted least squares (WLS) interpolation with a constant sampling of $0.05\, r_{200}$. Then we converted the integrated intensity profiles into differential intensity profiles, which we converted into absolute magnitude profiles ($M_B(\leq R)$ and $M_V(\leq R)$), from which we derived the local color profiles:

$$(B-V)(R) = M_B(R) - M_V(R). \tag{3.6}$$

Starting from the local color profiles, we calculated the K-correction for each radial bin like in Poggianti (1997). In fact, the K-correction is a function of two parameters: the first is the average color index and the second is the redshift of the source, which was assumed to be the mean cluster redshift. If a radial bin had $(B-V) \geq 0.8$ we adopted the K-correction valid for ETGs, if it had $0.8 > (B-V) \geq 0.5$ we applied typical correction for Sa galaxies, while if it had $(B-V) < 0.5$ we used the $K$-correction of Sc and Irregular galaxies.

This is clearly an approximation, in fact the K-correction should be applied to each galaxy singularly thanks to a precise knowledge of its morphology and redshift, which unfortunately are available only for the objects belonging to the spectroscopic sample. However, as long as the procedure in Section 3.1 is correct the average K-correction of the galaxy populations in each bin can reliably be calculated without introducing errors larger than 0.05 mag.

## 3.3 The faint objects correction

Quantifying the amount of light coming from sources fainter than our photometric cut is of fundamental importance for understanding if our photometric and color profiles can reliably reproduce the properties of the observed clusters.

In order to do it we used the luminosity function (LF) provided by Moretti et al. (2015) for the $V$-band data of the stacked WINGS sample. Such a parametrization is based on a double Schechter function:

$$\phi(L) = \left(\frac{\phi_V^b}{L_V}\right) \cdot \left(\frac{L}{L_V^b}\right)^{\alpha^b} \cdot e^{-L/L_V^b} + \left(\frac{\phi_V^f}{L_V}\right) \cdot \left(\frac{L}{L_V^f}\right)^{\alpha^f} \cdot e^{-L/L_V^f}, \quad (3.7)$$

where $\phi_V^b$ and $\phi_V^b$ are normalization constants, $L_V^b$ is the luminosity associated to $M_V^b = -21.25$ mag, $\alpha^b = -1.10$, $L_V^f$ is the luminosity associated to $M_V^f = -16.25$ mag, and $\alpha^f = -1.5$.

Under the assumptions that all the clusters have a similar LF and that $\phi(L)$ is not a function of $R$ (which is only an approximation of the real case, where the LF varies with $R$; see, e.g., Agulli et al. 2016, 2017), we could calculate an approximated LF correction $c_{LF}$ as the ratio between the total expected $V$-band cluster intensity $I_{tot}$ and the observed one $I_{obs}$:

$$c_{\rm LF} = \frac{I_{tot}}{I_{obs}} = \frac{\int_0^{L_{\rm BCG}} L\,\phi(L)\,dL}{\int_{L_{V,cut}}^{L_{\rm BCG}} L\,\phi(L)\,dL}, \quad (3.8)$$

where $L_{\rm BCG}$ is the $V$-band luminosity of the BCG, and $L_{V,cut}$ is the $V$-band luminosity at magnitude 20. The two integrals represent the luminosity density associated to a distribution of objects with LF $\phi(L)$ and luminosity within the integration interval. Both the integrals can be solved through the incomplete gamma function and lead to a correction of the order of $2-5\%$.

Being a very small value, we can conclude that our hypothesis of introducing a photometric cut at $m_V = 20$ mag cannot generate any significant bias; finally, since the $B$-band LF was not derived, we decided to not apply such a correction to our photometric profiles.

## 3.4 The mass profiles construction

In order to build the stellar mass profiles of our clusters, a four-steps procedure was followed:

- firstly, we built the stellar luminosity profiles of our photometric sample;
- secondly, we repeated the same procedure but selecting only the objects within the spectroscopic sample;
- thirdly, we built the stellar mass profiles for the spectroscopically-selected cluster members;

- finally, starting from the previously-derived profiles and from the faint objects correction, we obtained the total stellar mass profiles of the clusters.

Now we shall analyze each of these points into detail.

The construction of the luminosity profiles for the photometric sample was performed as described in Sections 3.1 and 3.2. The construction of the luminosity profiles of the spectroscopic sample, instead, presented three fundamental differences:

- the photometric completeness could reach values significantly smaller than the aforementioned 97%, which means that the associated correction in Equation 3.2 ($c_{ph}$) could not be approximated with 1 anymore. However, since the photometric sample is nearly 100% complete, Moretti et al. (2017) were able to precisely calculate the detection rate without making any prior assumption;
- no galaxy fraction correction was needed;
- the statistical field subtraction was not needed, as the membership of each object was known.

The spectro-photometric masses of all the galaxies in the spectroscopic sample either are public (Fritz et al. 2011) or have been measured by Moretti et al. (private communication) with the same SED-fitting procedure described by Fritz et al. (2007). This allowed us to build the spectroscopic stellar mass profiles through the following formula:

$$\mathcal{M}_{sp}(\leq R_n) = \sum_{i=1}^{n} cc(m_i, R_i) \cdot \mathcal{M}_i, \tag{3.9}$$

which is a sum analogous to the one in Equation 3.1, where $\mathcal{M}_i$ is the mass of the $i$-th galaxy cluster member and $cc(m_i, R_i)$ has been defined in Equation 3.2. As for the photometric profiles, the stellar mass profiles were also rebinned to have equally-spaced points every $0.05\, r_{200}$.

Finally, the integrated mass profiles were built starting from the previous ones thanks to the following formula:

$$\mathcal{M}_{tot}(\leq R) = c_{\rm LF}\, \mathcal{M}_{sp}(\leq R) \cdot \frac{L_{ph}(\leq R)}{L_{sp}(\leq R)}, \tag{3.10}$$

where $L_{ph}(\leq R)$ and $L_{sp}(\leq R)$ are, respectively, the integrated luminosity within the radius $R$ of the photometric and spectroscopic samples, and $c_{LF}$ is the above-mentioned correction for faint objects.

Behind this relation there is the implicit assumption that the measured mass-to-light ratio at each radius is representative of the true one in the cluster, which is generally true since the overall spectroscopic sample is more than 80% complete with respect to the photometric one for $m_V \leq 20$ mag.

## 3.5 The photometric and mass profiles

Table 3.1 compares the main parameters of our clusters.

Figures 3.2−3.24 show the photometric profiles of our galaxy clusters. In the upper plots we see the integrated magnitude profiles, in the central ones the integrated and local $(B-V)$ color profiles and in the lower ones the surface brightness profiles. Blue and green lines are, respectively, the $B$- and $V$-band data, while yellow and orange lines are the local and integrated colors.

Figures 3.25−3.45 present the light and mass profile of our clusters both for the photometric and spectroscopic samples. The upper panels display the integrated $V$-band luminosity of the photometric (green line) and spectroscopic (red line) samples, while the lower ones show the associated stellar mass profiles.

A number of considerations emerge from their analysis:

- most of the luminosity profiles seem to be still increasing at the maximum photometric radius;
- the $(B-V)$ integrated color typical of a moderately evolved mix of stellar populations ($\overline{(B-V)} \sim 0.75$) and usually shows a gradient between the central region, which is redder, and the outskirts, which are bluer; in the most extreme case (i.e., IIZW108) such gradient is equal to $\Delta(B-V)/\Delta r = 0.36$ mag $r_{200}^{-1}$. The local colors are, generally, more noisy than the integrated ones due to the lack of sources in some radial bins;
- the surface brightness profiles, although dominated by random fluctuations at the adopted spatial binning, show a clear cusp in the central region and very different gradients when the profiles are plotted in units of $r_{200}$;
- the spectroscopic and the photometric light and stellar mass profiles are quite different from cluster to cluster.

Concerning the last point we believe that the origin of the systematic difference between the photometric and spectroscopic profiles is due to the

observational difficulty of positioning the multi-object spectrograph fibers to get a simultaneous coverage in the whole cluster region, particularly in the dense core of the clusters. In most cases the spectra of the most luminous galaxies in the cluster center have not been obtained, and sometimes even the BCG spectrum is missing. The consequence is that the completeness correction $c_{ph}(m_i)$ (i.e., the ratio between the total number of objects in a given magnitude bin from the photometric sample and the corresponding number from the spectroscopic sample) could not be calculated in certain magnitude bins, so the lost flux clould not be redistribuited between the observed sources (e.g., in Equation 3.9), resulting in a net displacement of the two curves. The effect appears to be larger in the center and smaller in the outern regions, thus supporting our explanation. Clearly, the correct mass and light profiles are those based on the most complete photometric sample.

Table 3.1: Cluster name (Column 1), LF correction (Column 2), observed over total expected cluster luminosity (Column 3), color gradient (Column 4), number of substructures from Ramella et al. (2007) (Column 5), total luminosity of the substructures over the main cluster component luminosity (Column 6), effective radius in units of $r_{200}$ (Column 7), effective LF-corrected mass (Column 8), $r_{200}$ in units of kpc (Column 9), and integrated mass within $r_{200}$ (Column 10).

| Cluster | LF corr. | $L_{obs}/L_{exp}$ | $\Delta(B-V)/\Delta r$ mag $r_{200}^{-1}$ | $N_{sub}$ | $L_{sub}/L_{main}$ | $R_e/r_{200}$ | $\mathcal{M}_e$ $10^{13}$ $M_\odot$ | $r_{200}$ kpc | $\mathcal{M}_{200}$ $10^{13}$ $M_\odot$ |
|---|---|---|---|---|---|---|---|---|---|
| A85 | 1.03 | 0.66 | −0.27 | 2 | 0.72 | 0.87 | 0.91 | 2366 | 1.15 |
| A119 | 1.02 | 0.42 | −0.06 | 2 | 0.36 | - | - | 2087 | - |
| A147 | 1.03 | 0.85 | −0.29 | 2 | 0.34 | - | - | 1612 | - |
| A151 | 1.03 | 0.52 | −0.12 | 2 | 0.71 | 1.33 | 1.12 | 1779 | 1.00 |
| A160 | 1.03 | 0.61 | −0.11 | 3 | 0.44 | - | - | 1359 | - |
| A168 | 1.03 | 0.75 | −0.32 | 1 | 0.28 | 1.22 | 0.70 | 1323 | 0.67 |
| A193 | 1.03 | 0.93 | −0.17 | 0 | - | 0.29 | 0.18 | 1847 | 0.40 |
| A500 | 1.05 | 0.75 | −0.23 | 1 | 0.50 | 1.22 | 0.79 | 1895 | 0.71 |
| A754 | 1.03 | 0.58 | −0.18 | 2 | 0.97 | 0.88 | 2.00 | 2216 | 2.14 |
| A957 | 1.02 | 0.60 | −0.26 | 0 | - | 1.83 | - | 1550 | 0.41 |
| A970 | 1.04 | 0.72 | −0.32 | 1 | 0.30 | 0.76 | 0.83 | 2031 | 1.10 |
| A1069 | 1.05 | 0.66 | −0.32 | 1 | 0.50 | 1.59 | 0.95 | 1667 | 0.78 |
| A1631a | 1.03 | 0.84 | −0.15 | 0 | - | 1.11 | 2.33 | 1839 | 1.78 |
| A1983 | 1.03 | 0.63 | −0.22 | - | - | - | - | 1276 | - |
| A1991 | 1.04 | 0.77 | −0.20 | 1 | 0.40 | - | - | 1441 | - |
| A2107 | 1.02 | 0.72 | −0.17 | 0 | - | - | - | 1436 | - |
| A2382 | 1.04 | 0.76 | −0.18 | 0 | - | 1.28 | 1.12 | 1675 | 0.78 |
| A2399 | 1.04 | 0.85 | −0.27 | - | - | 1.08 | 0.81 | 1755 | 0.79 |

Table 3.1: Continued.

| Cluster | LF corr. | $L_{obs}/L_{exp}$ | $\Delta(B-V)/\Delta r$ mag $r_{200}^{-1}$ | $N_{sub}$ | $L_{sub}/L_{main}$ | $R_e/r_{200}$ | $\mathcal{M}_e$ $10^{13}$ $M_\odot$ | $r_{200}$ kpc | $\mathcal{M}_{200}$ $10^{13}$ $M_\odot$ |
|---|---|---|---|---|---|---|---|---|---|
| A2415 | 1.04 | 1.38 | −0.27 | 1 | 0.14 | 0.69 | 0.47 | 1661 | 0.76 |
| A2457 | 1.04 | 0.97 | −0.21 | 1 | 0.07 | 0.77 | 0.80 | 1634 | 0.95 |
| A2589 | 1.02 | 0.59 | −0.31 | 1 | 0.35 | - | - | 1978 | - |
| A2593 | 1.02 | 0.74 | −0.23 | - | - | - | - | 1700 | - |
| A2657 | 1.02 | 0.76 | −0.16 | 1 | 0.77 | - | - | 924 | - |
| A2665 | 1.04 | 0.57 | −0.29 | 1 | 0.03 | - | - | 1500 | - |
| A2717 | 1.03 | 0.62 | −0.10 | - | - | 1.87 | - | 1315 | 0.27 |
| A2734 | 1.04 | 0.68 | −0.14 | 3 | 0.52 | 1.39 | 1.23 | 1875 | 1.00 |
| A3128 | 1.04 | 0.63 | −0.19 | 3 | 1.53 | 1.00 | 2.45 | 2016 | 2.45 |
| A3158 | 1.04 | 0.61 | −0.22 | 1 | 0.65 | 1.08 | 1.82 | 2461 | 1.76 |
| A3266 | 1.04 | 0.47 | −0.24 | 0 | - | - | - | 3170 | - |
| A3376 | 1.03 | 0.52 | −0.26 | 2 | 0.66 | 1.55 | - | 2043 | 3.43 |
| A3395 | 1.03 | 0.25 | −0.10 | - | - | - | - | 2912 | - |
| A3528a | 1.03 | 0.55 | −0.21 | - | - | 1.34 | - | 2450 | 1.15 |
| A3528b | 1.03 | 0.49 | −0.30 | 1 | 0.25 | - | - | 2078 | - |
| A3530 | 1.03 | 0.52 | −0.09 | 0 | - | 1.61 | 3.91 | 1625 | 1.91 |
| A3532 | 1.04 | 0.52 | −0.17 | 0 | - | 2.48 | - | 1940 | 0.07 |
| A3556 | 1.03 | 0.63 | −0.10 | - | - | 1.39 | 3.51 | 1616 | 2.51 |
| A3558 | 1.03 | 0.38 | −0.25 | 0 | - | - | - | 2424 | - |
| A3560 | 1.03 | 0.27 | −0.12 | - | - | 2.45 | - | 2030 | 2.23 |
| A3667 | 1.04 | 0.29 | −0.02 | 3 | 1.16 | 2.42 | - | 2434 | 2.45 |
| A3716 | 1.03 | 0.89 | −0.10 | 1 | 0.64 | 0.39 | 2.14 | 2053 | 3.80 |
| A3809 | 1.04 | 1.01 | −0.26 | - | - | 1.13 | 1.26 | 1330 | 1.20 |

Table 3.1: Continued.

| Cluster | LF corr. | $L_{obs}/L_{exp}$ | $\Delta(B-V)/\Delta r$ mag $r_{200}^{-1}$ | $N_{sub}$ | $L_{sub}/L_{main}$ | $R_e/r_{200}$ | $\mathcal{M}_e$ $10^{13}$ $M_\odot$ | $r_{200}$ kpc | $\mathcal{M}_{200}$ $10^{13}$ $M_\odot$ |
|---|---|---|---|---|---|---|---|---|---|
| A3880 | 1.04 | 0.42 | −0.01 | 0 | - | 2.44 | - | 1656 | 1.12 |
| A4059 | 1.03 | 0.63 | −0.06 | - | - | 1.27 | - | 1818 | 1.57 |
| IIZW108 | 1.03 | 0.67 | −0.36 | 1 | 0.17 | 1.37 | 0.59 | 1478 | 0.48 |
| MKW3s | 1.03 | 0.63 | −0.23 | 1 | 0.12 | - | - | 1305 | - |
| Z8852 | 1.02 | 0.74 | −0.21 | 2 | 0.19 | - | - | 1690 | - |

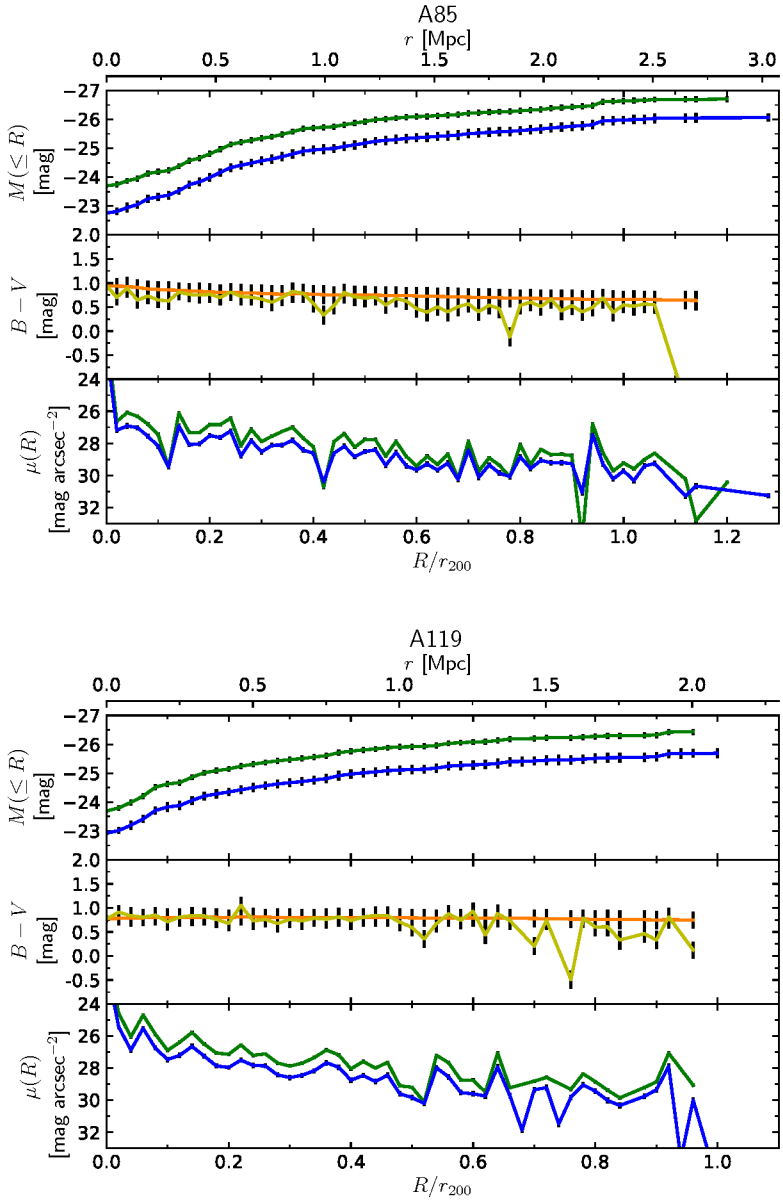


Figure 3.2: Photometric profiles of the clusters A85 and A119. Upper plot: integrated magnitude profiles, where the blue lines correspond to the $B$-band data, and the green lines to the $V$-band data. Central plot: color index profile with the orange lines corresponding to the integrated color index $(B-V)(\leq R)$ and the yellow lines to the local color index $(B-V)(R)$. Lower plot: surface brightness profiles, with the same color code of the upper plot.

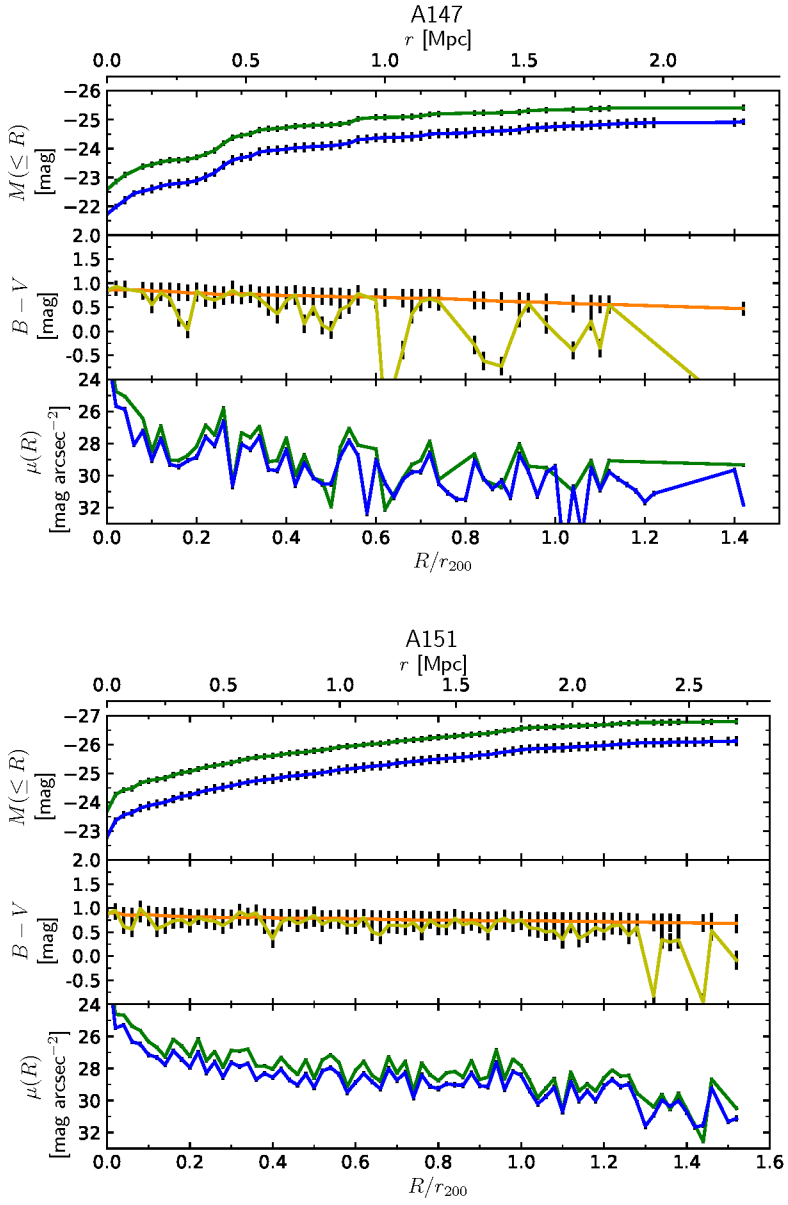


Figure 3.3: Photometric profiles of the Omega-WINGS galaxy clusters. Continued.

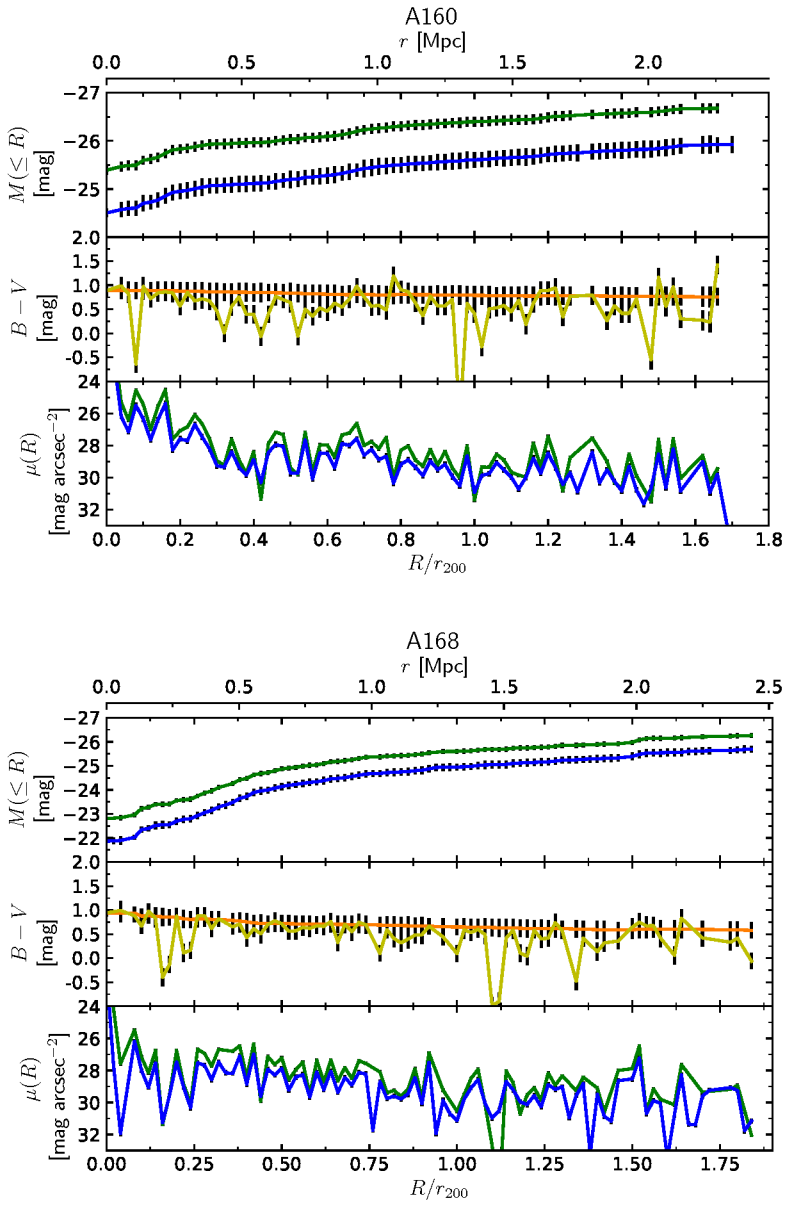


Figure 3.4: Photometric profiles of the Omega-WINGS galaxy clusters. Continued.

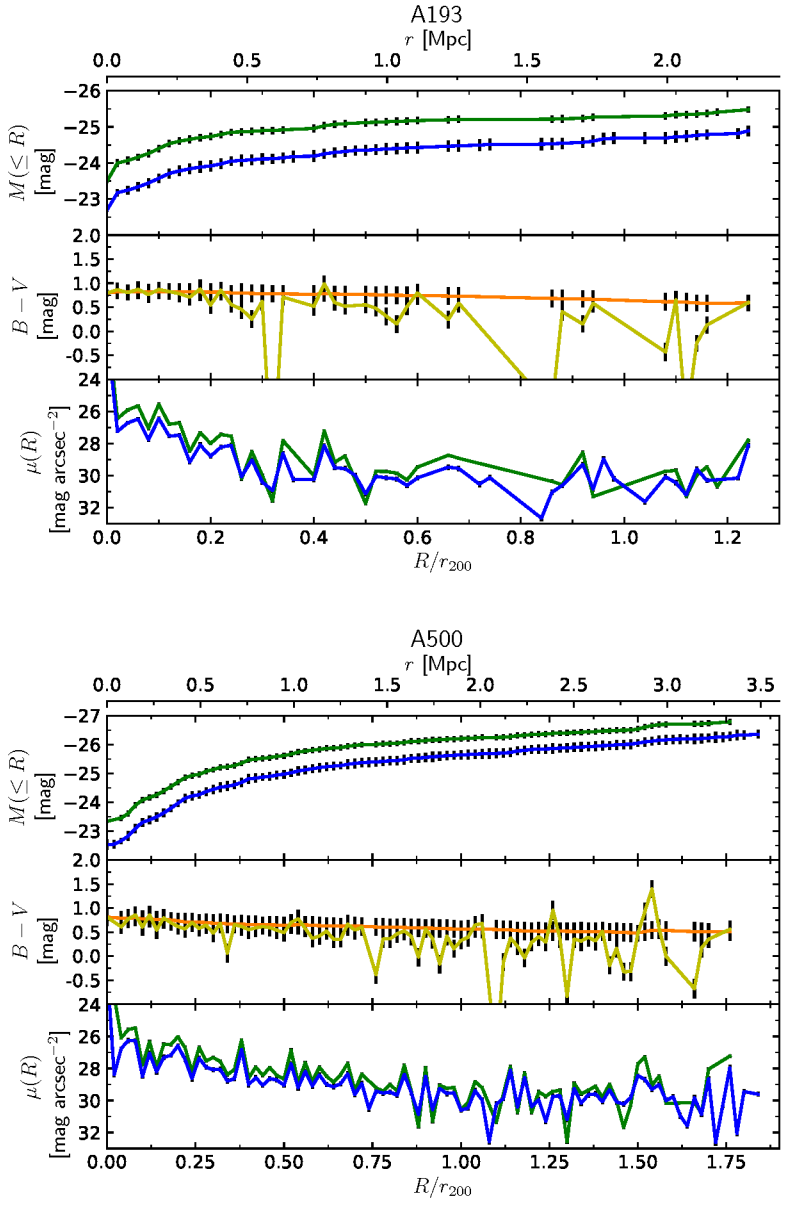


Figure 3.5: Photometric profiles of the Omega-WINGS galaxy clusters. Continued.

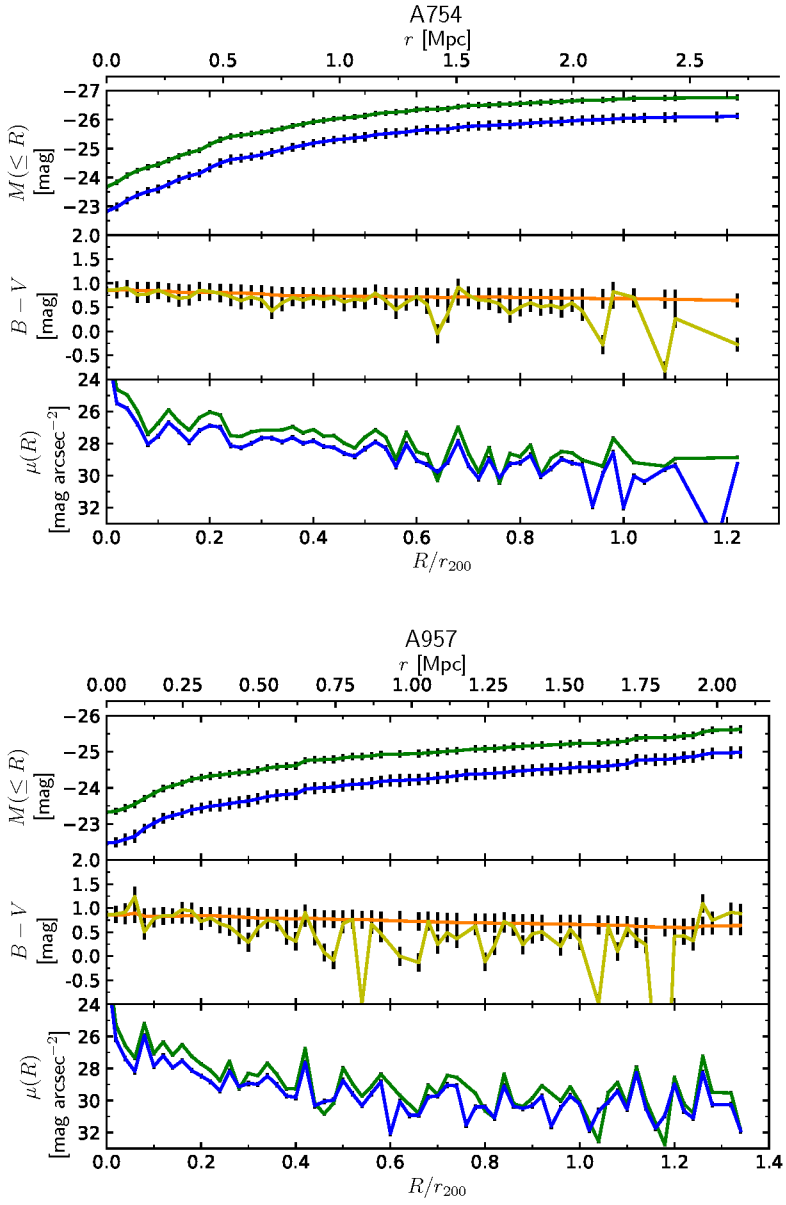


Figure 3.6: Photometric profiles of the Omega-WINGS galaxy clusters. Continued.

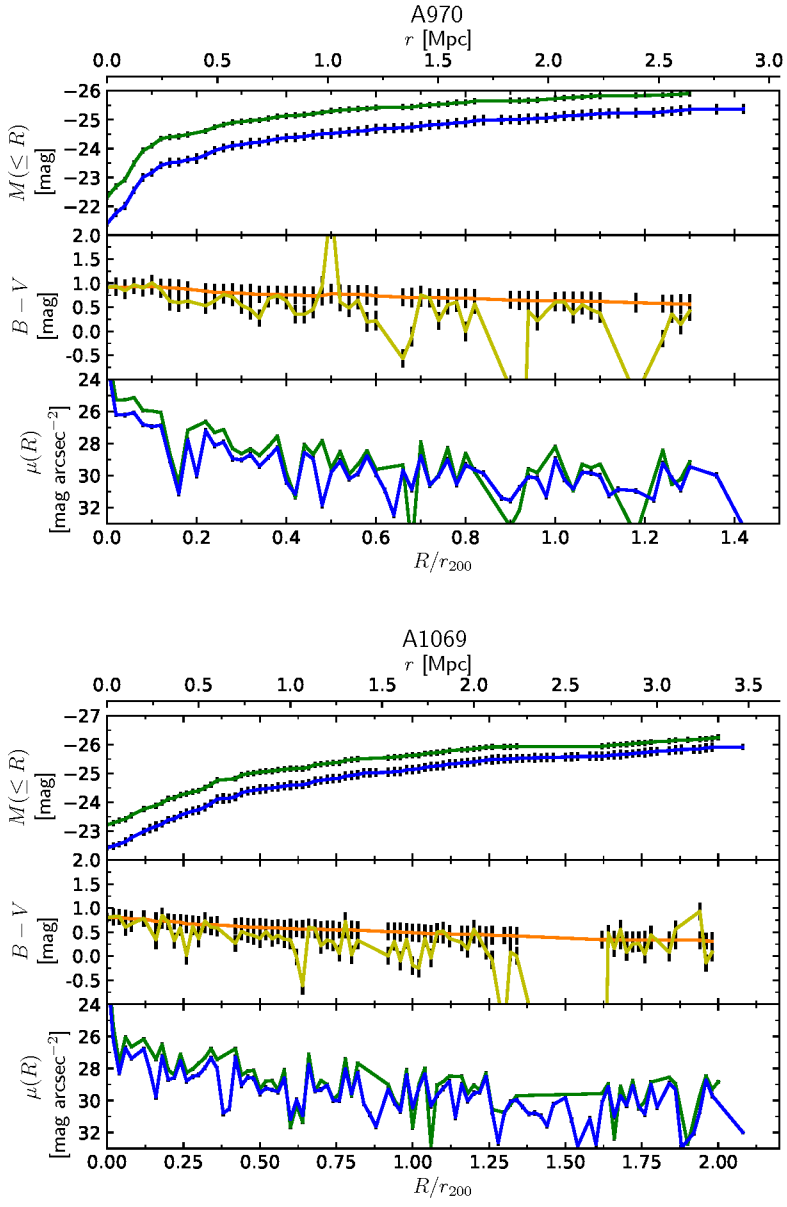


Figure 3.7: Photometric profiles of the Omega-WINGS galaxy clusters. Continued.

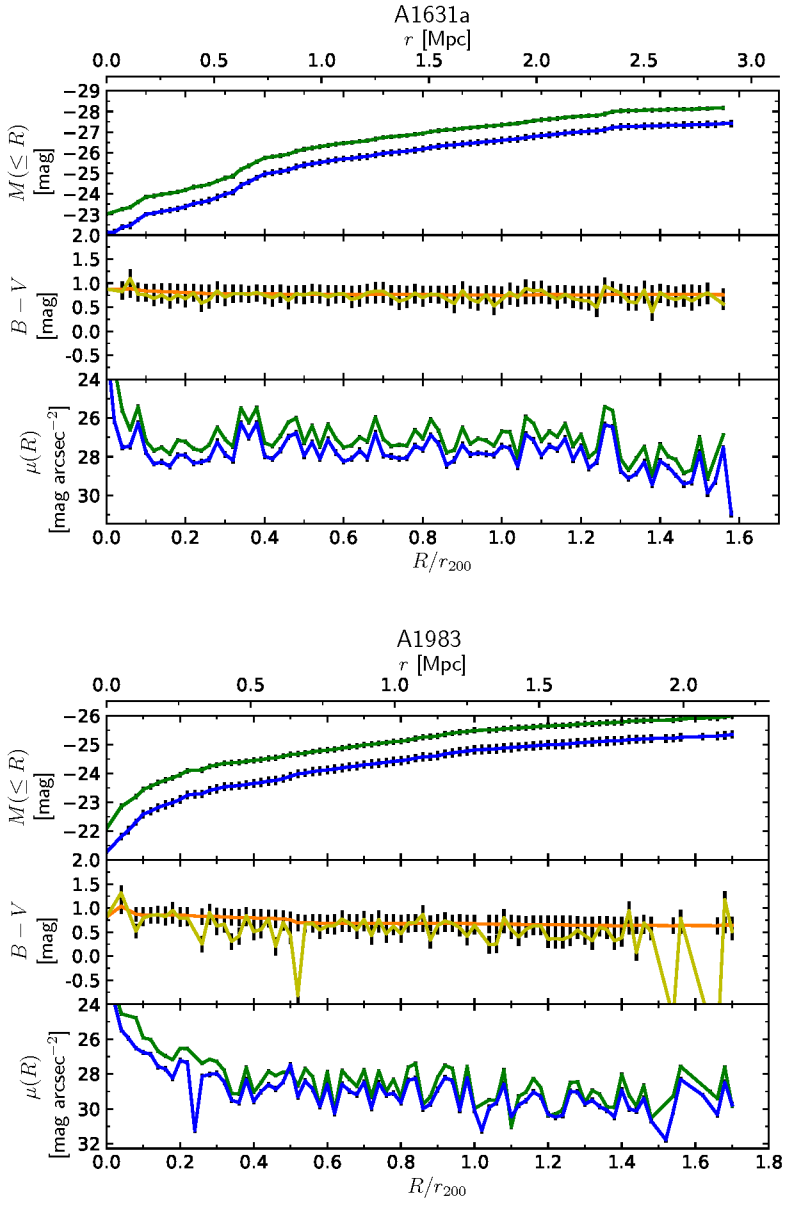


Figure 3.8: Photometric profiles of the Omega-WINGS galaxy clusters. Continued.

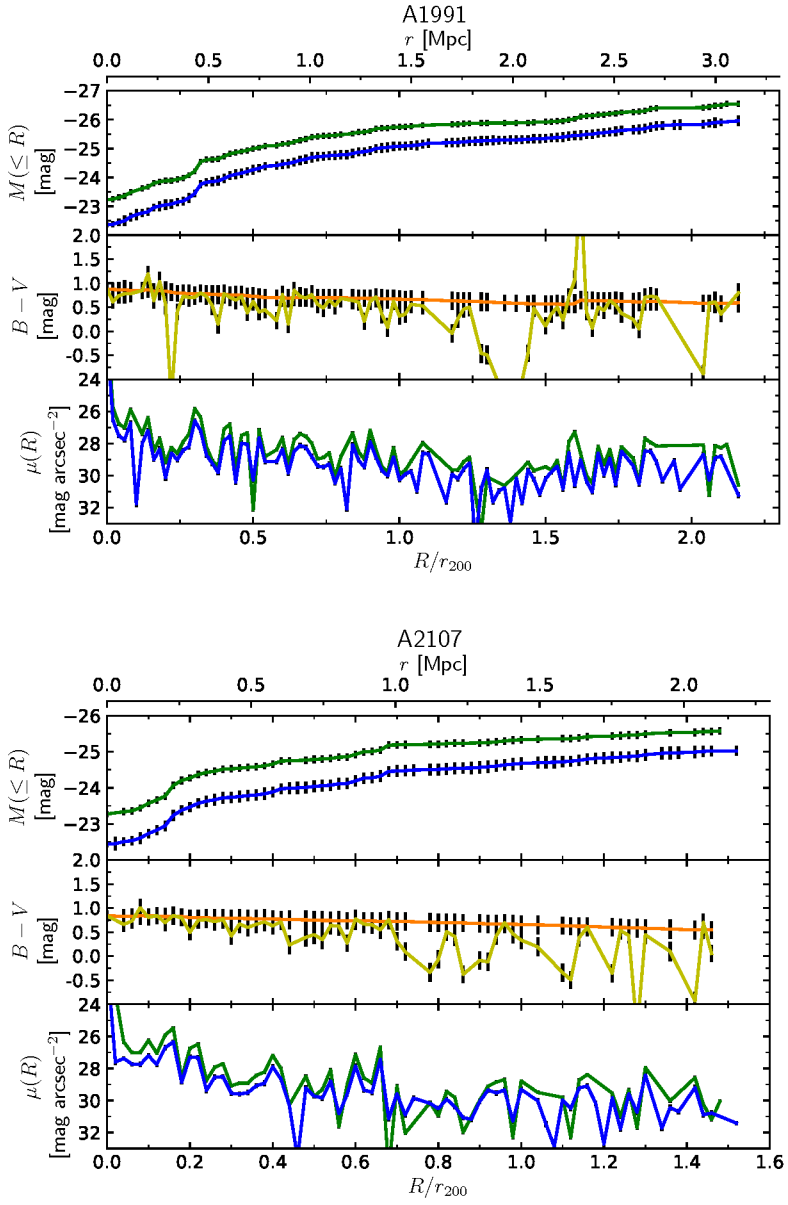


Figure 3.9: Photometric profiles of the Omega-WINGS galaxy clusters. Continued.

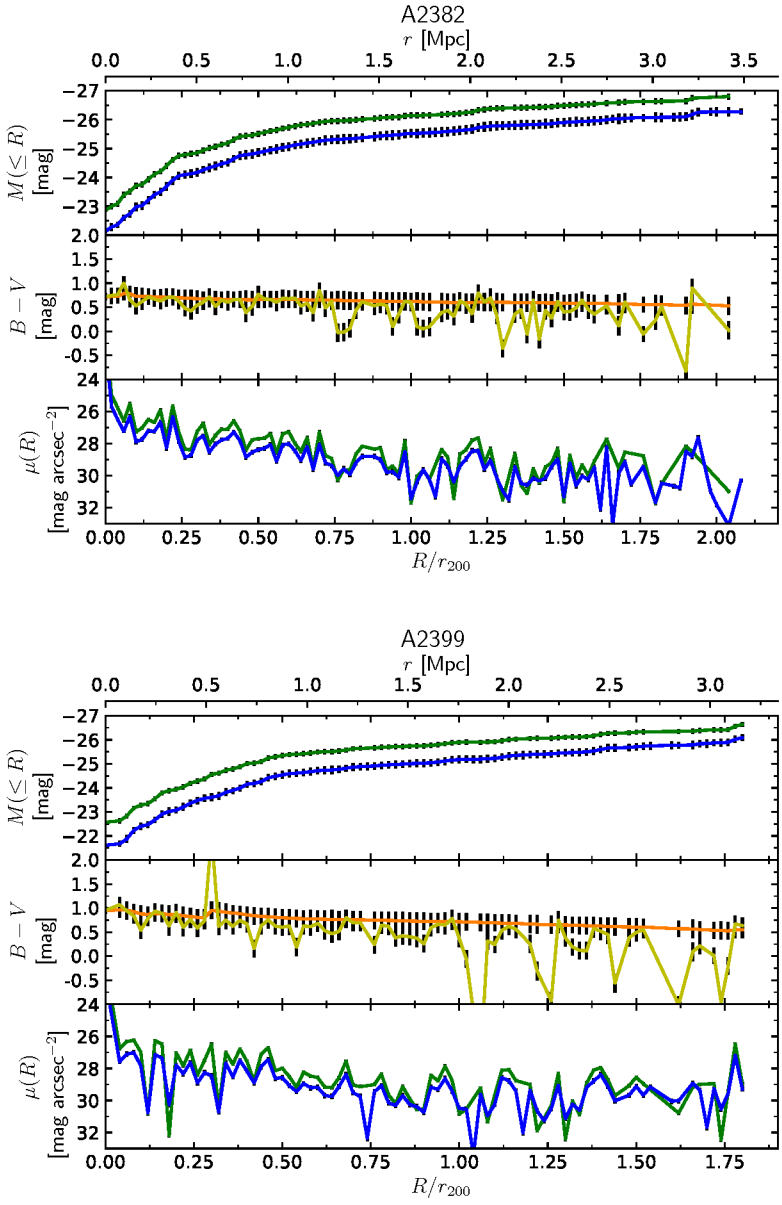


Figure 3.10: Photometric profiles of the Omega-WINGS galaxy clusters. Continued.

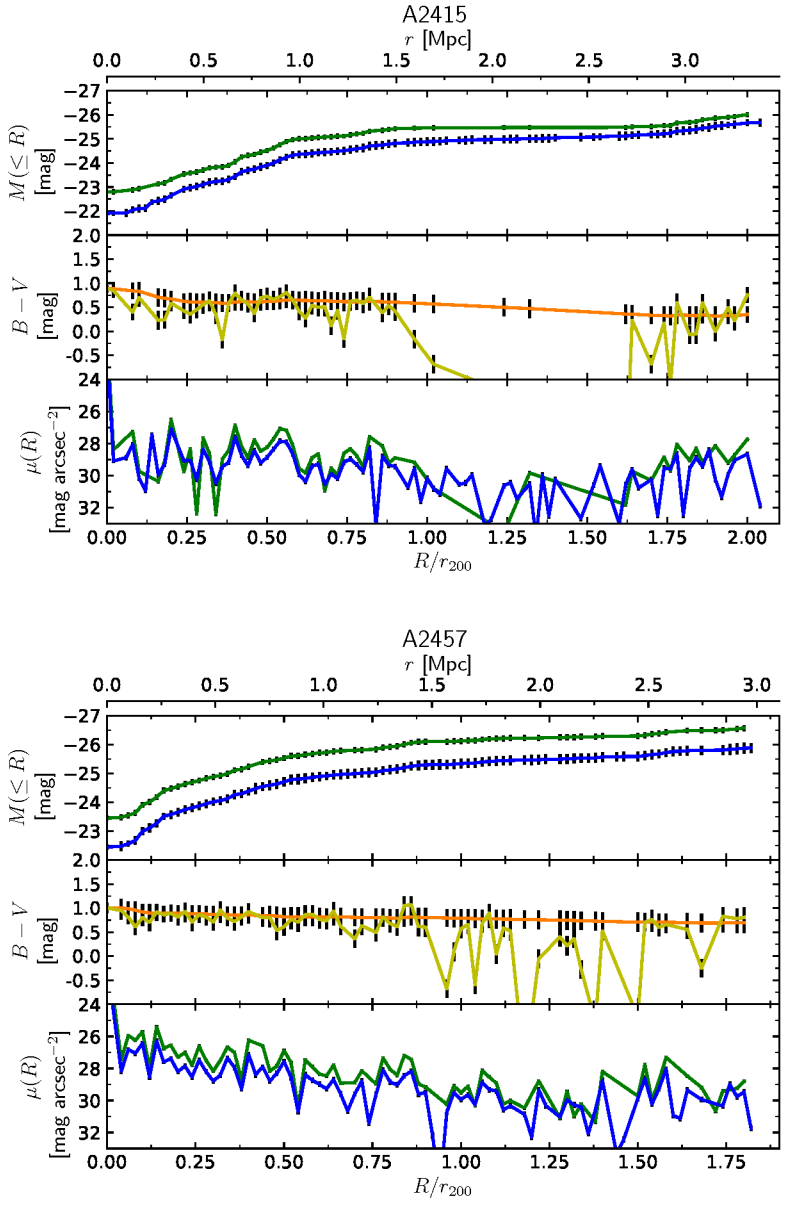


Figure 3.11: Photometric profiles of the Omega-WINGS galaxy clusters. Continued.

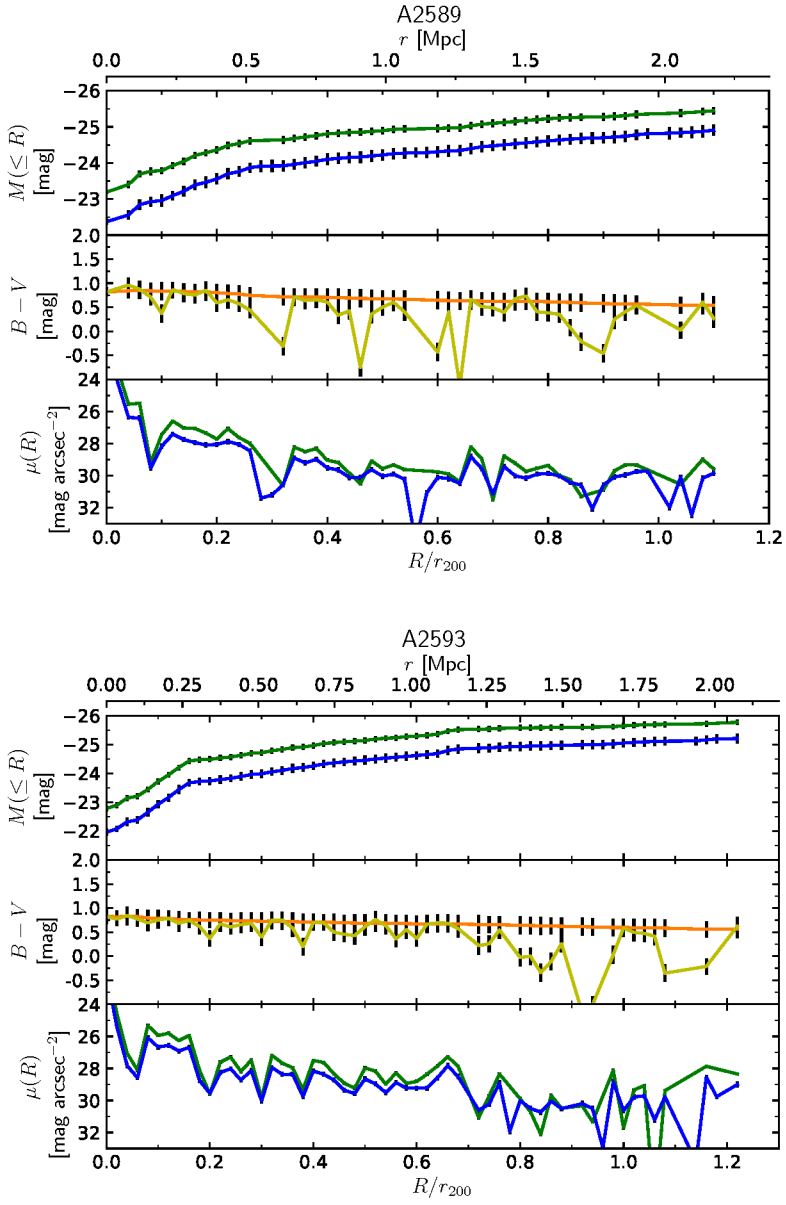


Figure 3.12: Photometric profiles of the Omega-WINGS galaxy clusters. Continued.

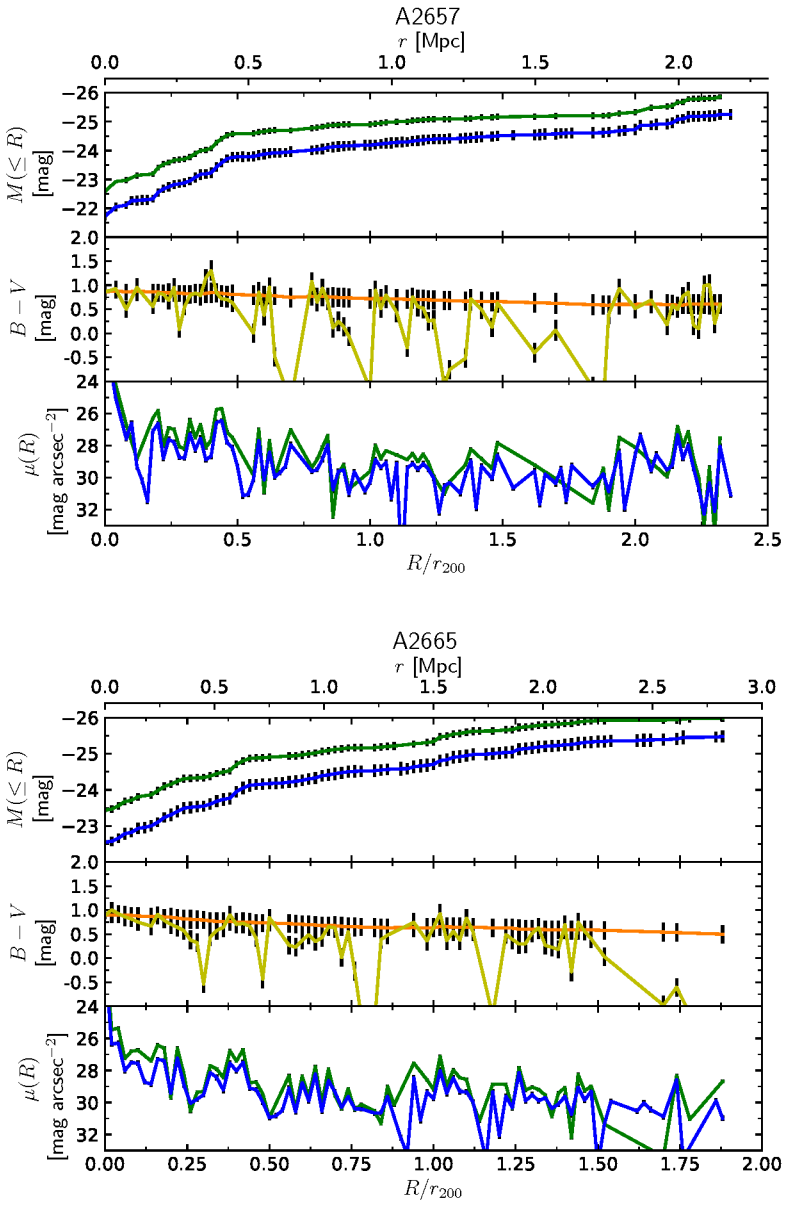


Figure 3.13: Photometric profiles of the Omega-WINGS galaxy clusters. Continued.

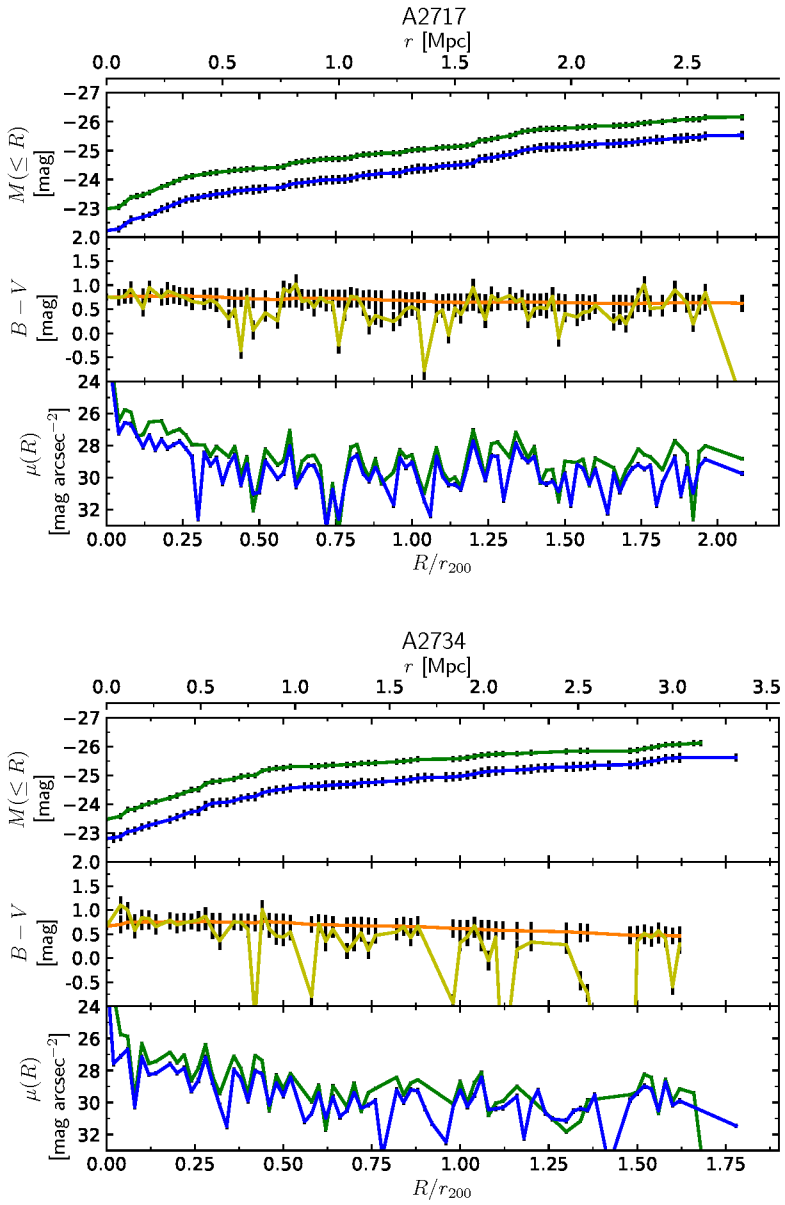


Figure 3.14: Photometric profiles of the Omega-WINGS galaxy clusters. Continued.

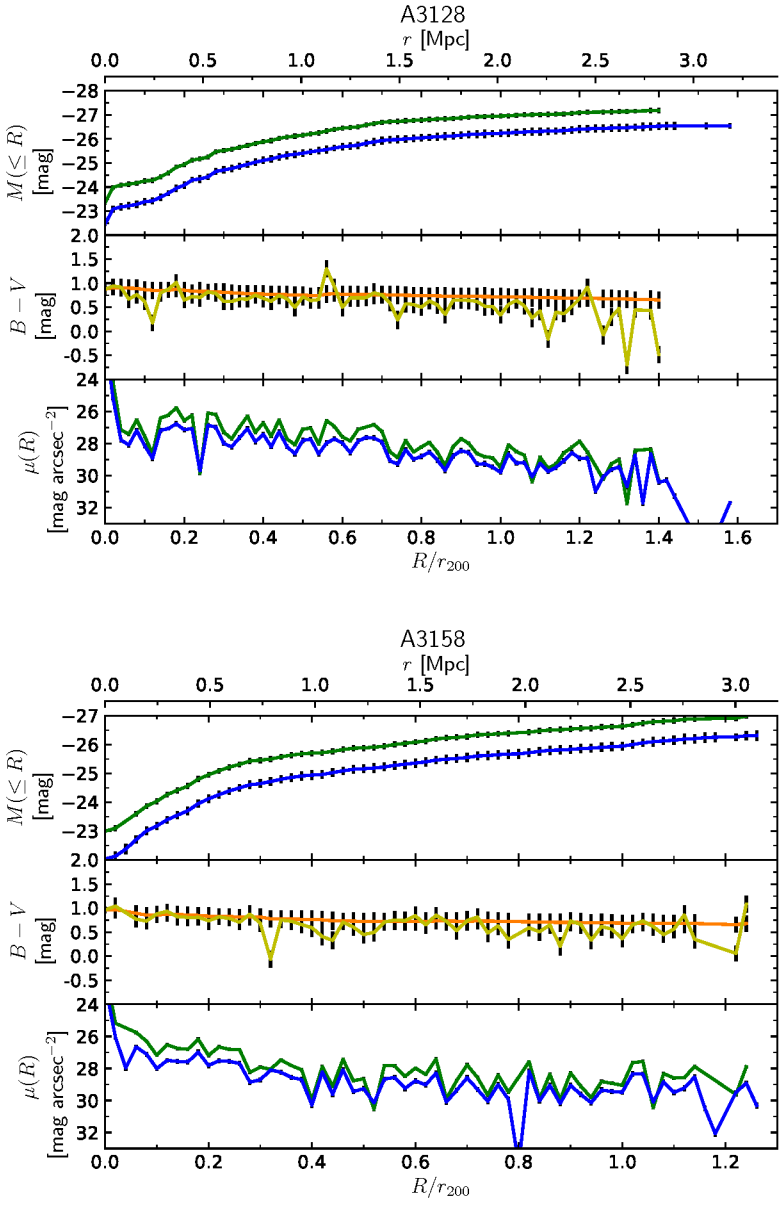


Figure 3.15: Photometric profiles of the Omega-WINGS galaxy clusters. Continued.

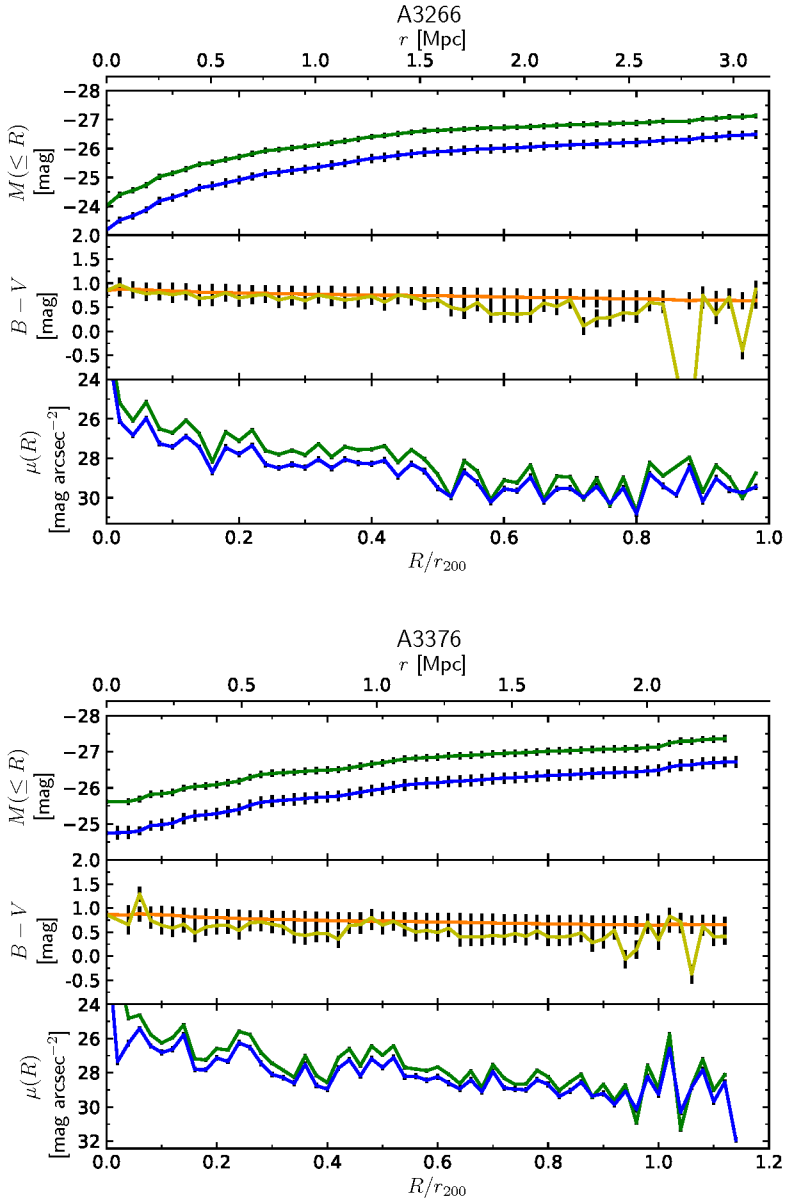


Figure 3.16: Photometric profiles of the Omega-WINGS galaxy clusters. Continued.

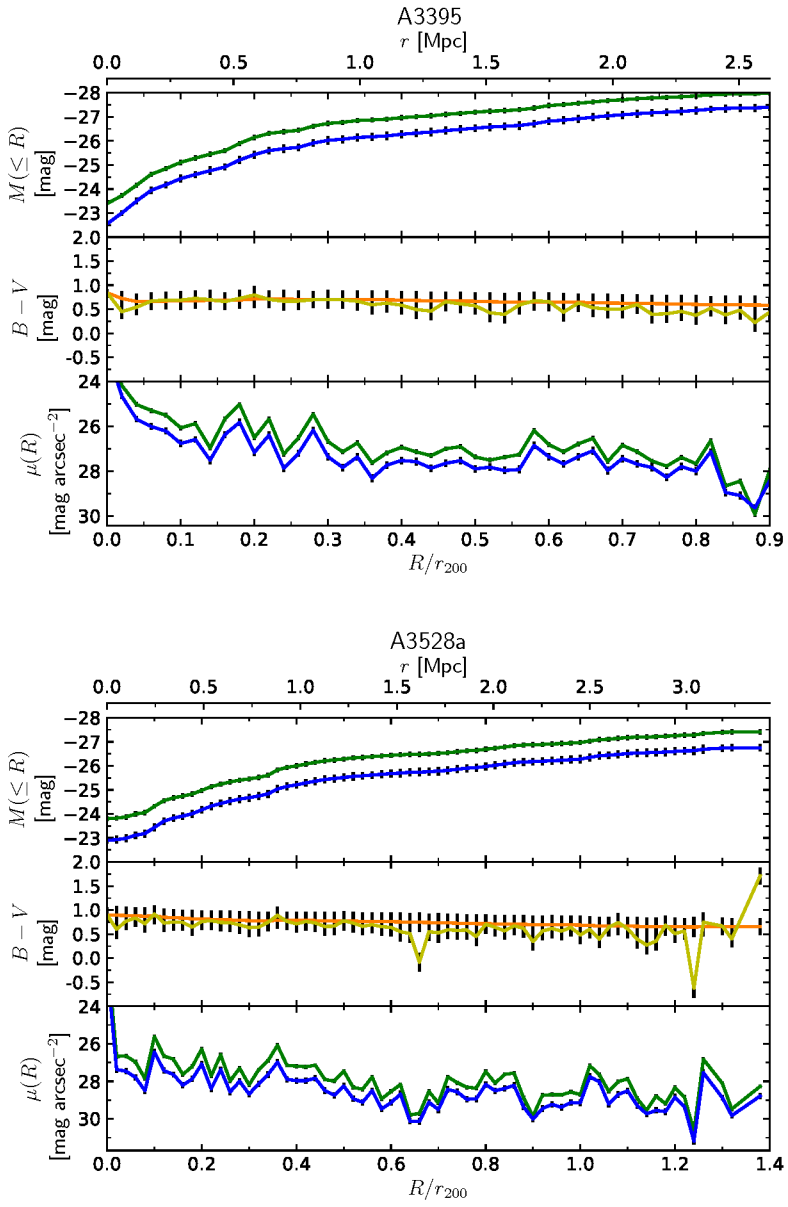


Figure 3.17: Photometric profiles of the Omega-WINGS galaxy clusters. Continued.

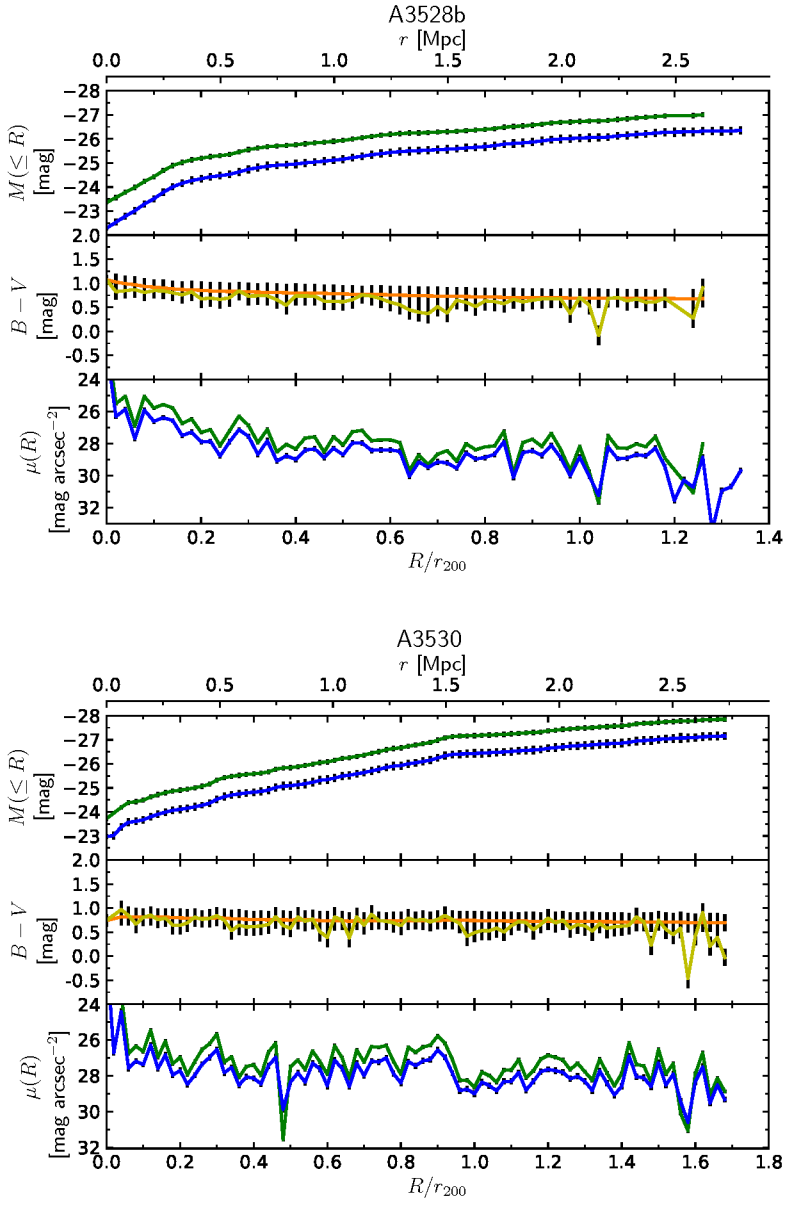


Figure 3.18: Photometric profiles of the Omega-WINGS galaxy clusters. Continued.

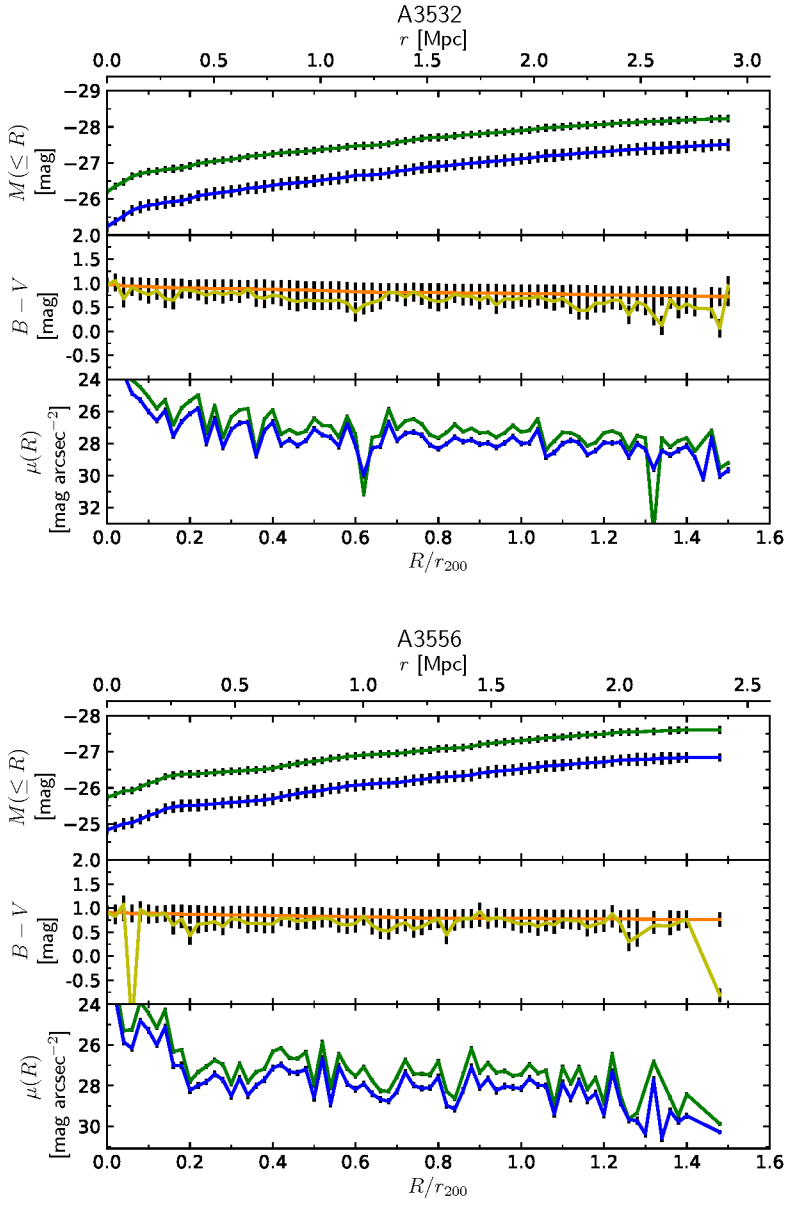


Figure 3.19: Photometric profiles of the Omega-WINGS galaxy clusters. Continued.

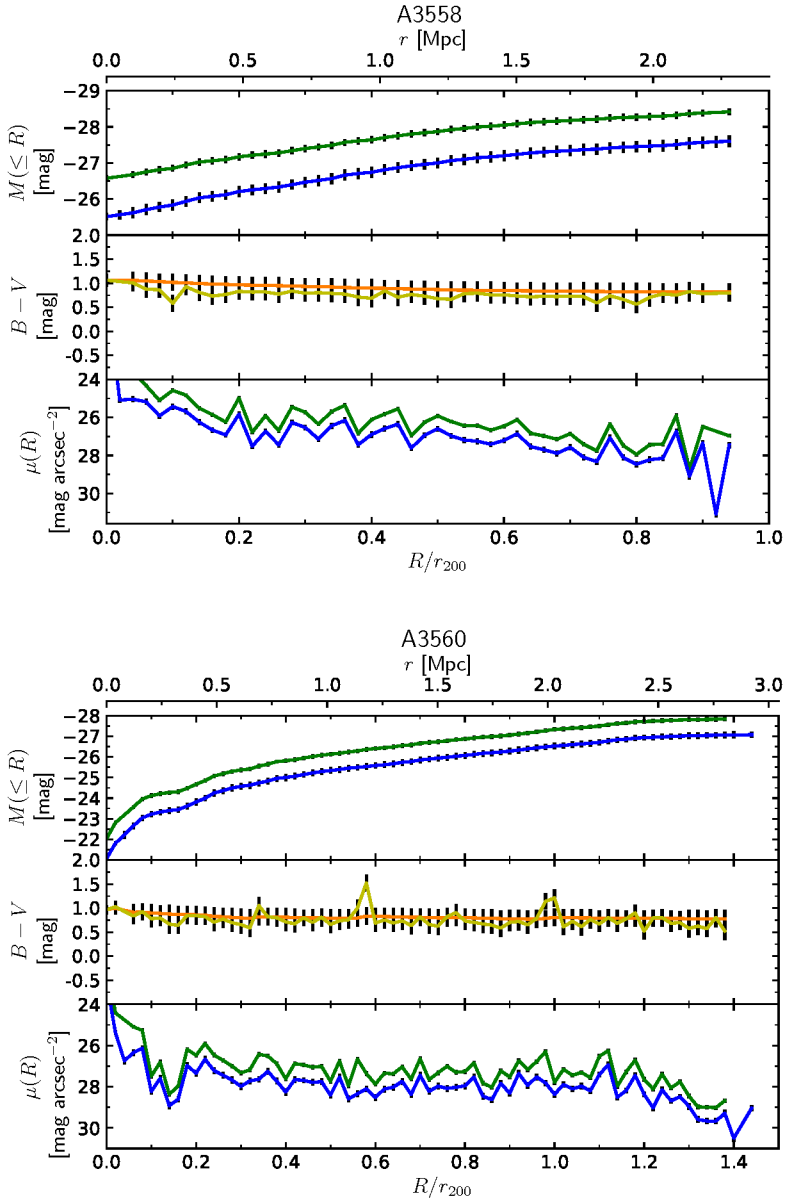


Figure 3.20: Photometric profiles of the Omega-WINGS galaxy clusters. Continued.

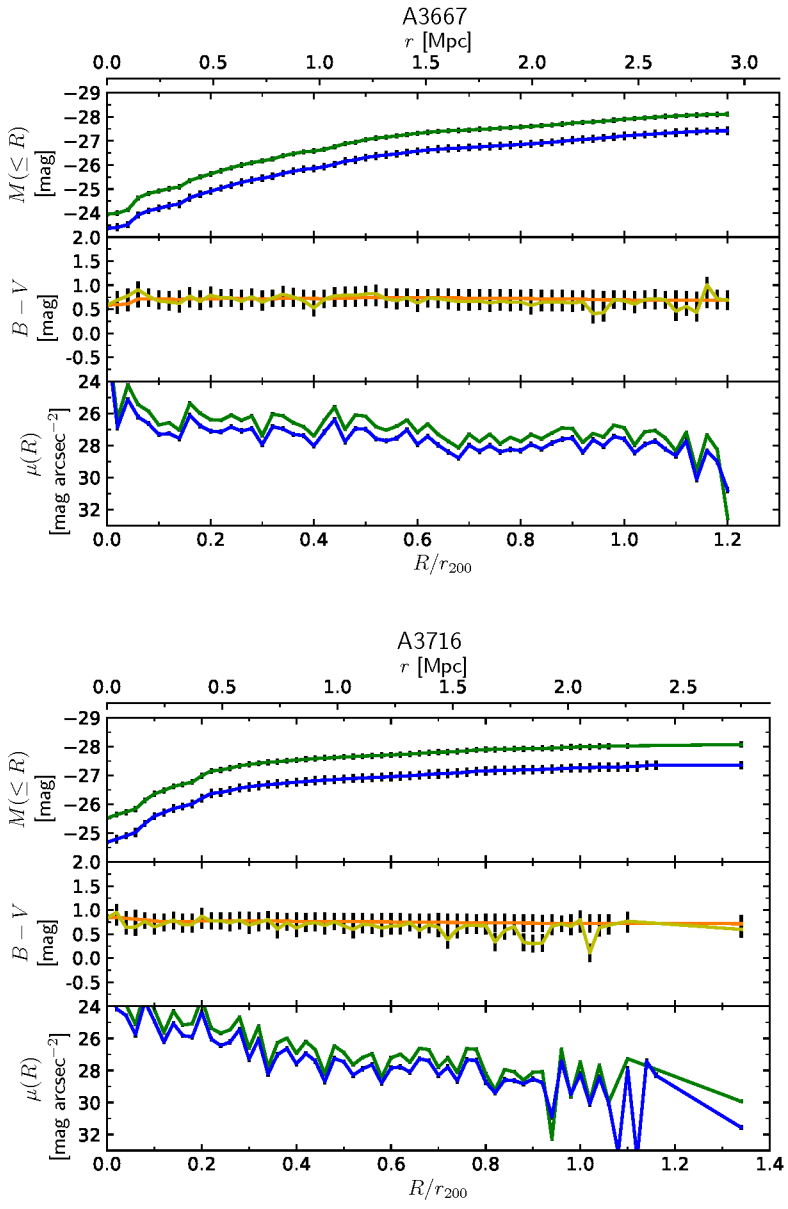


Figure 3.21: Photometric profiles of the Omega-WINGS galaxy clusters. Continued.

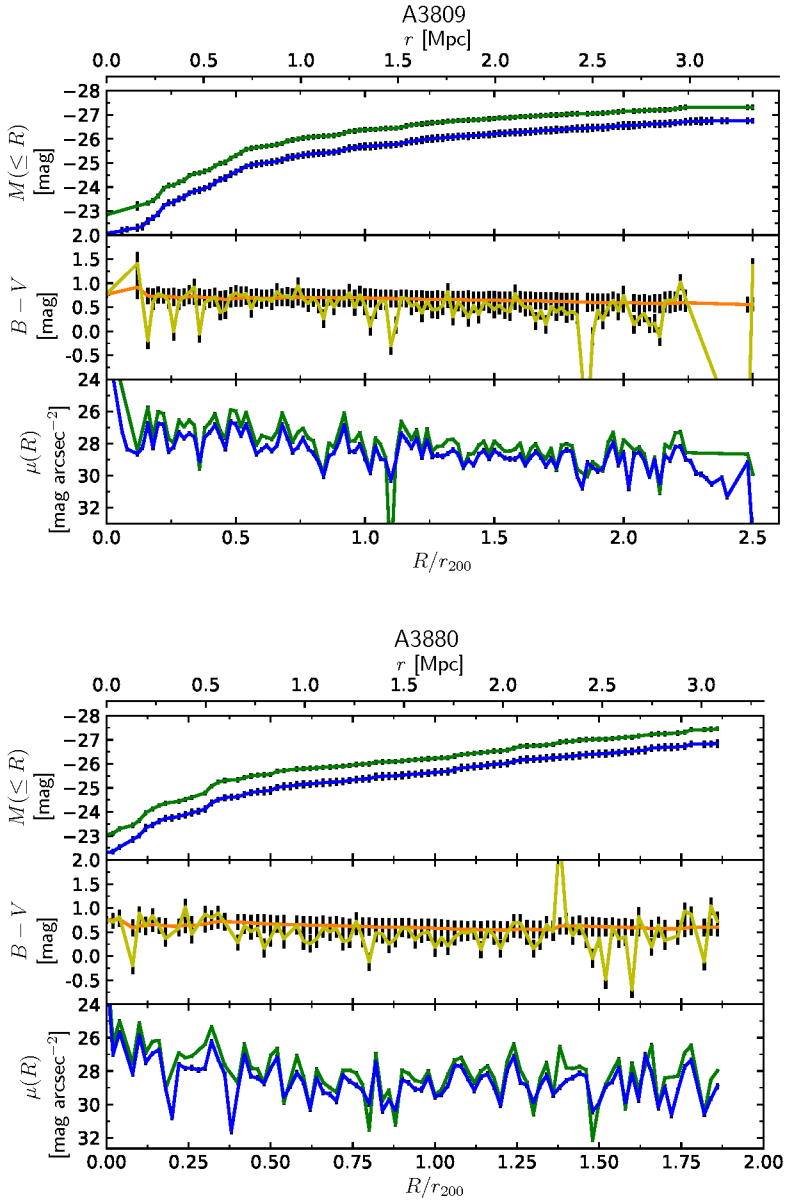


Figure 3.22: Photometric profiles of the Omega-WINGS galaxy clusters. Continued.

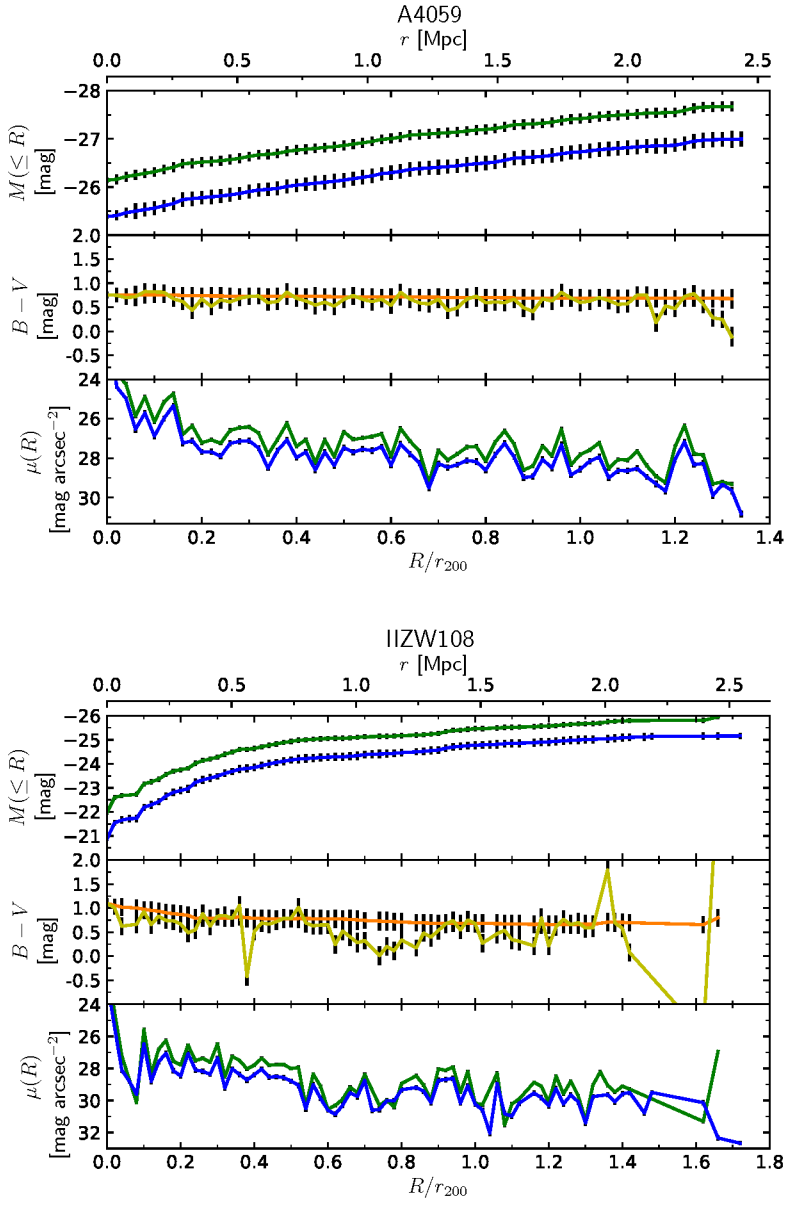


Figure 3.23: Photometric profiles of the Omega-WINGS galaxy clusters. Continued.

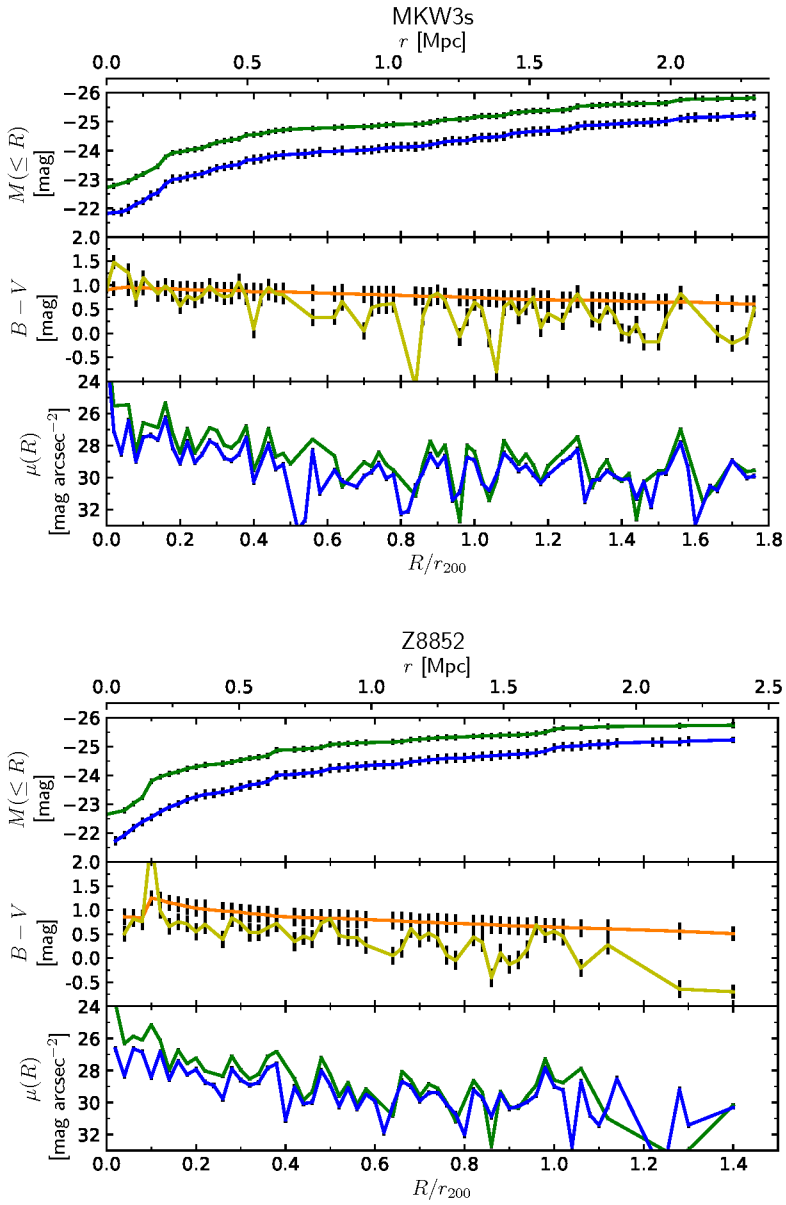


Figure 3.24: Photometric profiles of the Omega-WINGS galaxy clusters. Continued.

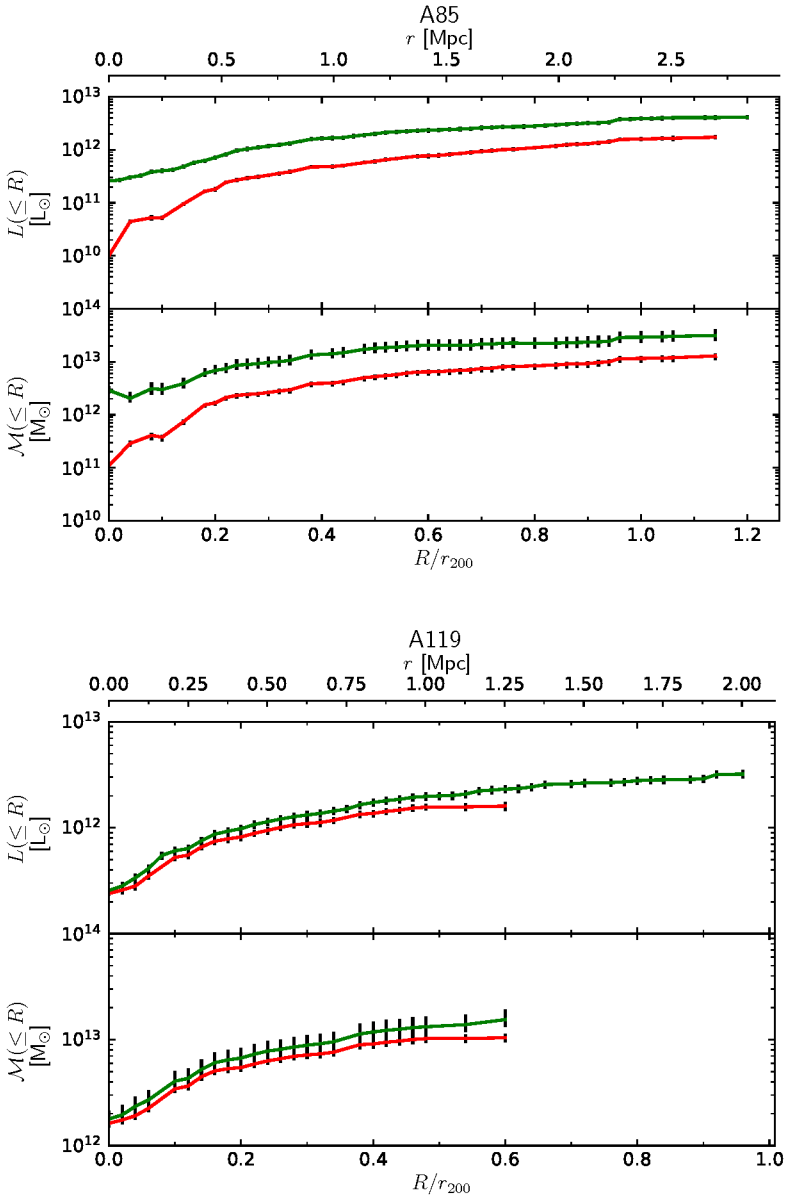


Figure 3.25: Luminosity and mass profiles of the Omega-WINGS galaxy clusters. Upper plot: $V$-band integrated luminosity profile for the objects in the photometric (green line) and spectroscopic (red line) samples. Lower plot: integrated mass profile for the objects in the photometric and spectroscopic samples, with the same color code as the upper plot.

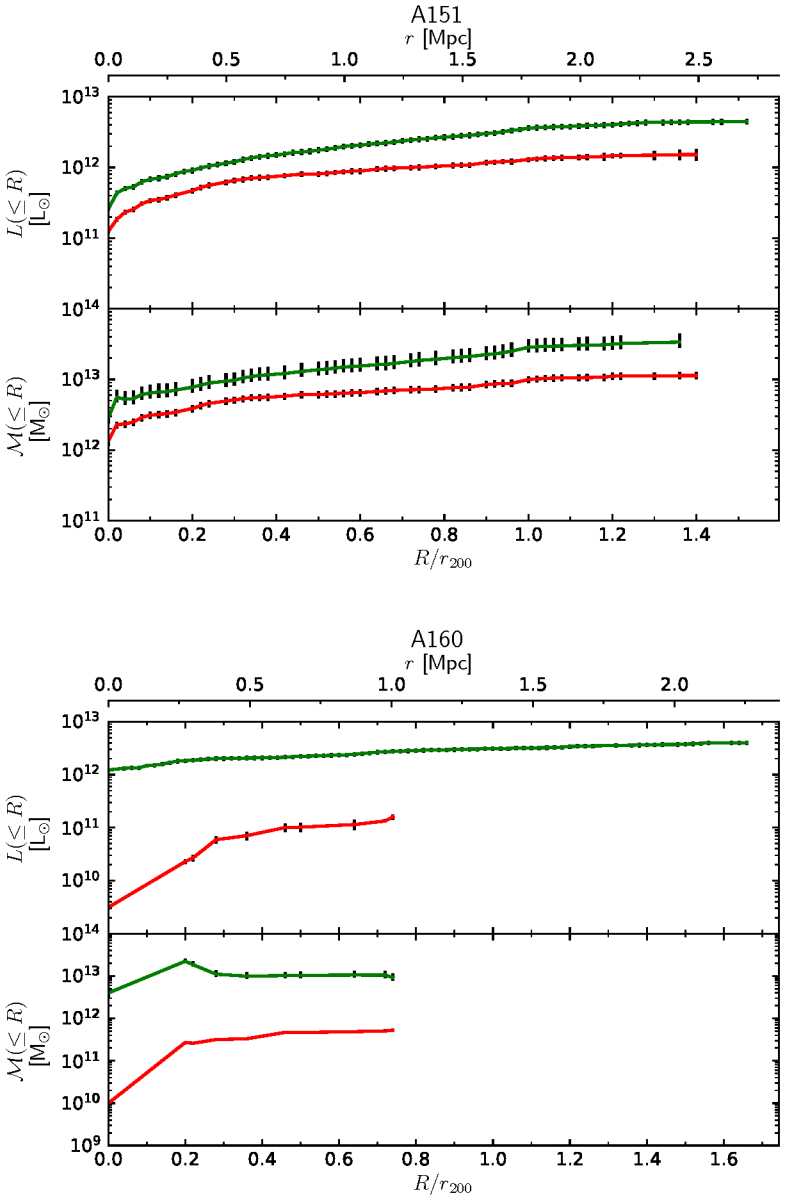


Figure 3.26: Luminosity and mass profiles of the Omega-WINGS galaxy clusters. Continued.

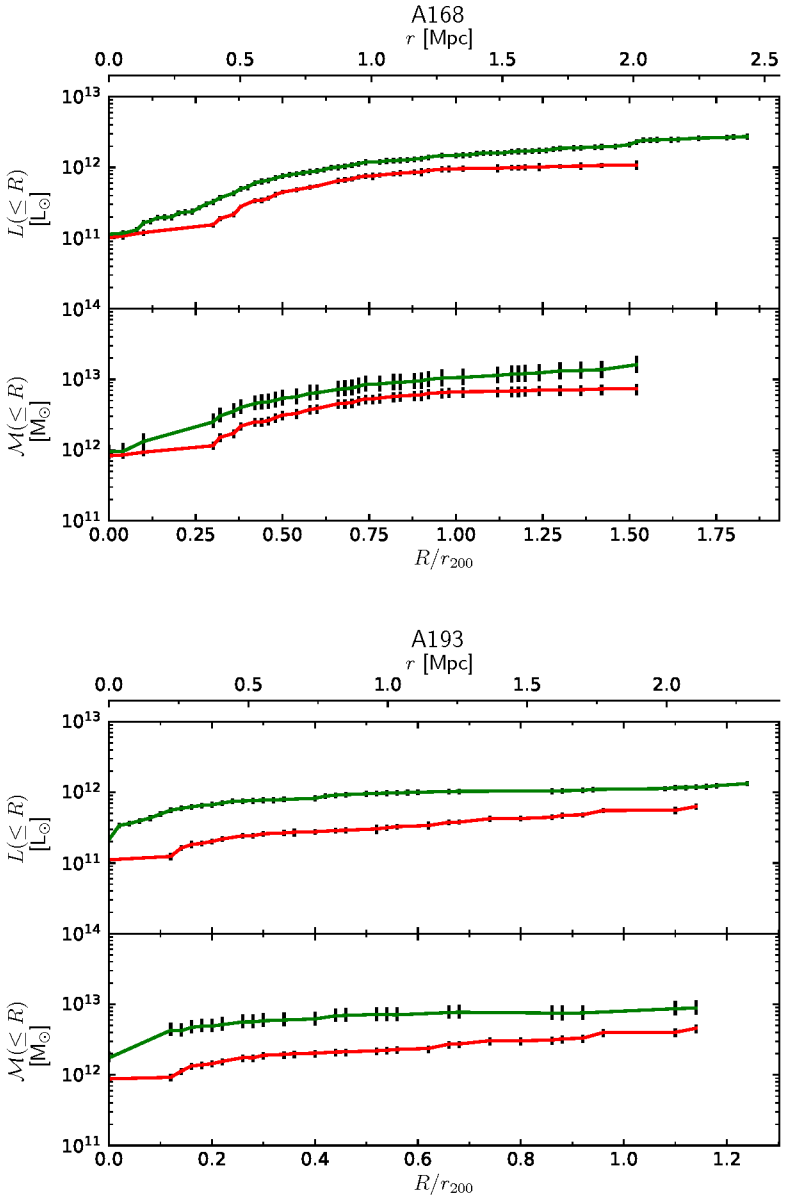


Figure 3.27: Luminosity and mass profiles of the Omega-WINGS galaxy clusters. Continued.

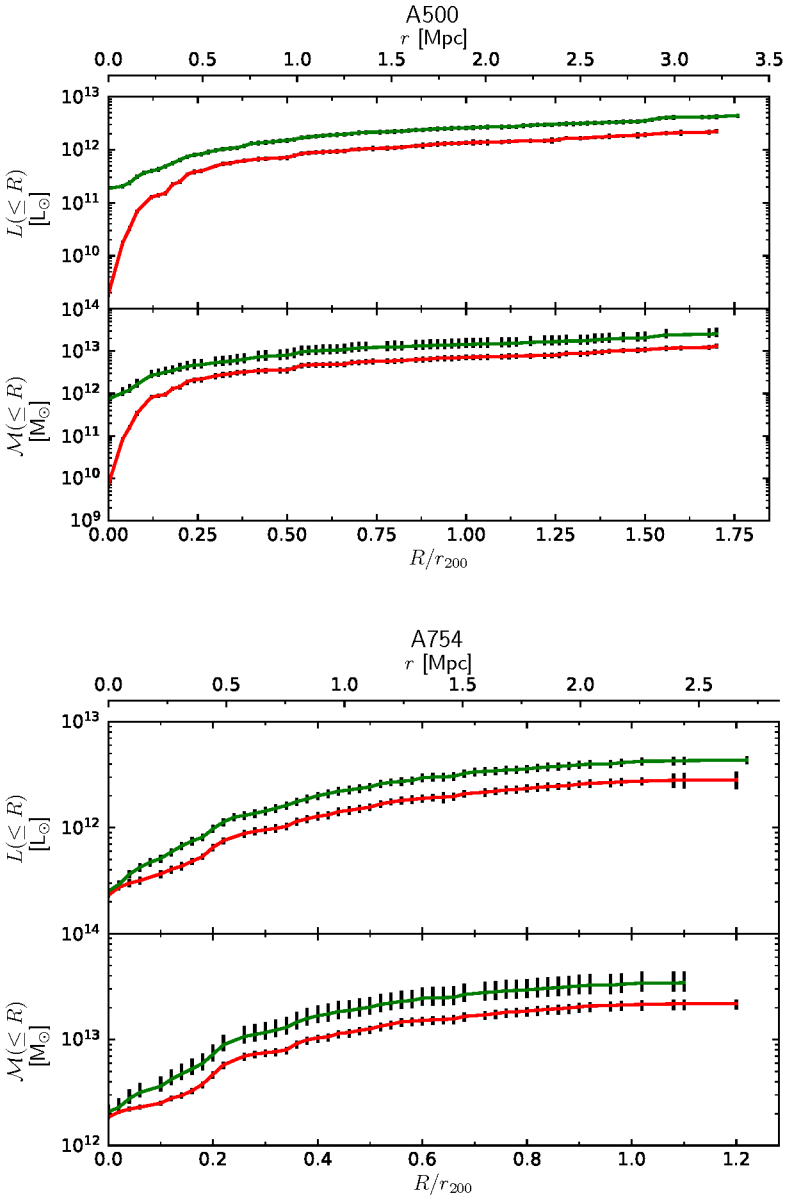


Figure 3.28: Luminosity and mass profiles of the Omega-WINGS galaxy clusters. Continued.

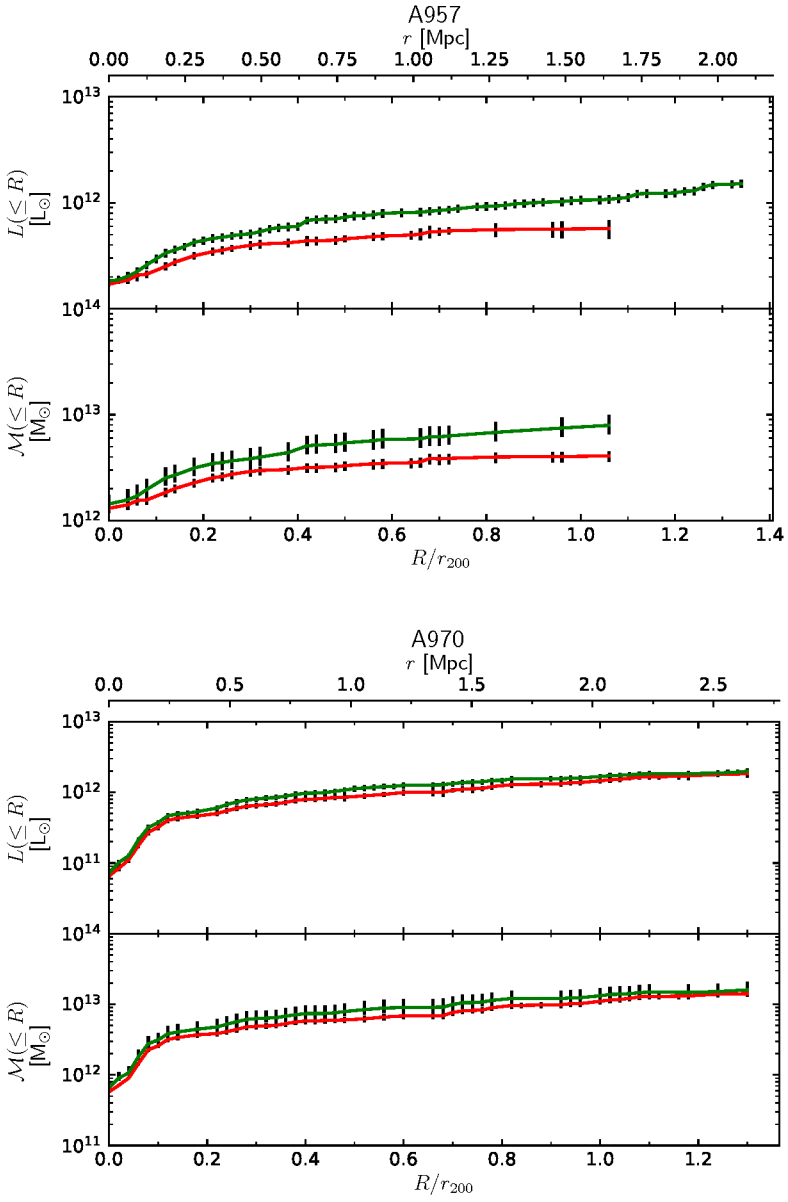


Figure 3.29: Luminosity and mass profiles of the Omega-WINGS galaxy clusters. Continued.

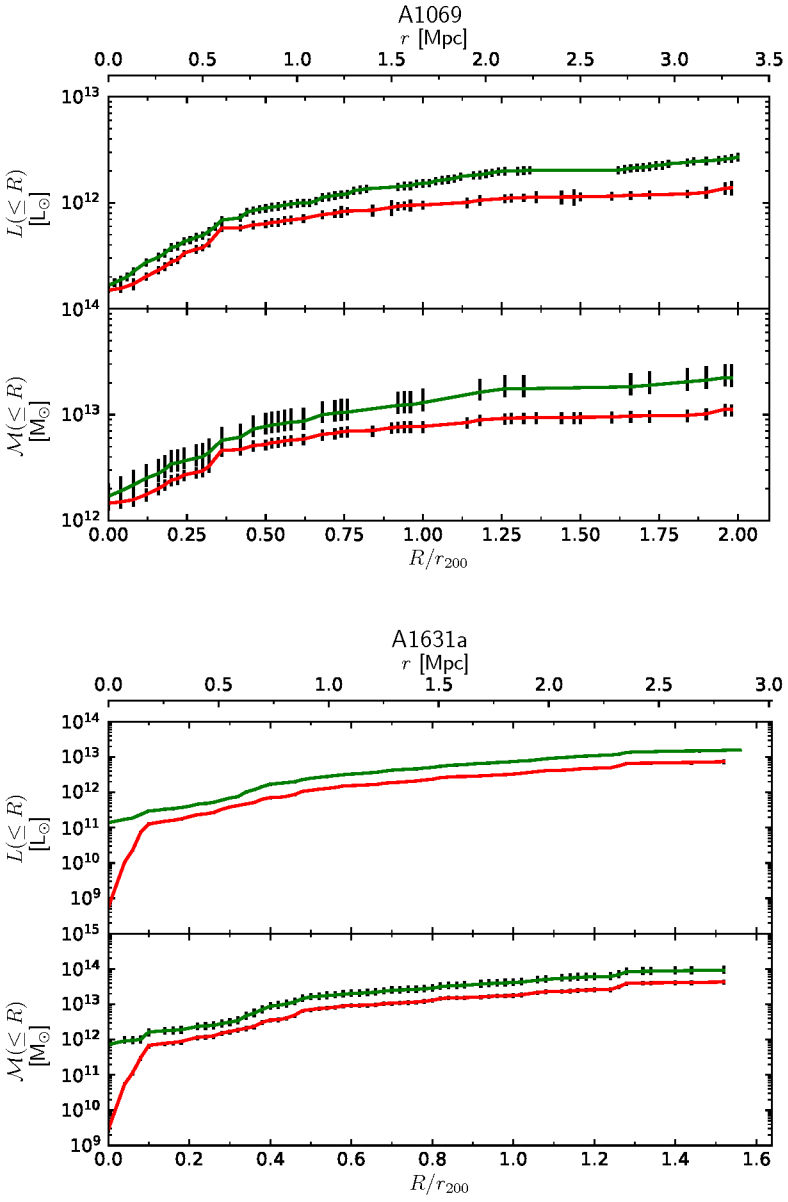


Figure 3.30: Luminosity and mass profiles of the Omega-WINGS galaxy clusters. Continued.

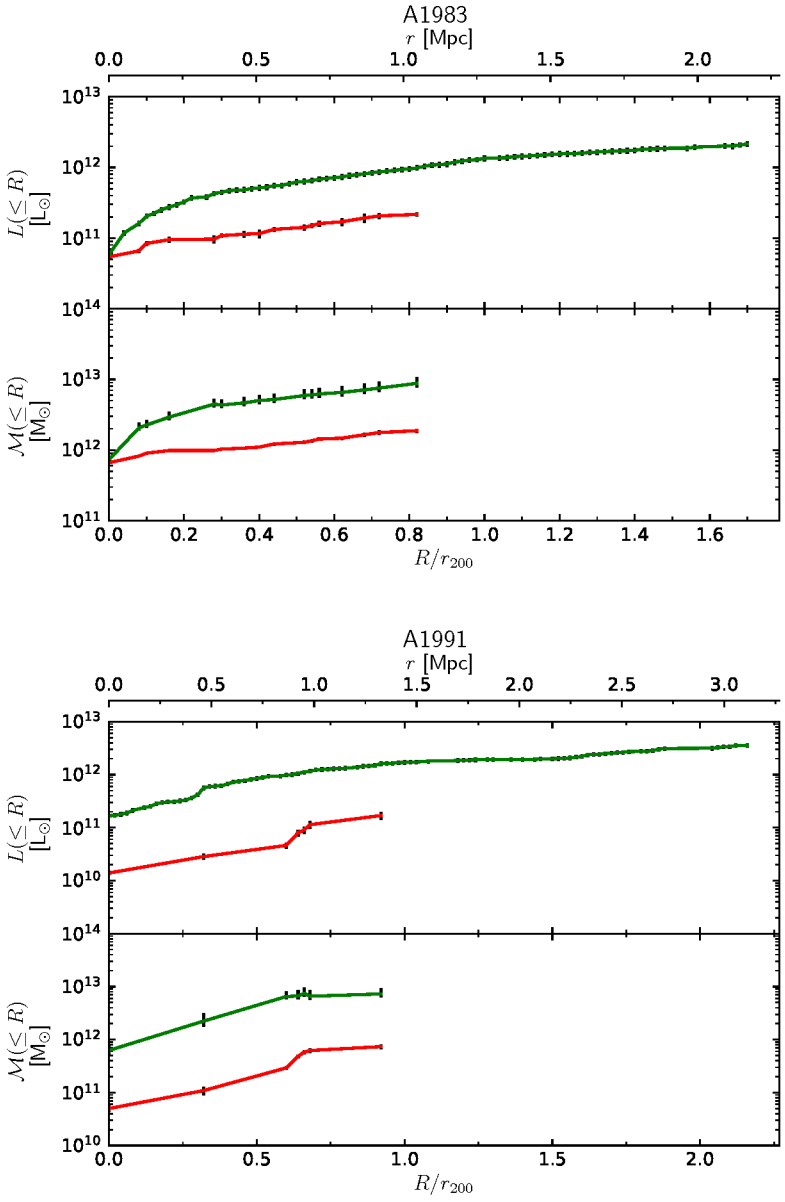


Figure 3.31: Luminosity and mass profiles of the Omega-WINGS galaxy clusters. Continued.

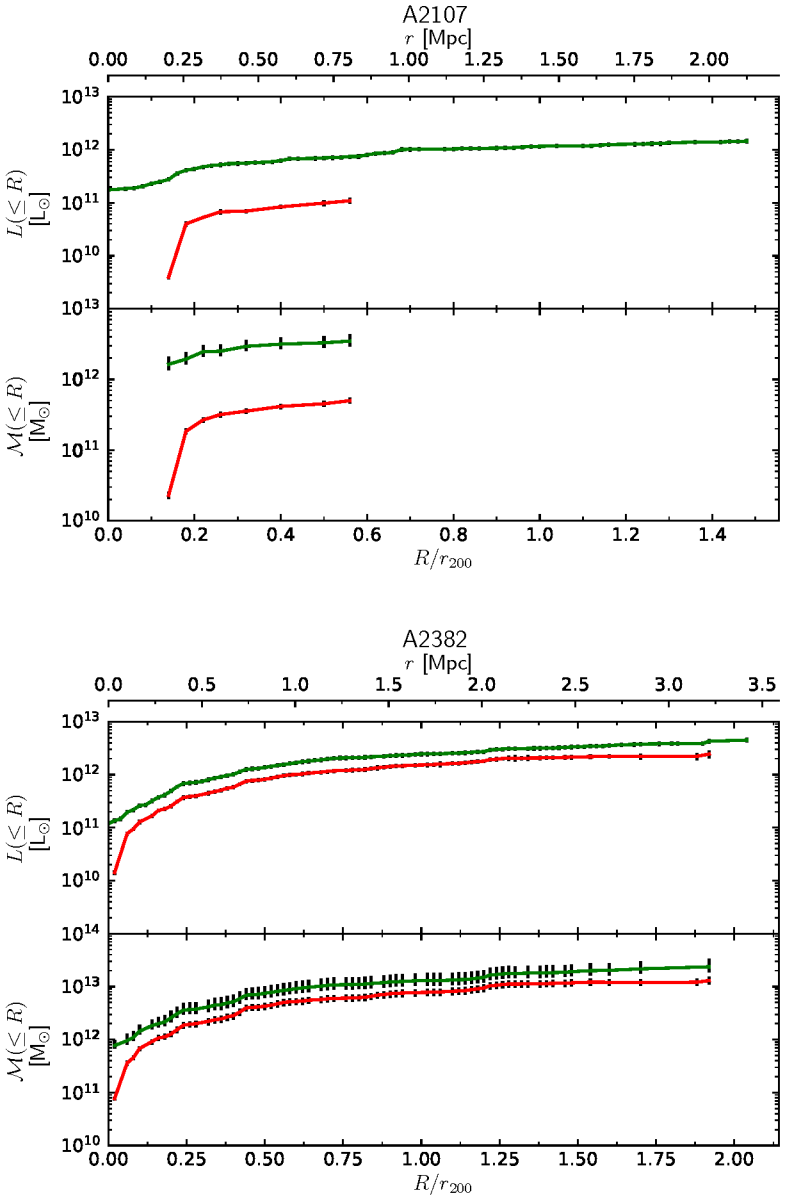


Figure 3.32: Luminosity and mass profiles of the Omega-WINGS galaxy clusters. Continued.

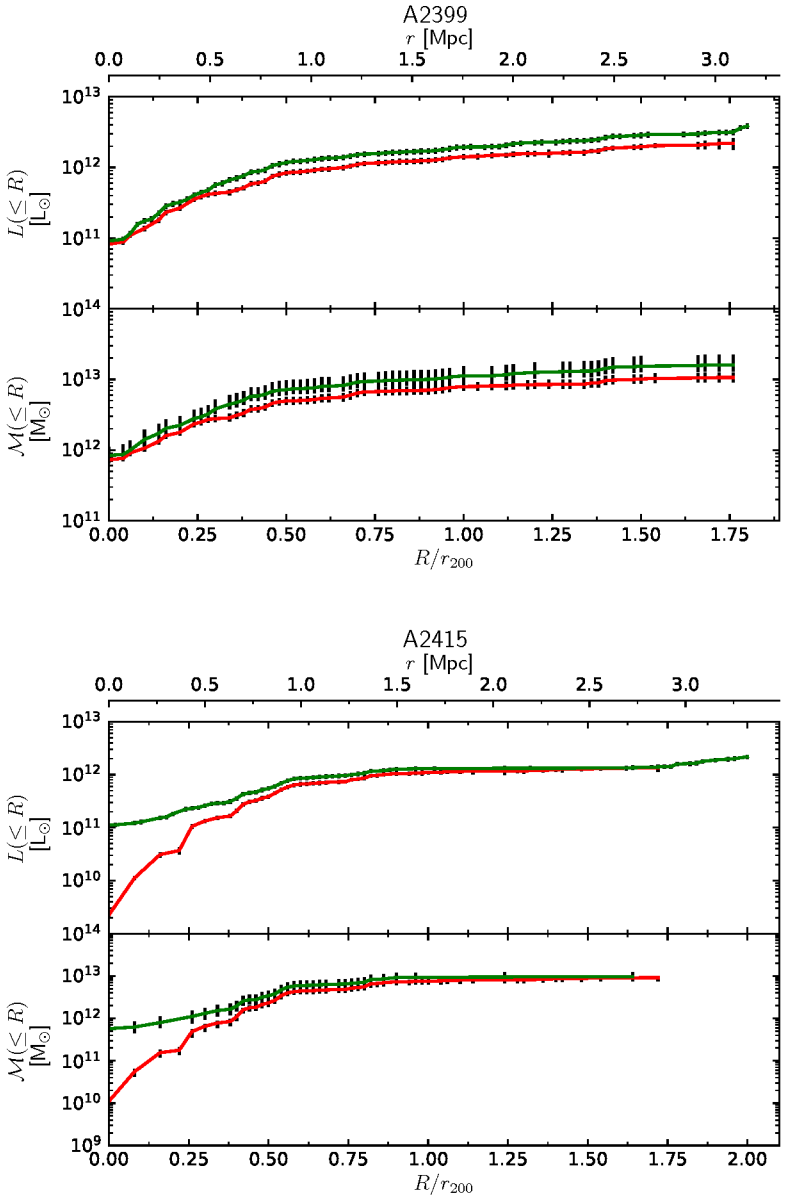


Figure 3.33: Luminosity and mass profiles of the Omega-WINGS galaxy clusters. Continued.

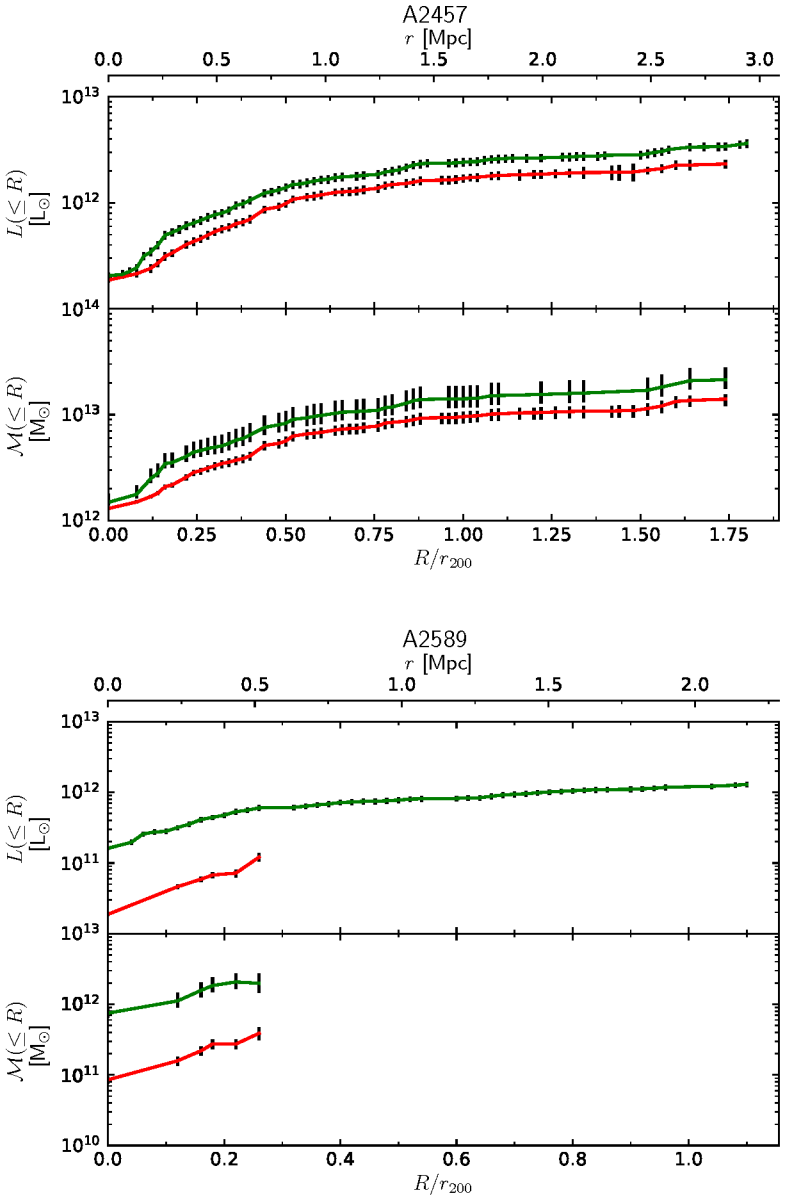


Figure 3.34: Luminosity and mass profiles of the Omega-WINGS galaxy clusters. Continued.

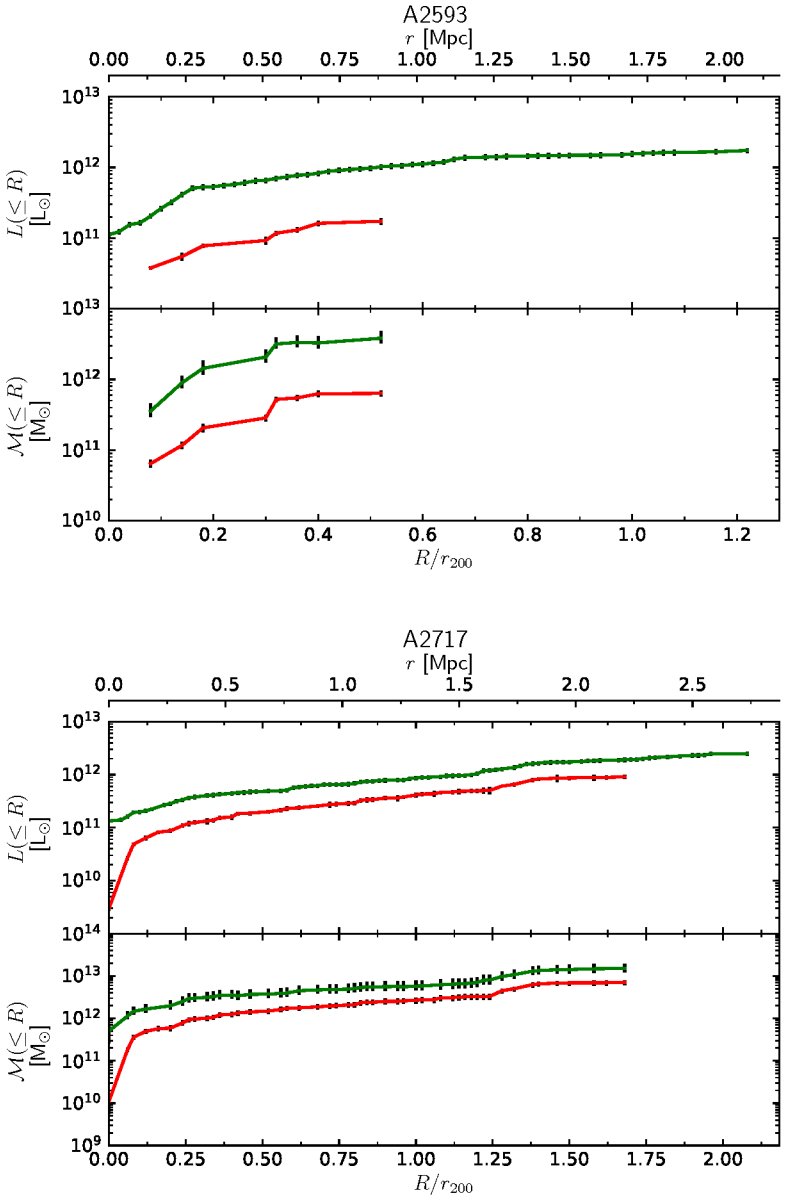


Figure 3.35: Luminosity and mass profiles of the Omega-WINGS galaxy clusters. Continued.

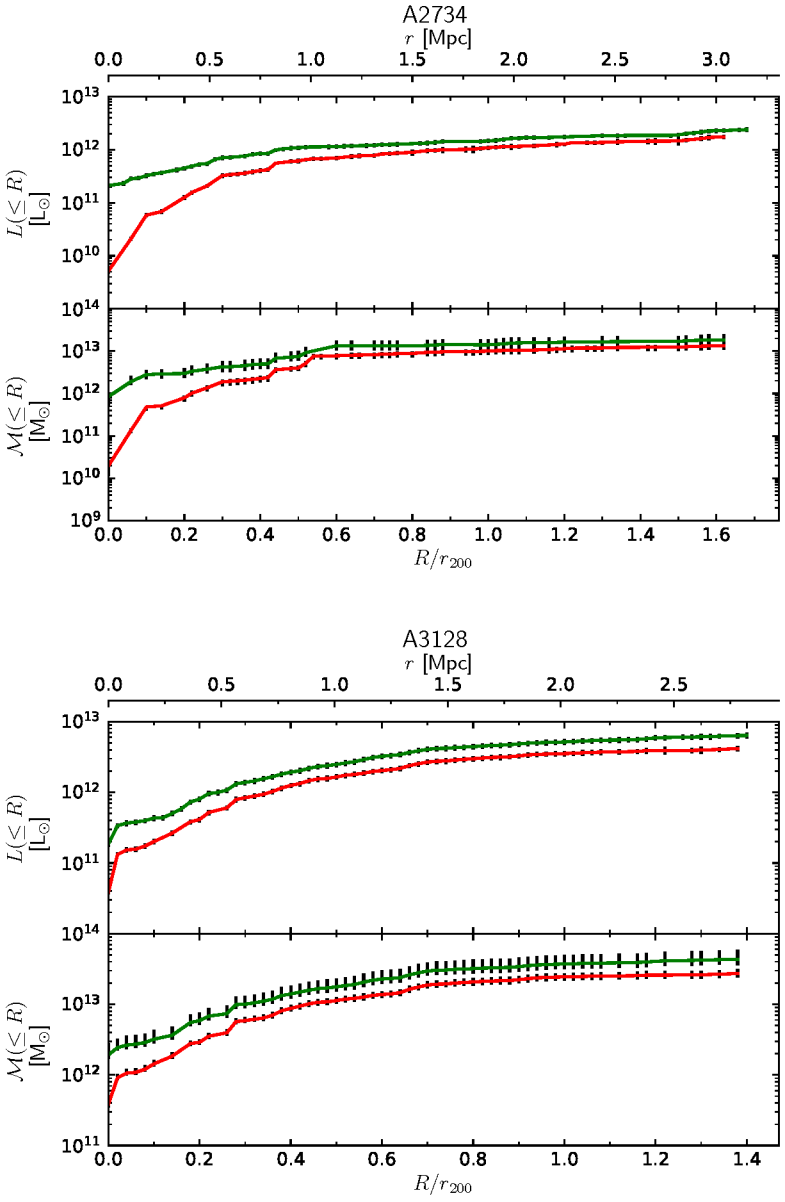


Figure 3.36: Luminosity and mass profiles of the Omega-WINGS galaxy clusters. Continued.

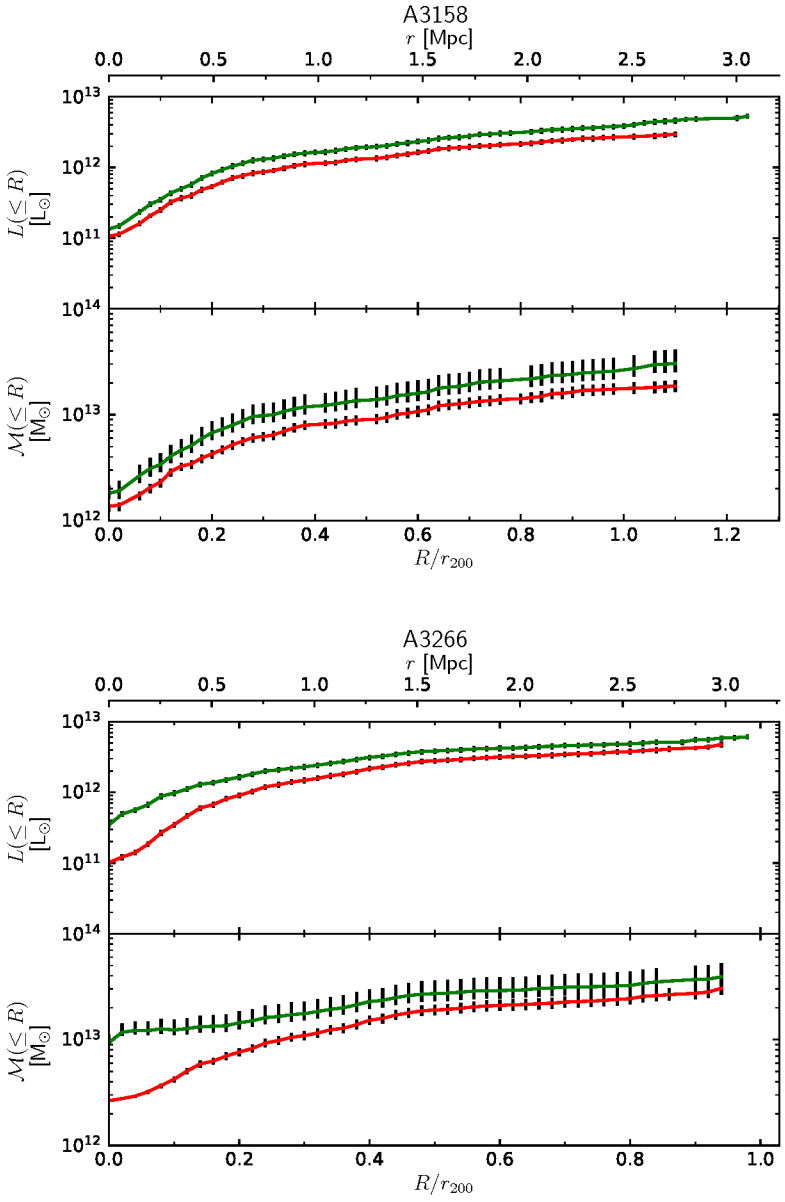


Figure 3.37: Luminosity and mass profiles of the Omega-WINGS galaxy clusters. Continued.

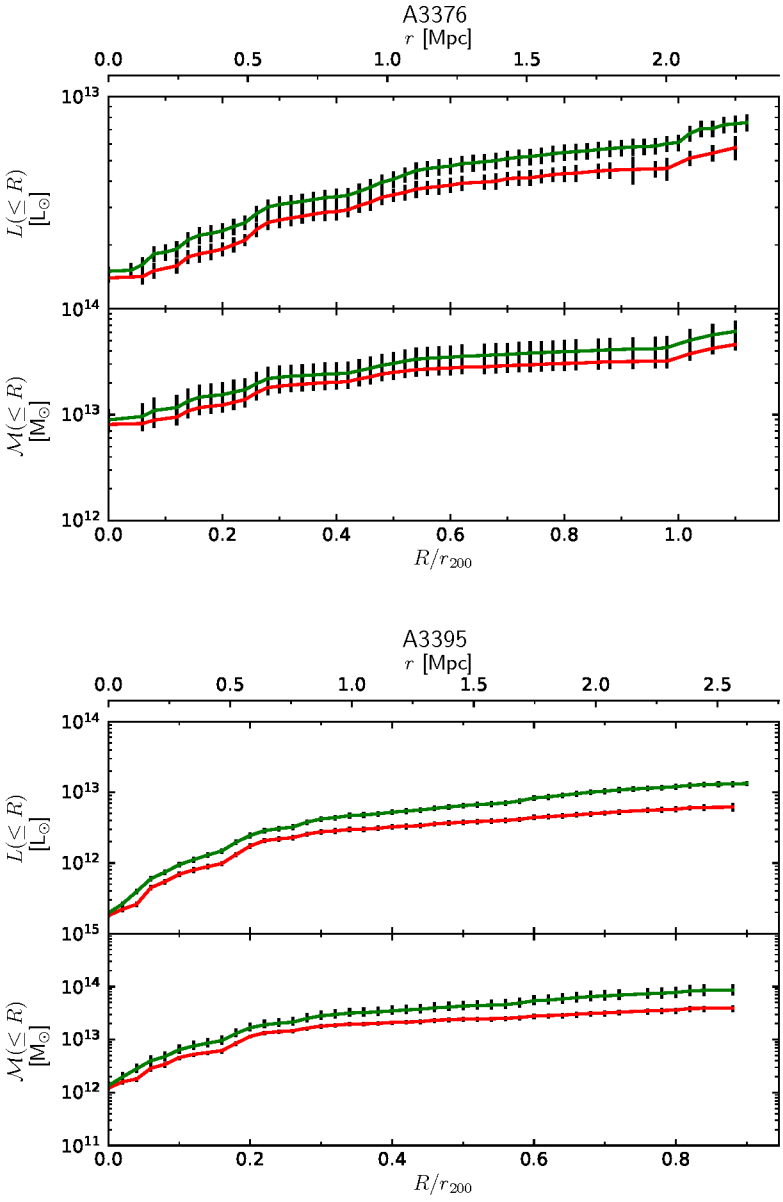


Figure 3.38: Luminosity and mass profiles of the Omega-WINGS galaxy clusters. Continued.

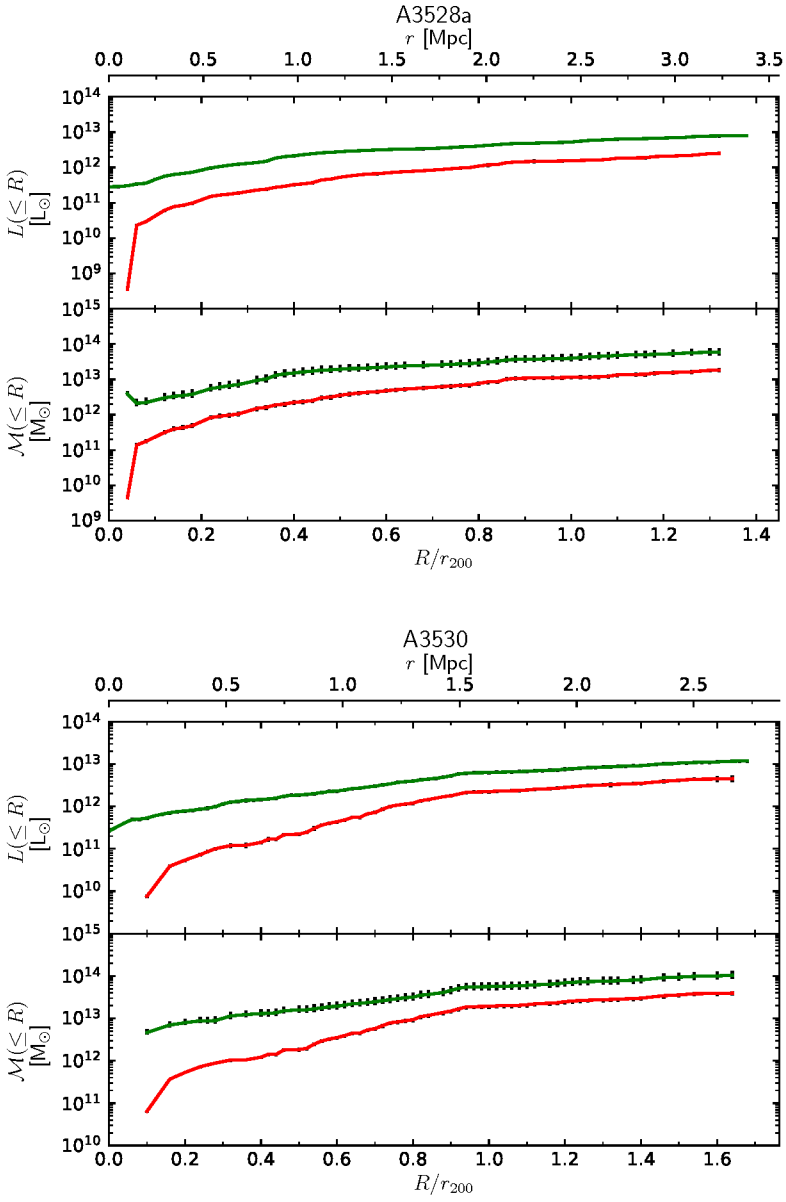


Figure 3.39: Luminosity and mass profiles of the Omega-WINGS galaxy clusters. Continued.

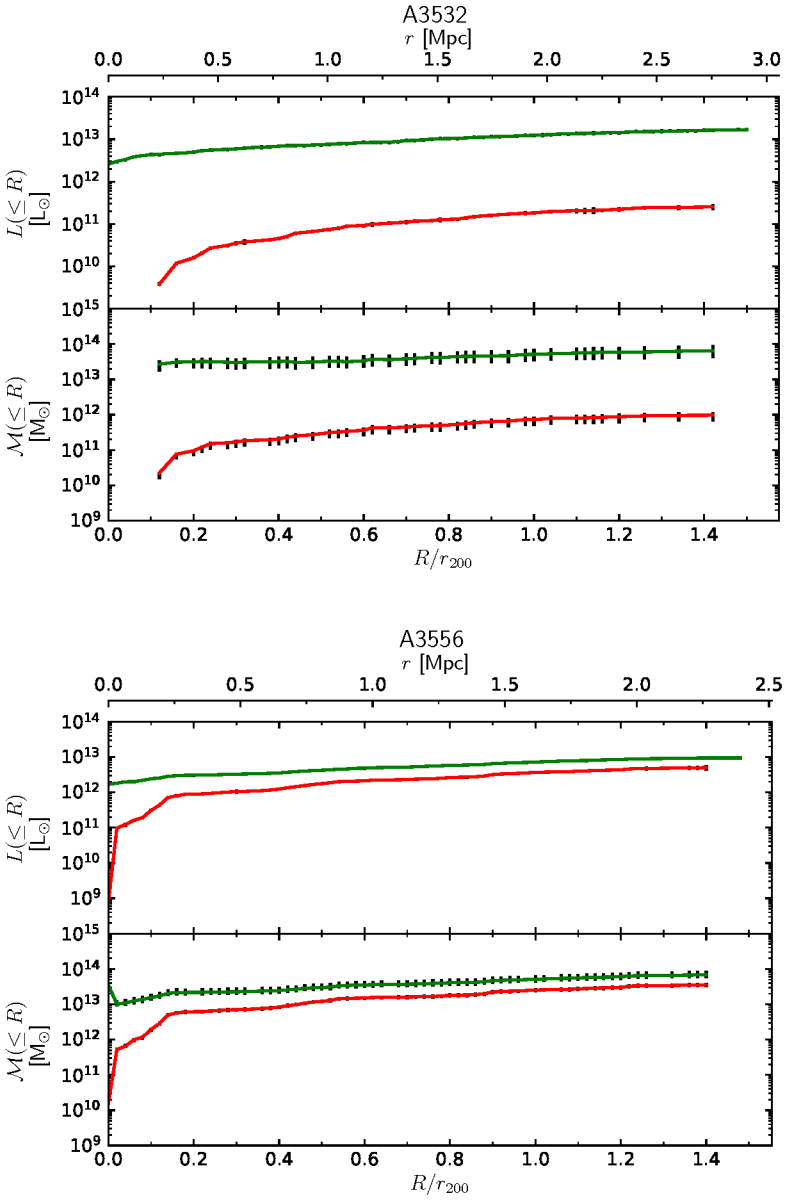


Figure 3.40: Luminosity and mass profiles of the Omega-WINGS galaxy clusters. Continued.

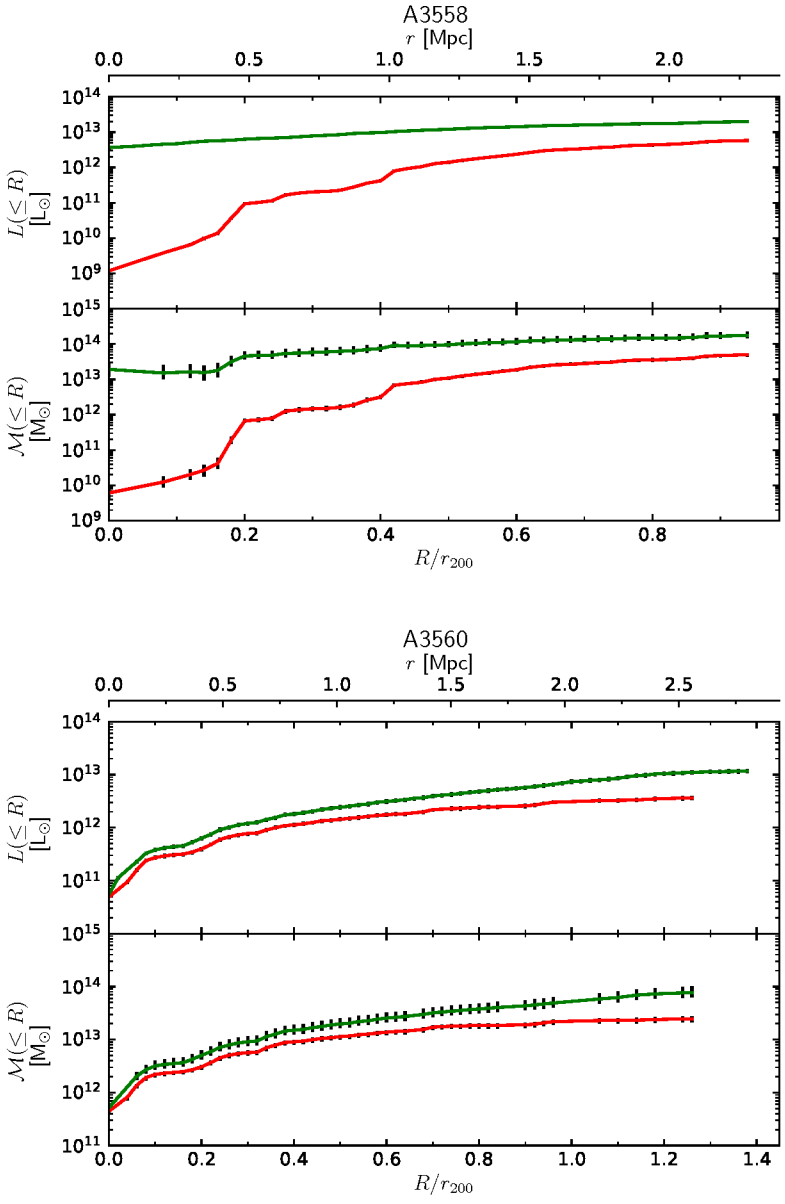


Figure 3.41: Luminosity and mass profiles of the Omega-WINGS galaxy clusters. Continued.

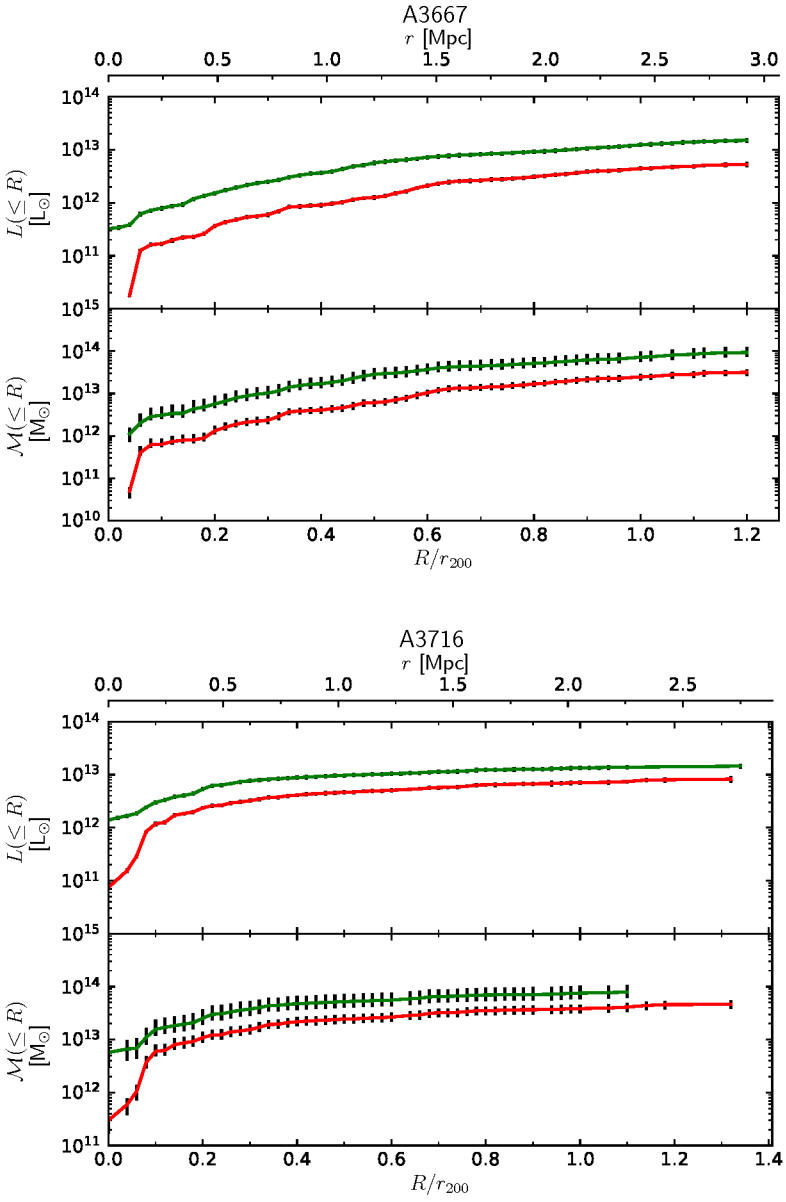


Figure 3.42: Luminosity and mass profiles of the Omega-WINGS galaxy clusters. Continued.

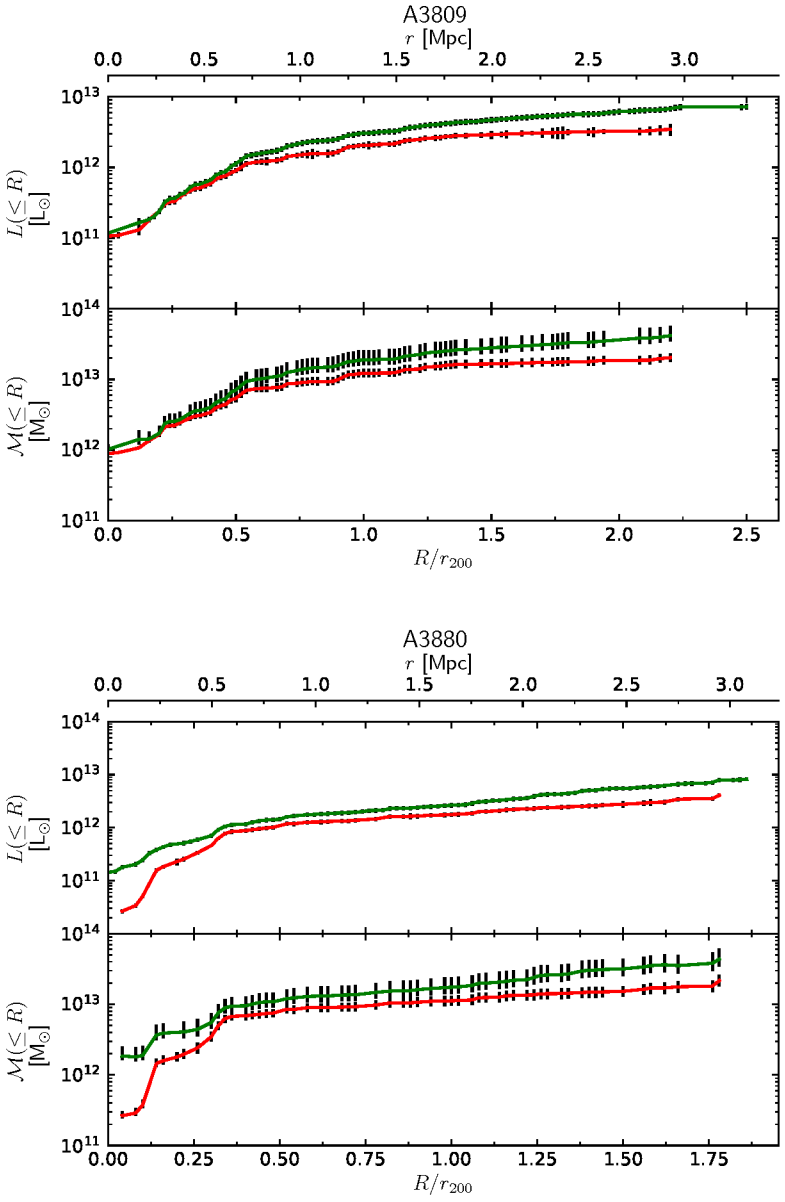


Figure 3.43: Luminosity and mass profiles of the Omega-WINGS galaxy clusters. Continued.

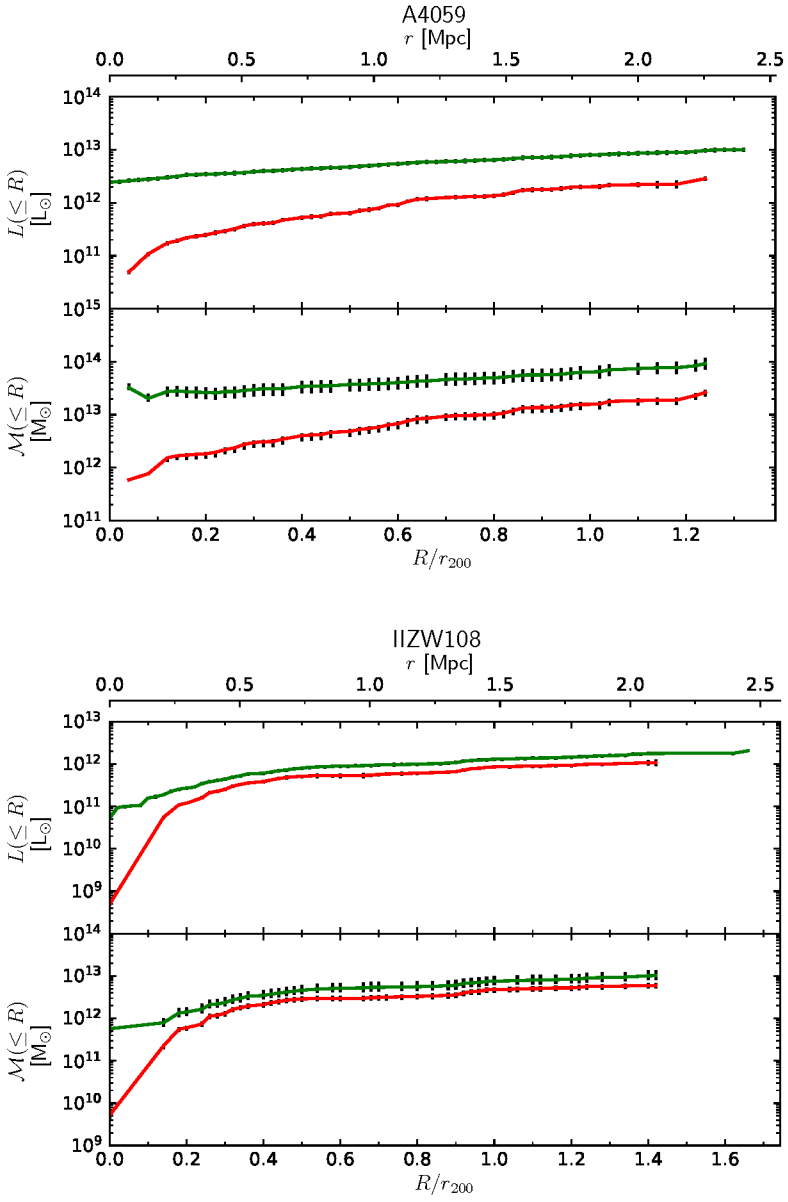


Figure 3.44: Luminosity and mass profiles of the Omega-WINGS galaxy clusters. Continued.

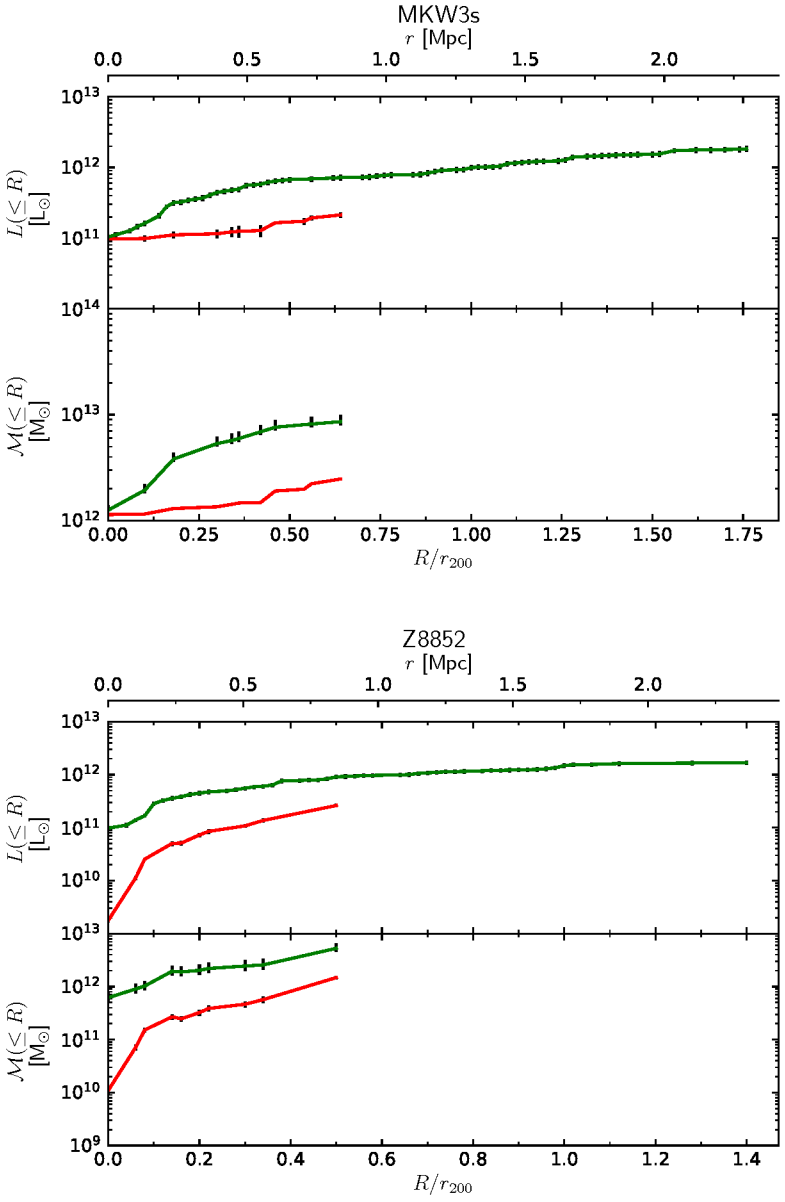


Figure 3.45: Luminosity and mass profiles of the Omega-WINGS galaxy clusters. Continued.

# Chapter 4

# The photometric profiles analysis procedure

In this chapter we analyze the previously-derived photometric profiles. In Section 4.1 we introduce the models that we used to fit our data, namely the King model (Section 4.1.1), the standard $\beta$-model (Section 4.1.2), and the Sérsic model (Section 4.1.3); in Section 4.2 we introduce the goodness-of-fit criteria used to discriminate between the different models (namely, the Akaike Information Criterion and the Bayesian Information Criterion), and we motivate our choice; in Section 4.3 we describe the fitting procedure and the best model selection; finally, in Section 4.4 we present and comment all the fits.

## 4.1 The modeling of luminosity profiles

As we noted in Section 3.5, the luminosity profiles appear to be still increasing at the largest possible radius. Therefore, we decided to reproduce their photometric profiles with some model from which we could obtain the cluster structural parameters.

The profile fitting was done on the integrated luminosity profiles, as the surface brightness profiles display an important level of statistical noise that could only be removed by enlarging the size of the radial bins. However, by enlarging the size of the radial bins we were going to lose spatial information, which is particularly important in the central region, where the surface brightness profiles display their central cusp. The choice of applying our fits to the luminosity profiles allowed us to have both a denser spatial sampling and a more controlled level of statistical fluctuations.

The models that we decided to adopt for fitting our data are the following

ones:

- the King model;
- the standard $\beta$-model;
- the Sérsic model.

Each of them will now be analyzed in detail.

### 4.1.1 The King model

The King (1962) model was created to reproduce the density profiles of globular clusters, but later it was adopted also to describe the intensity profiles of galaxies, expecially in the case of dwarf elliptical galaxies. Marmo et al. (2004) preliminary attemped to use it for fitting the WINGS cluster surface brightness profiles and other authors (e.g., Adami et al. 1998) to reproduce the number density profiles in galaxy clusters

The King profile is given by the following formula:

$$I(R) = k\left(1/\sqrt{R^2/R_c^2+1} - 1/\sqrt{R_t^2/R_c^2+1}\right)^{-2}, \tag{4.1}$$

where $k$ is the scale surface brightness, $R_c$ the core radius, and $R_t$ the tidal radius. In the case of galaxies, the core radius is the radius, calculated at 45° of inclination with respect to the major axis, where the intensity is equal to one half of the central intensity value. The tidal radius, instead, is the radius where the intensity value abruptly falls. Starting from these two quantities, one can also define the concentration parameter $c = \log(R_c/R_t)$.

The King law has a theoretical foundation. In fact, it describes the intensity profile of a spherically-simmetric stellar system, where the velocity dispersion of stars is isotropic and constant. Under these hypothesis, the tidal radius is the radius starting from which the centrifugal force depletes the system of its components.

An isothermal sphere is characterized by $c \to \infty$, while in the case of real objects: $c \sim 2.2$ for giant elliptical galaxies, and $c \sim 1$ for globular clusters.

The integral of this profile is given by:

$$\begin{aligned} L(\leq R) &= \int 2\pi R\, I(R)\, dR + L_{\rm ZP} \\ &= \pi k \left\{ R_c^2 \log\left(R^2/R_c^2+1\right) + 1/\sqrt{R_t^2/R_c^2+1}\, \left[ R^2/\sqrt{R_t^2/R_c^2+1} + \right.\right. \\ &\left.\left. +\ R_c^2 \left(1/\sqrt{R_t^2/R_c^2+1} - 4\sqrt{R^2/R_c^2+1}\right)\right]\right\} + L_{\rm ZP}, \end{aligned} \tag{4.2}$$

where $L_{ZP}$ is the zero-point luminosity level.

### 4.1.2 The standard $\beta$-model

The standard $\beta$-model (Cavaliere and Fusco-Femiano 1976) has traditionally been used to reproduce the intensity profile of an isothermal sphere of hot intracluster medium (ICM) in hydrostatic equilibrium (see e.g., Jones and Forman 1984). This appears to be a valid approximation only in the case of galaxy clusters with a regular X-ray morphology, although it is applied also to clusters where this is not verified.

The $\beta$-model can be expressed through the following formula:

$$I(R) = I_0 \left[1 + \left(\frac{R}{R_c}\right)^2\right]^{0.5-3\,\beta}, \tag{4.3}$$

where $I_0$ is the central surface brightness value, $R_c$ the core radius that we defined in Section 4.1.1, and $\beta$ is the ratio between the specific energy within hot ICM and the specific energy within galaxies. In other words:

$$\beta = \frac{\mu\, m_{\rm P}\, \sigma^2}{k\, T_{\rm ICM}}, \tag{4.4}$$

where $\mu$ is the mean molecular weight, $m_{\rm P}$ the proton mass, $k$ the Boltzmann constant and $T_{\rm ICM}$ the ICM temperature.

Thanks to the fits performed on ROSAT PSPC data, most authors have derived beta values of the order of $\beta \sim 0.5$ in the case of galaxy groups (see e.g., Ponman and Bertram 1993) and $\beta \sim 0.64$ for galaxy clusters (see e.g., Mohr et al. 1999).

In principle the $\beta$-model could be used to reproduce our luminosity profiles because the galaxy distribution, just like the ICM, should be a tracer of the potential well where the entire cluster resides. Its luminosity profile is equal to:

$$L(\leq R) = \int 2\pi R\, I(R)\, dR = \frac{2\pi R_c^2\, I_0}{3-6\beta} \left[1 + \left(\frac{R}{R_c}\right)\right]^{1.5-3\beta} + L_{\rm ZP}. \tag{4.5}$$

### 4.1.3 The Sérsic model

The Sérsic (1963, 1968) law is widely adopted for reproducing the bulges of both early- and late-type galaxies (see e.g., Caon et al. 1993; D'Onofrio et al. 1994; Andredakis et al. 1995). It is expressed by the following formula:

$$I(R) = I_e e^{-b_n\left[(R/R_e)^{1/n}-1\right]}, \tag{4.6}$$

where $R_e$ is the effective radius (i.e., the radius containing one half of the total luminosity), $I_e$ the effective intensity (i.e., the local value of the intensity at $R = R_e$), $n$ the Sérsic parameter, and $b_n$ a function of the $n$ parameter without an analytical expression. In fact, $b_n$ is defined as the parameter for which:

$$\Gamma(2n) = 2\gamma(2n, b_n), \tag{4.7}$$

where $\Gamma$ and $\gamma$ are, respectively, the gamma and lower incomplete gamma functions, i.e.:

$$\Gamma(x) = \int_0^{+\infty} z^{x-1} e^{-z}\, dz, \tag{4.8}$$

$$\gamma(x, y) = \int_0^{y} z^{x-1}\, e^{-z}\, dz. \tag{4.9}$$

While $R_e$ and $I_e$ control the size and luminosity of the source, the $n$ parameter defines the shape of the curve. In particular, for $n = 1$ the Sérsic law becomes the exponential law (Freeman 1970) for galaxy disks and pseudo-bulges, and for $n = 4$ it becomes the de Vaucouleurs (1948) law for classical bulges, which was also used by Marmo et al. (2004) for parametrizing the surface brightness profiles of WINGS clusters.

The integrated luminosity of the Sérsic model is given by:

$$L(\leq R) = \int 2\pi r\, I(R)\, dR = \frac{2\pi n\, R_e^2\, I_e\, e^{b_n}}{b_n^{2n}}\, \gamma\left(2n, b_n(R/R_e)^{1/n}\right) + L_{\rm ZP}, \tag{4.10}$$

where we chose to parametrize $b_n$ with the Prugniel and Simien (1997) approximation for $n \geq 0.5$ and with the MacArthur et al. (2003) approximation for $n < 0.5$.

## 4.2 The goodness-of-fit criterium choice

The models analyzed in Section 4.1 have a different number of free parameters: 4 in the case of the King law, and 3 for the $\beta$ and Sérsic models and the $\chi^2$ generally decreases as the number of free parameters increases. Therefore, a goodness-of-fit criterium is required for comparing the different models and selecting the one that best reproduces the data by keeping at minimum the number of free parameters.

Two of the most commonly-used goodness-of-fit criteria are:

- the Akaike (1973) information criterion (AIC):

$$\mathrm{AIC} = \chi^2 + 2k + \frac{2k\,(k+1)}{N-k-1}, \tag{4.11}$$

  where $k$ is the number of free parameters, and $N$ the number of data points to be fitted;

- the Bayesian information criterion (BIC, Schwarz 1978):

$$\mathrm{BIC} = \chi^2 + k \ln(N)\,. \tag{4.12}$$

The rule for both criteria is to choose the model able to minimize the AIC or BIC value.

A comparison between them can be found in Burnham and Anderson (2002), according to which both the AIC and the BIC can be obtained, by changing the prior, in the same Bayesian context. These authors identify two main theoretical advantages of the AIC over the BIC: firstly, the AIC is derived from the principles of information, while the BIC is not; secondly, the BIC prior is not sensible in the information theory context. Moreover, as a result of simulations, the authors also concluded that the AIC is less biased than the BIC.

Despite this, we chose to priviledge the BIC over the AIC for two main reasons: first, it is built starting from a vague or uniform prior (Burnham and Anderson 2002), which is a good assumption in our context, where we have no theoretical justification to privilege a particular category of models; secondly, it penalizes more strongly models with a higher number of free parameters (Kass and Raftery 1995), thus it reduces the risk of adopting over-complicated models (which will be particularly useful in Section 4.3).

In order to understand how strongly one model is favoured in comparison with another, we used the criterion defined by Kass and Raftery (1995), according to which, if we call $\Delta$BIC the difference between the BICs of the two models:

- $0 \leq \Delta\mathrm{BIC} < 2$ is not worth more than a bare mention;
- $2 \leq \Delta\mathrm{BIC} < 6$ indicates a positive evidence towards the lowest-BIC model;
- $6 \leq \Delta\mathrm{BIC} < 10$ indicates a strong evidence towards the lowest-BIC model;
- $\Delta\mathrm{BIC} \geq 10$ indicates a very strong evidence towards the lowest-BIC model.

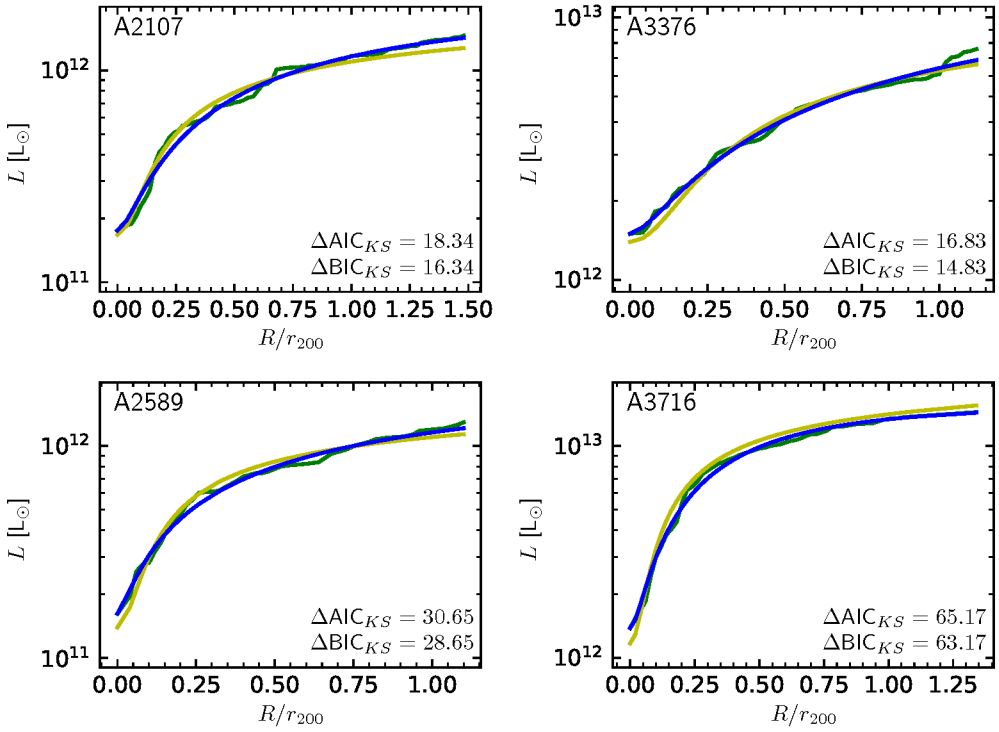


Figure 4.1: The growth curves of the 4 clusters (green lines) best-fitted with the King models (yellow lines) and the corresponding Sérsic fits (blue lines). The cluster name is displayed on the upper-left corner of each panel, while on the lower-right corner we plotted the discrepancy between the two models quantified with the two criteria defined in Section 4.2.

## 4.3 The profile fitting procedure

To have more reliable fits (expecially in the central regions, where the integrated luminosity steeply rises) we rebinned the profiles with a radial spacing of $0.02\,r_{200}$.

The King model offered the worst representation of the observed luminosity profiles, and the Sérsic model the best one. Figure 4.1 allows a visual comparison between the King model (yellow line), the Sérsic model (blue line), and the data (green line) in the case where the parameter $\Delta BIC_{KS}$, assumed the smalles values. In all these cases the King model is strongly disfavoured with respect to the Sérsic model. Moreover, in order to match the bulk of the data points, the King profile usually mismatched the central luminosity value, which is known with a high precision. As a consequence,

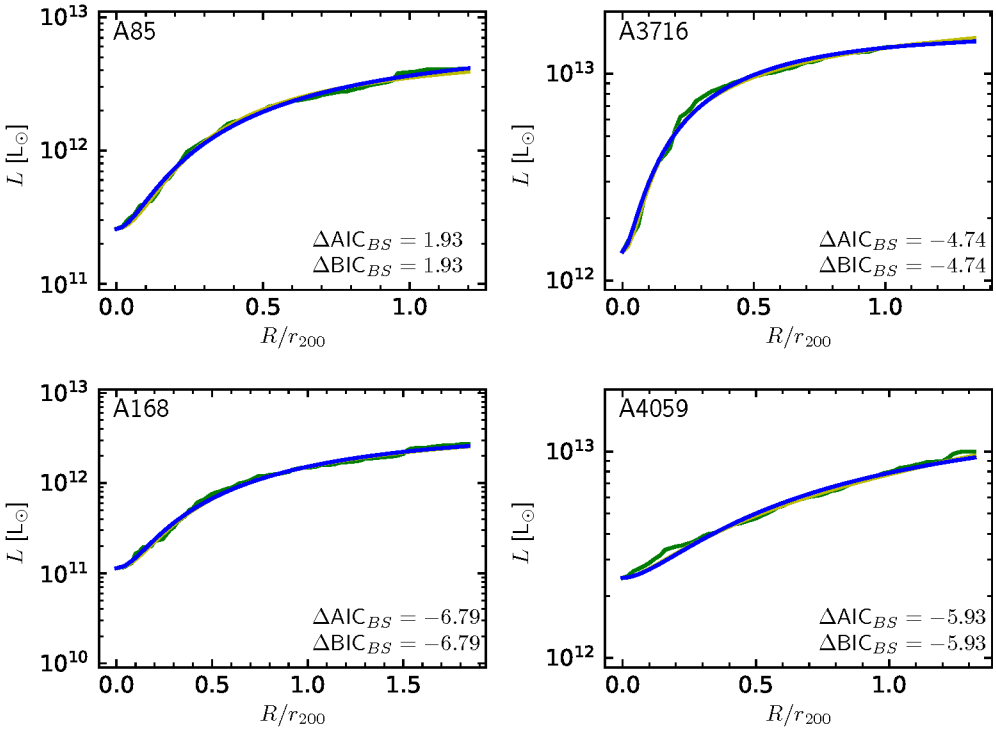


Figure 4.2: The light profiles of the 4 clusters (green lines) best-fitted with the $\beta$-models (yellow lines) and the corresponding Sérsic models (blue lines). The cluster name is displayed on the upper-left corner of each panel, while on the lower-right corner we plotted the discrepancy between the two models quantified with the two criteria defined in Section 4.2. Since the number of free parameters and data point is equal in the case of the two models, $\Delta\mathrm{BIC_{BS}} = \mathrm{BIC_{Beta}} - \mathrm{BIC_{Sersic}} = \Delta\mathrm{AIC_{BS}} = \mathrm{AIC_{Beta}} - \mathrm{AIC_{Sersic}} = \Delta\chi^2$.

the King model was rejected.

A better situation was found when comparing the standard $\beta$-model with the Sérsic model. In fact, in this case the two profiles are much more similar (see Figure 4.2 for a visual comparison), but except for a borderline case (namely, A85) all the beta models are strongly or very strongly disfavoured when compared with the Sérsic models. It is interesting to note, however, that most of the derived $\beta$ parameter values are compatible with those typical of the ICM in galaxy groups and clusters (Figure 4.3).

The integrated Sérsic profile was able to correctly reproduce most of the observed profiles, but the presence of luminosity bumps in the profile of a few clusters resulted in some poor fits. This issue was solved by fitting our

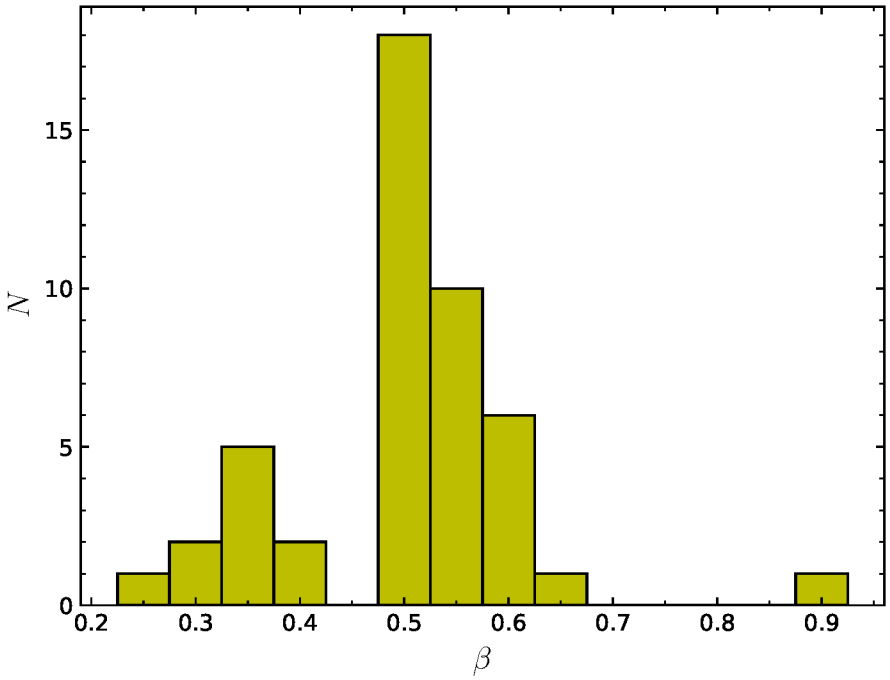


Figure 4.3: Histogram of all the $\beta$ parameters values derived starting from the growth curve fitting.

data also with a double Sérsic profile (i.e., the superposition of two Sérsic profiles), in analogy with the profiles of disk galaxies, which usually display two embedded components. However, to minimize the risk of adopting over-complicated models, we chose to privilege the single Sérsic models in every case, except when a strong or very strong evidence in support of the double Sérsic ones was present. This resulted in 39 single and 7 double Sérsic fits whose effective parameters are tabulated in Table 4.1. We note that for all the double Sérsic profiles the inner component is always smaller and fainter, but with a higher value of surface brightness than the outern one.

For a recap of the fitting parameters see Tables 4.2 and 4.3, while to see the fits look at Section 4.4.

The confidence intervals around the best fit parameters have been calculated with the following procedure: the $\chi^2$ was recomputed giving to all the points a constant weight calculated in such a way to have a final $\chi^2 = N - k$ (where $N - k$ is the number of degrees of freedom), then each parameter was individually modified until the $\chi^2$ reached the value $N - k + 9$ (i.e.,

the interval contained a probability of 99.73% of finding the true parameter value).

In the double Sérsic fits sometimes the threshold $N - k + 9$ could not be reached, and the limit was marked as *undefined*. This happens in two possible cases: first, when the Sérsic index $n_{in}$ cannot be safely constrained due to a very limited number of data points where the inner component dominates; second, when inside the central region the inner component is not significantly brighter than the outern one and the outern region displays a very disturbed profile no significant increase in the $\chi^2$ is possible by increasing the inner-component effective radius value $R_{e,in}$.

The confidence limits derived in this way are likely an overestimation of the structural parameters true errors because they have been calculated by ignoring the mutual correlations that exist between the parameters themselves. Nontheless, all of them are of the order of few percent (see Table 4.2).

## 4.4 The fits

Figures 4.4−4.26 we present the best-fit values for all the clusters of our sample.

Almost all the profiles seem to well represent both the luminosity and the surface brightness of our clusters, however at least in one case (i.e., A1631a) our best model selection criterion preferred a single Sérsic fit where a human analysis of the surface brightness profile would suggest a two-component model.

In a few cases the total asymptotic luminosity may have been overestimated. In fact, in the case of A151, A754, and maybe also A3560 the fitted profile intercepts with an increasing trend the very upper edge of the growth curve, which instead appears to flatten. A possible way to improve the quality of these fits could be the implementation of a simultanous minimization of the residuals of both the integrated luminosity and surface brightness profiles. Instead, the profiles of A1991, A2415, and A2657 display some significant sudden increases of the luminosity profile that could be due either to some ongoing major marger or to the presence of important background structures.

No fit displays a central surface brightness higher than the observed one (within the error); in fact, to avoid unphysical divergencies at small radii all the models with higher values were immediately rejected, even if their reduced $\chi^2$ and their AIC or BIC parameter were prefereable. The same was not done in case of much lower values, because the central surface brightness

has almost certainly been overestimated; in fact, the central point displays the luminosity of the BCG and of all the galaxies within $0.01\,r_{200}$ entirely collapsed to a single point, with no information on its real distribution. As a consequence, we chose not to constrain our best model selection for matching a likely unrealistic value.

In a few cases (i.e., A147, A1631a, A1991, A2657, A2717, A3128, A3532, A3556, and IIZW108) the fitted profile is unable to correctly reproduce the fluctuations of the luminosity profile at small radii, however this is not, generally, a problem. In fact, in case of infalling structures larger than the adopted spatial scale we expect to see such fluctuations. It is interesting to note that both A1991 and A2657 display important fluctuations at larger radii too. As a consequence, we can assume that these two systems either are experiencing some relevant merging event or are made of very strongly-bound substructures.

Finally, the presence/absence of a cool core (see e.g., Henning et al. 2009) does not seem to influence the number of components used to fit the luminosity profiles. In fact, 6 of the 7 clusters of our sample analyzed by Henning et al. (2009) can be parametrized with a single Sérsic profile, despite 2 of them (i.e., A119, and A4059) have a cool-core and the remaining 4 (i.e., A85, A3266, A3558, and A3667) do not. The only exception is A3158, which has no cool core and a double Sérsic parametrization. No connection seem to exist also between the cool core presence/absence and the best fit parameters values.

Table 4.1: Cluster name (Column 1), effective radius (Columns 2), effective luminosity (Columns 3) and average intensity within the effective radius (Columns 4).

| Cluster | $r_e$ kpc | $L_e$ $10^{12}$ $L_\odot$ | $\overline{I_e}$ $L_\odot$ pc$^{-2}$ |
|---|---|---|---|
| A85 | 2058 | 3.14 | 0.24 |
| A119 | 3548 | 3.87 | 0.10 |
| A147 | 838 | 0.73 | 0.33 |
| A151 | 2373 | 4.25 | 0.24 |
| A160 | 3302 | 3.31 | 0.10 |
| A168 | 1614 | 1.80 | 0.22 |
| A193 | 536 | 0.67 | 0.75 |
| A500 | 2312 | 2.96 | 0.18 |
| A754 | 1950 | 3.71 | 0.31 |
| A957 | 2837 | 1.26 | 0.05 |
| A970 | 1544 | 1.39 | 0.19 |
| A1069 | 2651 | 2.06 | 0.09 |
| A1631a | 2041 | 9.57 | 0.73 |
| A1983 | 2105 | 1.66 | 0.12 |
| A1991 | 2248 | 2.30 | 0.15 |
| A2107 | 1335 | 1.02 | 0.18 |
| A2382 | 2144 | 2.95 | 0.20 |
| A2399 | 1895 | 2.12 | 0.19 |
| A2415 | 1146 | 0.79 | 0.19 |
| A2457 | 1258 | 1.88 | 0.38 |
| A2589 | 2097 | 1.07 | 0.08 |
| A2593 | 1037 | 1.12 | 0.33 |
| A2657 | 2088 | 1.24 | 0.09 |
| A2665 | 2595 | 1.84 | 0.09 |
| A2717 | 2453 | 1.99 | 0.11 |
| A2734 | 2606 | 1.77 | 0.08 |
| A3128 | 2016 | 5.05 | 0.40 |
| A3158 | 2658 | 4.41 | 0.20 |
| A3266 | 4026 | 6.23 | 0.12 |
| A3376 | 3167 | 7.28 | 0.23 |
| A3395 | 6843 | 25.99 | 0.18 |
| A3528a | 3283 | 7.05 | 0.21 |
| A3528b | 2800 | 5.49 | 0.22 |
| A3530 | 2618 | 11.30 | 0.52 |

Table 4.1: Continued.

| Cluster | $r_e$ kpc | $L_e$ $10^{12}$ $L_\odot$ | $\overline{I_e}$ $L_\odot$ pc$^{-2}$ |
|---|---|---|---|
| A3532 | 4811 | 16.19 | 0.22 |
| A3556 | 2246 | 7.42 | 0.47 |
| A3558 | 3636 | 25.29 | 0.61 |
| A3560 | 4978 | 21.84 | 0.28 |
| A3667 | 5890 | 25.55 | 0.23 |
| A3716 | 801 | 7.78 | 3.86 |
| A3809 | 1503 | 3.54 | 0.50 |
| A3880 | 4037 | 9.52 | 0.19 |
| A4059 | 2309 | 7.88 | 0.47 |
| IIZW108 | 2025 | 1.53 | 0.12 |
| MKW3s | 2323 | 1.42 | 0.08 |
| Z8852 | 1301 | 1.12 | 0.21 |

Table 4.2: Cluster name (Column 1), parameters of the best single Sérsic decomposition (Columns 2−4), normalized $\chi^2$ value associated to the best single Sérsic decomposition (Column 5), AIC value associated to the best single Sérsic decomposition (Column 6), and BIC value associated to the best single Sérsic decomposition (Column 7).

| Cluster | $n$ | $R_e/r_{200}$ | log $(I_e\ [L_\odot\ \mathrm{pc}^{-2}])$ | $\chi^2_{\mathrm{BM}}$ | $\mathrm{AIC_{BM}}$ | $\mathrm{BIC_{BM}}$ |
|---|---|---|---|---|---|---|
| A85 | $1.48^{+0.07}_{-0.07}$ | $0.87^{+0.03}_{-0.02}$ | $-1.00^{+0.01}_{-0.01}$ | 0.33 | 23.93 | 30.06 |
| A119 | $4.08^{+0.08}_{-0.07}$ | $1.70^{+0.03}_{-0.03}$ | $-1.54^{+0.01}_{-0.01}$ | 0.12 | 11.01 | 16.43 |
| A147 | $1.36^{+0.13}_{-0.07}$ | $0.52^{+0.01}_{-0.02}$ | $-0.85^{+0.01}_{-0.01}$ | 1.44 | 67.71 | 73.20 |
| A160 | $4.76^{+0.15}_{-0.10}$ | $2.43^{+0.07}_{-0.02}$ | $-1.62^{+0.01}_{-0.01}$ | 0.18 | 19.26 | 26.29 |
| A168 | $1.13^{+0.06}_{-0.07}$ | $1.22^{+0.04}_{-0.04}$ | $-0.97^{+0.01}_{-0.01}$ | 0.66 | 54.49 | 61.48 |
| A193 | $3.98^{+0.32}_{-0.25}$ | $0.29^{+0.01}_{-0.01}$ | $-0.76^{+0.01}_{-0.01}$ | 0.34 | 18.86 | 24.00 |
| A500 | $2.42^{+0.14}_{-0.09}$ | $1.22^{+0.04}_{-0.02}$ | $-1.21^{+0.02}_{-0.01}$ | 0.30 | 29.60 | 36.78 |
| A754 | $2.05^{+0.06}_{-0.05}$ | $0.88^{+0.01}_{-0.02}$ | $-0.94^{+0.01}_{-0.01}$ | 0.22 | 17.16 | 23.07 |
| A957 | $4.37^{+0.29}_{-0.16}$ | $1.83^{+0.09}_{-0.04}$ | $-1.86^{+0.03}_{-0.01}$ | 0.37 | 27.61 | 33.95 |
| A970 | $3.79^{+0.13}_{-0.12}$ | $0.76^{+0.02}_{-0.01}$ | $-1.28^{+0.01}_{-0.01}$ | 0.47 | 29.98 | 35.95 |
| A1069 | $2.31^{+0.08}_{-0.07}$ | $1.59^{+0.03}_{-0.03}$ | $-1.48^{+0.01}_{-0.01}$ | 0.21 | 20.78 | 27.70 |
| A1631a | $0.17^{+0.03}_{-0.02}$ | $1.11^{+0.06}_{-0.03}$ | $-0.17^{+0.01}_{-0.01}$ | 1.39 | 108.58 | 115.61 |
| A1983 | $3.04^{+0.39}_{-0.08}$ | $1.65^{+0.18}_{-0.02}$ | $-1.41^{+0.05}_{-0.01}$ | 1.76 | 136.50 | 143.53 |
| A1991 | $1.63^{+0.15}_{-0.09}$ | $1.56^{+0.09}_{-0.03}$ | $-1.22^{+0.03}_{-0.01}$ | 0.94 | 83.90 | 91.26 |
| A2107 | $2.45^{+0.11}_{-0.09}$ | $0.93^{+0.02}_{-0.02}$ | $-1.23^{+0.01}_{-0.01}$ | 0.59 | 40.34 | 46.67 |
| A2382 | $2.17^{+0.06}_{-0.06}$ | $1.28^{+0.03}_{-0.03}$ | $-1.12^{+0.01}_{-0.01}$ | 0.25 | 26.82 | 34.22 |
| A2399 | $1.58^{+0.11}_{-0.10}$ | $1.08^{+0.03}_{-0.02}$ | $-1.10^{+0.02}_{-0.01}$ | 0.60 | 51.65 | 58.76 |
| A2415 | $0.43^{+0.24}_{-0.05}$ | $0.69^{+0.06}_{-0.02}$ | $-0.88^{+0.06}_{-0.02}$ | 1.65 | 95.13 | 101.26 |
| A2457 | $1.42^{+0.11}_{-0.05}$ | $0.77^{+0.02}_{-0.01}$ | $-0.79^{+0.01}_{-0.01}$ | 0.28 | 25.35 | 32.14 |
| A2589 | $4.09^{+0.18}_{-0.13}$ | $1.06^{+0.03}_{-0.02}$ | $-1.69^{+0.01}_{-0.01}$ | 0.28 | 18.21 | 23.70 |
| A2593 | $2.33^{+0.13}_{-0.09}$ | $0.61^{+0.01}_{-0.01}$ | $-0.94^{+0.01}_{-0.01}$ | 0.50 | 31.21 | 37.12 |

Table 4.2: Continued.

| Cluster | $n$ | $R_e/r_{200}$ | log ($I_e$ [$L_\odot$ pc$^{-2}$]) | $\chi^2_{\rm BM}$ | AIC$_{\rm BM}$ | BIC$_{\rm BM}$ |
|---|---|---|---|---|---|---|
| A2657 | $3.08^{+0.56}_{-0.19}$ | $2.26^{+0.25}_{-0.07}$ | $-1.52^{+0.05}_{-0.02}$ | 2.10 | 148.95 | 155.74 |
| A2665 | $2.24^{+0.17}_{-0.07}$ | $1.73^{+0.10}_{-0.03}$ | $-1.51^{+0.03}_{-0.01}$ | 0.67 | 51.47 | 58.26 |
| A2734 | $3.00^{+0.19}_{-0.12}$ | $1.39^{+0.06}_{-0.03}$ | $-1.59^{+0.02}_{-0.01}$ | 0.45 | 31.41 | 37.69 |
| A3128 | $1.54^{+0.07}_{-0.04}$ | $1.00^{+0.02}_{-0.02}$ | $-0.77^{+0.01}_{-0.01}$ | 1.22 | 86.56 | 93.26 |
| A3266 | $3.64^{+0.10}_{-0.09}$ | $1.27^{+0.03}_{-0.03}$ | $-1.44^{+0.01}_{-0.01}$ | 0.22 | 16.18 | 21.86 |
| A3376 | $2.75^{+0.13}_{-0.09}$ | $1.55^{+0.06}_{-0.03}$ | $-1.14^{+0.02}_{-0.01}$ | 0.20 | 16.79 | 22.87 |
| A3395 | $2.71^{+0.11}_{-0.04}$ | $2.35^{+0.14}_{-0.05}$ | $-1.19^{+0.02}_{-0.01}$ | 0.52 | 28.33 | 33.81 |
| A3528a | $1.54^{+0.08}_{-0.05}$ | $1.34^{+0.07}_{-0.03}$ | $-1.05^{+0.02}_{-0.01}$ | 0.47 | 36.20 | 42.82 |
| A3532 | $4.22^{+0.25}_{-0.09}$ | $2.48^{+0.15}_{-0.02}$ | $-1.18^{+0.03}_{-0.01}$ | 0.69 | 56.01 | 62.96 |
| A3556 | $2.73^{+0.30}_{-0.10}$ | $1.39^{+0.13}_{-0.03}$ | $-0.85^{+0.04}_{-0.01}$ | 0.87 | 64.57 | 71.32 |
| A3558 | $2.20^{+0.05}_{-0.03}$ | $1.50^{+0.03}_{-0.02}$ | $-0.67^{+0.01}_{-0.01}$ | 0.10 | 10.51 | 16.00 |
| A3667 | $2.10^{+0.08}_{-0.02}$ | $2.42^{+0.12}_{-0.02}$ | $-1.03^{+0.02}_{-0.01}$ | 0.48 | 33.99 | 40.32 |
| A3716 | $1.87^{+0.06}_{-0.12}$ | $0.39^{+0.01}_{-0.01}$ | $0.15^{+0.01}_{-0.02}$ | 0.30 | 21.98 | 28.06 |
| A3809 | $0.59^{+0.04}_{-0.03}$ | $1.13^{+0.02}_{-0.01}$ | $-0.50^{+0.01}_{-0.01}$ | 0.54 | 61.97 | 69.99 |
| A4059 | $1.80^{+0.13}_{-0.06}$ | $1.27^{+0.09}_{-0.03}$ | $-0.79^{+0.03}_{-0.01}$ | 0.28 | 23.60 | 30.22 |
| IIZW108 | $2.80^{+0.15}_{-0.08}$ | $1.37^{+0.04}_{-0.03}$ | $-1.40^{+0.02}_{-0.01}$ | 0.86 | 62.84 | 69.54 |
| MKW3s | $3.16^{+0.42}_{-0.13}$ | $1.78^{+0.18}_{-0.04}$ | $-1.57^{+0.05}_{-0.01}$ | 1.35 | 95.40 | 102.10 |
| Z8852 | $2.57^{+0.19}_{-0.12}$ | $0.77^{+0.03}_{-0.02}$ | $-1.16^{+0.02}_{-0.01}$ | 0.89 | 47.72 | 53.46 |

Table 4.3: Cluster name (Column 1), parameters of the best single Sérsic decomposition (Columns 2−7), normalized $\chi^2$ value associated to the best double Sérsic decomposition (Column 8), AIC value associated to the best double Sérsic decomposition (Column 9), and BIC value associated to the best double Sérsic decomposition (Column 10).

| Cluster | $n_{in}$ | $R_{e,in}/r_{200}$ | $\log(I_{e,in})$ $L_\odot$ pc$^{-2}$ | $n_{out}$ | $R_{e,out}/r_{200}$ | $\log(I_{e,out})$ $L_\odot$ pc$^{-2}$ | $\chi^2_{\rm BM}$ | AIC$_{\rm BM}$ | BIC$_{\rm BM}$ |
|---|---|---|---|---|---|---|---|---|---|
| A151 | $2.31^{undef}_{-1.62}$ | $0.03^{+0.02}_{-0.01}$ | $0.80^{+0.39}_{-0.19}$ | $1.88^{+0.81}_{-0.03}$ | $1.48^{+0.36}_{-0.01}$ | $-1.14^{+0.10}_{-0.01}$ | 0.26 | 30.10 | 42.76 |
| A2717 | $0.62^{undef}_{undef}$ | $0.06^{+0.12}_{-0.03}$ | $-0.04^{+0.48}_{-0.43}$ | $0.97^{+0.35}_{-0.03}$ | $1.95^{+0.78}_{-0.04}$ | $-1.31^{+0.09}_{-0.01}$ | 2.04 | 174.27 | 187.92 |
| A3158 | $0.51^{+2.83}_{-0.35}$ | $0.16^{undef}_{-0.02}$ | $-0.26^{+0.33}_{-0.09}$ | $0.69^{+1.01}_{-0.04}$ | $1.18^{+6.31}_{-0.07}$ | $-1.04^{+0.21}_{-0.02}$ | 0.18 | 22.34 | 33.71 |
| A3528b | $0.51^{+2.95}_{-0.37}$ | $0.11^{+0.27}_{-0.02}$ | $0.11^{+0.32}_{-0.10}$ | $1.16^{+0.97}_{-0.04}$ | $1.46^{+1.21}_{-0.06}$ | $-1.06^{+0.17}_{-0.01}$ | 0.19 | 23.37 | 35.13 |
| A3530 | $2.70^{undef}_{-1.79}$ | $0.05^{+0.04}_{-0.01}$ | $0.41^{+0.39}_{-0.16}$ | $0.52^{+0.17}_{-0.01}$ | $1.62^{+0.49}_{-0.03}$ | $-0.47^{+0.06}_{-0.01}$ | 0.42 | 45.60 | 59.18 |
| A3560 | $1.68^{undef}_{-1.65}$ | $0.04^{+0.04}_{-0.02}$ | $0.35^{+0.46}_{-0.37}$ | $1.13^{+0.22}_{-0.02}$ | $2.50^{+1.18}_{-0.05}$ | $-0.87^{+0.08}_{-0.01}$ | 0.68 | 55.71 | 68.11 |
| A3880 | $0.67^{+4.66}_{-0.64}$ | $0.16^{undef}_{-0.05}$ | $-0.34^{+0.43}_{-0.17}$ | $0.93^{+0.31}_{-0.02}$ | $2.50^{+1.75}_{-0.05}$ | $-1.03^{+0.10}_{-0.01}$ | 1.51 | 134.11 | 147.83 |

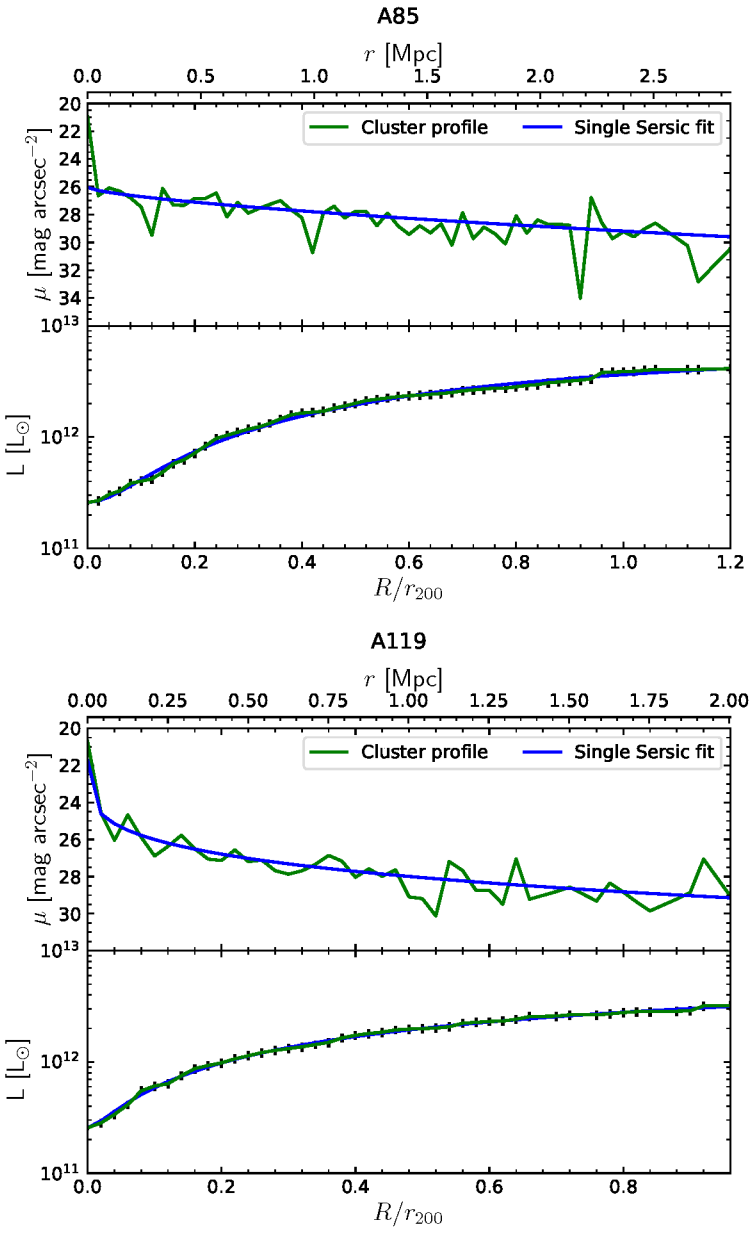


Figure 4.4: Photometric decomposition of the Omega-WINGS galaxy clusters luminosity profiles: $V$-band surface brightness and integrated luminosity profiles of the cluster A85 (green line) with the best single Sérsic fit (in blue).

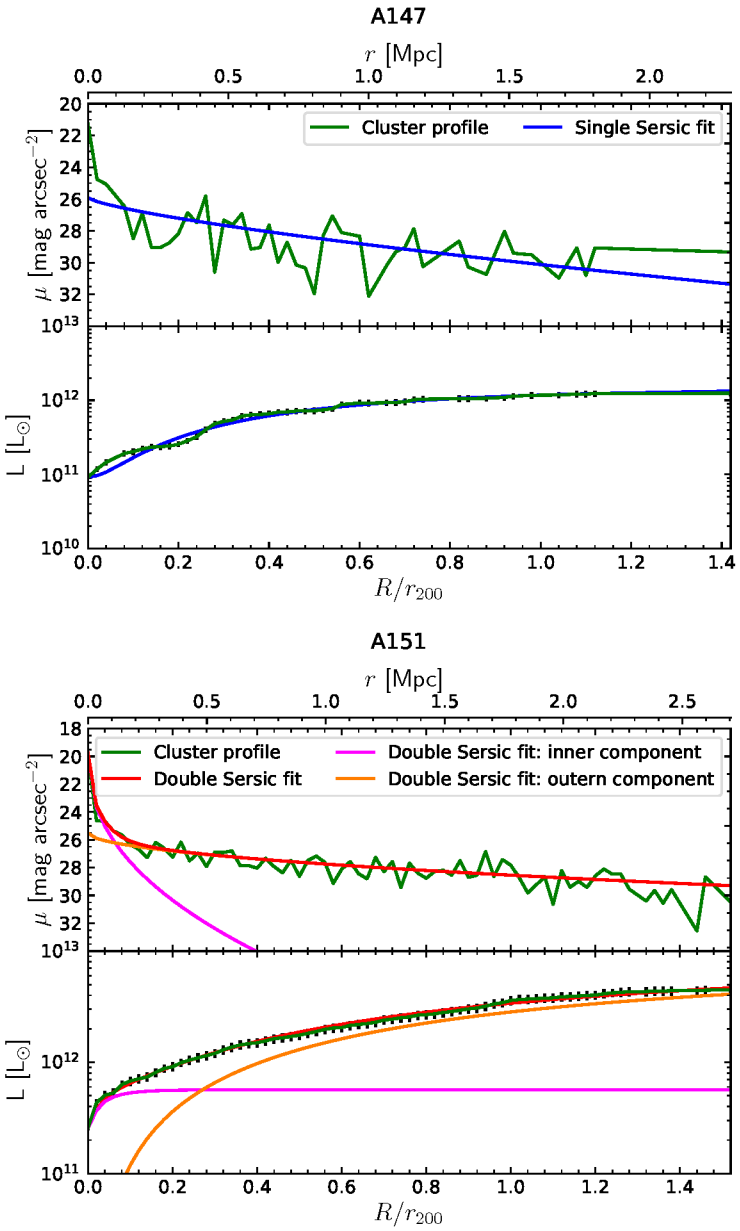


Figure 4.5: Photometric decomposition of the Omega-WINGS galaxy clusters luminosity profiles: $V$-band surface brightness and integrated luminosity profiles of the cluster A151 (green line) with the best double Sérsic fit (in red); the pink and orange lines give, respectively, the inner and outer Sérsic components.

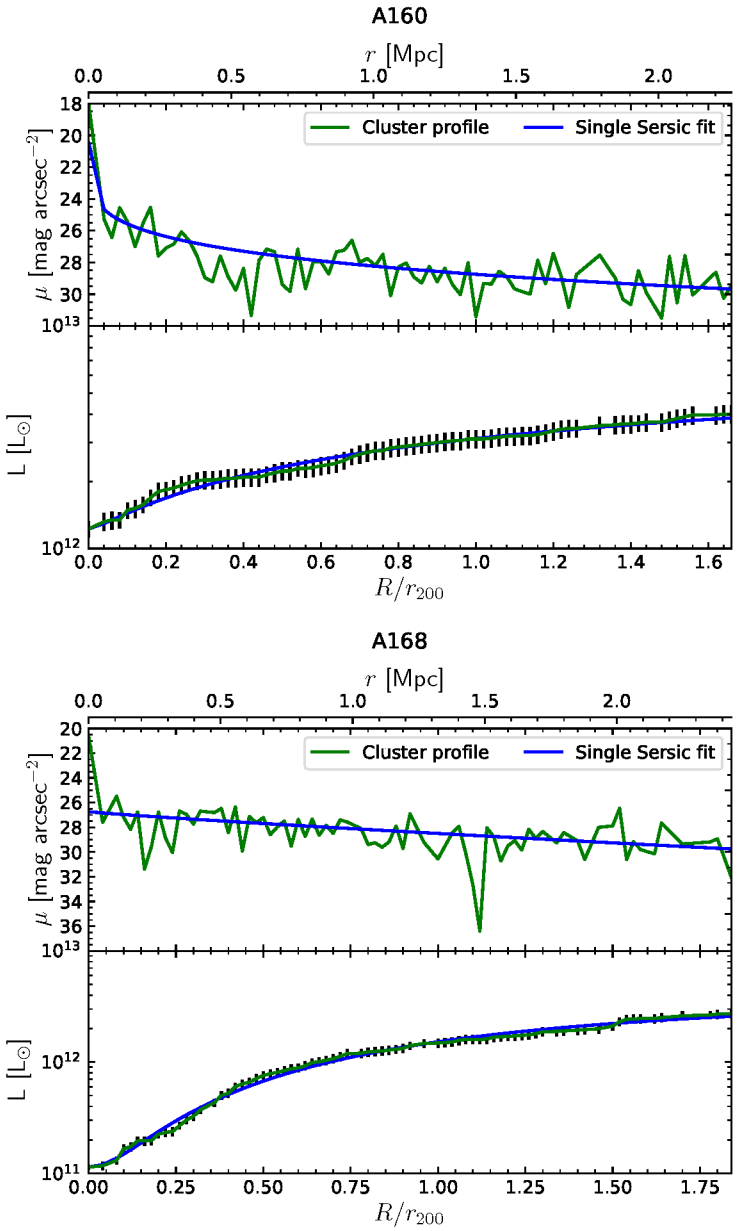


Figure 4.6: Photometric decomposition of the Omega-WINGS galaxy clusters luminosity profiles. Continued.

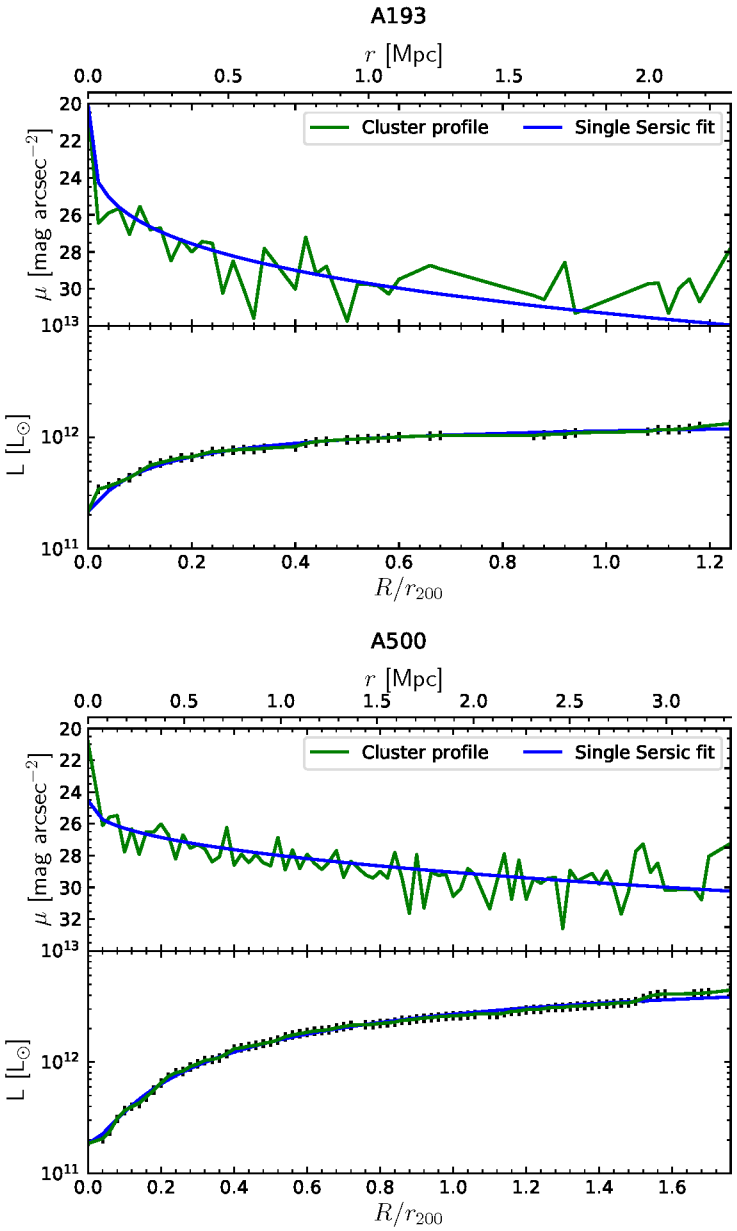


Figure 4.7: Photometric decomposition of the Omega-WINGS galaxy clusters luminosity profiles. Continued.

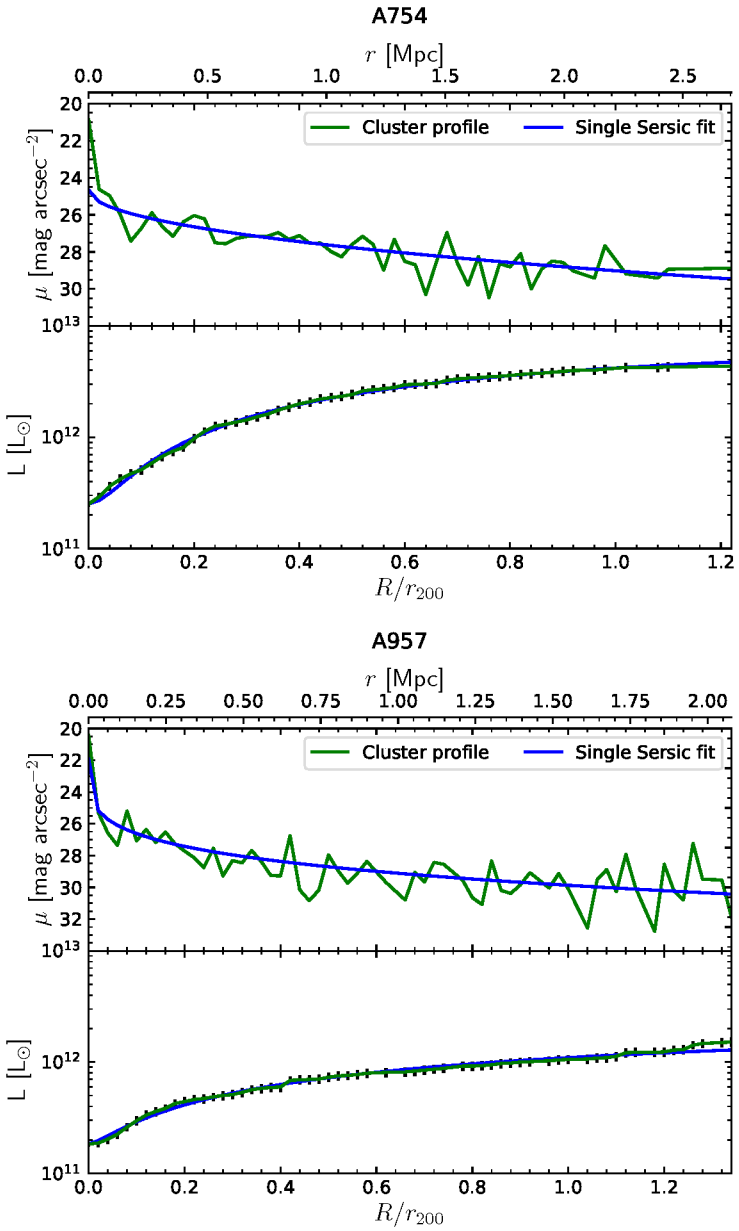


Figure 4.8: Photometric decomposition of the Omega-WINGS galaxy clusters luminosity profiles. Continued.

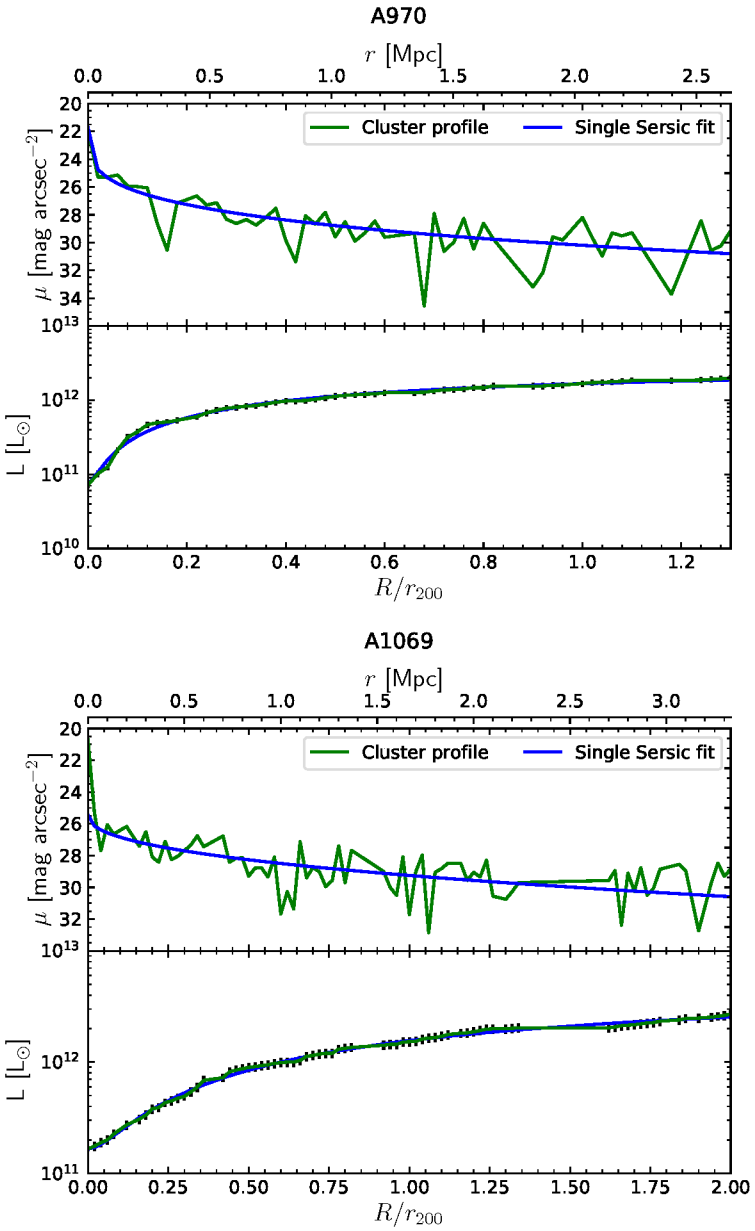


Figure 4.9: Photometric decomposition of the Omega-WINGS galaxy clusters luminosity profiles. Continued.

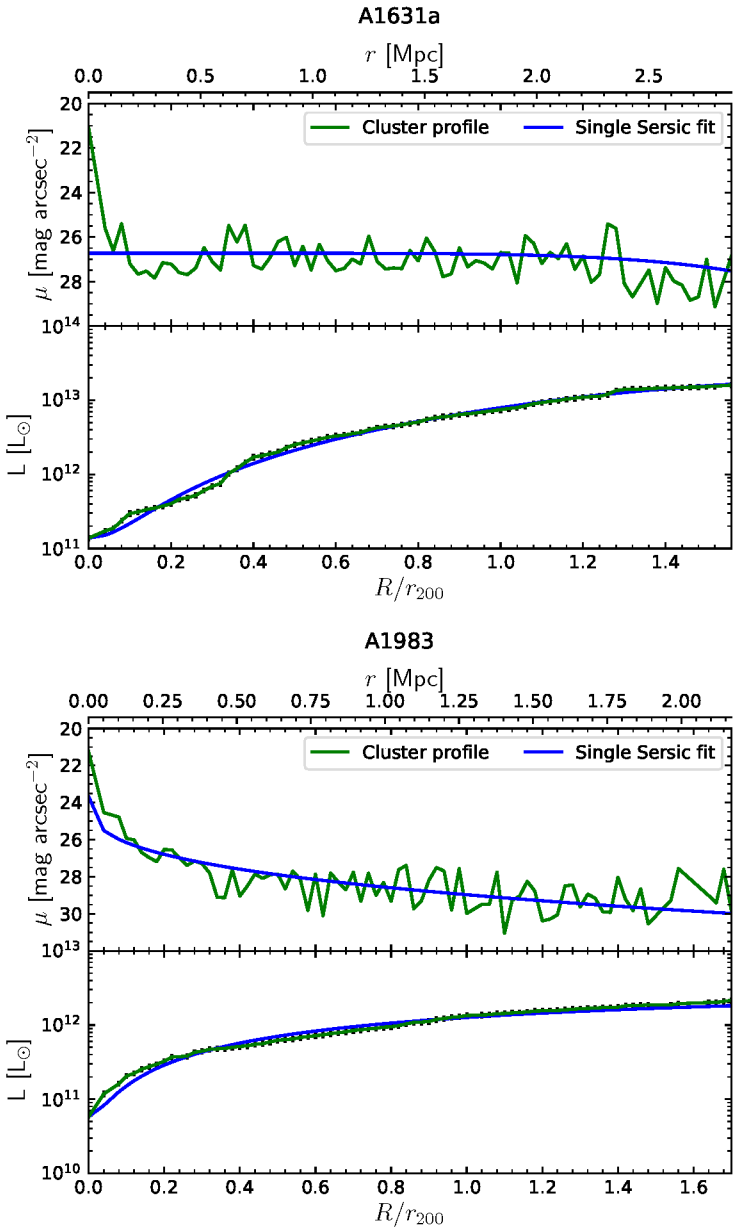


Figure 4.10: Photometric decomposition of the Omega-WINGS galaxy clusters luminosity profiles. Continued.

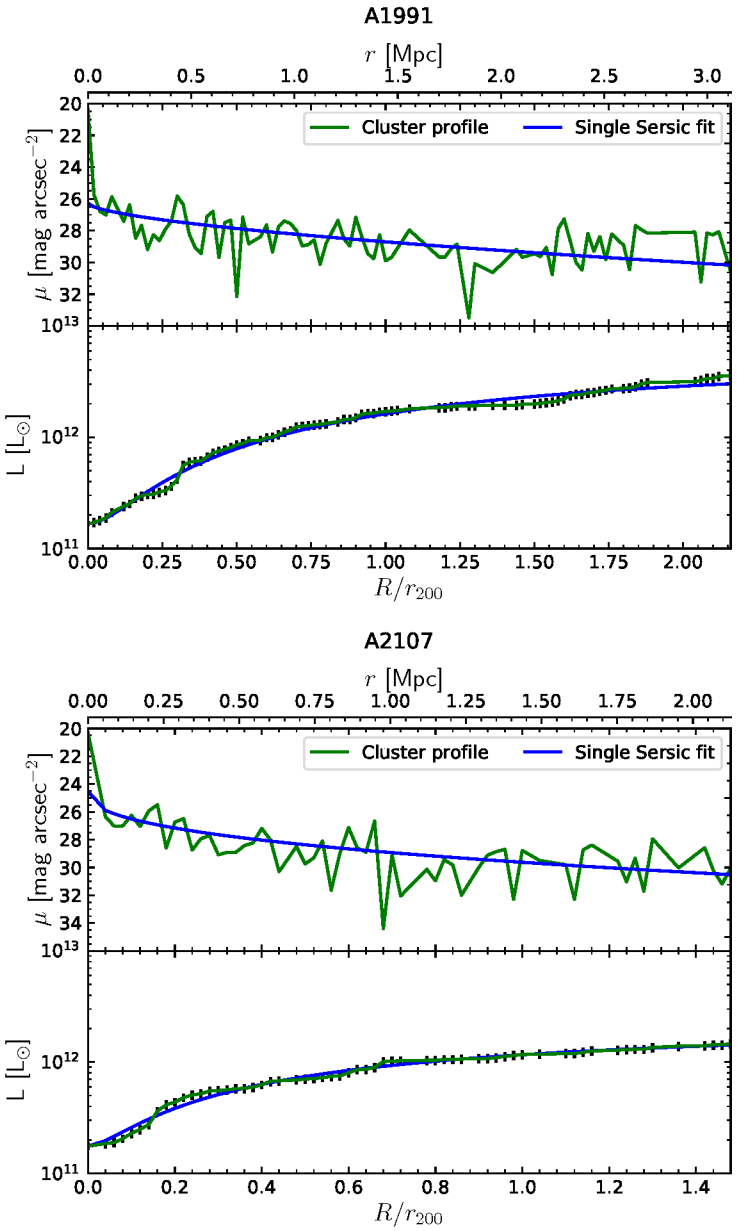


Figure 4.11: Photometric decomposition of the Omega-WINGS galaxy clusters luminosity profiles. Continued.

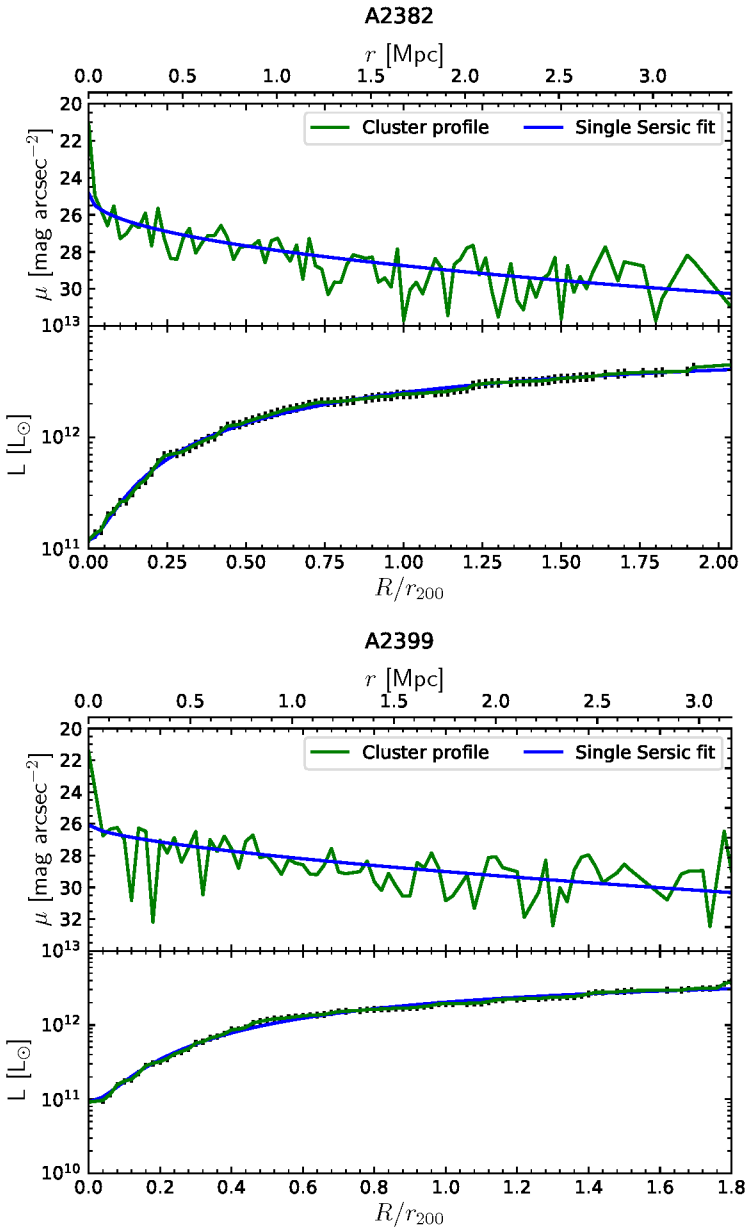


Figure 4.12: Photometric decomposition of the Omega-WINGS galaxy clusters luminosity profiles. Continued.

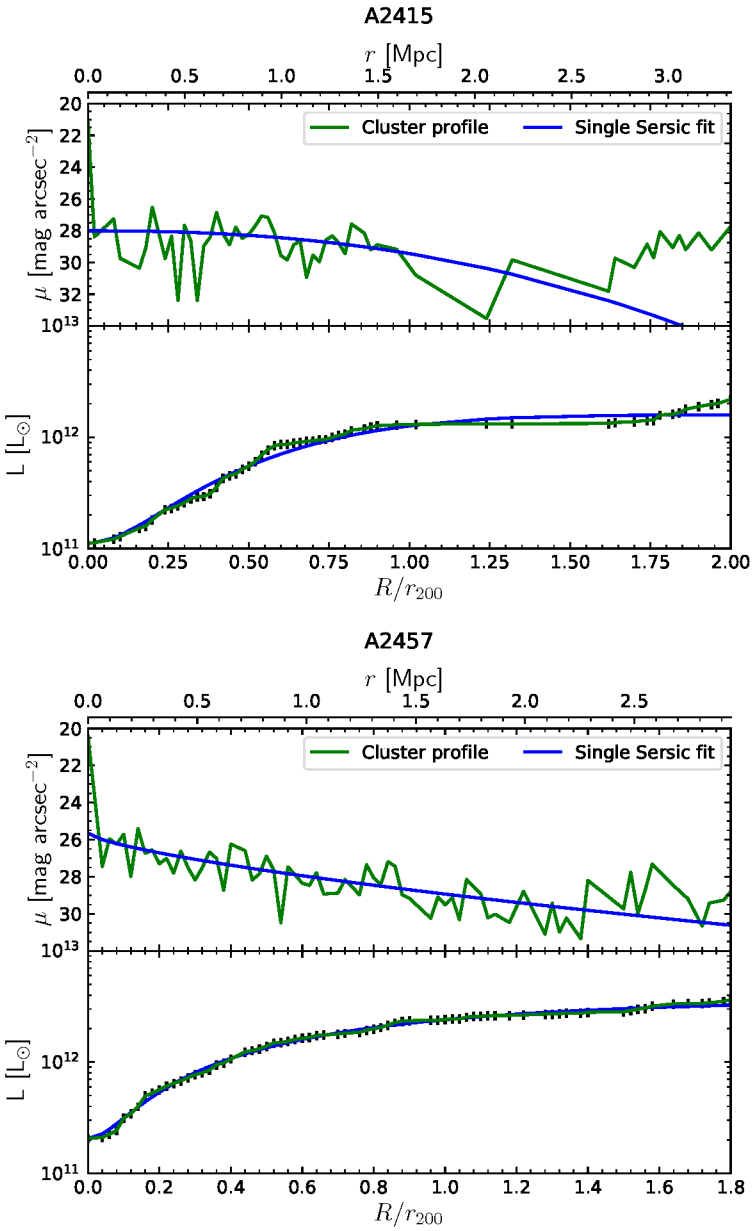


Figure 4.13: Photometric decomposition of the Omega-WINGS galaxy clusters luminosity profiles. Continued.

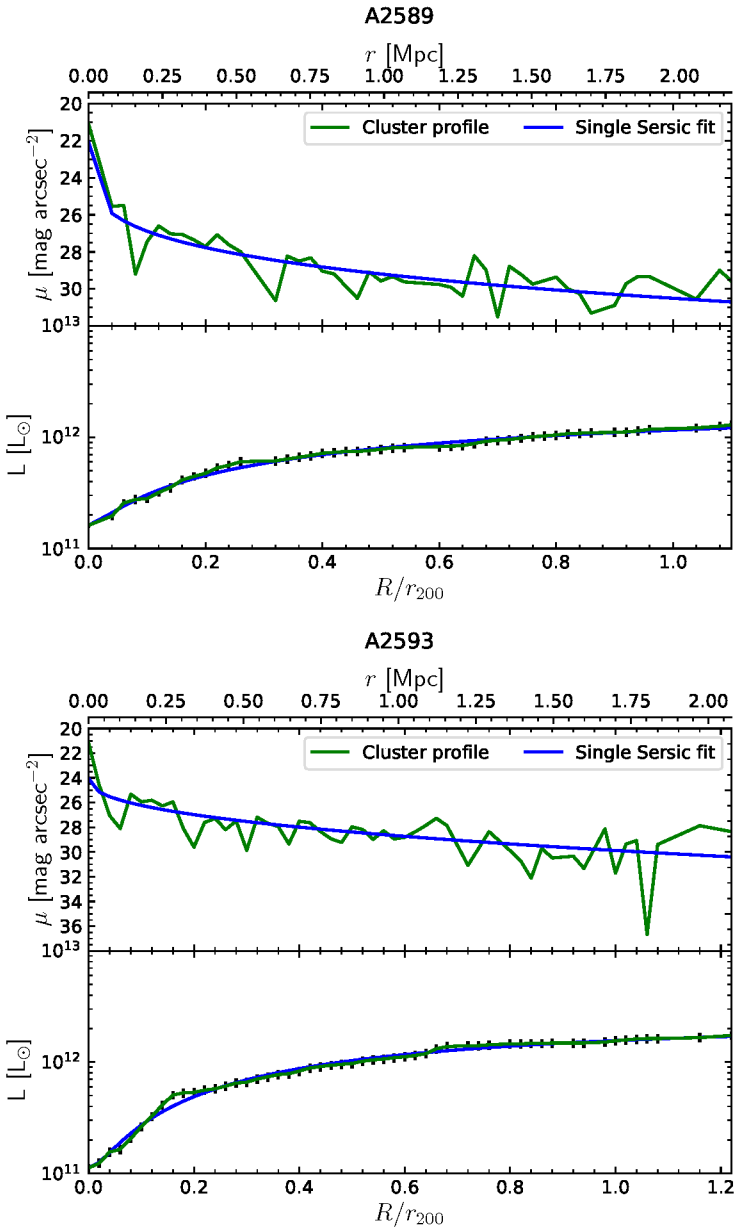


Figure 4.14: Photometric decomposition of the Omega-WINGS galaxy clusters luminosity profiles. Continued.

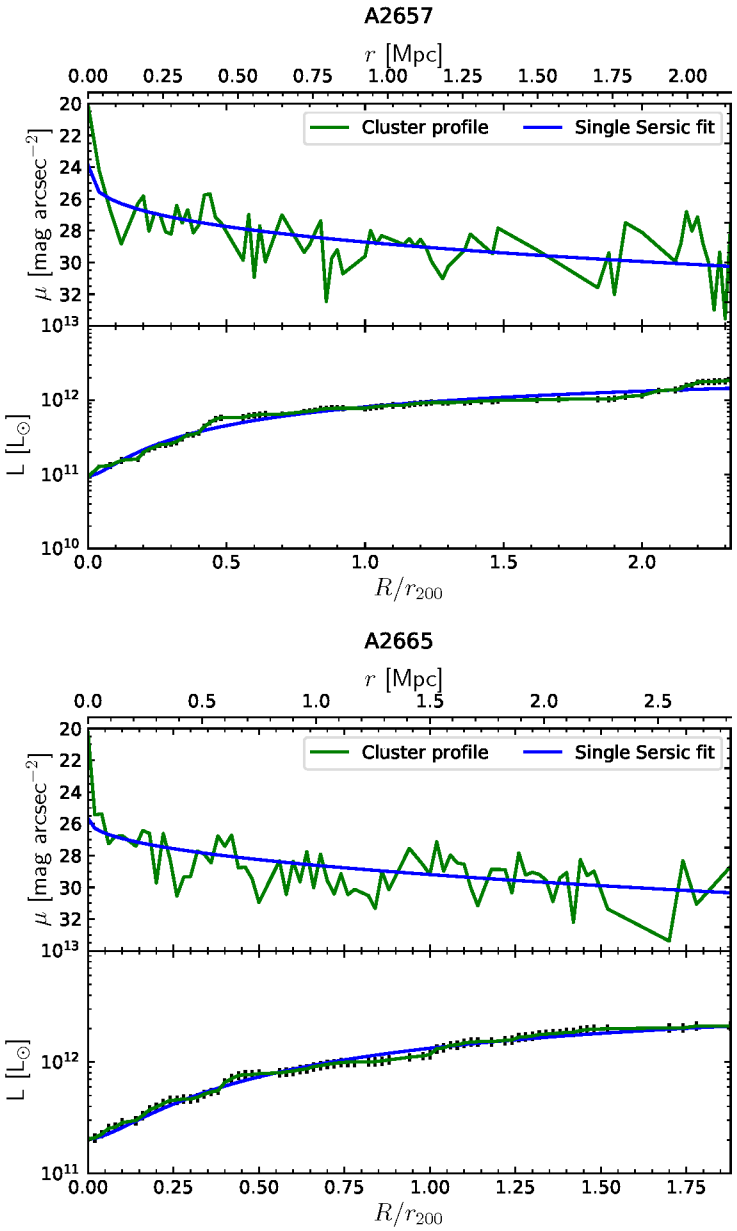


Figure 4.15: Photometric decomposition of the Omega-WINGS galaxy clusters luminosity profiles. Continued.

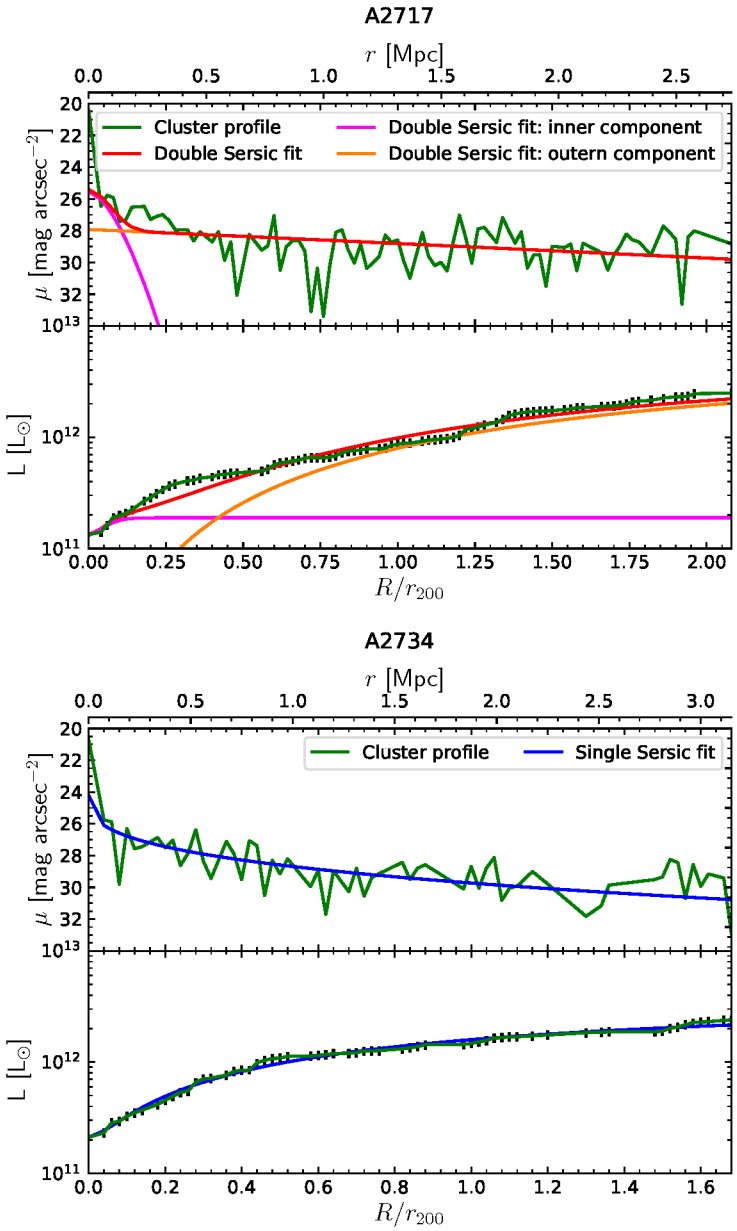


Figure 4.16: Photometric decomposition of the Omega-WINGS galaxy clusters luminosity profiles. Continued.

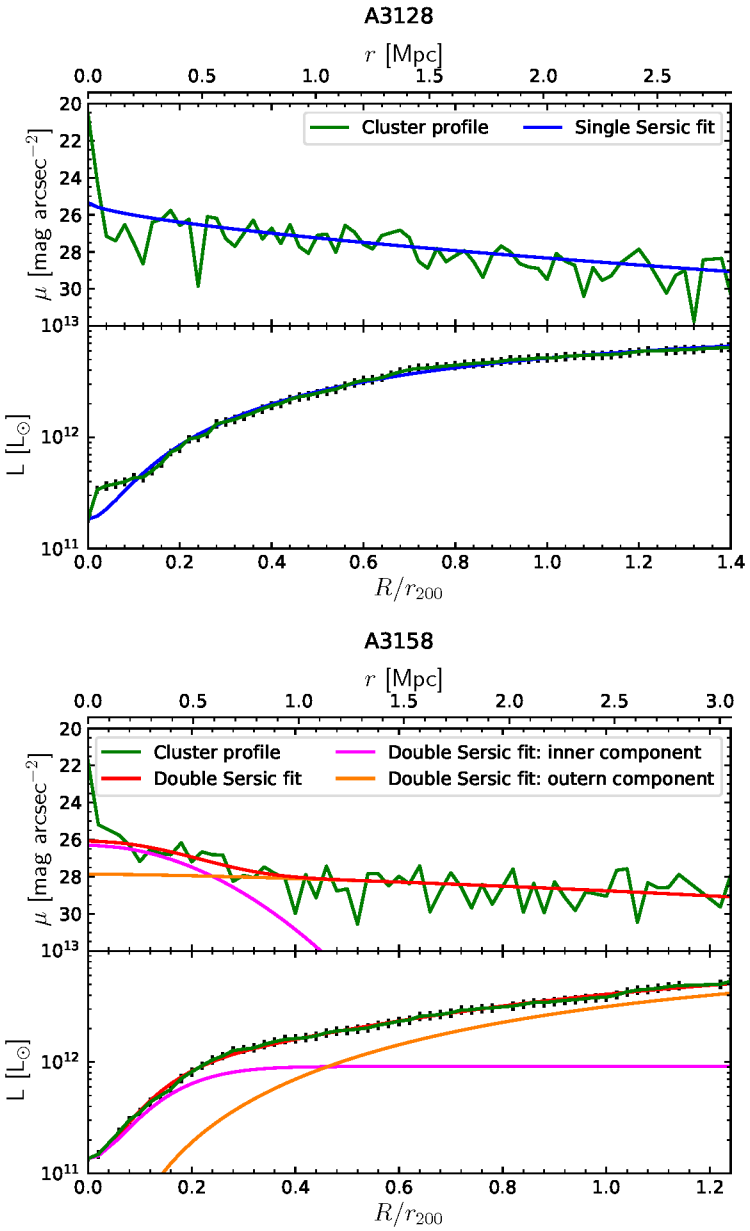


Figure 4.17: Photometric decomposition of the Omega-WINGS galaxy clusters luminosity profiles. Continued.

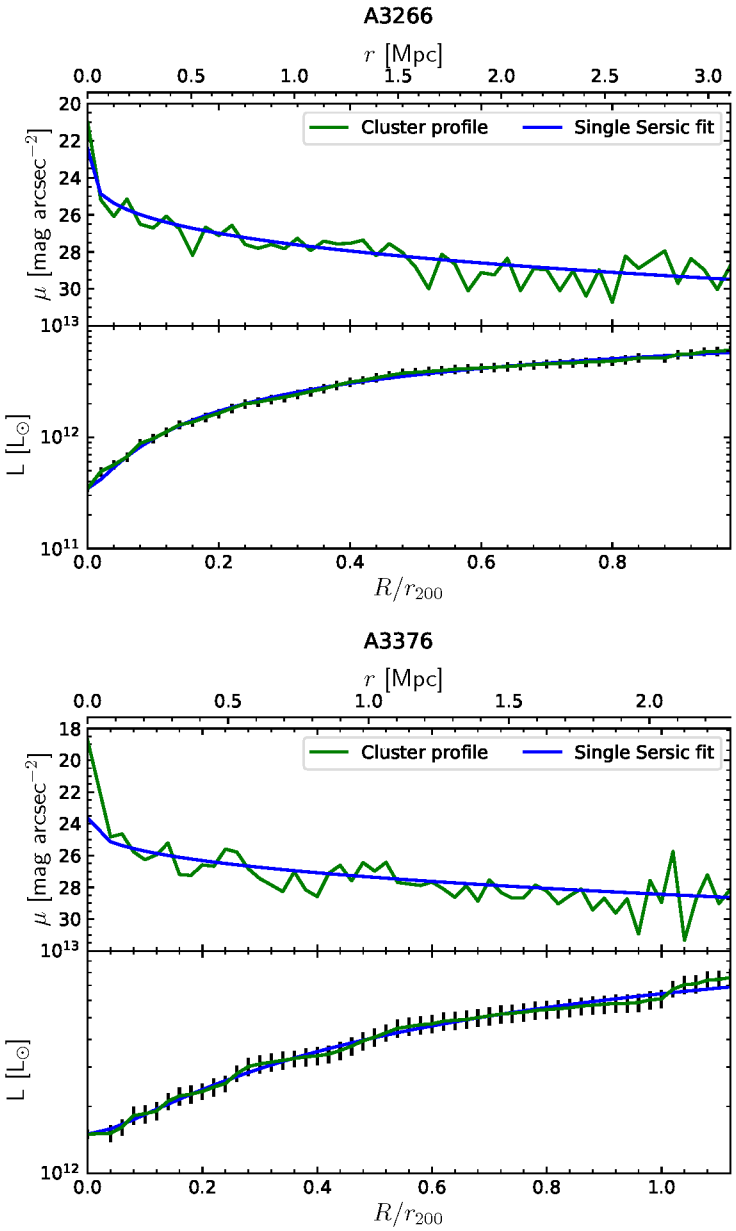


Figure 4.18: Photometric decomposition of the Omega-WINGS galaxy clusters luminosity profiles. Continued.

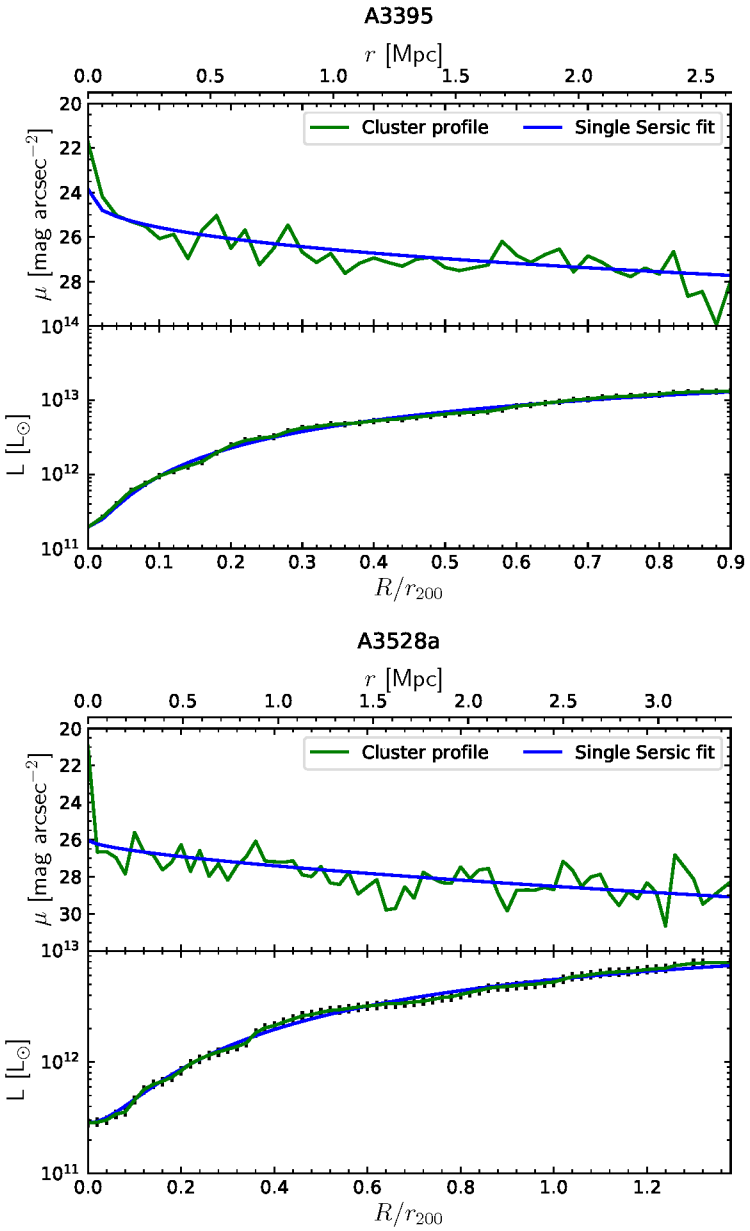


Figure 4.19: Photometric decomposition of the Omega-WINGS galaxy clusters luminosity profiles. Continued.

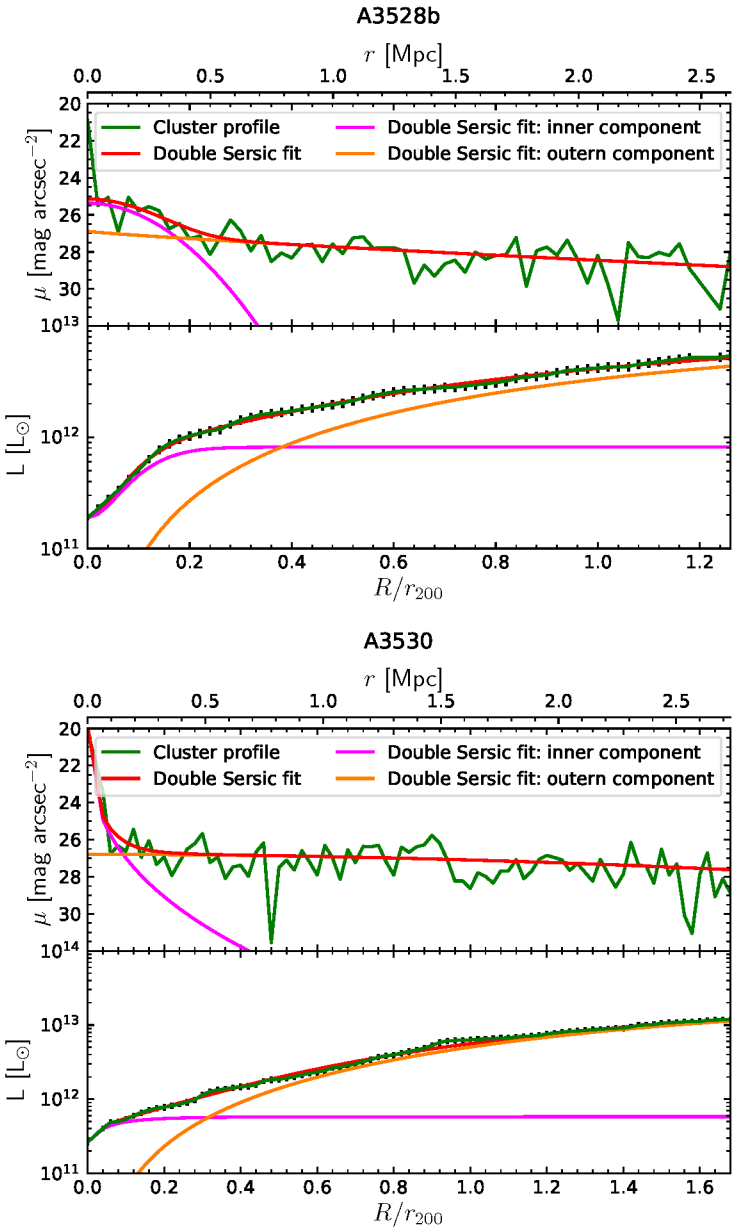


Figure 4.20: Photometric decomposition of the Omega-WINGS galaxy clusters luminosity profiles. Continued.

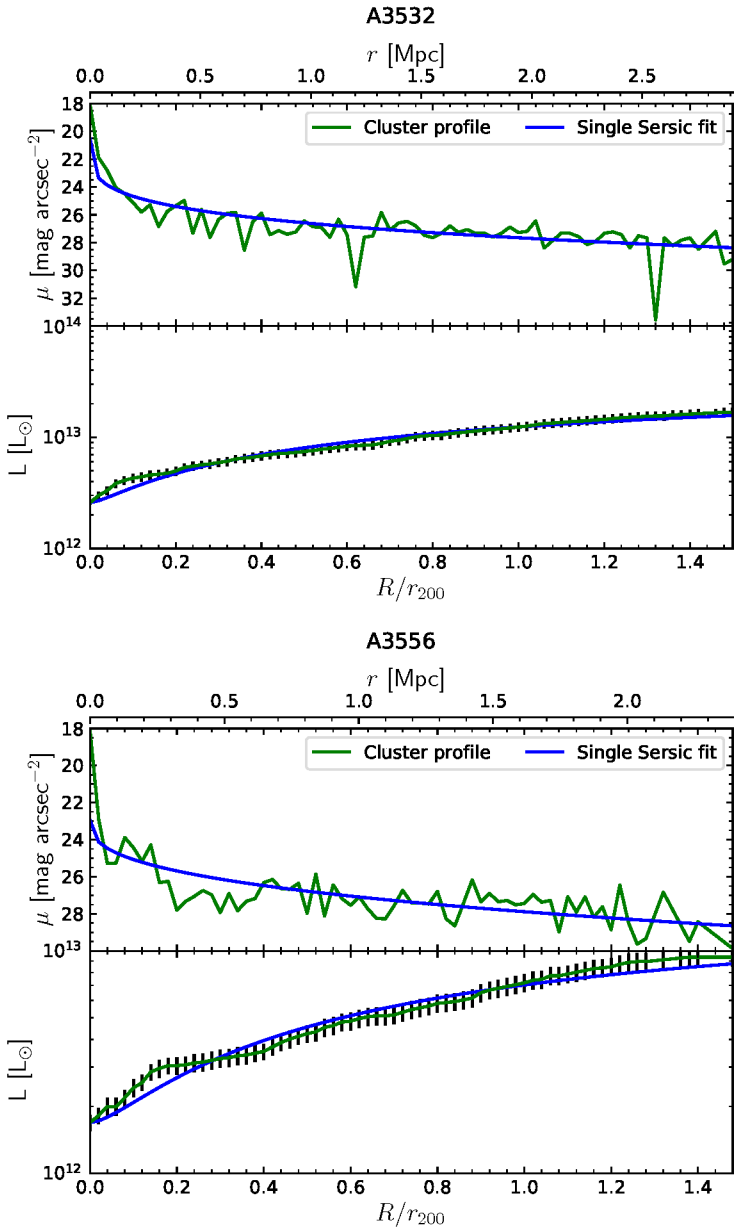


Figure 4.21: Photometric decomposition of the Omega-WINGS galaxy clusters luminosity profiles. Continued.

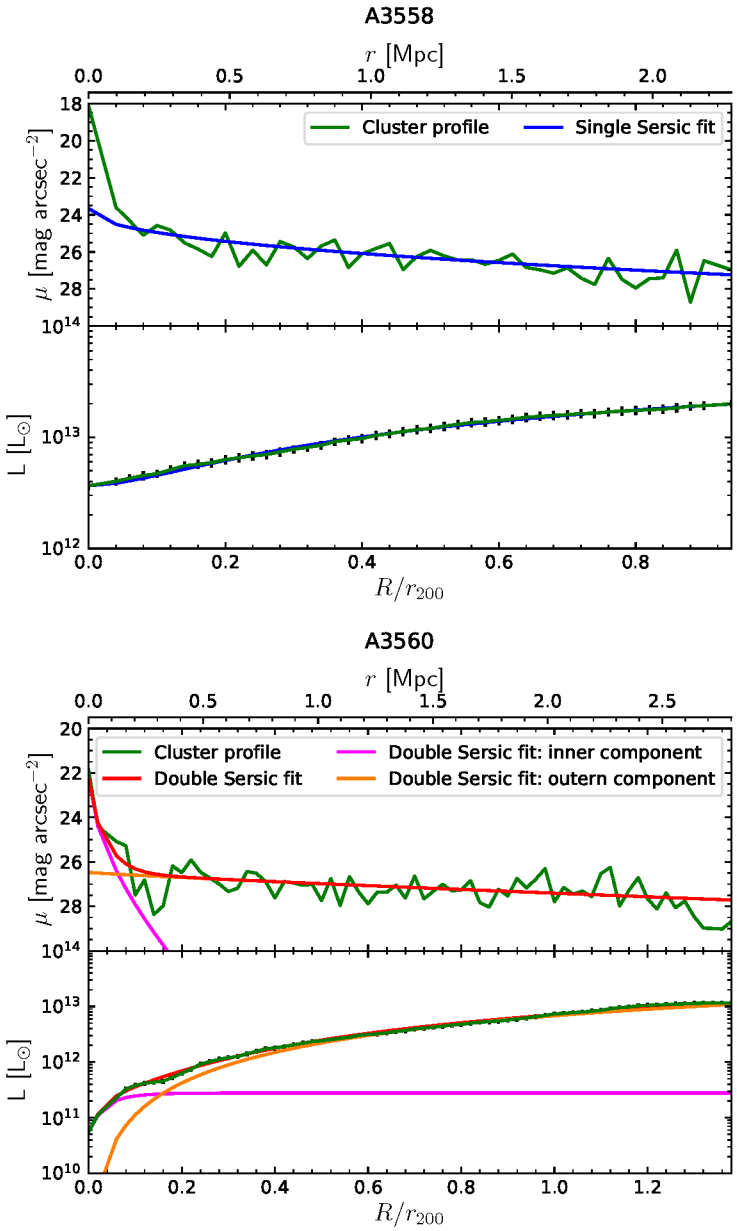


Figure 4.22: Photometric decomposition of the Omega-WINGS galaxy clusters luminosity profiles. Continued.

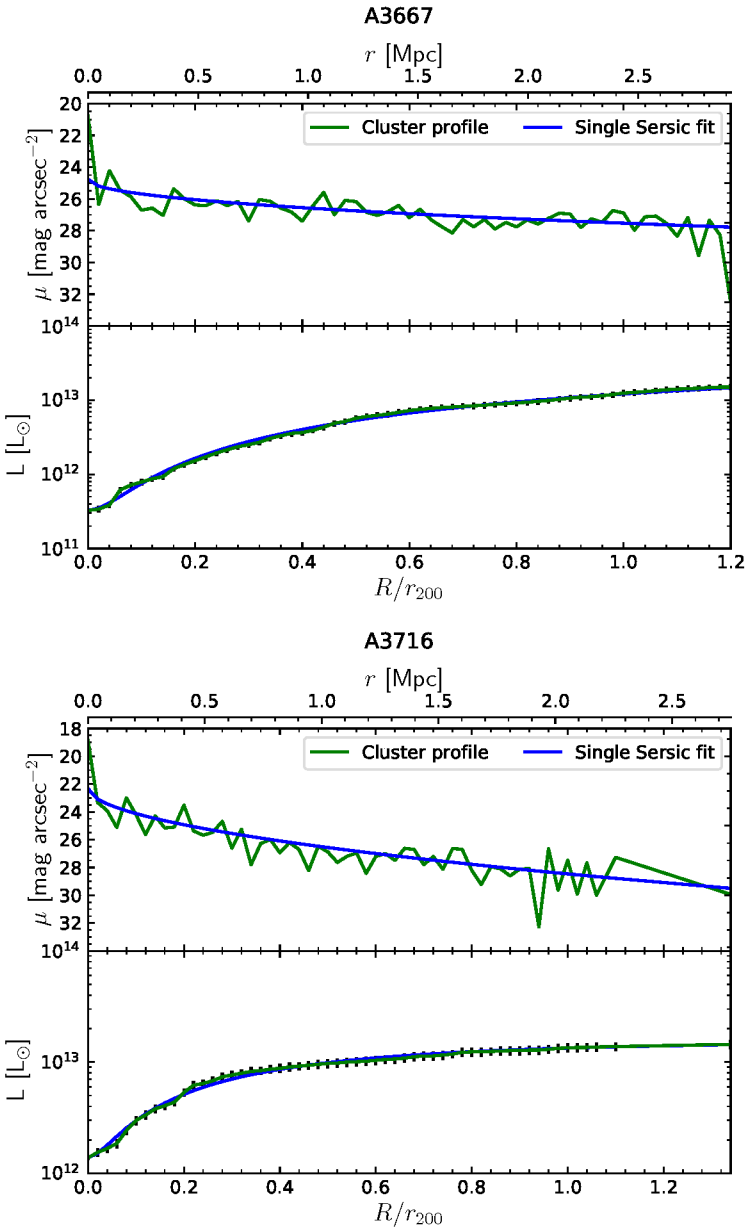


Figure 4.23: Photometric decomposition of the Omega-WINGS galaxy clusters luminosity profiles. Continued.

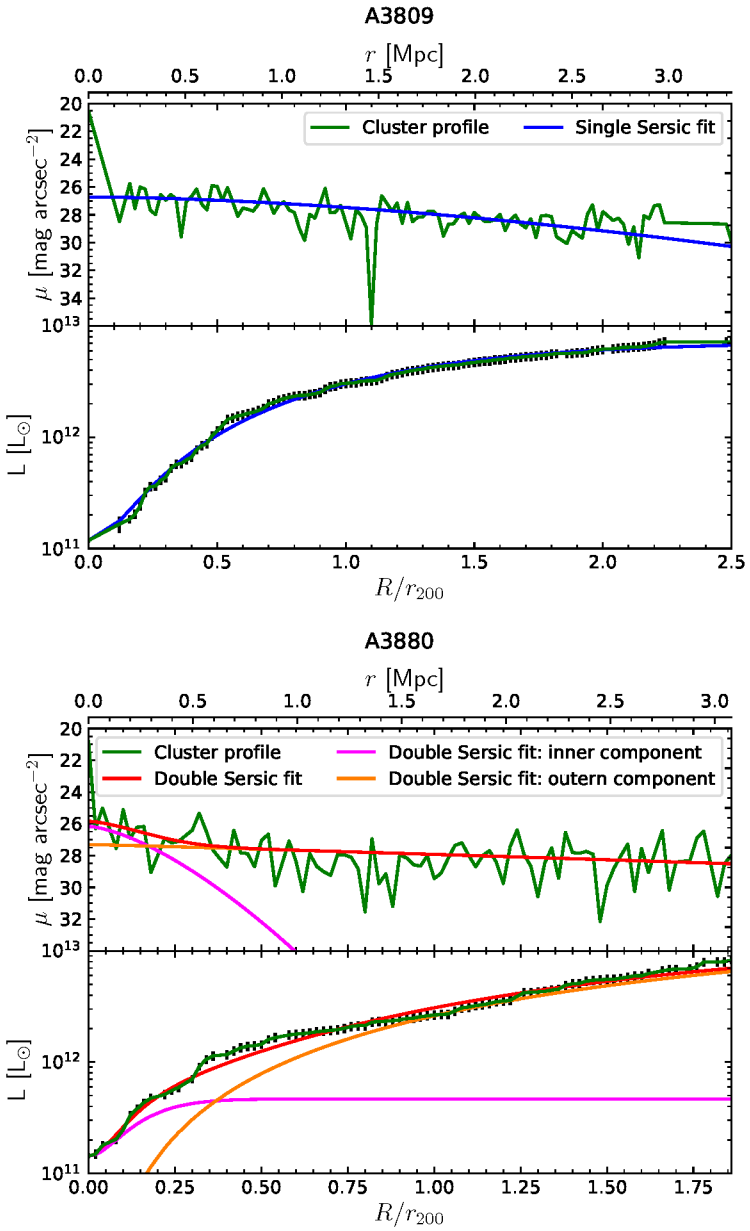


Figure 4.24: Photometric decomposition of the Omega-WINGS galaxy clusters luminosity profiles. Continued.

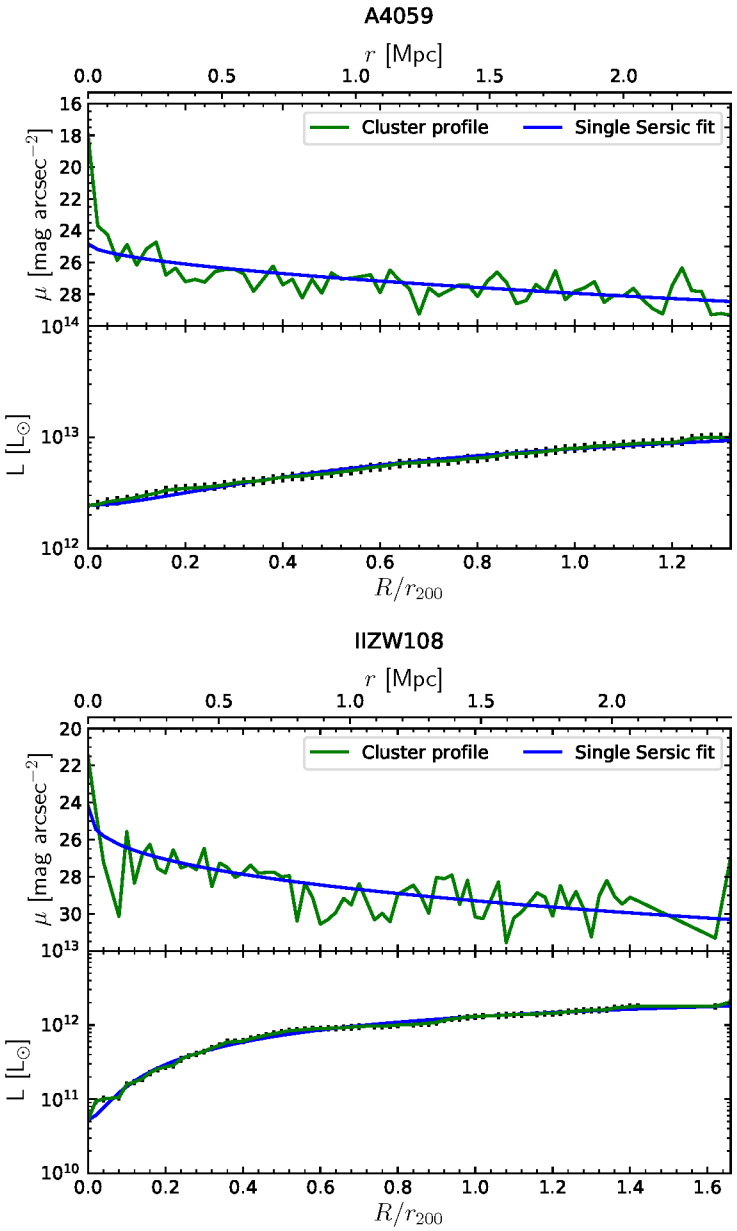


Figure 4.25: Photometric decomposition of the Omega-WINGS galaxy clusters luminosity profiles. Continued.

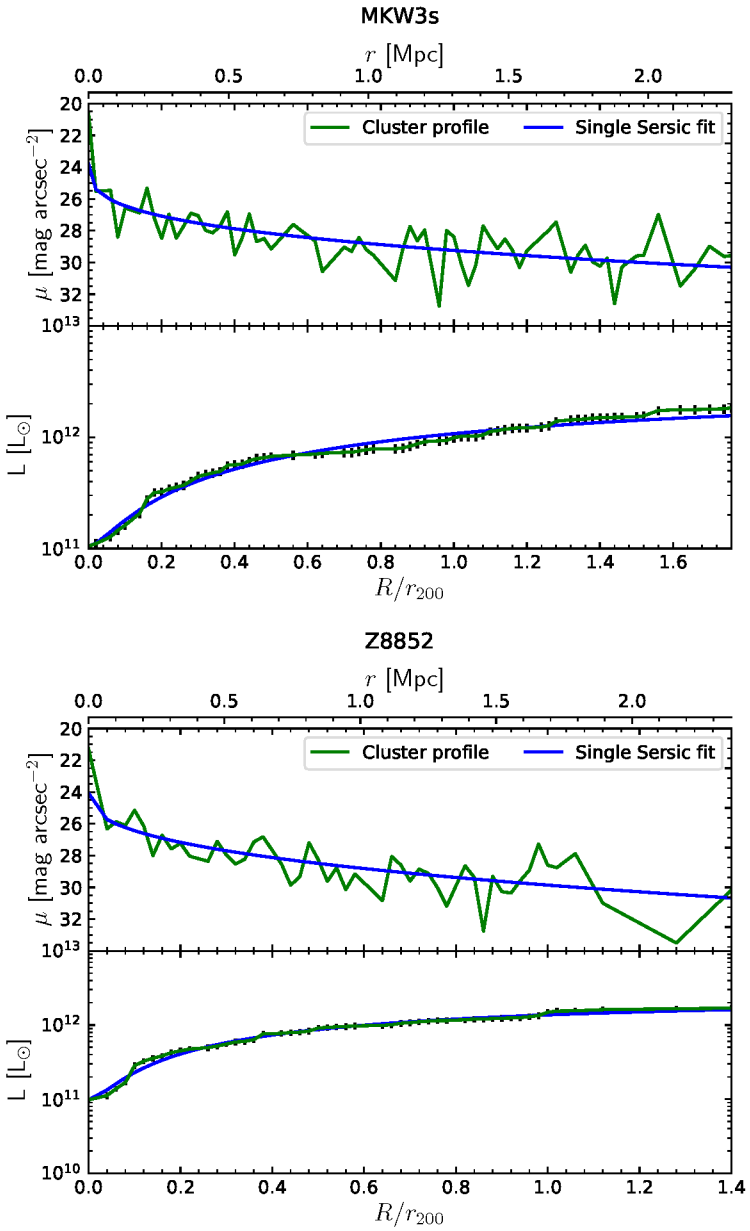


Figure 4.26: Photometric decomposition of the Omega-WINGS galaxy clusters luminosity profiles. Continued.

# Chapter 5

# Scaling relations among the structural parameters

In this chapter we analyze the main relations that we found among the clusters structural parameters. In Section 5.1 we start by showing the stacked profiles and the histograms of the various parameters. In Section 5.2 we introduce the first relations, suggesting that clusteres, like ETGs, are non-homologous structures. In Sections 5.3 we compare the average red sequence of Omega-WINGS ETGs with the color-magnitude relation found for galaxy clusters. Finally, in Section 5.4 we compare all the remaining main scaling relations valid for ETGs with those found for clusters.

## 5.1 General considerations

Figures 5.1 and 5.2 show the whole set of luminosity, surface brightness, mass and color profiles of the clusters stacked in four different plots and normalized to the effective structural parameters. Note that the cluster profiles show very different behaviors both in the central and in the outer regions. The central surface brightness spans a range of $\sim 6$ mag arcsec$^{-2}$, while the amount of light and mass within and beyond $R_e$ appears to differ of up to a factor of $\sim 2$ in units of $L_e$ and $\mathcal{M}_e$.

This is clearly an evidence of a marked difference in the global structure of clusters. Galaxy clusters do not seem to share a common light and mass distribution. The only similar behavior is visible in the stacked color profiles, showing that all the clusters have similar $(B-V)(\leq R)$ color profiles dominated by an old stellar population in the center and by a bluer one in the outer parts. Despite the large spread observed (around 0.3 mag), all the measured profiles are compatible with an average old mix of stellar

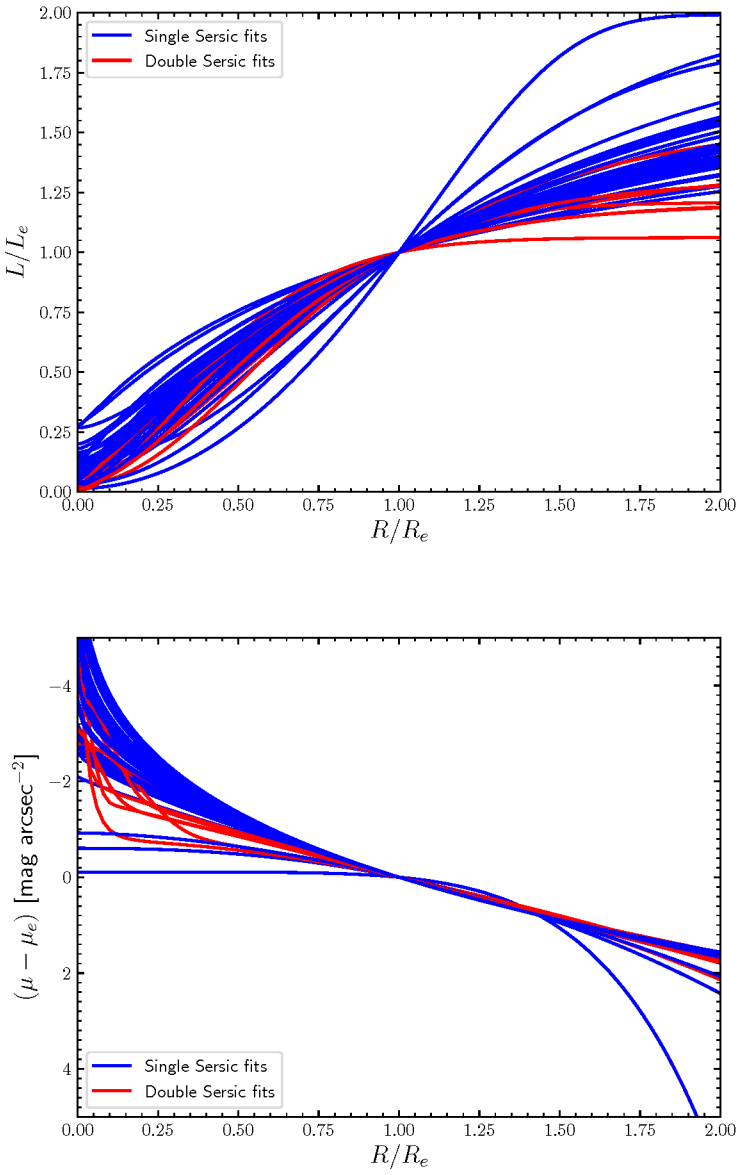


Figure 5.1: Superposition of the luminosity and surface brightness profiles associated to all the best fit models, normalized to the effective parameters. Blue and red lines are associated to the single and double Sérsic fits used to reproduce the luminosity profiles.

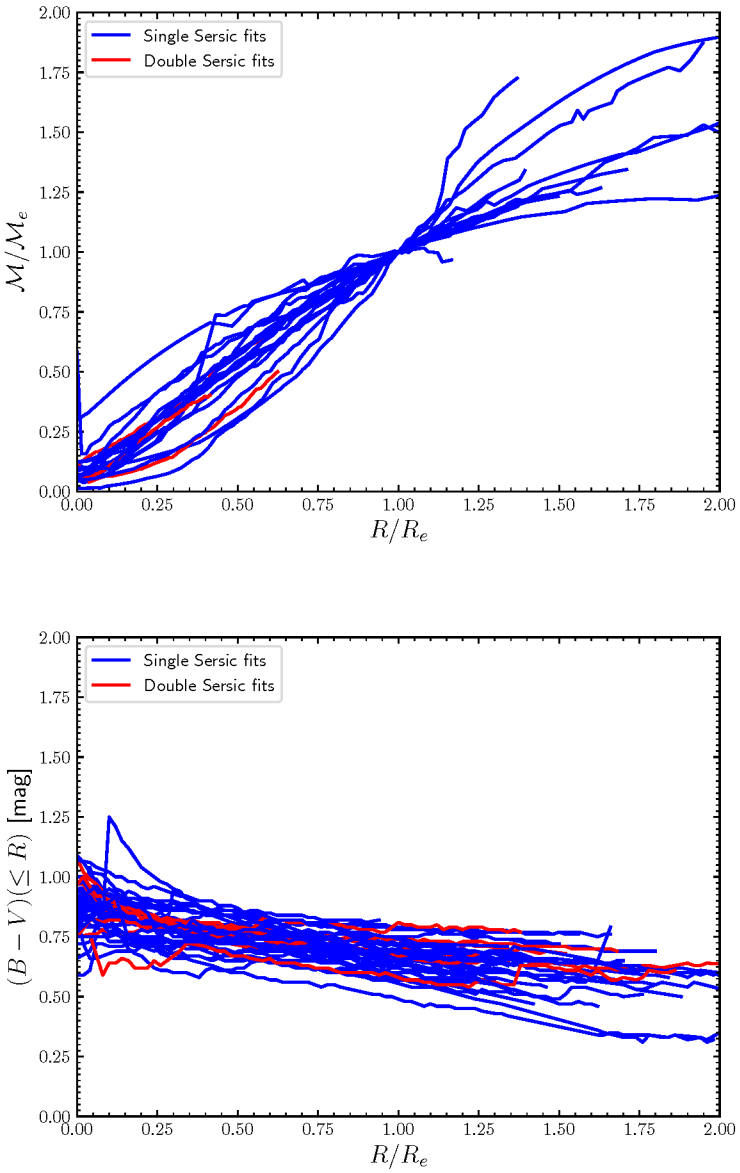


Figure 5.2: Superposition of the mass and color profiles (with the same normalization). The color code is the same as in Figure 5.1.

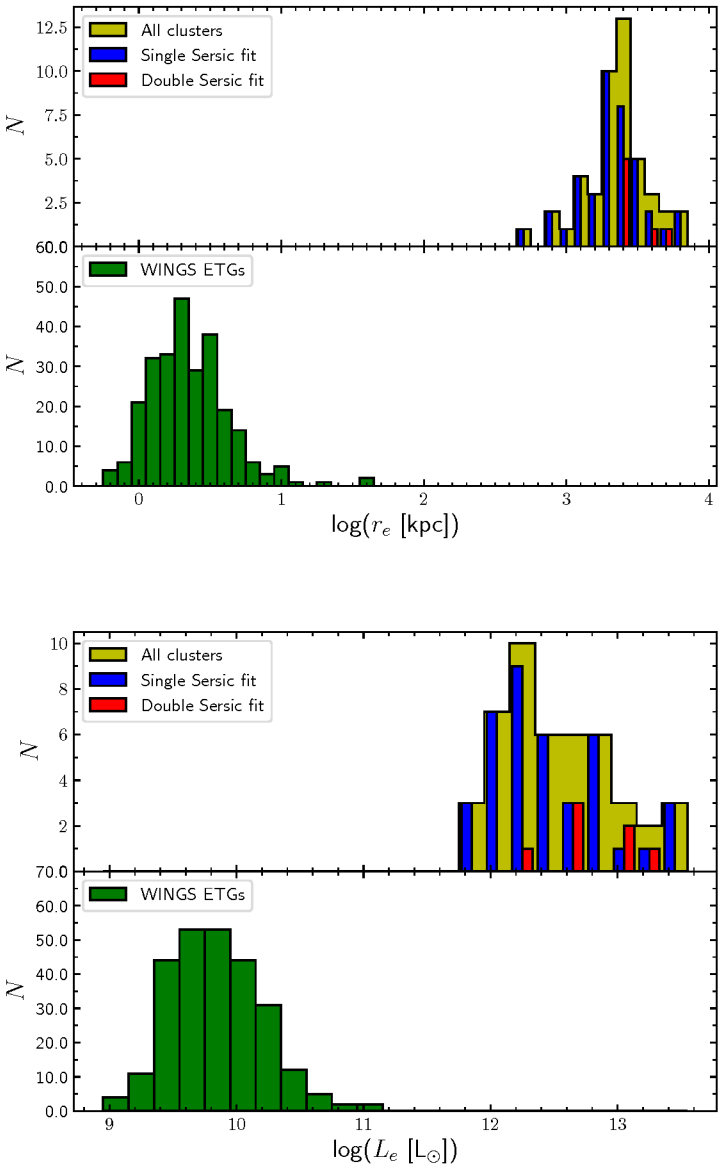


Figure 5.3: Histograms of the effective radius and luminosity distribution. Upper panels: single Sérsic fits data in blue, double Sérsic fits data in red, and all of them combined in yellow. Lower panels: ETGs data in green.

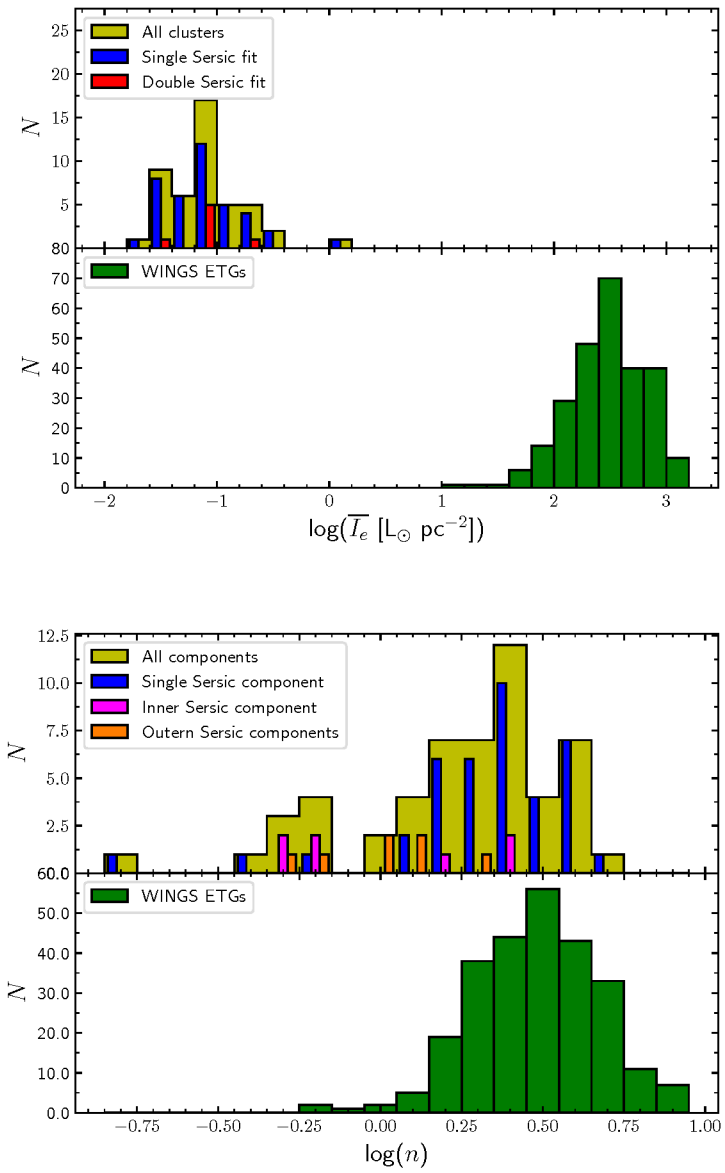


Figure 5.4: Histograms of the average effective intensity and Sérsic index distribution. Upper panels: single Sérsic fits data in blue, double Sérsic fits data in red (or inner Sérsic in pink and outern Sérsic in orange), and all of them combined in yellow. Lower panels: ETGs data in green.

populations.

Like in the case of galaxies, the best way to establish the main cluster properties is to study the relations among the structural parameters.

When available, we compared the measured parameters with those from a sample of 261 ETGs studied in our previous works (e.g., D'Onofrio et al. 2008; D'Onofrio et al. 2014), whose structural parameters (i.e., effective radius and luminosity, mass, velocity dispersion, Sérsic index, etc.) are available from the WINGS database. The idea is to quantify the correspondences and the differences between the structural parameters of clusters and ETGs.

Figures 5.3 and 5.4 provides the histograms of the observed distributions of the structural parameters. It is interesting to note that almost all the components follow some gaussian-like distribution. The range of values spanned by each parameter, although at different scales, is comparable. Note for example that the effective radii span in both samples a factor of $\sim 50$, while luminosities and average effective intensities span a larger interval (up to a factor of $\sim 100$ for galaxies and around 30 for clusters).

Once we observed that clusters and ETGs have a similar distribution of the photometric structural parameters at different scales, we decided to investigate the main relations known to be valid for ETGs.

## 5.2 The non-homology of galaxy clusters

The first relations that we decided to investigate are those connected to the homology of clusters.

A structure is homologous if it has scale-free properties. A virialized structure is not necessarily homologous. In the case of ETGs this has been proved by several works (Michard 1985; Schombert 1986; Capaccioli 1987; de Carvalho and da Costa 1988; Capaccioli 1989; Burkert 1993; Caon et al. 1993; Young and Currie 1994; Prugniel and Simien 1997) by showing that the light profiles of these galaxies are best fitted by the Sérsic law and that the Sérsic index $n$ correlates with the luminosity, the mass and the radius of the galaxies themselves.

Figure 5.5 shows the distribution of galaxy clusters with respect to the ETGs in the $r_e - n$ and $L_e - n$ diagrams in logarithmic units. The dashed lines gives the bi-weighted least square (BLS) fit of the two distributions. This kind of fit was applied because we do not know a priori which variable drives the correlation.

Two considerations emerge from these plots: first, both the classes of objects span the same range of $n$; second, the slope found for ETGs seems to be a plausible slope also for galaxy clusters. Considering that almost all

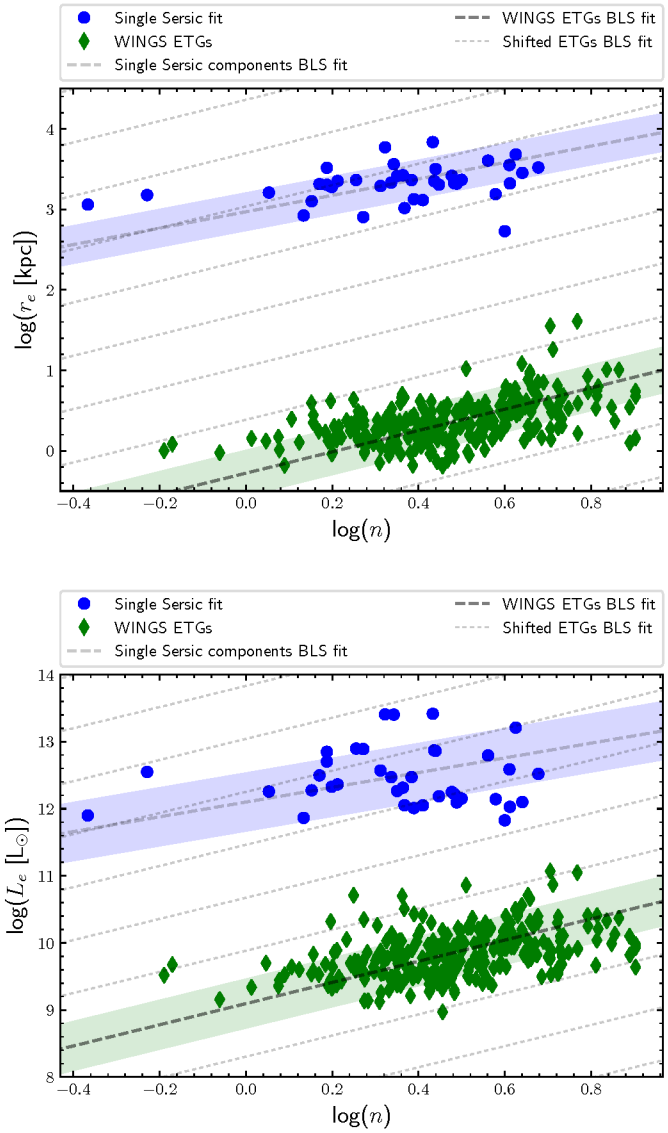


Figure 5.5: The $r_e - n$ and $L_e - n$ correlations in log units for ETGs (green dots) and clusters (blue dots). The grey dashed lines are parallel to the BLS fit of the WINGS ETGs. The bold grey dashed line is the BLS fit of our clusters. The filled areas are used to identify the limits of the rms standard deviation of the observed distributions, with the same color code of the sample to which they refer. We removed from the plot the cluster A1631a because a visual inspection of the surface brightness profile suggests the presence of a second cluster component in the same area.

the clusters are in the luminosity range $\sim 10^{12} - 10^{13} L_{\odot}$, while the galaxies span the range $\sim 10^{9} - 10^{11} L_{\odot}$, it is not surprising to see that the $L_e - n$ correlation, well visible in galaxies, is almost absent in clusters. The $r_e - n$ correlation, on the other hand, is well visible for both the types of structures. This means that clusters with the same luminosity can have very different structures with different values of $r_e$ and, of course, $n$. In other words, clusters are likely non-homologous systems, like ETGs.

The idea that clusters are non-homologous systems is not predicted by cluster simulations. We remember that the DM halos emerging from numerical simulations are structurally homologous systems with similar velocity dispersion profiles (Cole and Lacey 1996; Navarro et al. 1997). We do not have enough data at the moment to check the consistency of the DM profiles with the observed stellar light profiles, so we will addressed this problem in a future work.

## 5.3 The color-magnitude diagram of galaxy clusters

As a consequence of these impressive analogies with ETGs, we decided also to compare the color-magnitude (CM) relation $\overline{(B-V)}(\leq R) - M_V$ of clusters with the average red sequence slope found by Valentinuzzi et al. (2011) for the WINGS galaxies in the CM diagrams of the single clusters. In Figure 5.6 each cluster is represented by a dot with a $\overline{(B-V)}(\leq R)$ color that is the average integrated color index measured within different fractions of $r_{200}$ and a total magnitude $M_V$ that corresponds to the total magnitude of the cluster within $r_{200}$. Note that the WLS fit of the clusters is steeper than the average red sequence slope of the galaxies in clusters (equal to $-0.04$) only when the mapped region of the clusters is larger than $0.6\, r_{200}$. The plots clearly indicate that the most massive clusters are, on average, the reddest ones, while the less luminous clusters are the bluest ones (this is observed also in the red sequence of ETGs). Note also that in the central region all the clusters seem to have approximately the same color.

The WLS fits of our data (bold dashed lines) provide the following relations valid for different fractions of the clusters areas (in $r_{200}$ units):

$$\begin{aligned}
\overline{(B-V)}(\leq 0.2\, r_{200}) &= +1.15 \pm 0.39 + 0.01 \pm 0.02\, M_V(r_{200}) \\
\overline{(B-V)}(\leq 0.6\, r_{200}) &= -0.47 \pm 0.35 - 0.04 \pm 0.01\, M_V(r_{200}), \\
\overline{(B-V)}(\leq 1.0\, r_{200}) &= -1.59 \pm 0.36 - 0.08 \pm 0.01\, M_V(r_{200}), \\
\overline{(B-V)}(\leq 1.4\, r_{200}) &= -2.23 \pm 0.35 - 0.11 \pm 0.01\, M_V(r_{200}),
\end{aligned} \tag{5.1}$$

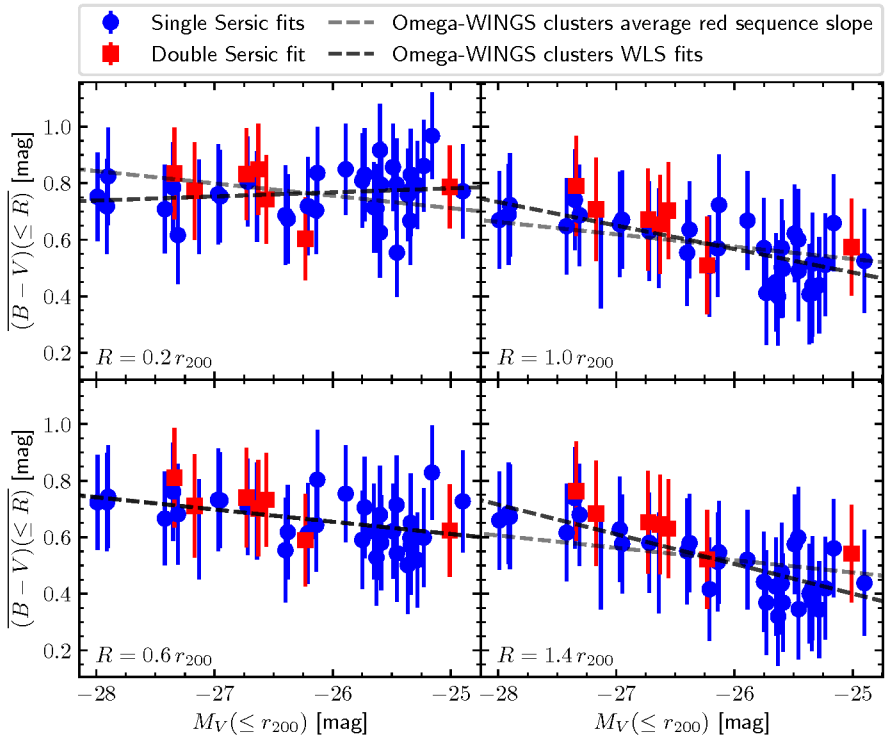


Figure 5.6: The color-magnitude relation for the whole sample of clusters considering different cluster areas. On the $x$-axis we have the integrated $V$-band absolute magnitude within $r_{200}$, and on the $y$-axis the average of all the integrated colors within the considered radius (plotted on the lower-left corner of the panel). The blue dots refers to the single Sérsic clusters, the red squares to the double ones. The grey dashed line gives the average red sequence slope observed for the CM relations of the galaxies of the WINGS clusters derived by Valentinuzzi et al. (2011). The average red sequence slope has been plotted here by matching the intercept of the line to the mean color of the distribution. The bold dashed line is the WLS fit of the observed distribution.

while the corresponding average red sequence slopes for the galaxies of the WINGS clusters in the same areas matched to the barycenter of the point distribution (light grey dashed lines) are:

$$\begin{aligned}
\overline{(B-V)}(\leq 0.2\,r_{200}) &= -0.38 \pm 0.16 - 0.04 \pm 0.01\,M_V(r_{200}),\\
\overline{(B-V)}(\leq 0.6\,r_{200}) &= -0.48 \pm 0.17 - 0.04 \pm 0.01\,M_V(r_{200}),\\
\overline{(B-V)}(\leq 1.0\,r_{200}) &= -0.56 \pm 0.17 - 0.04 \pm 0.01\,M_V(r_{200}),\\
\overline{(B-V)}(\leq 1.4\,r_{200}) &= -0.62 \pm 0.18 - 0.04 \pm 0.01\,M_V(r_{200}).
\end{aligned} \tag{5.2}$$

The CM relation of galaxy clusters is found here for the first time. Its existence should find an explanation in the current models of cluster formation and evolution. We will dedicate a future work to a possible theoretical interpretation of what is observed.

In addition to the CM relation we note that a correlation between the mean effective luminosity of clusters $L_e$ and the color gradient $\Delta(B-V)/\Delta r$ is significant in our data (see Figure 5.7 and Table 3.1):

$$\Delta(B-V)/\Delta r = -1.47 \pm 0.32 + 0.10 \pm 0.03 \log(L_e). \tag{5.3}$$

The color gradient $\Delta(B-V)/\Delta r$ is negative because clusters, like ETGs, are redder in the center and bluer in the outskirts, and it appears to be larger in the fainter clusters. This is at variance with the case of ETGs, where the optical gradient seem not to correlate with the galaxy luminosity (see e.g., La Barbera et al. 2010).

## 5.4 The main scaling relations of galaxy clusters

Table 5.1 presents the data of the mutual correlations among the structural parameters of galaxies and clusters. The following figures show the most famous ETGs parameters correlations extended to the domain of galaxy clusters.

Figure 5.8 compares the Kormendy relation (Kormendy 1977; Hamabe and Kormendy 1987; Capaccioli et al. 1992; D'Onofrio et al. 2017) of ETGs with that of our clusters. The green diamonds correspond to the WINGS ETGs, the blue dots to the single Sérsic fits, the red squares to the general parameters of the double Sérsic profiles, the pink triangles to the inner components of the double Sérsic fits and the orange reversed triangles to the outern components of the double Sérsic profiles.

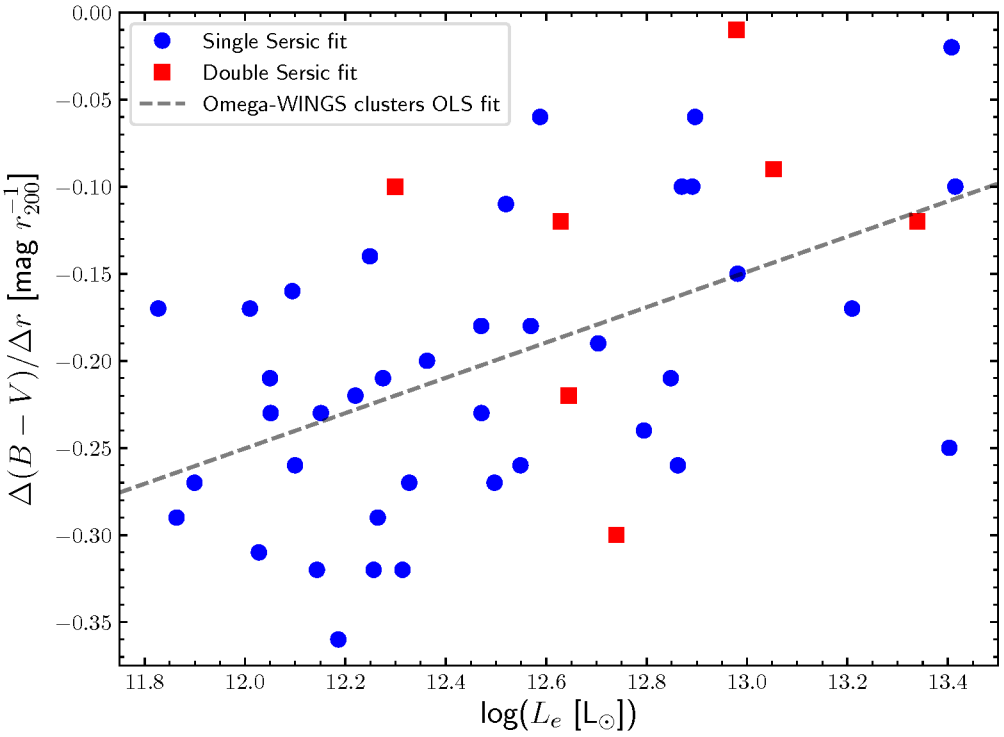


Figure 5.7: The color gradient as a function of the effective luminosity of the clusters. Color code as in the previous figures.

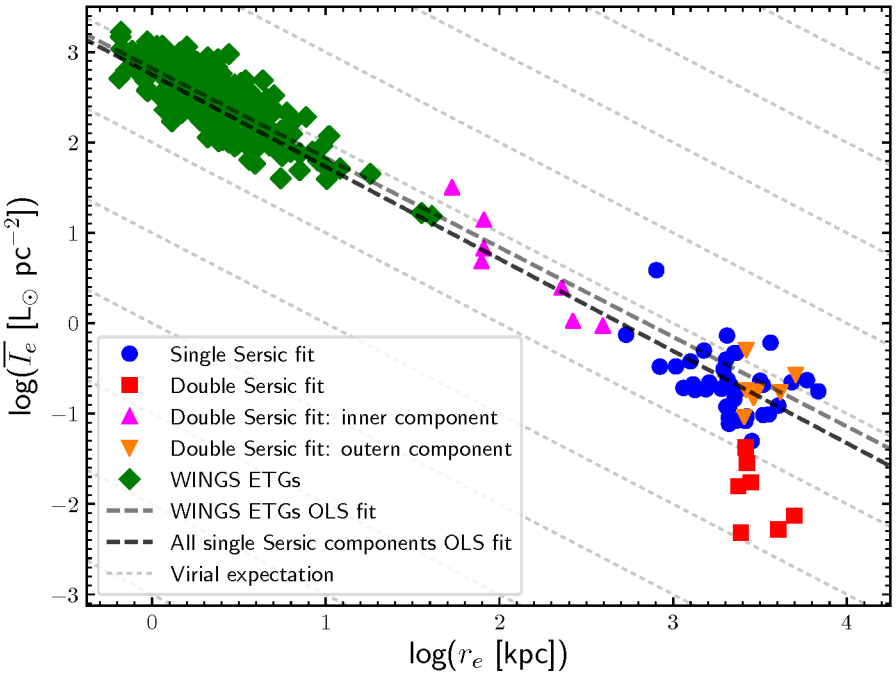


Figure 5.8: The Kormendy $\overline{I_e} - r_e$ relation for ETGs and galaxy clusters. Green diamonds are ETGs. The blue circles are associated to single Sérsic fits of galaxy clusters, the red squares to double Sérsic fits, the pink triangles to the inner components of double Sérsic fits, and the reversed orange tringles to the outern components of the double Sérsic fits.

It is interesting to note that the effective parameters of galaxy clusters follow the same relation previously found for ETGs. Clusters reside along the high-radii tail of galaxies and share the same Zone of Exclusion (for more details see Section 6.1) of ETGs. The ordinary least squares (OLS) linear interpolation of both the samples provides the same slope within the errors (see Table 5.1), compatible with that expected by the scalar virial theorem (light grey dashed lines) when a constant mass-to-light ratio is assumed. For a better explanation of the observed distribution in the $\overline{I_e} - r_e$ plane see Chapter 6.

Figure 5.9 shows the $L_e - r_e$ and the $\mathcal{M}_e - r_e$ relations between the effective luminosity/mass and the effective radius. Again we see that the distribution of ETGs and clusters follows the expected behavior on the basis of the Virial theorem (see Table 5.1). The position of each object in these planes depends on the zero-point of the virial relation, which is different for each system. To see such effect note how the position in the $\mathcal{M}_e - r_e$ diagram depends on the central velocity dispersion $\sigma$ (color scale on the right plot). The velocity dispersion values on the plot are those tabulated by D'Onofrio et al. 2008 for all the galaxies, and were provided us by Biviano et al. (2017) for the clusters.

To complete the series of plots dedicated to the virial equilibrium of our clusters, we also show the Faber-Jackson (FJ; 1976) $L_e - \sigma$ relation. A plot similar to Figure 5.10 will be shown and discussed in Chapter 6.

This set of figures clearly shows that ETGs and clusters share the same virial relations. The occasional deviations come from the different zero-points of the different systems in each diagram.

Finally, we analyze the stellar mass-to-light ratios of ETGs and clusters. Figure 5.11 shows the distribution of the $\mathcal{M}/L$ ratios as a function of the total luminosities. We see that ETGs span a factor of 10 in $\mathcal{M}/L$ and that the stellar mass-to-light ratio does not correlate with the luminosity. This seems in contradiction with the claimed relation between the dynamical $\mathcal{M}/L$ ratio and the luminosity (see e.g., Cappellari et al. 2006, or Cappellari 2008). The mean stellar $\mathcal{M}/L$ ratio of galaxy clusters spans a much smaller interval of values and again no correlation is seen with the luminosity. The combination of the two samples seems to suggest a trend with $L$ of the mass-to-light ratio, but this is a misleading conclusion originated from the absence of clusters with low $\mathcal{M}/L$ values.

These figures provide further evidence that nearby clusters are dominated by an old stellar population almost over the whole extension of their profiles, an observational fact that must be reproduced by models of cluster formation and evolution.

We conclude by observing that the ratio between the luminosity of cluster

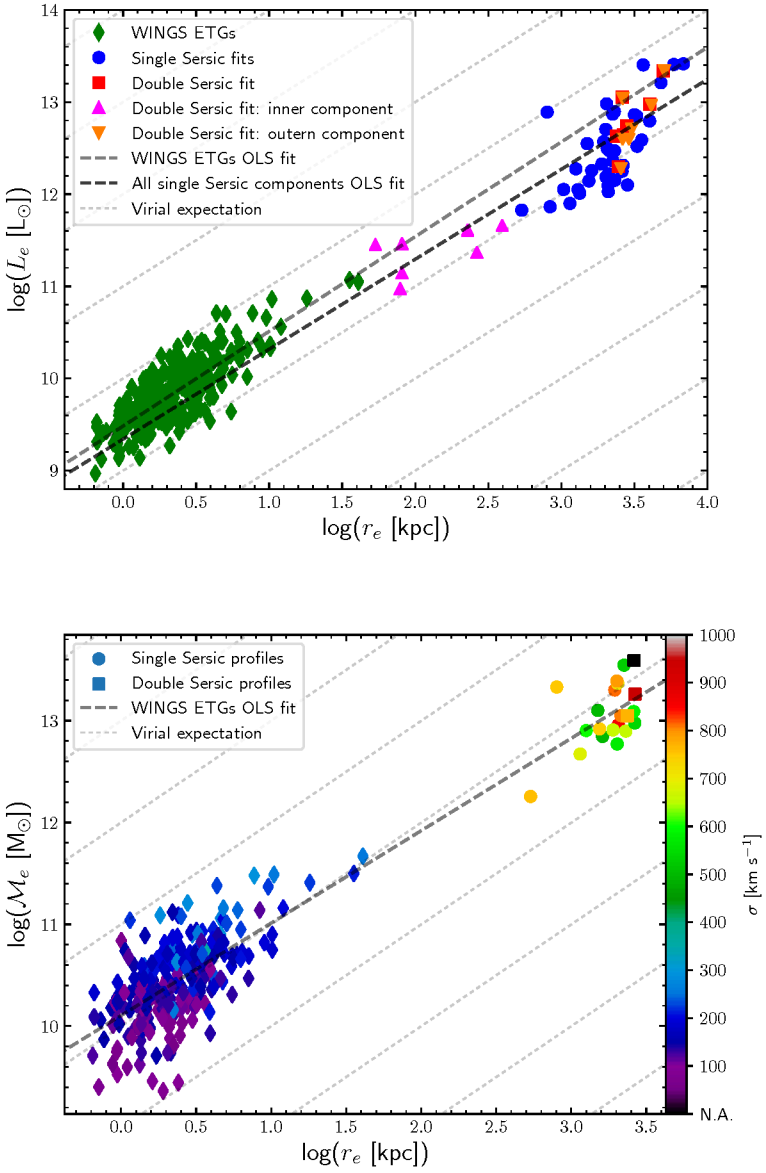


Figure 5.9: Left plot: $L_e - r_e$ relation for ETGs and clusters. Right plot: $\mathcal{M}_e - r_e$ relation for the same samples. The symbols are as those in the previous figure, the colors represent the velocity dispersion of each point (color bar on the right).

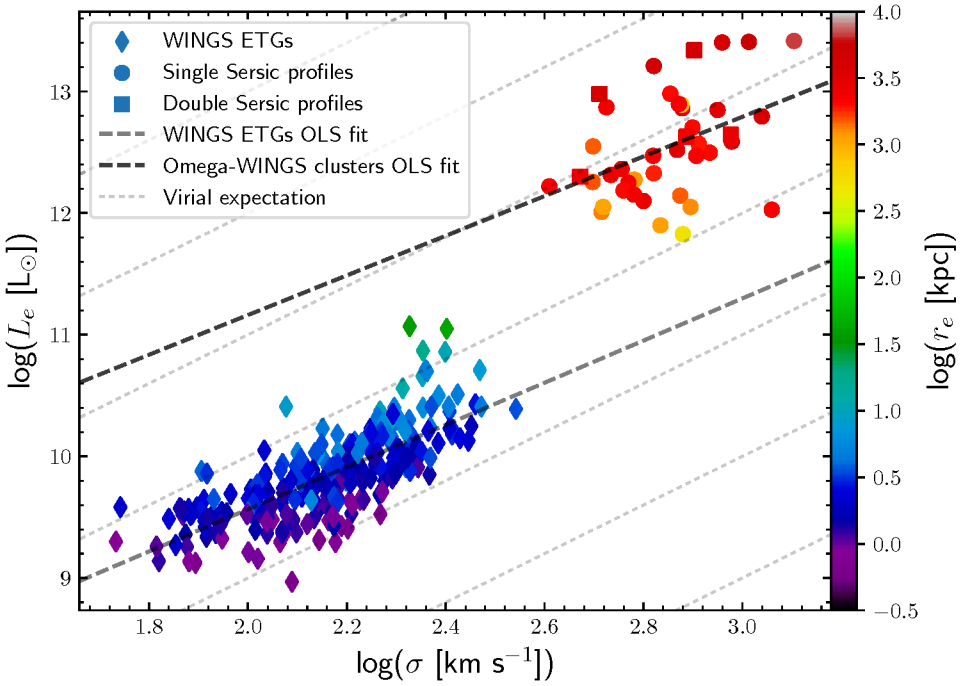


Figure 5.10: $L_e - \sigma$ relation for the WINGS ETGs and our galaxy clusters. The symbols are as those in the previous figures, the colors represent the effective radius (color bar on the right).

substructures and the main cluster component measured by Ramella et al. (2007) mildly correlates with the cluster velocity dispersion (see Figure 5.12 and Table 5.1). This is a somewhat expected result, as the velocity dispersion should increase when a merging occurs.

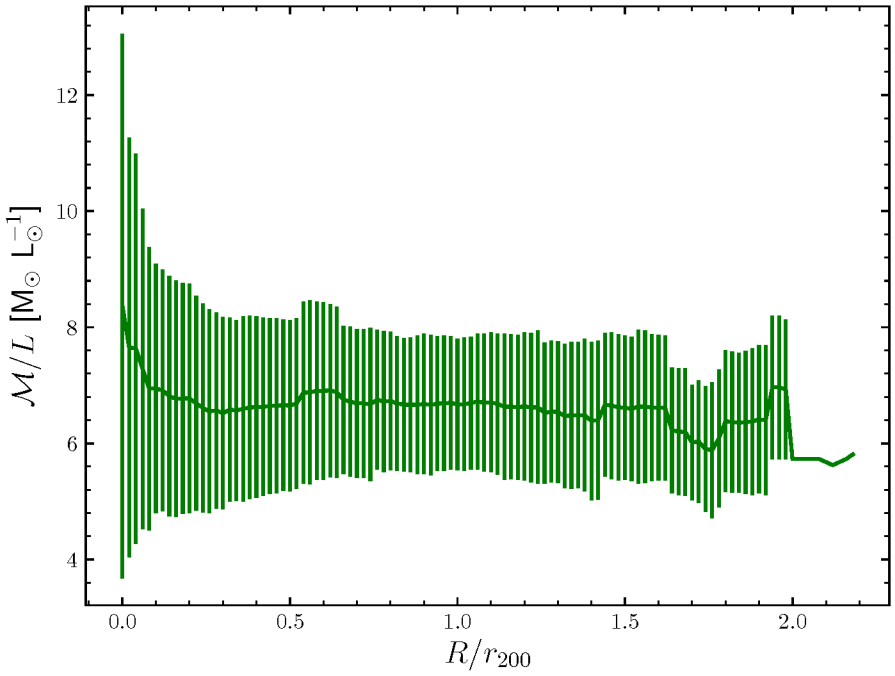


Figure 5.11: Average value and dispersion of the mass-to-light ratio of all the clusters at different radii in units of $r_{200}$.

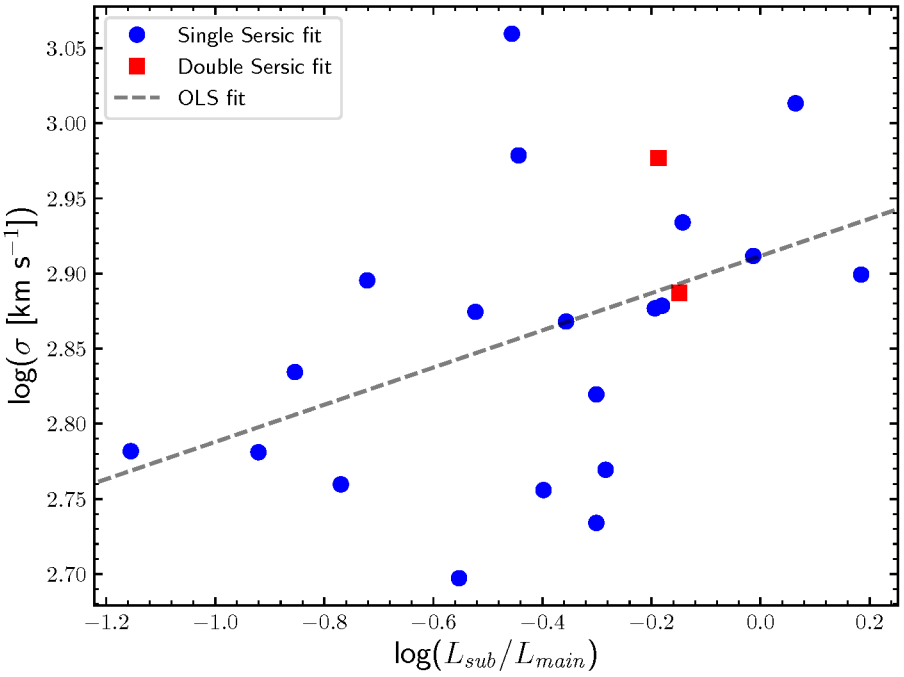


Figure 5.12: Correlation between the cluster velocity dispersion calculated by Biviano et al. (2017) and the amount of cluster light inside the subtructures identified by Ramella et al. (2007).

Table 5.1: Summary of all the discussed OLS/WLS relations: $y$- and $x$-axis (Column 1), sample used to compute the relation (Column 2, where g = galaxies, and c = clusters), sample size (Column 3), zero-order polynomial term (Column 4), first-order polynomial term (Column 5), RMS (Column 6), Pearson Correlation Coefficient PCC (Column 7), Pearson p-value in logarithmic units (Column 8, where the unreported values indicate a probability smaller than $3\times10^{-7}$, which comes from the 5 RMS criterion), Spearman's Rank Correlation $\rho$ (Column 9), Spearman p-value in logarithmic units (Column 10, where the unreported values again indicate a probability smaller than $3 \times 10^{-7}$).

| $y - x$ | Sample | $N$ | $c_0$ | $c_1$ | RMS | PCC | $\log(p_{\rm P})$ | $\rho$ | $\log(p_{\rm S})$ |
|---|---|---|---|---|---|---|---|---|---|
| $\overline{(B-V)}(\leq 0.2\,r_{200}) - M_V(r_{200})$ | c | 46 | $1.15 \pm 0.39$ | $-0.15 \pm 0.15$ | 0.08 | 0.15 | $-0.48$ | 0.21 | $-0.73$ |
| $\overline{(B-V)}(\leq 0.6\,r_{200}) - M_V(r_{200})$ | c | 46 | $-0.47 \pm 0.35$ | $-0.04 \pm 0.01$ | 0.07 | $-0.46$ | $-2.66$ | $-0.46$ | $-2.67$ |
| $\overline{(B-V)}(\leq 1.0\,r_{200}) - M_V(r_{200})$ | c | 46 | $-1.59 \pm 0.36$ | $-0.08 \pm 0.01$ | 0.07 | $-0.69$ | $-6.41$ | $+0.67$ | $-5.95$ |
| $\overline{(B-V)}(\leq 1.4\,r_{200}) - M_V(r_{200})$ | c | 46 | $-2.23 \pm 0.35$ | $-0.11 \pm 0.01$ | 0.07 | $-0.78$ | - | $-0.75$ | - |
| $\Delta(B-V)/\Delta r - \log(L_e)$ | c | 46 | $-1.47 \pm 0.32$ | $0.10 \pm 0.03$ | 0.07 | 0.51 | 3.59 | 0.50 | $-3.37$ |
| $\log(\overline{I_e}) - \log(r_e)$ | g | 261 | $2.82 \pm 0.02$ | $-0.99 \pm 0.05$ | 0.21 | $-0.79$ | - | $-0.75$ | - |
| $\log(\overline{I_e}) - \log(r_e)$ | c | 53 | $2.75 \pm 0.29$ | $-1.02 \pm 0.09$ | 0.31 | $-0.84$ | - | $-0.57$ | $-5.09$ |
| $\log(L_e) - \log(r_e)$ | g | 261 | $9.48 \pm 0.02$ | $1.03 \pm 0.05$ | 0.40 | 0.80 | - | 0.75 | - |
| $\log(L_e) - \log(r_e)$ | c | 53 | $9.34 \pm 0.29$ | $0.97 \pm 0.10$ | 0.33 | 0.70 | - | 0.64 | $-5.94$ |
| $\log(\mathcal{M}_e) - \log(r_e)$ | g | 261 | $10.10 \pm 0.03$ | $0.91 \pm 0.06$ | 0.31 | 0.64 | - | 0.59 | - |
| $\log(\mathcal{M}_e) - \log(r_e)$ | c | 20 | $10.10 \pm 0.03$ | $0.91 \pm 0.06$ | 0.26 | 0.54 | $-1.94$ | 0.40 | $-1.16$ |
| $\log(L_e) - \log(\sigma)$ | g | 261 | $6.09 \pm 0.21$ | $1.73 \pm 0.10$ | 0.23 | 0.75 | - | 0.78 | - |
| $\log(L_e) - \log(\sigma)$ | c | 41 | $7.90 \pm 1.59$ | $1.63 \pm 0.56$ | 0.39 | 0.42 | $-2.25$ | 0.38 | $-1.88$ |
| $\log(r_e) - \log(\sigma)$ | c | 41 | $1.93 \pm 0.33$ | $1.56 \pm 0.68$ | 0.47 | 0.34 | - | 0.35 | - |
| $\log(r_e) - \log(n)$ | g | 261 | $-0.28 \pm 0.04$ | $1.33 \pm 0.08$ | 0.26 | 0.49 | - | 0.49 | - |
| $\log(r_e) - \log(n)$ | c | 38 | $2.97 \pm 0.07$ | $1.02 \pm 0.12$ | 0.24 | 0.33 | $-1.35$ | 0.40 | $-1.91$ |
| $\log(L_e) - \log(n)$ | g | 261 | $9.09 \pm 0.05$ | $1.58 \pm 0.09$ | 0.32 | 0.44 | - | 0.47 | - |

Table 5.1: Continued.

| $y - x$ | Sample | $N$ | $c_0$ | $c_1$ | RMS | PCC | $\log(p_{\rm P})$ | $\rho$ | $\log(p_{\rm S})$ |
|---|---|---|---|---|---|---|---|---|---|
| $\log(L_e) - \log(n)$ | c | 38 | $12.08 \pm 0.09$ | $1.08 \pm 0.22$ | 0.48 | 0.05 | $-0.12$ | $-0.12$ | $-0.31$ |
| $\log(\sigma) - \log(L_{sub}/L_{main})$ | c | 22 | $2.92 \pm 0.03$ | $0.12 \pm 0.06$ | 0.08 | 0.43 | $-1.36$ | 0.49 | $-1.68$ |

# Chapter 6

# The Fundamental Plane of ETGs and galaxy clusters

We dedicate this chapter to the Fundamental Plane. In Section 6.1 we introduce the concept, in Section 6.2 we describe the connected problem, and in Section 6.3 we present a new solution. In Section 6.4 we discuss the details of our solution, in Section 6.5 its connection to the luminosity, the SFR and the velocity dispersion of the system. In Section 6.6 we introduce its link to the Faber-Jackson relation, and in Section 6.7 its connection to the star formation activity in galaxies.

## 6.1 Introduction on the Fundamental Plane

The Fundamental Plane (FP) is the following relation:

$$a \log(r_e) + b \log(\overline{I_e}) + c \log(\sigma) + d = 0, \tag{6.1}$$

connecting the effective radius $r_e$ (i.e., the radius containing one half of the total luminosity), the average intensity within the effective radius $\overline{I_e}$, and the velocity dispersion $\sigma$ of any virialized system. Its origin is still unclear, even after decades from its discovery (Djorgovski and Davis 1987; Dressler et al. 1987) in the case of ETGs. The unsolved question has two aspects: firstly, the FP coefficients are significantly different from the virial expectation for homologous galaxies ($a \sim 1.2$ instead of 2, and $b \sim -0.7$ instead of $-1$); secondly, the scatter around the plane is very small along the whole FP extension, which spans several orders of magnitude. The observed coefficients are found to depend on the filter band adopted (see e.g., Scodeggio et al. 1998; Hyde and Bernardi 2009), on the fitting procedure (see e.g., Sheth and Bernardi 2012) and on the magnitude limit of the selected galaxy sample (see

e.g., D'Onofrio et al. 2008), but in all cases are significantly different from the virial expectation.

The first interpretation of the tilt was related to the behaviour of the stellar populations of galaxies through their stellar mass-to-light ratio which was seen to vary with luminosity ($\mathcal{M}/L \sim \mathcal{M}^{\alpha}$, with $\alpha \sim 0.25$; Faber et al. 1987). Subsequent, independent measurements found similar values of $\alpha$ (see e.g., Pahre et al. 1998; Gerhard et al. 2001; Borriello et al. 2003; Treu et al. 2005).

An alternative explanation was that galaxies are progressively non-homologous systems along the FP (Hjorth and Madsen 1995; Capelato et al. 1995; Busarello et al. 1997; Prugniel and Simien 1997; Graham and Colless 1997; Pahre et al. 1998; Bertin et al. 2002; Trujillo et al. 2004; Nipoti et al. 2006; La Barbera et al. 2010). This scenario was supported by the observation that the light profiles and dynamics of ETGs deviate systematically from homology (Michard 1985; Capaccioli 1987; de Carvalho and da Costa 1988; Capaccioli 1989; Burkert 1993; Schombert 1986; Caon et al. 1993; Young and Currie 1994; Prugniel and Simien 1997). Ciotti et al. (1996) however pointed out that a strong fine-tuning between stellar mass-to-light ratio and the Sérsic index $n$ is required to explain with just structural non-homology both the tilt of the FP and the small scatter around it (the so-called $\mathcal{M}/L - n$ conspiracy). Cappellari et al. (2006, 2013) also excluded an important contribution of non-homology to the tilt using integral models of the ETGs mass distribution based on 2D kinematic maps. Along the same line, the galaxy mass distribution estimated from gravitational lensing by Bolton et al. (2008) did not seem to support an important role for non-homology.

Subsequently, the interpretations of the tilt proposed a number of possible mechanisms: metallicity effects (Gerhard et al. 2001), dark matter distribution and amount (Tortora et al. 2009; Secco 2001; Secco and Bindoni 2009), dissipation effects during galaxy collapse (see e.g., Oñorbe et al. 2005; Dekel and Cox 2006; Robertson et al. 2006; Hopkins et al. 2008), variable initial mass function (IMF, Chiosi et al. 1998), star formation history (SFH), etc., but the contribution of DM and IMF was also excluded by Ciotti et al. (1996) on the basis of a required strong fine-tuning argument, and observing that the observed SFH of galaxies is hardly reconciled with the widely accepted hierarchical paradigm of the $\Lambda$-CDM cosmology.

More recently, D'Onofrio et al. (2013) proposed the existence of a fine-tuning mechanism able to explain the properties of the FP based on the observed mutual correlation between galaxy mass, mass-to-light ratio and Sérsic index. Increasing evidences now exist that the main driver of stellar population properties in ETGs is the velocity dispersion, with a second order effect due to galaxy environment (see e.g., La Barbera et al. 2014). The slope

of the IMF, for example, has been found to correlate with $\sigma$ (Cenarro et al. 2001; van Dokkum and Conroy 2010; La Barbera et al. 2013). At the same time merging events, gas accretion and feedback processes seem to have a significant role for the evolution of ETGs, in particular in the center of groups and clusters. The question therefore is: to what extent all these processes have affected the FP properties of the nearby ETGs that we see today?

In addition to the tilt, the small observed scatter ($\sim 20-25\%$) around the FP is also unexplained. Forbes et al. (1998) and Terlevich and Forbes (2002) found a correlation between the residuals of the FP and the age of the galaxies (ETGs with higher/lower surface brightness have younger/older ages). Gargiulo et al. (2009) claimed that the FP residuals anti-correlate with the mean stellar age, while a strong correlation exists with [$\alpha$/Fe]. Graves et al. (2009) proposed that the stellar population variations contribute at most to 50% of the total thickness and that correlated variations in the IMF or in the central DM fraction make up the rest. Magoulas et al. (2012) found that the residuals about the FP show significant trends with environment, morphology and stellar population, with the strongest trend being with age. Unfortunately, even if the data are even better today, the systematic errors in age, [Z/H] and [$\alpha$/Fe] are still large and not well understood, as different packages for stellar population synthesis provide very different results.

The above discussion clearly reveals that a general consensus about the origin of the FP and its properties is still lacking. We remind that even the distribution of galaxies in the $\mu_e - r_e$ plane, i.e., one of the projections of the FP, is poorly understood. Kormendy (1977) showed that ETGs do not follow the distribution expected for galaxies of the same total luminosity, but are tilted with respect to this line, while Bender et al. (1992) and Burstein et al. (1997) noted that in this plane galaxies seem to avoid a region of space: the so called Zone of Exclusion (ZoE). They claimed that the slope of the ZoE and the progressive displacement of the Hubble types from this line is consistent with the hierarchical clustering scenario with a $n = -1.8$ power-law density fluctuation spectrum (plus dissipation). Moreover, Nigoche-Netro et al. (2008) showed that the Kormendy relation coefficients vary with the width of the magnitude range and with the brightness of the galaxies within it.

The same considerations can be done for the Faber-Jackson (1976) relation, connecting a galaxy luminosity with its velocity dispersion (see, e.g., Nigoche-Netro et al. 2010). The slope and zero-point of such relation changed progressively from the original $L \propto \sigma^{\sim 4}$ to the contemporary $L \propto \sigma^{\sim 2}$. This relation is considered a projection of the FP and, as such, was also related to the Virial Theorem, even though alternative explanations are possible.

## 6.2 The Fundamental Plane problem

We assume that ETGs are gravitationally bound stellar systems which satisfy the Virial Theorem equation:

$$\overline{V^2} = \frac{G\mathcal{M}_{tot}}{\overline{r}}, \tag{6.2}$$

where $\mathcal{M}_{tot}$ is the total galaxy mass, $\overline{r}$ a suitable mean radius, and $\overline{V^2}$ a mean kinetic energy per unit mass. By definition every kind of virialized system must belong to the Virial Plane (VP) in the space defined by the variables $\mathcal{M}_{tot}$, $\overline{r}$ and $\overline{V^2}$. Unfortunately, these are not observable quantities. Therefore, in the case of ETGs, the Virial Equation 6.2 is usually written as follows:

$$\mathcal{M}_{tot} = \frac{K_V \sigma^2 r_e}{G}, \tag{6.3}$$

where $r_e$ is the effective radius and $K_V = 1/(k_v k_R)$ takes into account projection effects, density distribution and stellar orbits distribution. The term $K_V$ parameterizes our ignorance about the orientation, 3D structure and dynamics of ETGs. The formal expression of $K_V$ (which is a dimensionless quantity) assumes: $\overline{V^2} = k_v \sigma^2$, and $\overline{r} = k_r r_e$.

Introducing the mean effective surface brightness $\overline{I_e} = L/2\pi r_e^2$, one gets such expression for the Virial Plane (VP):

$$r_e = \frac{K_V}{2\pi G} \left(\frac{\mathcal{M}_{tot}}{L}\right)^{-1} \overline{I_e}^{-1} \sigma^2, \tag{6.4}$$

or, in logarithmic form:

$$\log(r_e) = 2\log(\sigma) - \log(\overline{I_e}) + \log(K_V) - \log\left(\frac{\mathcal{M}_{tot}}{L}\right) - \log(2\pi G). \tag{6.5}$$

This formulation of the Virial Theorem is directly comparable with the FP of Equation 6.1 rewritten with $\log(r_e)$ as independent variable empirically derived from observations.

Note that for a given mass $\mathcal{M}_{tot}$ and zero-point there are infinite values of $\mu_e - r_e$ which satisfy Equation 6.5: all the points belonging to a plane obey such equation. We can therefore define the VP as *the locus of points of the $\mu_e - r_e$ space which reproduce a constant mass $\mathcal{M}_{tot}$ for an assigned zero-point.*

The zero-point of Equation 6.5 is given by the quantity:

$$ZP_{FP} = \log(K_V) - \log\left(\frac{\mathcal{M}_{tot}}{L}\right) - \log(2\pi G), \tag{6.6}$$

so that each galaxy has its own zero-point characterized by a peculiar $\mathcal{M}/L$ (dark matter and stellar content) and $K_V$ (degree of non-homology). If ETGs were perfectly homologous systems (same $K_V$) with similar $\mathcal{M}/L$ the $ZP_{FP}$ would be a constant and all galaxies would be distributed along one VP. In other words, the Virial Theorem does not provide any constraints on the position of a galaxy in the $\mu_e - r_e$ space. Two galaxies with the same mass and zero-point, but with a different combination of $\mathcal{M}/L$ and $K_V$, may share the same VP. In general, Equation 6.5 defines a family of planes filling the $\mu_e - r_e$ space for all galaxies.

In the $\mu_e - r_e$ space each VP is parallel to the others, so that in principle one should observe a cloud and not a plane, unless a mechanism constraining all galaxies on the observed FP is in action.

The connection between the FP and the VP clearly links the tilt of the plane to the properties of the stellar population, to the DM content and the galaxy structure and dynamics. It is therefore not surprising that all the proposed solutions have tried to demonstrate the link of the zero-point with these galaxy properties. The existence of the FP, with its tilt and small scatter, requires a connection between $K_V$ (structure) and $\mathcal{M}/L$ (DM and stellar populations). This is the so-called fine-tuning problem.

## 6.3 The new proposed solution

The new proposed solution comes from the observation that a galaxy of a given mass $\mathcal{M}_{tot}$ has not a defined position in the $\mu_e - r_e$ space. Its virial equilibrium is guaranteed by all possible combinations of the variables that fit the virial equation. It would be useful to have at least another constraint to better define the location of a galaxy in the $\mu_e - r_e$ space.

In order to find such a constraint we consider that a galaxy of a given mass $\mathcal{M}_{tot}$ has also a total luminosity $L_{tot}$. The luminosity of a galaxy ultimately depends on the luminosities of its stars, which in turn depends on the star radius and the effective temperature at the star surface.

The common way of introducing the luminosity in the FP problem was through the mass-to-light ratio, but we note that luminosity is actually a quantity independent on the virial equilibrium, being only the product of the SF history of galaxies.

On the basis of such consideration we look for the various expressions that can give the total luminosity of galaxies. We know that the integrated bolometric luminosity $L$ of a galaxy of age $T_G$ can be expressed as:

$$L(T_G) = \int_0^{\infty} \int_0^{T_G} \int_{\mathcal{M}_L}^{\mathcal{M}_U} S\left(\mathcal{M}, t, Z(t)\right) f_\lambda\left(\mathcal{M}, \tau', Z(\tau')\right)\, d\mathcal{M}\, dt\, d\lambda, \quad (6.7)$$

where $S(\mathcal{M}, t, Z(t))$ is the stellar birth-rate, $f_\lambda(\mathcal{M}, \tau', Z(\tau'))$ is the monochromatic flux of a star of mass $\mathcal{M}$, metallicity $Z(t)$ and age $\tau' = T_G - t$, and $\mathcal{M}_L$ and $\mathcal{M}_U$ the minimum and maximum star masses that are formed. The stellar birth rate $S(\mathcal{M}, t, Z(t))$ can be expressed as the total mass converted into stars per unit time (e.g., $\mathrm{M}_\odot\ \mathrm{yr}^{-1}$) or the total number of stars formed per unit time at the time $t$ with the chemical composition $Z(t)$. We adopt the first definition for the sake of consistency with the definition of other quantities in usage here that are related to the star formation. Separating the $S(\mathcal{M}, t, Z(t))$ into the product of the SFR $\Psi(t, Z(t))$ and the initial mass function $\Phi(\mathcal{M}, Z(t))$, and neglecting here the dependence on the metallicity (it can be easily introduced whenever necessary) the above integral becomes

$$L = \int_0^{\infty} \int_o^{T_G} \Psi(t) F_\lambda(\tau')\, dt\, d\lambda, \quad (6.8)$$

where,

$$F_\lambda(\tau') = \int_{\mathcal{M}_L}^{\mathcal{M}_U} \Phi(\mathcal{M}) f_\lambda(\mathcal{M}, \tau')\, d\mathcal{M}, \quad (6.9)$$

where $F_\lambda(\mathcal{M}, \tau')$ is the integrated monochromatic luminosity at each epoch provided by a single stellar population of age $\tau'$ and $f_\lambda(\mathcal{M}, \tau')$ is the monochromatic luminosity emitted by a star of mass $\mathcal{M}$ and age $\tau'$ or $t$ in general. Finally, we define the luminosity per unit mass of a single stellar population as:

$$L_{sp}(t) = \int_0^{\infty} F_\lambda(t)\, d\lambda, \quad (6.10)$$

and finally:

$$L = \int_0^{T_G} \Psi(dt) L_{sp}(t)\, dt. \quad (6.11)$$

We can rewrite Equation 6.11 for the total luminosity considering the average values of the involved variables as:

$$L \sim \overline{\Psi(t) \times L_{sp}}\, T_G \sim \overline{\Psi}\, \overline{\frac{L}{\mathcal{M}}}\, T_G, \tag{6.12}$$

where $\overline{\Psi(t)}$ is the time average of the current SFR, and $T_G$ is the age of the galaxy. In the above average, $\overline{L/\mathcal{M}}$ indicates the mean stellar light-to-mass ratio representative of the whole stellar content. The total emitted light today is the result of the whole SFH independently on the events that have contributed to the increase of the SFR or its quenching. We further note that within the time average values of $\overline{\Psi(t) \times L_{sp}}$ are encrypted the contributions of the IMF.

Now we remember that the luminosity of ETGs correlates with the velocity dispersion of their stars through the FJ relation (Faber and Jackson 1976). The best way for writing such relation is:

$$L = L_0 \left(\frac{\sigma}{\sigma_0}\right)^{\beta}, \tag{6.13}$$

where $\sigma_0$ is a reference zero-point normalization in velocity dispersion, $\beta$ is the exponent derived through the fit of the data (often written in log form) and $L_0$ is a reference luminosity for the galaxy with $\sigma = \sigma_0$. Measured values for $\beta$ range from 2 to 5 depending on the width of the magnitude range and the luminosity of the sampled galaxies within the magnitude range (see e.g., Nigoche-Netro et al. 2010).

The origin of this correlation is far from clear. Why, in fact, should $L$ and $\sigma$ be correlated? The SF is a local phenomenon originating by micro-physical processes inside clouds of gas and dust, while the velocity dispersion of a galaxy is a direct consequence of the mass potential well. How do the two things communicate? A priori there is no reason for such a connection. A posteriori we understand the $L - \sigma$ relation on the basis of the connection between mass and luminosity in each single star and on the basis of the Virial Theorem. We will explore this issue again later on.

In the following we will often prefer to write Equation 6.13 in the form $L = L_0\sigma^{\beta}$, i.e., dropping the term $\sigma_0$. In this way we can simplify the calculations as follows. For the moment we emphasize that in this form the parameter $L_0$ has units of [g s$^{-1}$], i.e., consistent with a SFR if $\beta = 2$.

The direct comparison of Equation 6.12 and Equation 6.13 tells us that the parameter $L_0$ of the FJ relation is connected to the mean SFR. We can in fact write:

$$L_0 = \overline{\Psi(t) \times L_{sp}}\, T_G/\sigma^{\beta}. \tag{6.14}$$

In this parameter $L_0$ the complex relationship between the galaxy dynamics and the SFH is therefore encrypted.

Now, remembering that $L_{tot} = 2\pi\overline{I_e}r_e^2$, and passing to the logarithms, Equation 6.13 (in its simplified form) can be rewritten as:

$$\begin{aligned} \log(r_e) &= (\beta/2)\log(\sigma) - (1/2)\log(\overline{I_e}) + \\ &\quad +(1/2)\log(L_0) - (1/2)\log(2\pi). \end{aligned} \tag{6.15}$$

At this point we can consider Equations 6.1 (the FP), 6.5 (the VP), and 6.15 (the FJ) using $\sigma$ as dependent variable:

$$\begin{aligned} \log(\sigma) &= A\log(r_e) + B\log(\overline{I_e}) + C, \\ \log(\sigma) &= \frac{1}{2}\log(r_e) + \frac{1}{2}\log(\overline{I_e}) + \frac{1}{2}\log(\mathcal{M}/L) + \\ &\quad -\frac{1}{2}\log(K_V) + \frac{1}{2}\log(2\pi G), \\ \log(\sigma) &= \frac{2}{\beta}\log(r_e) + \frac{1}{\beta}\log(\overline{I_e}) - \frac{1}{\beta}\log(L_0) + \frac{1}{\beta}\log(2\pi), \end{aligned} \tag{6.16}$$

where the coefficients $A$, $B$ and $C$ are related to those of Equation 6.1. Then we take the difference FP-VP and FP-FJ. These differences must be equal on the intersecting lines. After some algebra, it follows that:

$$\log(\overline{I_e}) = \frac{(2/\beta) - (1/2)}{(1/2) - (1/\beta)}\log(r_e) + \Pi, \tag{6.17}$$

where $\Pi$ can be defined as:

$$\begin{aligned} \Pi &= \frac{1}{2}\log(K') = \frac{[\frac{1}{2}\log(K_V) - \frac{1}{2}\log(\mathcal{M}/L)}{[\frac{1}{2} - \frac{1}{\beta}]} + \\ &\quad +\frac{-\frac{1}{\beta}\log(L_0) - \frac{1}{2}\log(2\pi\ G) + \frac{1}{\beta}\log(2\pi)]}{[\frac{1}{2} - \frac{1}{\beta}]}, \end{aligned} \tag{6.18}$$

which also defines the dimensional constant $K'$.

Now we ask ourselves if Equation 6.13 could represent the plane we are looking for in the $\mu_e - r_e$ space.

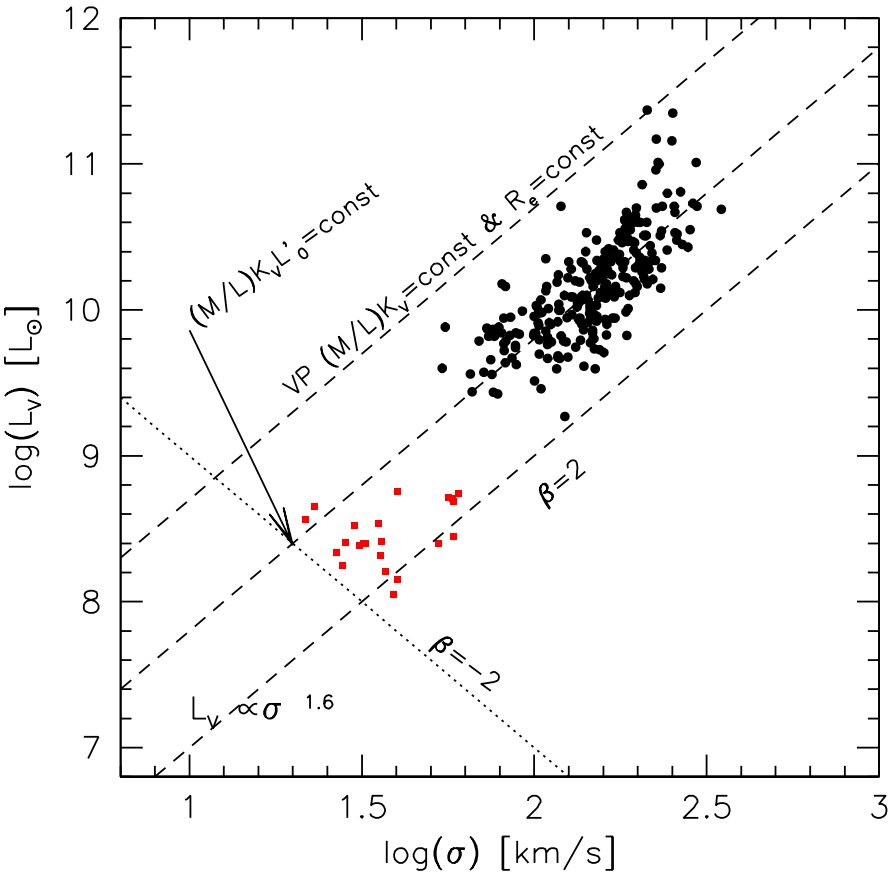


Figure 6.1: Distribution of ETGs in the $L-\sigma$ plane. The dashed lines mark the position of the VPs ($\beta = 2$) for galaxies with different effective radii and zero-point. The dotted line marks one possible PFJ plane with $L'_0 = constant$ with slope equal to $-2$ (see text). The classical FJ relation seems to result from the intersection of the PFJ and the VP planes. The filled circles are normal ETGs. The red squares are dwarf galaxies of the WINGS database with masses around $10^8 - 10^9$ $M_\odot$.

Firstly, we observe that in the FJ relation $L_0$ is nearly constant for almost all ETGs (in the mass range $10^9 - 10^{12}$ $M_\odot$) of different $\sigma$. The value of $L_0$ valid for all our ETGs is $1.6 \times 10^{29}$ gr $s^{-1}$. So this relation is not the one we are looking for as a second virtual plane representing the total luminosity of

a galaxy in the $\mu_e - r_e$ space.

Furthermore, for $\beta = 2$, which is a good possible fit for the FJ relation (see Figure 6.1), in Equation 6.17 the slope of the $I_e - r_e$ relation is undefined.

Looking at Figure 6.1 we note that there are alternative mathematically correct values of $\beta$ that could give the total luminosity of a galaxy $L_{tot}$. In other words we should find the correct value for $\beta$ on the basis of the observed distribution of galaxies in the FP projections that provides the total luminosity of each single galaxy. We will see below that the best value is $\beta = -2$.

Figure 6.1 shows with dashed lines the slope of the $\beta = 2$ lines in the $L - \sigma$ space. The dotted line, instead, marks the planes with $\beta = -2$. Therefore, heareafter we will write Equation 6.13 with $\beta = -2$ as $L = L'_0\,\sigma^{-2}$, dropping again the normalization constant but remembering of its existence. The values of $L'_0$ are in this case the intercepts with the $\log(\sigma) = 0$ axis and have the same unit of $L_0$ (i.e., that of a characteristic luminosity). With this equation we can assign to $L'_0$, which is very different from galaxy to galaxy, the primary role of capturing the SFH of each object leaving to $\sigma$ the secondary role of indicating how the velocity dispersion affects the SFR (note that $\sigma$ could only change in the limited interval provided by the scatter of the FJ relation).

Since $L'_0$ and $L_0$ are correlated, we have for $\beta = 2$ that $L_0 = L'_0\sigma^{-4}$. It follows, on the basis of Equation 6.12, that also $L'_0$ is connected to the SFR:

$$L'_0 = \overline{\Psi(t)\,L_{sp}}\,T_G\,\sigma^2. \tag{6.19}$$

Now substituting $L'_0$ to $L_0$ in Equation 6.15 we obtain a plane in the $\mu_e - r_e$ space which is tilted in the right direction with respect to the VP and with the notable property of having a significantly different zero-point for each galaxy.

This is the second virtual plane of the $\mu_e - r_e$ space that we are looking for. It represents the total luminosity of a galaxy with a zero-point different for each object, as it is the case for the total mass in the VP (with $\mathcal{M}/L$ and $K_V$ as zero-points).

We call this plane the "PFJ plane" (pseudo-FJ) for keeping in mind its origin from the FJ relation and we define it as follows: *The PFJ plane is the locus of points defined by the values of $\mu_e - r_e$, which reproduce a constant luminosity $L_{tot}$ for an assigned zero-point $L'_0$.* This plane contains, as the VP, only one galaxy and all PFJ planes are parallel each other in the $\mu_e - r_e$ space.

The different inclination of the VP and PFJ planes suggests that they intersect somewhere in the $\mu_e - r_e$ space, forming a line in such space. Along

this line it resides only one object, the one with mass $\mathcal{M}_{tot}$, luminosity $L_{tot}$ and zero-points $Z_{FP}$ and $Z_{PFJ} = 1/2\log(L'_0)$. In other words, along this line the product $(\mathcal{M}/L)K_V L'_0$ is constant.

It is clear that if the zero-points of the VP and PFJ planes vary in a coordinated way, the result will be the formation of several parallel lines in the $\mu_e - r_e$ space, each one containing one galaxy. The plane that best fits this distribution of parallel lines is the plane of real galaxies in the $\mu_e - r_e$ space (i.e., the FP). Therefore, we define the FP as follows: *The FP is the plane in the $\mu_e - r_e$ space that best fits all the parallel lines formed by the intersections of the VP and PFJ planes. In this plane the quantity $(\mathcal{M}/L)K_V L'_0$ is constant.* In this framework, the existence of a FP for real galaxies implies that a close connection must exist between $(\mathcal{M}/L)$, $K_V$ and $L'_0$ (or, in other words, between mass, luminosity, structure and SFR).

A graphical sketch representing the mechanism at the origin of the FP is given in Figures 6.2 and 6.3. Figure 6.2 shows two possible VPs for two galaxies (in black and grey) and one PFJ plane for one galaxy. The intersecting lines formed in the $\mu_e - r_e$ space by the VP and PFJ planes for galaxies of masses $\mathcal{M}_{tot}$ and luminosities $L_{tot}$ mark the locus in which galaxies might reside, in edge on Figure 6.3.

Consequently, the FP plane is naturally tilted with respect to both the VP and PFJ planes. Its tilt is now connected to the global variation of the zero-points of the VP and PFJ planes ($Z_{FP}$ and $Z_{PFJ}$), and the small scatter observed around the plane originates from the fine-tuning effect linking $\mathcal{M}/L$, $K_V$ and $L'_0$ (i.e., linking the galaxy mass, structure and dynamics with the SFR).

## 6.4 The observed projections of the Fundamental Plane

Could we demonstrate observationally that the FP originates from the existence of the VP and PFJ planes?

Observations have shown that not only the FP of ETGs is tilted with respect to the VP and that the scatter around the plane is small ($\sim 20\%$), but also that the distribution of galaxies in the FP projections is far from random. The best known example is the $\log(\overline{I_e}) - \log(r_e)$ plane. Kormendy (1977) first noted a correlation between these variables with a slope different from that predicted on the basis of the total luminosity. Capaccioli et al. (1992), Bender et al. (1992) and Burstein et al. (1997) further noted that galaxies seem to avoid a region of this space that they called ZoE.

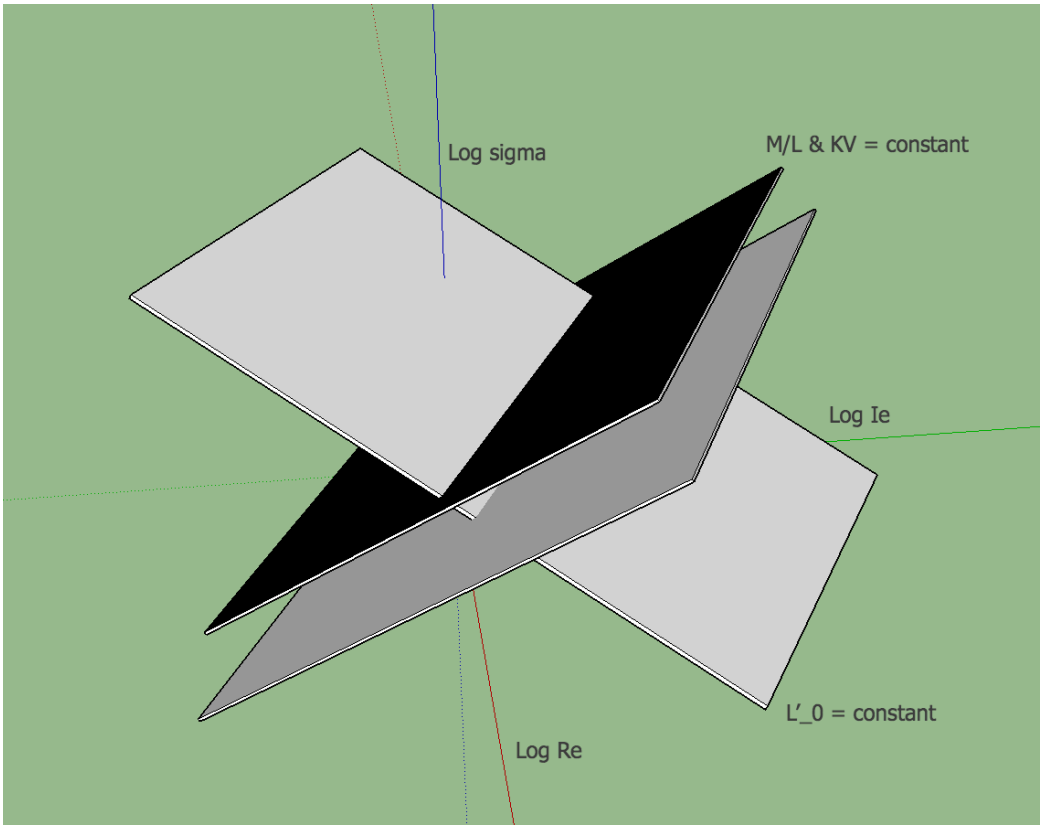


Figure 6.2: General view of the $\mu_e - r_e$ space with two possible VPs and one PFJ plane.

We will see here that the projections of the FP, in particular the $\log(\overline{I_e}) - \log(r_e)$ plane, the $\log(\overline{I_e}) - \log(\sigma)$ plane and the $\log(\sigma) - \log(r_e)$ plane can greatly help us to constrain the value of $\beta$.

The central velocity dispersions were taken from the literature (Bernardi et al. 2003; Smith et al. 2004), while the SFRs from Fritz et al. (2007). For deriving them, the authors used a SED-fitting tecnique that consisted in measuring the SFR at four different cosmic epochs:

- $2 - 20$ Myr, when stellar populations are characterized by lines in emission and the strongest ultraviolet emission;
- $20 - 600$ Myr, when the Balmer lines reach their maximum intensity in absorption and the Cak line is almost non detectable;
- $0.6 - 5.6$ Gyr, when the Balmer absorption lines become less and less intense, as the age increases, and the Cak absorption line reaches its maximum intensity;

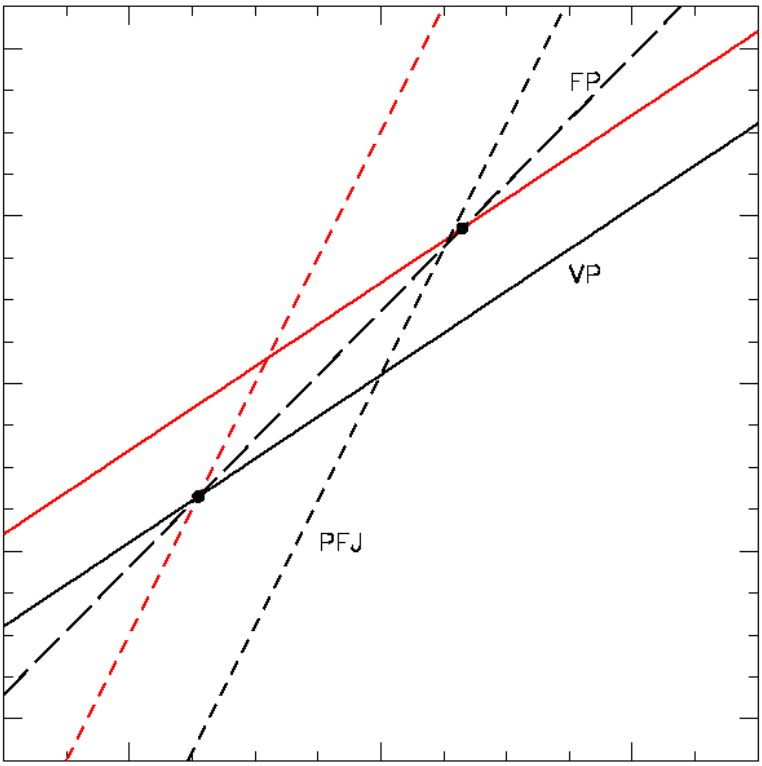


Figure 6.3: Two possible VP and PFJ planes seen edge-on for two ETGs of masses $M_1$ and $M_2$ and luminosities $L_1$ and $L_2$ respectively are shown with black (VP) and red lines (PFJ). The FP results in this case from the connection of the two intersections of the VP and PFJ planes. For many galaxies the FP is the plane best that best fits all the intersecting lines.

- $5.6 - 17.8$ Gyr, when the main features reach an asymptotic value for these SSP. With these data we define the time average $\overline{\Psi}$ as the sum of the four SFRs obtained for the different cosmic epochs.

In the previous section we obtained an equation for the distribution of galaxies with similar $\mathcal{M}/L$, $K_V$ and $L'_0$ in the $\log(\overline{I_e}) - \log(r_e)$ relation. The zero-point of Equation 6.17 varies as $\mathcal{M}/L$, $K_V$ and $L'_0$ vary in the FP space.

Note that the slope of this relation depends only on the value of $\beta$ (i.e., on the exponent of the PFJ plane).

Therefore, the question is: where are the projections of the intersecting lines located, i.e., the lines of constant $\mathcal{M}/L$, $K_V$ and $L'_0$ in these 2D planes?

Figure 6.4 shows the $\log(\overline{I_e}) - \log(r_e)$ plane where we have adopted the solution of Equation 6.18 with $\beta = -2$. Note how this value of $\beta$ naturally reproduces the slope of the observed distribution of galaxies. It follows that the so-called ZoE is, in this context, a natural limit reached today by the values of $\mathcal{M}/L$, $K_V$ and $L'_0$ during the cosmic evolution. In the figure we plotted with different colors different ranges for the $\mathcal{M}/L$ ratios available for the galaxies of the WINGS database in the V-band (Moretti et al. 2014). Note that there is not a clear trend of the galaxy distribution with the $\mathcal{M}/L$ ratios, even if the higher mass-to-light ratios seem more frequently distributed far from the ZoE. The dotted line is in fact the locus where the product of $\mathcal{M}/L$, $K_V$ and $L'_0$ is constant and not simply that where $\mathcal{M}/L = constant$.

Figure 6.5, instead, is a plot of the $\log(\overline{I_e}) - \log(r_e)$ distribution for objects of very different masses, covering a range from $\sim 1$ $M_\odot$ to $\sim 10^{14}$ $M_\odot$ (i.e., from stars to galaxy clusters). The data for the globular clusters are taken from Pasquato and Bertin (2008), while those for stars are taken from the SIMBAD database[1]. A similar plot was done by Dantas et al. (2000) using the $k$-space over the range going from GCs to galaxy clusters.

Note that the $\log(\overline{I_e}) - \log(r_e)$ relation seems to be valid on every scale. In this figure the ZoE is well visible in grey. The various virialized systems are not randomly distributed. Their position in the diagram depends on their structure and luminosity. The plot demonstrates that for all the kinds of virialized systems there is a similar link between structure, dynamics and luminosity. All structures are distributed along lines parallel to the ZoE with $\beta = -2$. The position of all systems in the diagram should be determined in some way by the fine-tuning relation linking the luminosity of the stellar population and the dynamics of the system governed by the total mass.

For stars the $\mathcal{M}/L$ ratio increases as far as we move away from the ZoE, going from the main sequence stars of A spectral type to that of M type stars. Therefore, if the dominating stellar population inside a stellar system is made of late-type stars, we will observe a higher $\mathcal{M}/L$ that will likely place the galaxy far from the ZoE[2].

Note also that this diagram is done for the V-band, so that there is a natural selection effect working on, since the lower $(\mathcal{M}/L)$ (due to bright

[1]The selected stars span the spectral types from A0 to M5. They are: $\alpha$ Cor B., Sun, 70 Oph A, 61 Cyg A, EZ Aqu.

[2]Assuming that the DM contribution is approximately the same for all galaxies, which is not exactly the case.

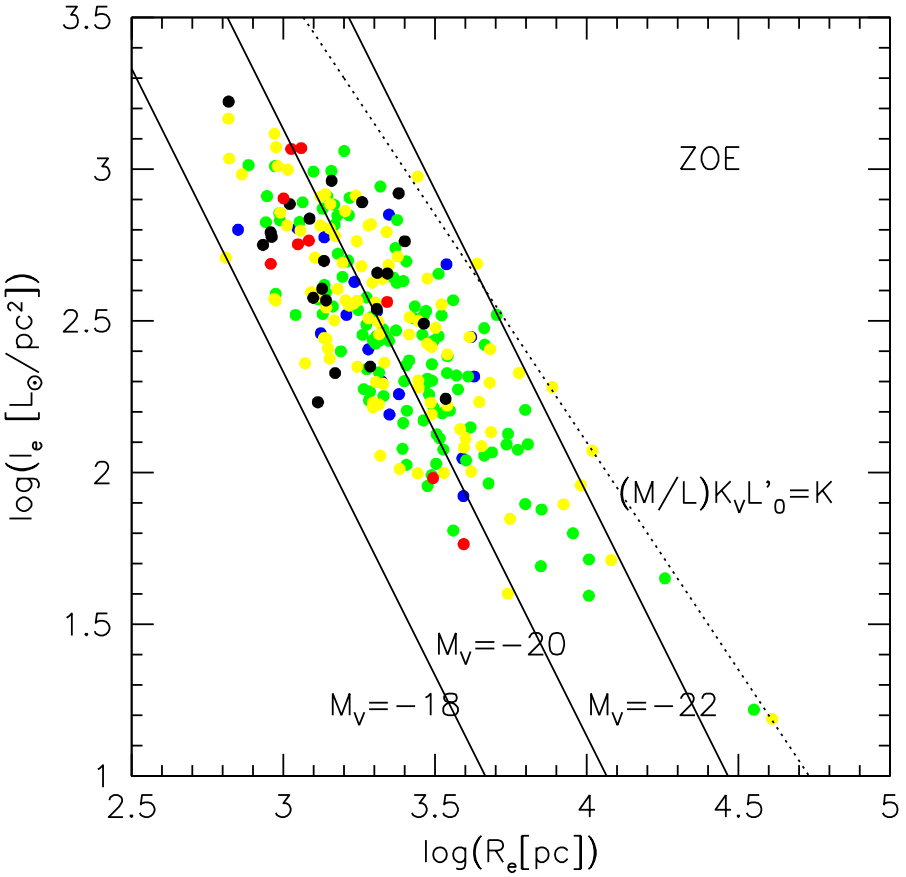


Figure 6.4: The $\log(\overline{I_e}) - \log(r_e)$ plane of the WINGS ETGs. Galaxies are plotted with different colors according to their measured stellar mass-to-light ratio (blue dots: $\mathcal{M}/L = 1$; green: $\mathcal{M}/L = 3$; yellow: $\mathcal{M}/L = 5$; black: $\mathcal{M}/L = 7$; red: $\mathcal{M}/L > 8$). The solid lines give the locus of constant galaxy luminosity. The dotted lines mark the locus of constant total mass-to-light ratio, $K_V$ and $L'_0$ (i.e., the projections of the intersecting lines originating the FP when $\beta = -2$).

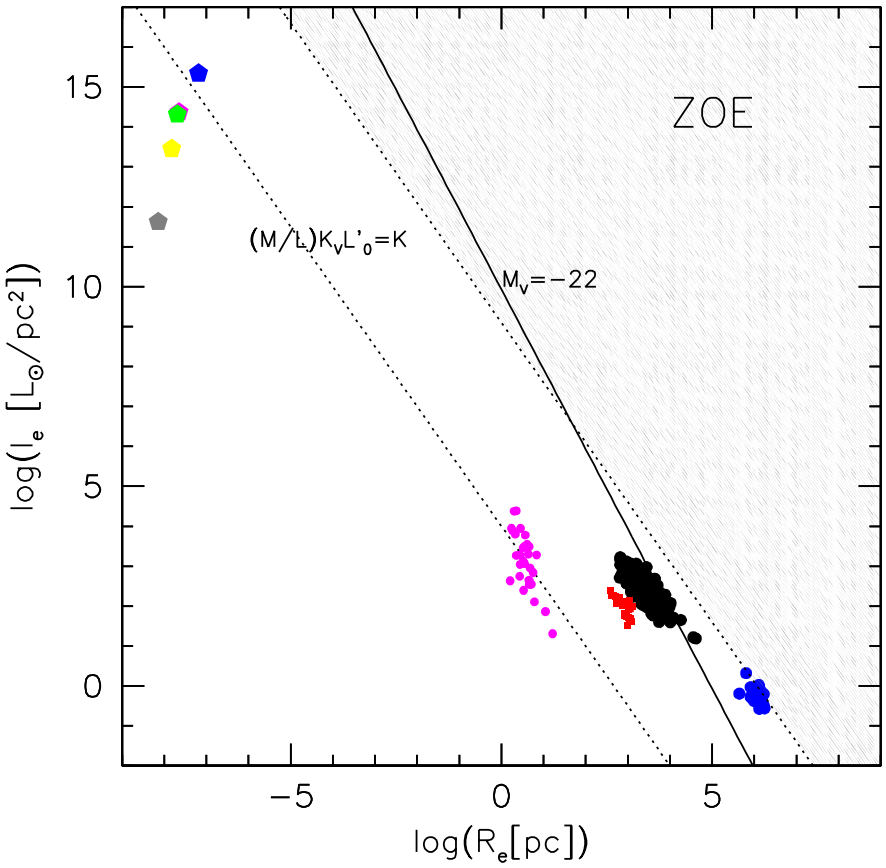


Figure 6.5: The $\log(\overline{I_e}) - \log(r_e)$ plane for objects of different masses that are known to be close to the virial equilibrium: main sequence stars (blue pentagon = $\alpha$ Cor B; magenta = Sun; green = 70 Oph A; yellow = 61 Cyg A; grey = EZ Aqu), globular clusters (magenta dots), dwarf galaxies (red dots), normal ETGs (black dots) and galaxy clusters (blue dots). The solid line gives the locus of constant absolute magnitude ($M_V = -22$ mag), while the dotted lines are parallel to the ZoE and mark the positions of the different constant values of $(\mathcal{M}/L) \cdot K_V \cdot L'_0$. The shaded area in grey is the ZoE.

stars that dominate the galaxy luminosity), progressively moves the galaxies toward the ZoE.

The galaxy clusters appear shifted with respect to the ZoE because these systems contain several spiral galaxies with low $\mathcal{M}/L$ and have a lot of DM, while globular clusters have a solar mass-to-light ratio because their stellar population is dominated by stars with high $(\mathcal{M}/L)$.

For the other FP projections we obtain:

$$\begin{aligned} \log(\overline{I_e}) &= (\beta - 1)\log(\sigma) + const, \\ \log(\sigma) &= \frac{1}{2-\beta}\log(r_e) + const, \end{aligned} \tag{6.20}$$

where the constant zero-points also depend on the combination of $\mathcal{M}/L$, $K_V$ and $L'_0$. Again the $\beta = -2$ value determines the distribution of galaxies and the position of the ZoE in the respective diagrams (see Figure 6.6).

In conclusion, the observed distribution of ETGs in the FP projections suggests that the fine-tuning between structure and stellar population could be indeed at the origin of the FP properties. Each galaxy in the $\mu_e - r_e$ space can be represented by two virtual planes that intersect each other. The first plane is provided by the Virial Theorem and fixes the mass of a galaxy once the $\mathcal{M}/L$ and $K_V$ are given. The other plane represents the total luminosity and comes from the $L = L'_0\,\sigma^{-2}$ relation, where in the parameter $L'_0$ the role played by the star formation history is encrypted.

In the next section we will further discuss the connection between luminosity, star formation and velocity dispersion in ETGs.

## 6.5 The connection between luminosity, SFR and velocity dispersion

We have seen that the FP could originate from a fine-tuning of the zero-points of two planes, the VP and the PFJ plane. This link implies a close connection between the SF history of ETGs and their structural and dynamical characteristics. The FP projections seem to confirm such link in the observed non random distribution of galaxies.

Here we will see that a strong link between luminosity, the time average SFR and the central velocity dispersion exists. In fact, Equations 6.12 and 6.13 can be coupled into a single one:

$$L^2 = L_0\,\frac{\overline{L}}{\mathcal{M}}\,\overline{\Psi}\,T_G\left(\frac{\sigma}{\sigma_0}\right)^2, \tag{6.21}$$

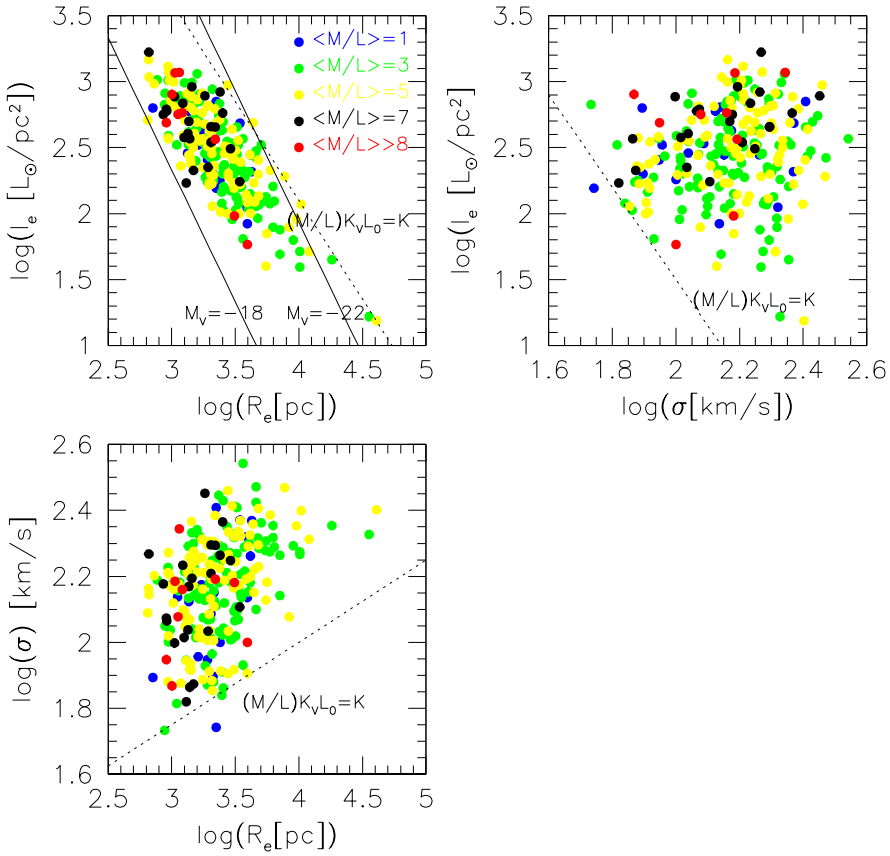


Figure 6.6: The different projections of the FP on the $\mu_e - r_e$ axes. The dotted lines mark a possible position for the ZoE. Color code as in Figure 6.4.

so that it is possible to predict the validity of the following relation:

$$L = q\sqrt{\overline{\Psi}}\sigma, \tag{6.22}$$

where $q = \sqrt{L_0 \frac{\overline{L}}{\mathcal{M}} T_G}/\sigma_0$ is a dimensional constant.

All these considerations tell us that we should look at the correlation of three variables $L$, $\sigma$ and $\overline{\Psi}$. These are mutually connected because the mass $\mathcal{M}$ correlates with the velocity dispersion $\sigma$ through the virial relation and the light $L$ correlates with the time average star formation rate $\overline{\Psi}$. Consequently $\sigma$ and $\overline{\Psi}$ are connected. Figure 6.7 provides the observed correlation among these variables.

The 3D correlation between these variables derived with the $R$ program[3] gives:

$$\log(L) = 0.48(\pm 0.06)\log(\overline{\Psi}) + 1.00(\pm 0.13)\log(\sigma) + 7.81(\pm 0.26) \tag{6.23}$$

with an RMS = 0.215 ($R = 0.64$ and $p$-value $< 1.2 \times 10^{-16}$). The partial correlation coefficients of $\log(L)$ with $\log(\sigma)$ and $\log(\overline{\Psi})$ are, respectively, 0.44 and 0.43, indicating a robust 3D relation. This is in remarkable good agreeement with the theoretical expectation seen above, putting in evidence that there is such a connection at the basis of the zero-points variations of the VP and PFJ planes.

## 6.6 More on the FJ and PFJ planes

We now consider in more detail the meaning of the $L - \sigma$ plane. The FJ plane contains two measured quantities: the galaxy luminosity and the stellar velocity dispersion. At variance with the VP that is defined for one galaxy only in the $\mu_e - r_e$ space assigning the mass and zero-point, the FJ plane contains all real galaxies at the same time. Along the fitted relation the zero-point $L_0$ is nearly constant for almost all galaxies (let say between $10^9$ and $10^{12}$ $M_\odot$).

The first thing to note is that in the FJ plane the points of constant $\mathcal{M}/L$, $K_V$ and $L'_0$ are the galaxies themselves (see again Figure 6.1). Note how the selected solution with $\beta = -2$ used for the $\log(\overline{I_e}) - \log(r_e)$ relation gives here the series of parallel zero-points that provide the luminosities of all galaxies for each $\sigma$, reproducing the observed FJ relation when they are considered all together. The FJ relation seems to originate from the intersections of the

[3]https://www.r-project.org.

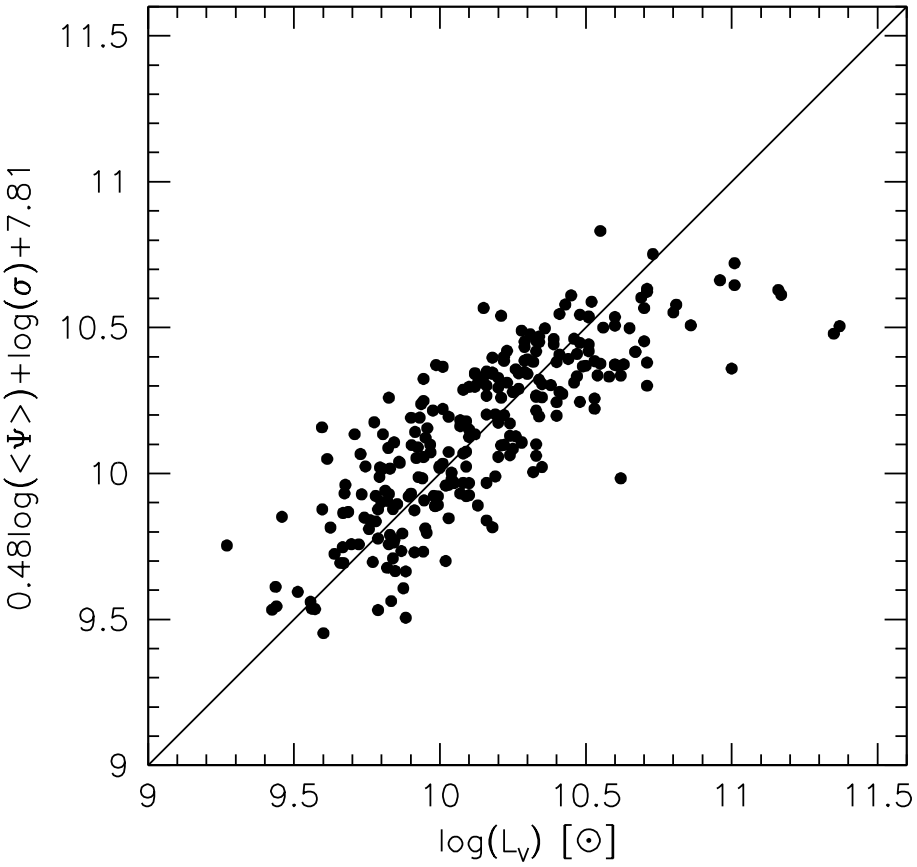


Figure 6.7: The mutual correlation between $L$, $\overline{\Psi}$ and $\sigma$ in log units. Color code as in Figure 6.4.

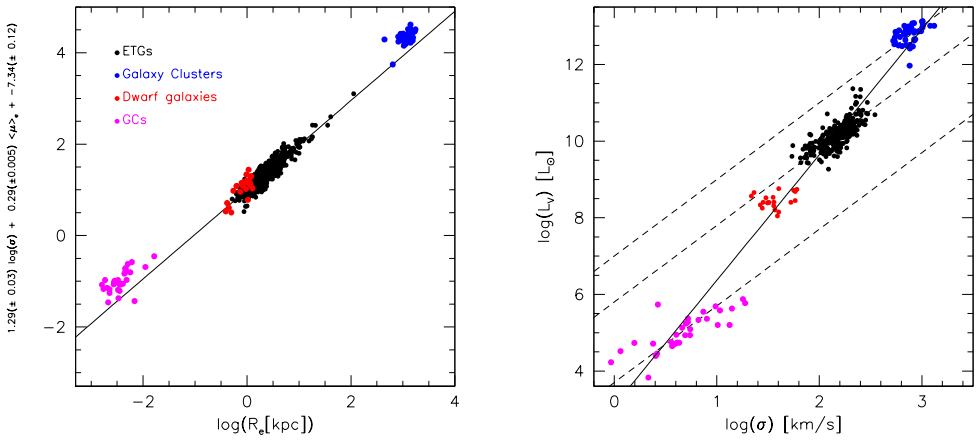


Figure 6.8: Left panel: an edge-on view of the FP for ETGs with overplotted the position of all other types of stellar systems. Right panel: the same systems on the FJ relation. The color code is the same as in Figure 6.5. The solid line with a slope of 3.26 is obtained from the fit of all systems together.

"projections" in the $L-\sigma$ space (having collapsed $I_e$ and $r_e$ in the variable $L$) of all the parallel virtual planes that represent the total luminosity of galaxies with the "projections" arising from the virial planes (the dashed lines where $\mathcal{M}/L$, $K_V$ and $r_e$ are constants). The intersections of the $L = L'_0\,\sigma^{-2}$ lines with the VP projections fix the exact position of galaxies in the $L-\sigma$ space. This is the relation expected for all virialized stellar systems having similar zero-point $L_0$.

Therefore, in this context it is possible to explain why the residuals from the FJ relation correlate with $\mathcal{M}/L$ (Cappellari et al. 2006) and with galaxy sizes (Desmond and Wechsler 2017).

Figure 6.8 shows the FP derived here for the present ETG sample (solid line). It has been obtained as in D'Onofrio et al. (2008) using the MIST fit kindly provided us by La Barbera (private communication). The FP coefficients obtained for this sample are: $a = 1.29$, $b = 0.29$ (note that here $\overline{\mu_e}$ has been used instead of $\overline{I_e}$), and $c = -7.24$.

Dwarf galaxies ($\mathcal{M} \sim 10^8 - 10^9$ M$_\odot$), globular clusters and galaxy clusters deviate from the main galaxy relation. This occurs because these systems have a systematically-different zero-point in their VP and PFJ planes (i.e., they have different $\mathcal{M}/L$, $K_V$ and $L'_0$ values.)

The left and right panels of Figure 6.8 clearly show that all stellar systems behave in a similar way. All systems satisfy the FP and FJ relations, but with

slightly different zero-points with respect to that typical of galaxies. These ZP variations depend on the different link between the virialized structure and its stellar population.

The larger exponent observed in many cases for the FJ relation (4, instead of 2) in this case could ultimately depend on the heterogeneity of the galaxy sample (i.e., on the inclusion of galaxies characterized by very different masses and luminosities). An example is seen in the right panel of Figure 6.8, where we get a slope of 3.26 for the FJ by fitting together all stellar systems.

In any case the FJ law is a relation that provides a further element to the virial relation, linking mass (and the virialized system internal gravitational energy) to the production of radiant energy i.e., to the object luminosity. The mechanisms of energy production can be very different and can yield to widely different $\mathcal{M}/L$ values even among stellar systems, where the mechanism is roughly the same, ultimately associated with nuclear reactions in the star interior.

If we now take Equation 6.18 with $\beta = -2$, giving the zero-point of the relationship between the effective surface brightness $I_e$ and the effective radius $r_e$ (the varies with $\mathcal{M}/L$, $K_V$ and $L'_0$ and hence with $Z_{FP}$), after few steps we get:

$$K' = \frac{K_V}{4\pi^2 G}\frac{L}{\mathcal{M}}L'_0 \tag{6.24}$$

where $L'_0 = L\sigma^{-2}$ and $K'$ is a parameter different for each cosmic epoch (with units of [g$^2$ cm$^3$ sec$^{-6}$] or [L$_\odot^2$ pc$^{-1}$] when the normalization factor in $L'_0$ is not taken into account), the gravitational constant is given in cgs units or expressed as $G = 4.3 \times 10^{-3}$ pc M$_\odot^{-1}$ km$^2$ s$^{-2}$ and the term $K_V$ is a function of the Sérsic index $n$ (Bertin et al. 2002). $K'$ will follow the evolution of the main galaxy parameters by changing the position of a galaxy in the $\log(\overline{I_e}) - \log(r_e)$ plane. As a consequence, the whole FP is expected to vary its tilt across the cosmic epochs.

Figure 6.9 shows the relation between $L'_0$ derived from Equation 6.24 and the total galaxy luminosity $L$. Here we used the stellar $\mathcal{M}/L$ being $\mathcal{M}/L$ unknown for our galaxies. We observe that the link of $L'_0$ and $L$ is far from being trivial: $L'_0$ is derived in fact from a complex combination of $\mathcal{M}/L$ and $K_V$. The fit between these variables is done here with the classical unweighted bisector linear regression analysis (Feigelson and Babu 1992). We used this method because there is not a priori a dependence of one variable on the other and the errors for both are poorly determined. We note that the residuals of this relation mildly depend on the central velocity dispersion $\sigma$. The correlation coefficient is only 0.11, but the probability of a correlation by chance is $p = 6.5 \times 10^{-2}$, indicative of a possible dependence. This hidden

correlation with $\sigma$ provides a further support to the idea that $L'_0$ is a proxy of $\overline{\Psi}$ and there is a 3D dependence between luminosity, SFR and velocity dispersion.

Furthermore, Figure 6.10 gives a clear indication that both $L$ and $L'_0$ are correlated with the time average SFR of the galaxies measured by Fritz et al. (2007). The residuals of these correlations present again a significant dependence on $\sigma$. The probability of correlation by chance between the residuals of the $\log(L) - \log(\overline{\Psi})$ relation and $\log(\sigma)$ is $p = 7.2 \times 10^{-1}$. For the residuals of the $\log(L'_0) - \log(\overline{\Psi})$ relation the probability of correlation by chance with $\log(\sigma)$ is instead $p = 2.4 \times 10^{-2}$. In both cases this correlations reveal the presence of a second hidden parameter (i.e., $\sigma$), which is significant for the 261 ETGs of our sample. This is a further element in favor of the 3D relation $L - \overline{\Psi} - \sigma$.

In summary, we have played with two different correlations: the first one is that between mass $\mathcal{M}$ and velocity dispersion $\sigma$ provided by the virial theorem; the second one is that between luminosity $L$ and mean SFR $\overline{\Psi}$. Since mass and luminosity are connected through the $\mathcal{M}/L$ ratio the FJ relation can be derived assuming that $L_0 = r_e L/G\mathcal{M}$. The residuals of the $L - \sigma$ relation depend on $\overline{\Psi}$ (or proxy of it likes $\mathcal{M}/L$), while the residuals of the $L - \overline{\Psi}$ relation depend on $\sigma$. It follows that the 3D relation provided by $L - \sigma - \overline{\Psi}$ (in logarithmic units) originates from such mutal correlations.

With this in mind we now better understand why we should use the $L = L'_0\,\sigma^{-2}$ relation for building the second virtual plane in the $\mu_e - r_e$ space. In fact, in order to build such a plane we need to use the direct correlation between $L$ and $\overline{\Psi}$ valid for each galaxy and not the one between $L$ and $\sigma$ valid for all galaxies (this is in fact the virial plane rewritten). What we want is to express the galaxy luminosity independently from its mass. The $L - \overline{\Psi}$ relation has $\sigma$ as second hidden parameter, as we have seen.

In the next section we will further explore the consequences of our findings for the problem of the star formation activity in galaxies.

## 6.7 The star formation activity in galaxies

Equation 6.14 provides a link between $L_0$ and the mean SFR of galaxies. It does not give a direct link between the current SFR, the velocity dispersion and $L_0$. What we are looking for, instead, is a more direct link between these quantities. How are they connected? We will show in Appendix that the FJ relation can be interpreted as a possible translation of the Stefan-Boltzmann's law valid for stars to the case of stellar system, putting in evidence that it is always possible to express the energy of a system with the more convenient

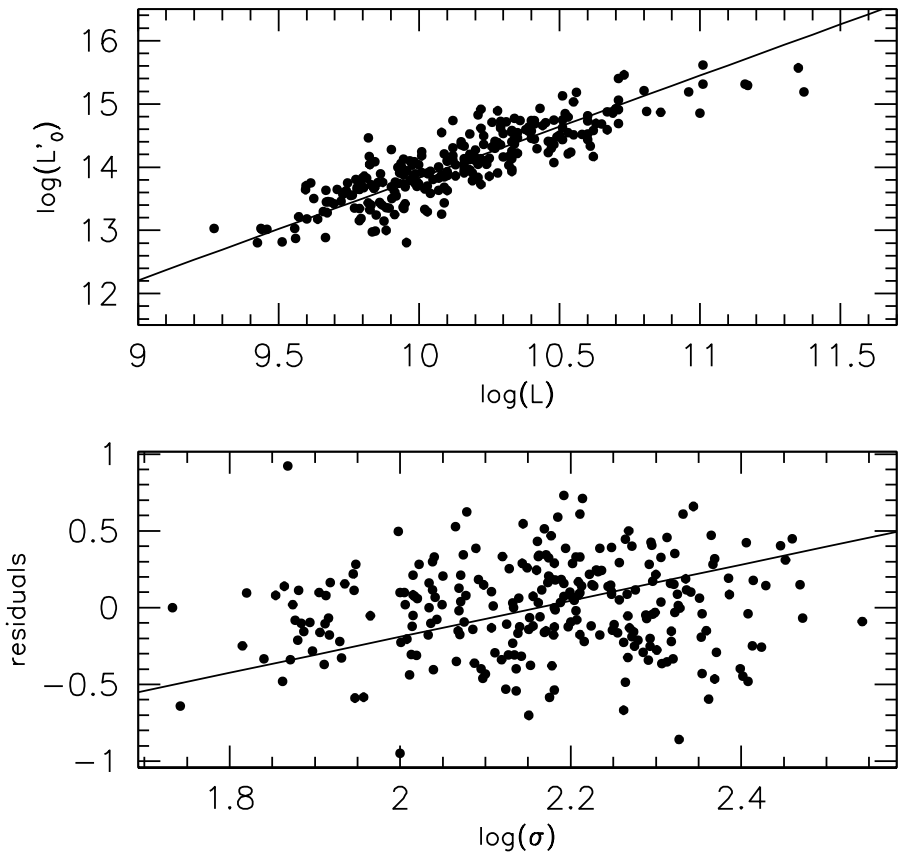


Figure 6.9: Upper panel: plot of $L_0'$ derived from Equation 6.24 versus the measured total galaxy luminosity $L$. Lower panel: plot of the residuals from the best fit of the above relation versus the measured velocity dispersion $\sigma$ in log units.

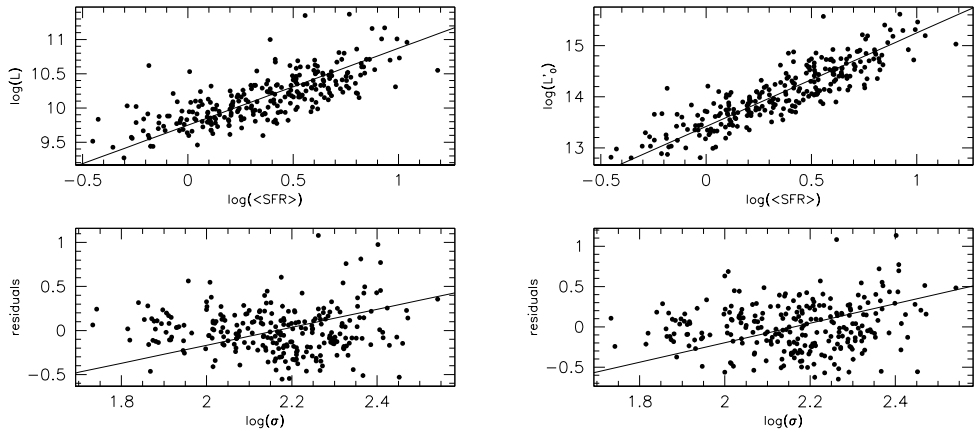


Figure 6.10: Left panel: $\log(L) - \log(\overline{\Psi})$ plot. Right panel: plot of $\log(L'_0) - \log(\overline{\Psi})$, which is the time-averaged SFR. Note that the residuals of these relations mildly depend on $\log(\sigma)$.

units (the ones we can measure).

Doing this exercise we noted that the galaxy luminosity can be expressed at any time $t$ as:

$$L_G = \overline{\alpha_s}\, N_s\, \overline{\mathcal{M}_s v_s^2}, \tag{6.25}$$

where the quantities underneath $^-$ are weighted time-averages over the whole stellar population. Here $N_s$ is the number of stars in the galaxy, $\mathcal{M}_s$ their mass and $v_s^2$ their velocity dispersion. The constant $\alpha_s$ is different for each galaxy and represents the ratio between the total energy emitted in the form of electromagnetic radiation and the total kinetic energy of a galaxy. This relation is valid for any stellar system in virial equilibrium.

In this context the quantity $L_0$ can be expressed by the relation:

$$\frac{L_0}{\alpha_s} = \mathcal{M}_g = \int_0^t \Psi(t) dt, \tag{6.26}$$

where we have explicitly written the mass of the galaxy as the integral of its star formation rate and we have highlighted the time-dependence of this parameter.

We can now recast Equations 6.24 and 6.26 in a different way putting in evidence the star formation rate of a galaxy. From this expression we can argue that at any epoch $t$ after the virialization the SFR could be given by:

$$\Psi(t) = \frac{d}{dt}\left(\frac{4\pi^2 GK'(t)}{\alpha_s(t)K_V(t)}\frac{\mathcal{M}(t)}{L(t)}\frac{1}{\sigma^4(t)}\right). \quad (6.27)$$

This theoretical relation is important because it allows the derivation of the global SFR of a virialized galaxy at any time $t$ taking into account the structure, the dynamics and the light produced by its stars. This relation explains why we have a fine-tuning between structure and stellar population and, consequently, why we observe the FP and the ZoE. The existence of the $L - \overline{\Psi} - \sigma$ relation should in other words be the final output of such fine-tuning.

Equation 6.27 tells us that at each cosmic epoch $t$ after virialization the SFR in a galaxy is not free. An unperturbed galaxy can form stars only at the rate permitted by Equation 6.27 along the whole cosmic history. In other words, once the mass and the potential well of a galaxy are given, the star formation proceeds according to the galaxy dynamics and the expected evolution of the stellar populations formed. If a galaxy does not merge with others and does not experience a significant infall of new gas, its SFR will not be considerably modified, continuing its evolution according to Equation 6.27. However, we know that ETGs experienced repeated merging events and infall of gas during their evolution. During major mergers galaxies are perturbed in their virial equilibrium and the validity of Equation 6.27 is probably lost for the time required to recover the virial equilibrium (approximately the free-fall time). At the same time large infall of gas, ram-pressure events and feedback forces could switch on/off the SFR compressing or stripping the gas component. Therefore, these external influences should be reflected in some way in the properties of the FP (and its projections) and the FJ relations. Variations are expected in the FP and FJ relations of ETGs when they are subject to merging and infall/quenching events perturbing the SFR. Observations of high-redshift ETGs should therefore shed light on the mechanism originating the FP.

In the case of our sample of nearby ETGs these events are exceptions. Merging and large infall or quenching events are in the far past history of these objects. They had time to recover their structure (virial equilibrium) and their SFR should therefore follow the behavior expected from Equation 6.27. Note that for these ETGs the central velocity dispersion is high and the SFR is low. This is expected on the basis of Equation 6.27.

Could we test in some way the validity of Equation 6.27 through observations? Unfortunately, this requires a database of masses, luminosities, SFRs and velocity dispersions of galaxies at different redshifts, while ours limited only to the nearby objects. However, considering that at $t = 0$ the SFR was

0, we can predict that the mean SFR of today galaxies will be approximately given by:

$$\overline{\Psi} = \frac{L_0}{\alpha_s \Delta t} \sim \frac{1}{2}\frac{\mathcal{M}_G}{T_G}, \tag{6.28}$$

where $\Delta t = T_G$ is the galaxies luminosity-weighted age.

Figure 6.11 shows the mean SFR measured by Fritz et al. (2007) in 4 distinct epochs from the direct fit of the galaxy SEDs versus the mean SFR obtained by Equation 6.28. The correlation (c.c. = 0.6 and RMS $\sim$ 2.8 but significant at a $\sim 7\,\sigma$ confidence level) appears consistent with the theoretical expectation, taking into account the various sources of errors affecting both quantities, even if the sample is biased and the correlation may be driven by few points at high SFR values. This test gives therefore a marginal indication for the validity of Equation 6.27.

We believe that this equation is important to understand the FP and the star formation history in galaxies. Simulations are today the only way to test the validity of Equation 6.27. To what extent merging/feedback events could change the mainstream of SF that each galaxy has encrypted in it since the beginning of the virial equilibrium? At which redshift the FP and FJ relations of ETGs are in place? These are all questions for the upcoming JWST telescope. A study of the FP and FJ relations for high redshift objects observed during the phase of their maximum activity in SF will likely shed more light on the validity of Equation 6.27.

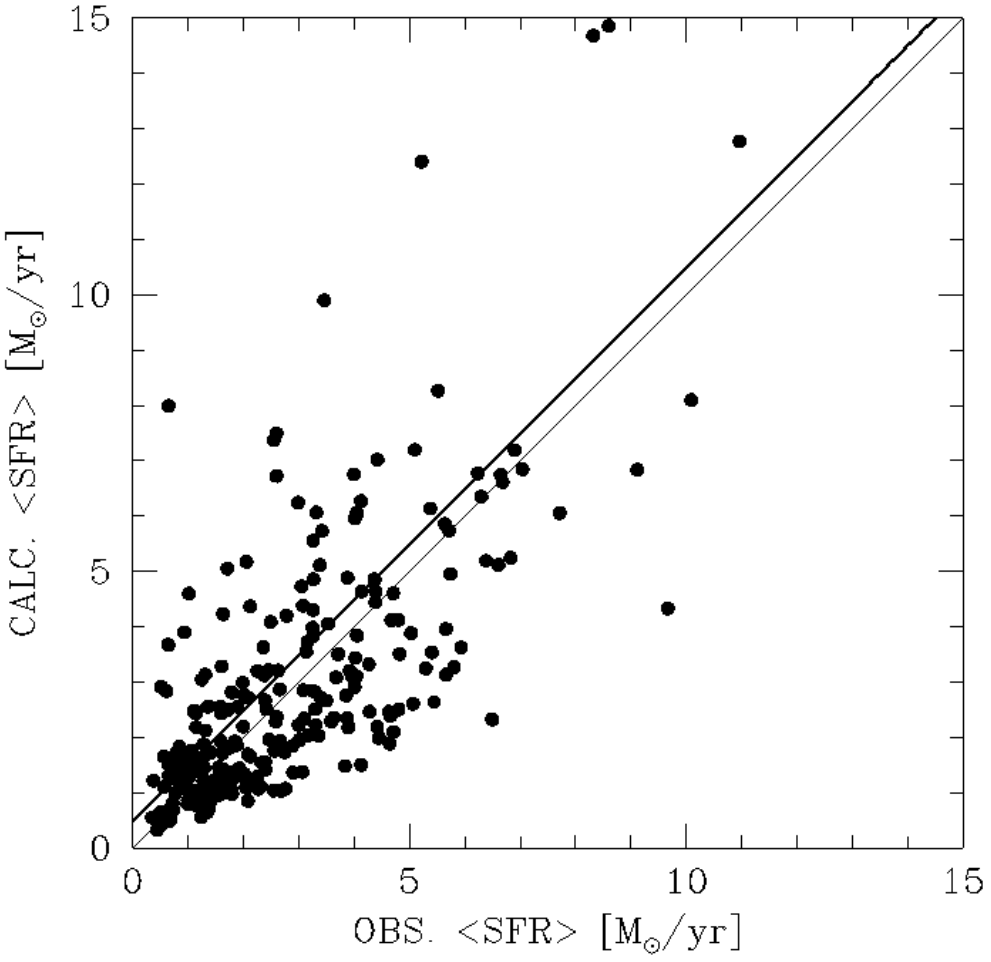


Figure 6.11: Plot of the mean observed SFR measured by Fritz et al. (2007) for the galaxies of the WINGS database using the fitted SEDs versus the mean SFR calculated on the basis of the prediction of Equation 6.27. The thin line is the one-to-one relation, while the thick line is the fitted distribution.

# Chapter 7

# Summary, conclusions, and future prospects

This Chapter is aimed at summarizing and drawing the conclusions of this PhD thesis work. In Section 7.1 we present the summary and conclusions, and in Section 7.2 the future prospects of our work.

## 7.1 Summary and conclusions

The aim of this section is to present a summary and the conclusions of our work on galaxy clusters (Section 7.1.1) and galaxies (Section 7.1.2).

### 7.1.1 The photometric decomposition of galaxy clusters

We have produced the stellar light (and mass) profiles of 46 (and 42) nearby galaxy clusters observed by the WINGS and Omega-WINGS surveys. The best fit of the luminosity growth profiles was obtained with the Sérsic law and compared with the King model and the standard $\beta$-model. From the analysis of the light profiles we derived the main cluster parameters (effective radius, total luminosity and mass, effective surface brightness, $(B-V)$ colors and Sérsic index). Then we used such parameters, in combination with the measured velocity dispersion of the clusters, to test the main scaling relations already analyzed in the past for ETGs.

When fitting the light profiles, we found that 7 out of 46 clusters are best fitted by a double Sérsic profile (an inner brighter structure plus an outer fainter one). The presence of multiple components seems disconnected from other cluster properties such as the number of substructures visible in the optical images or a difference in the stellar populations content. It seems

also not linked to the presence of the BCG in the center of the clusters.

All the analyzed relations confirm that the clusters of our sample are well virialized structures. Notably, the same relations valid for ETGs are visible for clusters, at different scales, providing a clear indication that a scale-free phenomenon of mass accretion regulated by gravitation is at work. Like ETGs, clusters also exhibit a degree of non-homology (different values of the Sérsic index even for clusters with the same luminosity) in their visible light and stellar mass profiles, and a quite robust correlation of the Sérsic index with the effective radius. This is a somewhat unexpected property on the basis of numerical simulations (see e.g., Cole and Lacey 1996; Navarro et al. 1997), which predict self-similar dark matter halos with Navarro-Frenk-White profiles.

The most interesting and new relation found here for the first time is the existence of a color-magnitude relation for clusters. When it is calculated considering only the galaxies within an area of $0.6\,r_{200}$, the CM slope perfectly matches the average red sequence slope found for the galaxies in the Omega-WINGS clusters. The CM cluster relation appears even more clearly when the analysis of the cluster properties is pushed beyond $0.6\,r_{200}$. The blue (red) clusters are the faint (bright) ones. The existence of such relations must find an explanation in the current paradigm of galaxy and cluster formation. In fact, it is not easy to understand why the most massive structures preferentially host the older and redder galaxies, while the less massive clusters host the younger and bluer ones. In fact, the hierarchical accretion scenario predicts that the first structures to form are the smallest ones, while the biggest ones are the latest.

To what extent the CM cluster relation is a cluster environment effect? What model of cluster formation and evolution is consistent with such data? All these questions are left to future investigations.

Finally we observed that the cluster luminosity correlates with the intrinsic $(B-V)$ color gradient measured within $r_{200}$. We see that the faintest clusters show the largest color gradients. This behavior is not observed in ETGs, where the optical color gradient appears uncorrelated with the galaxy luminosity (La Barbera et al. 2010).

### 7.1.2 The Fundamental Plane

We have shown that the origin of the FP can be traced back to the validity of two basic physical relations: the virial dynamical equilibrium and the $L-\overline{\Psi}-\sigma$ relation linking the galaxy luminosity, the time-averaged SFR and the velocity dispersion. When it is written as $L=L_0'\,\sigma^{-2}$ this relation provides a second virtual plane in the $\mu_e - r_e$ space, whose zero-point varies

in a coordinated way with the VP. This fine-tuning is at the origin of the properties of the FP. The coupling of these relations could also explain the existence of the downsizing phenomenon and the nature of the ZoE in the FP projections.

Since, as demonstrated by Zaritsky (2012), a Fundamental Manifold can be constructed for all stellar systems, the easy prediction is that in general the FP and FJ relations are different for each class of stellar system (GCs, dwarf galaxies, late-type galaxies, normal ETGs, cluster of galaxies) that are dominated by velocity dispersion. The diversity is originated by the different zero-points of the VP and PFJ planes or, in other words, by the different SFH and the different coupling between structure, dynamics and stellar populations. The combination of the virial equilibrium, of the $L = L'_0\,\sigma^{-2}$ relation and the validity of the PFJ law for galaxy systems constrain objects of similar characteristics to the same FP, which is the locus of constant $\mathcal{M}/L$ ratio, $K_V$ and $\overline{\Psi}$ at each time epoch.

The projection of the intersecting lines connecting the VP and $L = L'_0\,\sigma^{-2}$ planes explains the properties observed for ETGs in the $\log(\overline{I_e}) - \log(r_e)$ plane and, in particular, the existence of the ZoE that, in this framework, is the natural limit reached by the stellar and dynamical evolution of a stellar system today.

The existence of the FP for nearby ETGs provides a natural constraint to the possible SFR activities, dynamical and structural transformations that these objects might experience. Once formed and virialized in a given potential well, the global SFR of an unperturbed ETG could not deviate from the track imposed by Equation 6.27. In other words, the evolution of the SFR depends on the transformations in mass, luminosity, structure and dynamics (unless new merging phenomena occur at later epochs).

Equation 6.27 should be studied now through photometric and dynamical simulations following the details of the mass assembly in stars and their relative luminosities. Naively, we can predict that, since the stellar mass is generally increasing while luminosity and stellar velocity dispersions could vary with the generations of stars, the resulting SFR will probably see various peaks at different redshift epochs depending on the galaxy dynamics.

It will be interesting to see if Equation 6.27 will help to quantify the problem of the star formation across the cosmic epochs and to constrain in some way the mass quenching phenomenon. Firstly, it will be important to verify if the two principal types of galaxies in the color-magnitude (or stellar mass), color-concentration, and color-morphology diagrams can be reproduced (Strateva et al. 2001; Kauffmann et al. 2003; Brinchmann et al. 2004; Baldry et al. 2004, 2006; Driver et al. 2006; Bamford et al. 2009). We know that in these plots there are two main regions: the so-called "blue cloud"

(or main sequence), where galaxy mass correlates with the star formation rate, and the "red sequence" where there is no such correlation and galaxies are passive. The origin of this bi-modality is commonly attributed to the bulge and disk structure of galaxies. In general, disks are bluer in color than bulges (e.g., Peletier and Balcells 1996) and galaxies with lower stellar mass and lower Sérsic index tend to be bluer (and, hence, to have higher SFRs) than higher stellar mass and higher Sérsic index systems (Baldry et al. 2004; Driver et al. 2006; Baldry et al. 2006; Bamford et al. 2009). Similar trends are observed for luminosity and stellar light concentration (Strateva et al. 2001; Driver et al. 2006). This idea fits with the found dependence of the SFR on the Sérsic index and the velocity dispersion found here. Unfortunately, all these relationships are complicated by the effects of the environment, so that disentangling the various effects on the star formation efficiency is quite difficult.

## 7.2 Future prospects

In this section we show that several of the previously-derived Omega-WINGS clusters surface brightness profiles, once normalized to the effective radius and shifted in surface brightness, are almost perfectly superposed to the corresponding BCG profiles (Section 7.2.1). Upon the empirical definition of "good BCG-cluster matches" between the profiles through the parameter RMS($\Delta\mu$) $\leq$ 0.4 mag, we find that 24 clusters out of the 45 used ($\sim$ 53%) turn out to have the same Sérsic index of the corresponding BCGs. This fraction remains higher than 35% even if RMS($\Delta\mu$) $\leq$ 0.3 mag. Using as control sample the 2nd ranked brightest galaxies of the same clusters, the fraction of good matches decreases to $\sim$ 1%. We conclude that up to 50% of present day BCGs and clusters have very similar Sérsic index. This finding is marginally confirmed by the data extracted from the Illustris simulation.

### 7.2.1 The connection between the BCG and galaxy cluster profiles

Figure 7.1 shows four best matches obtained between the equivalent surface brightness profiles of the BCGs and the corresponding profiles of the clusters. The green curves are the data for the BCGs while the orange curves are the Sérsic fit of the surface brightness distribution of the galaxy clusters. Both curves are re-scaled on the basis of the respective effective radius $R_e$. The value of the constant shift in surface brightness required to get the match is

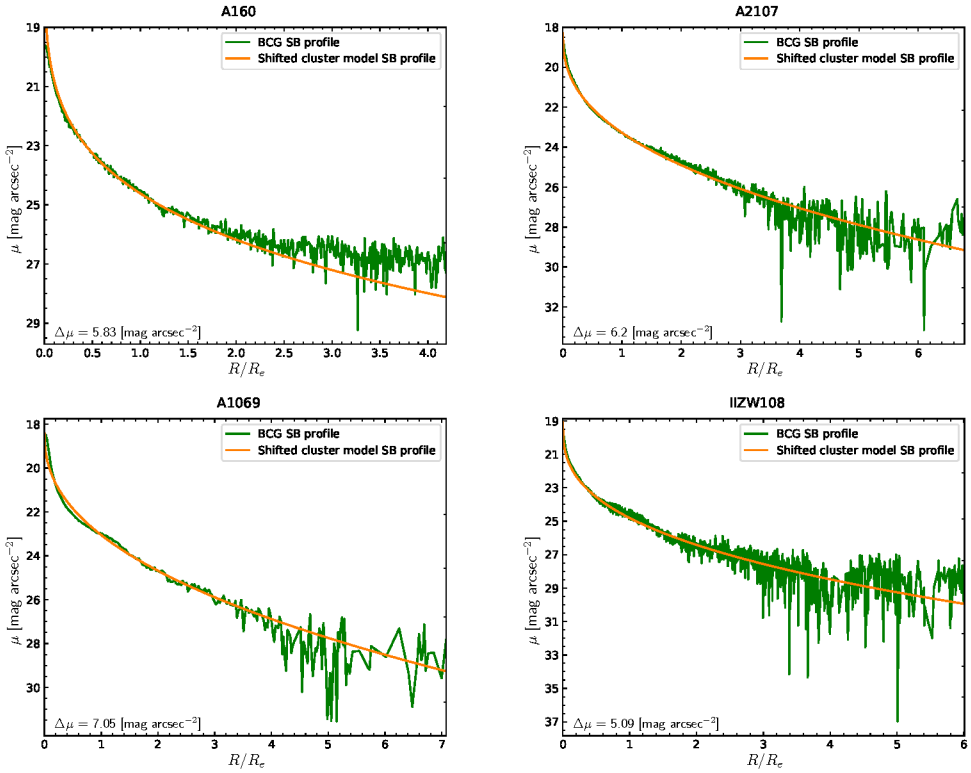


Figure 7.1: The four best matches obtained between the surface brightness profiles of the BCGs and clusters. The cluster name and the adopted $\Delta\mu$ are reported, respectively, over and on the lower-left corner of each plot. The data are in green, and the model in orange.

reported in the corner of each panel. Note that the BCG and cluster profiles are almost perfectly superposed in the whole range $0 < R/R_e \leq 3$.

Matches of this quality are obtained for 24 BCGs over a total sample of 45 objects ($\sim 53\%$) for which GASPHOT found a good Sérsic index. We used 45 out of 46 clusters as the BCG determination for Z8852 was uncertain. Upon inspection of the matched profiles, we decided to adopt an empirically-working criterium to judge in a less qualitative way the goodness of the observed matches. We therefore classified as "good matches" those profiles in which the RMS of the residuals $\Delta\mu = \mu_{\rm CL} - \mu_{\rm BCG}$ evaluated in the interval $0 < R/R_e \leq 3$ are lower than 0.4 mag. A different and more precise criterium can certainly be adopted to identify the best matches, but given the large errors in the determination of $n$ ($\Delta n \sim \pm 1$) and $R_e$ ($\sim 20\%$) we cannot obtain a significant variation in the fraction of the identified best matches. In fact, by setting the value of RMS($\Delta\mu$) to 0.3 mag, the percentage of best

matches decreases to $\sim 35\%$, which is anyway a considerable fraction for a random phenomenon to occur.

In order to exclude that the good matches are originated by the normalization with the effective radius, we derived the same surface brightness residuals using a control sample of galaxies. We choose the 2nd ranked brightest galaxies of the same clusters.

The black line in Figure 7.2 gives in the left panel the histogram of the RMS of the $\Delta\mu$ residuals calculated in the range $0 < R/R_e \leq 3$. We clearly see a peak at RMS($\Delta\mu$) $\sim 0.25$ mag whereas the galaxies of the control sample (2nd BCG) represented by the red line are almost randomly distributed. In particular, the fraction of best matches (RMS($\Delta\mu$) $< 0.4$ mag) is $\sim 53\%$ for the BCGs versus a value of $\sim 1\%$ for the 2nd ranked BCGs. The right panel, instead, shows the histogram of the Sérsic index for the two population of galaxies (BCGs and 2nd BCGs). Note how the two distributions are systematically shifted and peak at different values of $n$.

We therefore conclude that the observed match between the BCG and cluster light profiles is not due to a chance alignment determined by the normalization of the profiles, but it is a physical phenomenon. The two systems (BCGs and clusters) share in at least $30 - 40\%$ of cases almost the same Sérsic index.

Figure 7.3 shows in the left panel the comparison between the Sérsic index of the BCGs and that of clusters. The red symbols mark the matches with RMS($\Delta\mu$) $< 0.4$ mag. It is clearly seen here that 24 out of 45 clusters have approximately similar Sérsic indexes of their BCGs within the errors.

Figure 7.3 shows in the left panel the comparison between the Sérsic index of the BCGs and that of clusters. The red symbols mark the matches with an RMS of the residuals lower than 0.4 mag. It is clearly seen here that 24 out of 45 clusters have approximately the same Sérsic index with respect to their BCGs, within the errors.

The right panel of the same figure shows the histogram of the Sérsic index for the BCGs that share good matches with the cluster profiles (RMS($\Delta\mu$) $<$ 0.4 mag) and those that do not (RMS($\Delta\mu$) $\geq 0.4$ mag). Note the different superposition in the values of $n$ for the two samples.

### 7.2.2 Comparison with numerical simulations

The fact that BCGs have approximately the same Sérsic index of clusters, when we look at their equivalent circular growth curves normalized to the respective effective radii, implies that their potential wells have similar degree of concentration inside $3R_e$ or more. Is this predicted by modern numerical simulations in the $\Lambda$-CDM hierarchical framework?

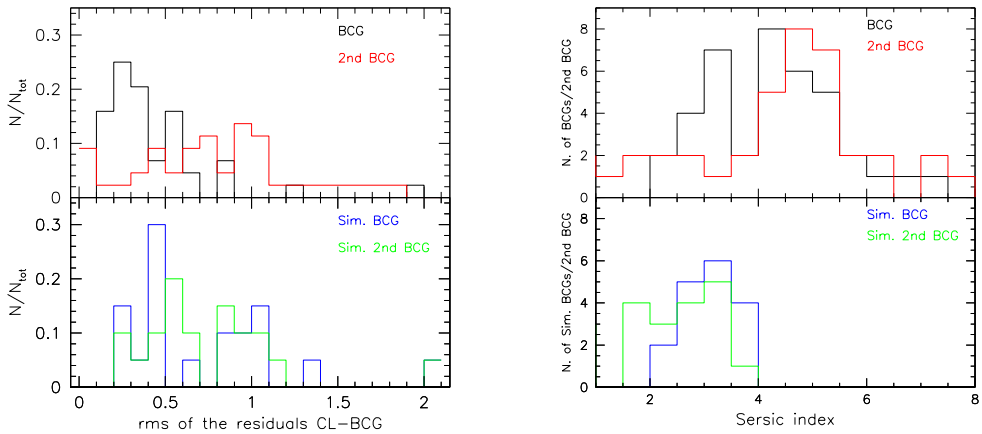


Figure 7.2: Left panel: in the upper box the black histogram gives the number of BCGs as a function of the RMS of the $\Delta\mu$ residuals, while the red histogram is that measured using the 2nd ranked brightest cluster galaxies. The lower box shows the same quantities for the galaxies simulated by the Illustris simulation. In blue we have the histogram of the matches between the BCG and the cluster, while in green that for the 2nd BCG. Right panel: the upper box shows the distribution of the Sérsic index for BCGs (black line) and 2nd BCGs (red line). The lower box shows the same distribution for the simulated BCGs (blue line) and 2nd BCGs (green line).

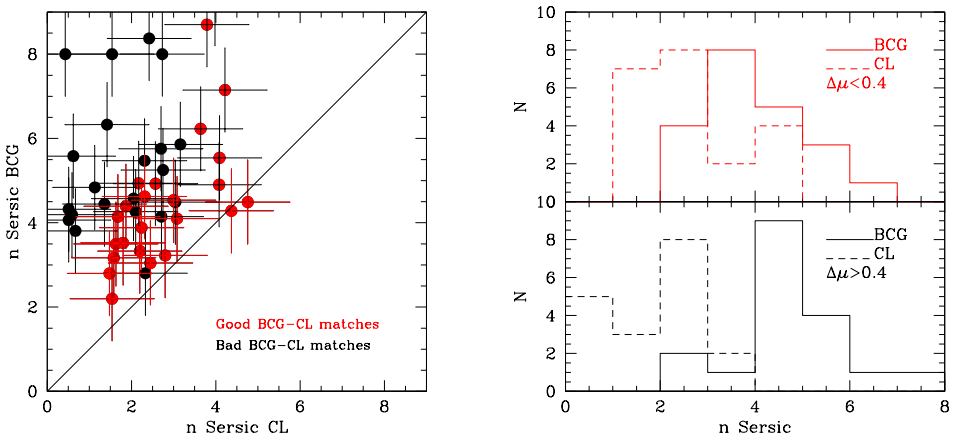


Figure 7.3: Left panel: the Sérsic index $n$ of clusters (CL) and BCGs. The red dots mark the objects in which the RMS of the residuals of $\Delta\mu$ is lower than 0.4 mag; Right panel: histogram of the Sérsic index values for the sample of BCGs with RMS($\Delta\mu$) $< 0.4$ mag (upper box in red color) and RMS($\Delta\mu$) $\geq 0.4$ mag (lower box in black color).

To check this we used the data provided by the Illustris simulation (Vogelsberger et al. 2014). We extracted the 20 most massive clusters (with masses ranging from $2.77 \times 10^{13}$ to $2.55 \times 10^{14}\, h^{-1}\, M_{\odot}$) at redshift $z = 0$. No other selection criteria (such as the degree of relaxation or the X-ray emission) was applied for the selection of the simulated clusters. This is not the case for the WINGS sample, where clusters were selected on the basis of their X-ray emission. We used the light emitted in the V-band from the star particles of the simulation together with their comoving coordinates $(x', y', z')$ inside the cosmological box. Setting $z' = 0$ we built the projected growth curves in circular annuli for each BCG-cluster pair, as we did for the WINGS objects. It was therefore possible to derive the effective radii of both systems and normalize the curves shifting each other in surface brightness. Figure 7.4 shows four matches obtained between BCGs and clusters. The RMS of matched curves was again calculated between 0 and $3R_e$.

We observe that in $\sim 50\%$ of the cases RMS($\Delta\mu$) $\leq 0.5$ (see Figure 7.2 left bottom panel), while this does not happen for the 2nd BCGs. This is quite similar to what we see for real galaxies, even if the peak of the distribution is slightly shifted to higher RMS with respect to that of observed BCGs (RMS($\Delta\mu$) $\sim 0.5$). For the simulated data the distribution of the residuals for BCGs and 2nd BCGs is not so different as in real galaxies. This is

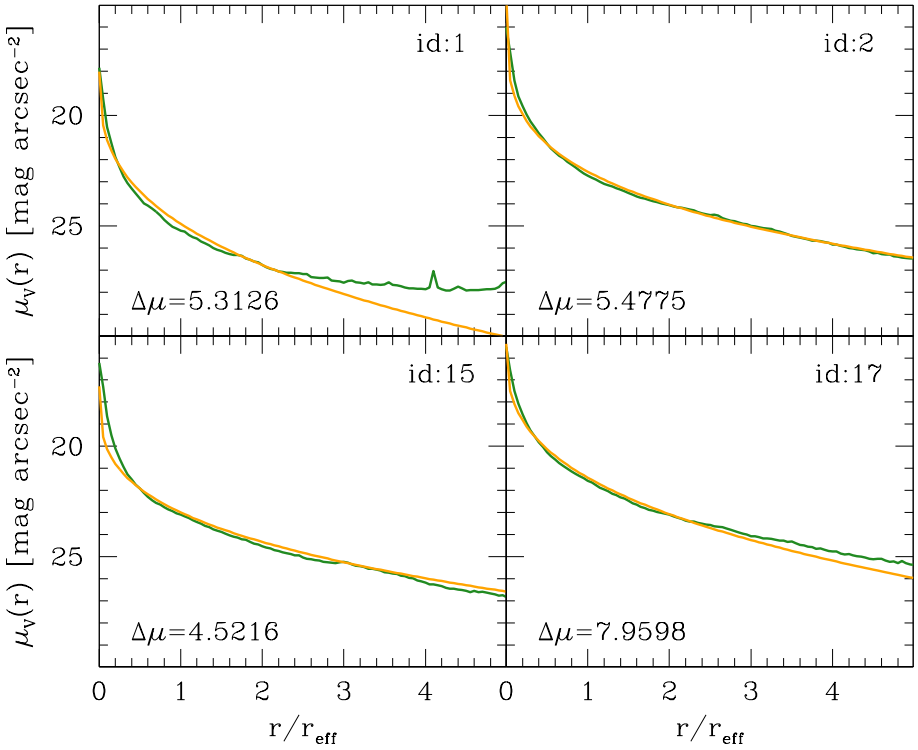


Figure 7.4: The four panels show the matches obtained from the analysis of the growth curves of the BCGs and the corresponding clusters extracted from the Illustris simulations. Colors are as in Figure 7.1. The shift in surface brightness is reported in the bottom left corner of each panel.

confirmed by the fact that the Sérsic index distribution for both objects is very similar (Figure 7.2 right bottom panel), while this is not the case for real galaxies.

Our conclusion is that there is only a marginal agreement between simulated structures and observations that seems to confirm the possibility that many BCGs and clusters share the same light profiles. It seems that numerical simulations do not provide yet Sérsic index and effective radii in full agreement with observations (see below).

### 7.2.3 A possible explanation

The present finding naturally raises a number of questions: what do the observed matches physically mean in the context of the BCG-cluster connection? How could this match be explained in the current hierarchical scenario of structure formation and evolution provided by the Λ-CDM cosmology? Which type of clusters present such match with the BCGs?

Let us start from the last question. In order to find a possible answer we tried to correlate the residuals RMS of the RMS($\Delta\mu$) with several measured properties of the clusters and the BCGs extracted from the WINGS database. We explored the correlations of RMS($\Delta\mu$) with the BCG and cluster flattening $b/a$, central velocity dispersion RMS($\Delta\mu$) (in log units), effective radius $r_e$ and effective surface brightness $\mu_e$. We also looked at the number of observed 2D substructures in the clusters, at the cD versus E morphological classification, at the X-ray luminosity of the clusters, at the total stellar masses, at the local density around the BCGs and finally the magnitude difference between the first and second ranked brightest cluster galaxies. We did not find any significant correlation, with the only exception of the central velocity dispersion $\sigma$ of the BCGs that seems to systematically increase for objects with larger RMS($\Delta\mu$). We got a correlation coefficient in the relation RMS($\Delta\mu$) vs log($\sigma$(BCG)) of 0.27, a RMS of 0.08 and a significance of $2.5 \times 10^{-2}$ using 35 BCGs with measured values of $\sigma$. The correlation therefore is quite poor and the significance is marginal, but prompted us to look at the correlation of the Sérsic index $n$ with the central velocity dispersion $\sigma$ and with the effective radius $R_e$ of the BCGs and the clusters.

Figure 7.5 shows in the left panel the $\log(n) - \log(\sigma)$ relation for the BCGs of our sample. The black dots mark the galaxies that have RMS($\Delta\mu$) $\geq 0.4$, while the red dots those with RMS($\Delta\mu$) $\leq 0.4$. The black and red lines give the corresponding least square fit of the observed distributions. Note that in the case of the BCGs that do not share the same profile of the clusters the $\log(n) - \log(\sigma)$ relation is significant, while for those matching the cluster profiles the relation does not seem to exist. For the black sample

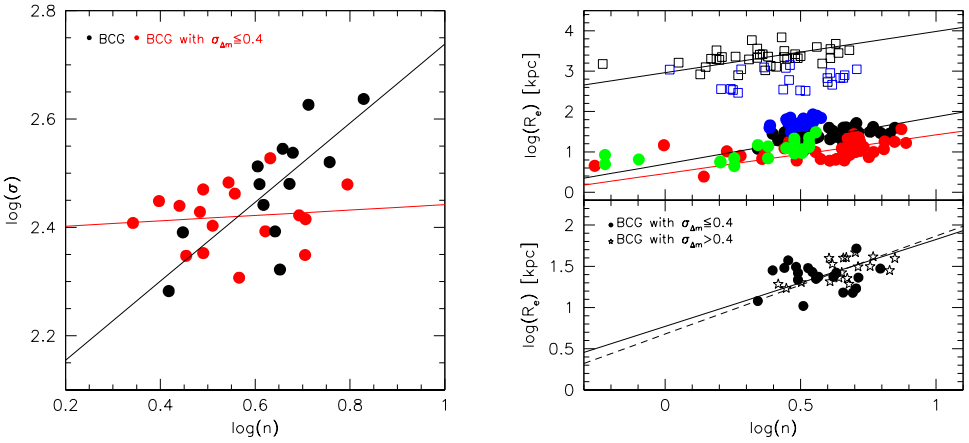


Figure 7.5: Left panel: the $\log(n) - \log(\sigma)$ relation for the BCGs of our sample. The black dots mark the galaxies that have RMS$(\Delta\mu) \geq 0.4$ mag, while the red dots those with RMS$(\Delta\mu) < 0.4$ mag. The black and red lines give the corresponding least square fit of the observed distributions. Upper right panel: the $\log(n) - \log(r_e)$ relation for BCGs (black dots), 2nd BCG (red dots) and clusters (open squares). The blue filled (open) circles (squares) mark the values found for the simulated BCGs (clusters), while the green dots mark the 2nd BCGs of the Illustris simulation. Lower right panel: the $\log(n) - \log(r_e)$ relation for the BCGs with RMS$(\Delta\mu) < 0.4$ (filled circles) and RMS$(\Delta\mu) > 0.4$ (open stars).

the correlation coefficient is 0.75 (with 13 points) and the significance of the correlation is $6.5 \times 10^{-4}$. For the red sample the correlation coefficient is 0.10 (with 17 points) and the significance of the correlation is $6.7 \times 10^{-1}$.

We clearly see in this figure that the $\log(n) - \log(\sigma)$ correlation appears when the sample of BCGs that do not fit the cluster profiles is used. This is a possible indication that the origin of this correlation likely resides in the effects of the merging events experienced by the BCGs along their history. Once a merger occurs it is well know even in N-body simulations that both the Sérsic index and the central velocity dispersion of the clusters progressively change. In this framework one might therefore be tempted to say that the observed $\sim 50\%$ of BCGs that do not share the same profiles of clusters are those in which the merging events have altered significantly the shape of the original galaxy.

The upper right panel of Figure 7.5 shows instead the $\log(n) - \log(R_e)$ relation for BCGs, 2nd BCGs and clusters. Note that all systems are non-homologous, i.e. the shape of their profiles varies with the effective radius. The slopes of the relations are pretty similar in all systems (1.17 for BCGs, 0.96 for 2nd BCGs and 1.02 for clusters). This is telling us that all virialized systems follow the same rules in assembling the luminous matter. After a merging event both $n$ and $R_e$ could change, but the slope of the $\log(n) - \log(r_e)$ relation does not seem to vary. The lower panel of the same figure shows in fact that the fitted relations are pretty similar for both types of galaxies.

It is interesting to see that the data coming from numerical simulations seem to follow the same trends of real galaxies despite the evidence that the effective radii are too small for clusters and a bit higher for BCGs. This could be related to limitations in cosmological simulations due to approximations made in subgrid physics (see Natarajan et al. 2017, for a comprehensive discussion).

Coming to the first two questions we should say that there is no simple interpretation for the observed high percentage of good matches between cluster and BCG profiles. Clearly our result reinforces the idea of a strong connection between the BCG and the cluster as a whole. In principle we do not see a plain contrast with the hierachical scenario of the $\Lambda$-CDM cosmology as long as the smaller and denser DM structures are the first to appear and the first to experience the baryonic matter collapse. These structures later evolve and grow and eventually might result in potential wells with similar shape at the different scales traced by the luminous matter.

The results of De Lucia and Blaizot (2007) seem to confirm what we observe. In their Figure 5 they show that the assembly history of the BCGs follows the evolution of the dark matter and stellar content of its own halo

with a delay time due to dynamical friction.

The phenomenon is not trivial. Observations have not revealed a clear physical parameter for distiguishing the clusters where the profiles are similar to the BCG profiles. The only indication coming from observations is that the properties observed today for the BCGs likely depends on the number of succesive merging experienced across their history. This led us to suspect that the BCG-cluster connection starts at very early times and only the subsequent evolution progressively disrupt the link between them.

In conclusion we have several unanswered questions: when was the BCG-cluster match established? Does the hierarchical growth of the DM structures forming the cluster leave unaltered the photometrical properties at the center? Why have the merging events experienced by the BCG not altered the BCG-cluster connection?

Possible answers could come from deeper analyses of numerical simulations that take into account the baryon collapse in the dark matter halos and from observations of BCGs and clusters at larger redshifts.

We cannot further address such issue in this PhD thesis, so we simply conclude by noting that the observed match between the BCG and cluster profiles, here seen for the first time, is a step forward towards understanding the problem of the BCG-cluster connection and it is potentially a useful proxy of the degree of evolution of the cosmological structures.

# Appendix A

# A possible origin for the FJ relation

In this Appendix we aim at demonstrating that the FJ relation with $\beta = 2$ could be seen as a sort of translation of the Black Body Stefan-Boltzmann law, valid for individual stars, to the case of an entire galaxy, made by an assembly of stars in which the temperature is replaced by the velocity dispersion. During this analysis the link connecting $L_0$ and $L'_0$ with the SFR of galaxies will appear again.

It goes without saying that there is not an immediate straight correlation between the physical situations in stars and galaxies; however, we will convincingly see that such analogy is possible and also argue that dynamics (via the velocity dispersion) and stellar populations in a galaxy (via the light emitted by stars) are each other intimately related. To demonstrate that this is possible we proceed as follows.

## A.1 The case of single stars

A star of mass $\mathcal{M}_s$, radius $r_s$, luminosity $L_s$, and effective temperature $T_{es}$ is an assembly of N heavy particles (nuclei, ions, and atoms, whereas electrons can be neglected) in thermal motion with mean temperature $\overline{T}$ and in virial equilibrium, i.e., satisfying the condition:

$$\mathcal{M}_s v_s^2 \equiv \left| \frac{G\mathcal{M}_s^2}{r_s} \right| \equiv E_V, \tag{A.1}$$

where $v_s$ is the mean particle velocity in a gram of matter, $\mathcal{M}_s = N\overline{m_p}$ with N is the number of heavy particles and $\overline{m_p}$ their mean mass, and finally $E_V$ stands for the "virial energy".

Consider first the total bolometric luminosity of a star (i.e., the total energy emitted per second by the surface). This is usually derived from the Stefan-Boltzmann law, since stars are in good approximation Black Body systems.

In a star we can measure the luminosity $L_s$, the effective temperature $T_{es}$, and the radius $r_s$ which are related by the well known Black Body law:

$$L_s = 4\pi r_s^2 \sigma_{\rm SB} T_{es}^4, \tag{A.2}$$

where $\sigma_{\rm SB}$ is the Stefan-Boltzmann constant. The suffix SB is to distinguish it from the velocity dispersion that we indicated with the same symbol.

It is worth recalling that the luminosity can be derived from the energy content of the Black Body according to:

$$U_{\rm BB}(T) = \frac{8\pi\Omega}{h^3c^3}(kT)^4\frac{\pi^4}{15}, \tag{A.3}$$

where $k$ is the Boltzmann constant, $\Omega$ the total volume and $U_{\rm BB}(T)$ the total energy of the Black Body. From this we obtain the luminosity of the star

$$L_s = \frac{U_{\rm BB}(T)}{\Omega}4\pi r_s^2 c = \frac{3U_{\rm BB}(T)c}{r_s}. \tag{A.4}$$

At this point we verify that the gravitational energy, the mean kinetic energy of the particles, and the Black Body energy content of the whole star with mean temperature $\overline{T}$ are comparable to each other. Taking the Sun as a typical star, for which we assume $r_s = 6.94\,10^{10}$ cm, $\mathcal{M}_s = 1.99\,10^{33}$ g, mean internal temperature $\overline{T} \simeq 5\times10^6$ K, and central value $T \simeq 10^7$, [1] we obtain:

- the mean density of kinetic energy of the $N$ particles in the star is:

$$\overline{E_k} = \frac{1}{\Omega}\sum_i^N \frac{m_p v_p^2}{2} = \frac{3}{2}nkT \simeq 3.47\times10^{15}\ \text{erg cm}^3, \tag{A.5}$$

[1] The elementary theory of stellar evolution by combining the equations for hydrostatic equilibrium, mass conservation and physical state of the plasma (e.g., $P = \frac{k}{\mu m_H}\rho T$), provides a simple relation for the mean temperature inside a star:

$$\bar{T} \geq 4.58\times10^6 \mu \frac{\mathcal{M}}{\mathcal{M}_\odot}\frac{r_\odot}{r}\,\text{K},$$

where $\mathcal{M}$ and $r$ are the total mass and radius of the star and $\mu$ the mean molecular weight of the gas. For a solar-like star $\mu \simeq 1$, so that $\bar{T} \simeq 5\times10^6$. The central temperature is higher than this and close to $10^7$.

where $m_p$ and $v_p$ are the mass and velocity of each particle and $n = N/\Omega$ is the number density of particles;

- the mean density of gravitational energy is:

$$\overline{E_g} = \frac{3G\mathcal{M}_s^2}{4\pi r_s^4} \simeq 2.72 \times 10^{15} \text{ erg cm}^3; \tag{A.6}$$

- the mean energy density of the photons is:

$$\overline{U_{\rm BB}(T)} = \frac{8\pi^5}{15h^3c^3}(kT)^4 \simeq 1.15 \times 10^{15} \text{ erg/cm}^3, \tag{A.7}$$

for a mean temperature of $10^7$ K.

Within the numerical approximation the three energies are of the same order. Strictly speaking, one should have $\overline{E_g} \simeq \overline{E_k} + \overline{U_{\rm BB}}$. Within the approximation our estimates fulfill this constraint. Analogous estimates can be made for other types of star with similar conclusions. In other words , there seems to be a relationship between the gravitational energy density and the sum of the electromagnetic and kinetic energy densities. Finally, using the virial condition we can also estimate the mean velocity of the particles in a star (the Sun, in this example), which is about $v_s \simeq 200$ km s$^{-1}$, depending on the exact value adopted for the temperature.

Given these premises, the luminosity of a star can be derived from

$$L_s = \left| \frac{dE_i}{dt} \right|, \tag{A.8}$$

where $E_i$ is the total internal energy (sum of the nuclear and gravo-thermal contributions). We may generalize the above relation by supposing that the luminosity can be expressed as:

$$L_s = \alpha_s E_V \equiv \alpha_s \mathcal{M}_s \overline{v_p}^2 \equiv \alpha_s \overline{U_{\rm BB}} \frac{4}{3}\pi r_s^3, \tag{A.9}$$

where $\alpha_s$ is a suitable proportionality factor with the dimension of an inverse of time. In other words we link the luminosity $L_s$ to the internal properties of the star, in particular to the mean velocity of the constituent heavy particles.

However, the same luminosity can be expressed by means of the surface Black Body with temperature equal to the effective temperature $T_{es}$ of the star (e.g., $5.78 \times 10^3$ K for the Sun and $3 \times 10^3$ for a RGB star).

$$L = \overline{U'_{\rm BB}} 4\pi c r_s^2, \tag{A.10}$$

where $U'_{\rm BB}$ is the energy of the black body at the surface temperature. This implies that the ratio of the external to the internal Black Body energies is $U'_{\rm BB} \simeq 10^{-13} U_{\rm BB}$. The size of the proportionality coefficient can be understood as due to the $T^4$ dependence of the Black Body energy density and the natural variation of the temperature from the surface to the inner regions of a star. The typical temperature gradient of a Sun-like star is $\|\Delta T/\Delta r\| \simeq 10^{-4}\,{\rm K\,cm^{-1}}$, where $\Delta T = T - T' \simeq T$ and $\|\Delta r\| = \|r - r'\| \simeq r'$ if $r$ and $T$ refer to a inner region (close to the center) and $r'$ and $T'$ to the surface. Therefore $T'/T \simeq 10^{-4}$.[2]

It follows from all this that $\alpha_s \simeq 10^{-14} c/r_s$. Inserting the value for the light velocity and the radius of a typical star (like the Sun) one obtains $\alpha_s \simeq 10^{-14}$ s$^{-1}$.

The factor $c/r_s$ secures that the energy density is translated to energy lost per unit time (a power). What we have done so far is a simple rephrasing of the classical expression for the luminosity. The reason for writing the star luminosity in this apparently curious way will become manifest as soon as we move to galaxies (i.e., to systems hosting billions of stars).

The whole discussion above has been checked against stars like the Sun, so that one expects that by changing type of stars the value of $\alpha_s$ should change. This is shown in Figure A.1. As expected, $\alpha_s$ spans a wide range, passing from dwarfs to massive stars, but this will not affect our final conclusions.

## A.2 The case of galaxies

We extend now the above consideration and formalism to the case of a galaxy with mass $\mathcal{M}_G$ and radius $r_G$, a large assembly of stars each of them shining with the luminosity $L_{s,i}$. In brief, the luminosity of the galaxy is the sum of the luminosity of all the stars inside it. The luminosity of each star can be expressed as proportional to the total kinetic energy of gas particles, therefore we may write:

[2]The values assumed for the central and surface temperature of the Sun amply justify a ratio $T'/T \simeq 0.0001$ or lower and a proportionality factor $10^{-13}$ in the relationship between the energy densities $U_{\rm BB}$ and $U'_{\rm BB}$.

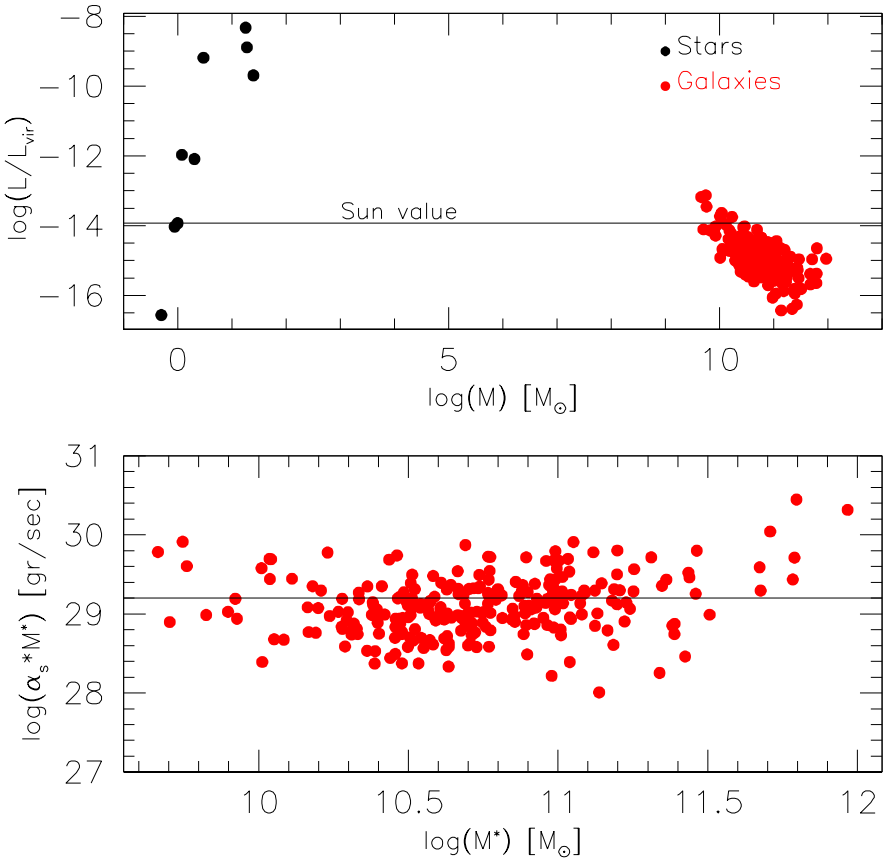


Figure A.1: Upper panel: $\alpha_s$ (in the case of stars) and $\alpha_G$ (in the case of galaxies) plot as a function of the virialized system mass. Note the large range of values spanned by $\alpha_s$ at varying the mass of the star from a dwarf to a massive object. Finally, note that the values $\alpha_G$ for the galaxies fall in a range typical of the low mass (old) stars. Lower panel: plot of $L_0 = \alpha_s \cdot \mathcal{M}_G$ (using the stellar mass, instead of the total galaxy mass) versus the galaxy masses. The solid line gives the observed value for $L_0$ in the FJ relation.

$$L_G = \sum_{i=1}^{N_s} \alpha_{s,i} \mathcal{M}_{s,i} v_{s,i}^2, \tag{A.11}$$

where $N_s$ is the total number of stars within the galaxy, and $\alpha_{s,i}$, $\mathcal{M}_{s,i}$ and $v_{s,i}$ are the basic quantities characterizing each star. In analogy with Equation A.1, the galaxy luminosity can be rewritten as:

$$L_G = \overline{\alpha_s} N_s \overline{\mathcal{M}_s v_s^2}, \tag{A.12}$$

where the quantities beneath $^-$ are weighted averages over the whole stellar population. Note that for galaxies of the same "size" (mass and radius) these values will be very similar.

Now, thanks to the homologous nature of the gravitational collapse at all scales, it is possible to note that the quantity $\overline{v_s}$ (i.e., the mean velocity of particles inside a star), turns out to be comparable to the velocity dispersion of stars within a galaxy, here named $\sigma_G$ (in km s$^{-1}$). It is then possible to write:

$$L = L_0 \sigma_G^2, \tag{A.13}$$

where:

$$L_0 = \overline{\alpha_s} N_s \overline{\mathcal{M}_s} \equiv \overline{\alpha_s} \mathcal{M}_G. \tag{A.14}$$

It can be shown that even for a galaxy there is a relationship between the total gravitational energy, the total kinetic energy of the stars, and the total radiative energy emitted by stars, so that the relation A.14 can be replaced by:

$$L_0 = \overline{\alpha_G} \mathcal{M}_G \equiv \frac{c}{r_G} \mathcal{M}_G, \tag{A.15}$$

where $\alpha_G$ refers to the galaxy as a whole. Like in the case of stars, $\overline{\alpha_G}$ has the dimension of an inverse of time.

To demonstrate the validity of Equation A.15 we consider a generic mean stellar content of $N_s \simeq 10^{12}$ (for sake of simplicity Sun-like) objects (i.e., with mass $\mathcal{M}_\odot = 2 \times 10^{33}$ g, radius $r_\odot = 6.94 \times 10^{10}$ cm, surface temperature $T_s \simeq 5780$ K), total mass $\mathcal{M}_G = 10^{12}\, \mathcal{M}_\odot$, total radius $r_G \simeq 100$ kpc. In this example we ignore the contribution to the mass given by Dark Matter (DM). According to the current understanding of the presence of DM in galaxies, the ratios of the dark-to-baryonic matter (BM) both in mass and radii of the spatial distributions (supposed to be spherical) $\mathcal{M}_{\rm DM} \simeq \beta \times \mathcal{M}_{\rm BM}$ and $r_{\rm DM} = \beta \times r_{\rm BM}$. This means that within the volume occupied by the BM

there is about $1/\beta^2 \times \mathcal{M}_{\rm DM}$ (Bertin et al. 1992; Saglia et al. 1992; Bertin et al. 2002). For the current estimates, $\beta \simeq 6$ DM in the internal regions of a galaxy where stars are located; therefore, it can be neglected.

The energy density of the photons emitted by all the stars in the galaxy evaluated at any arbitrary point inside the galaxy is given by:

$$U_{\rm BB,G} = \int_0^{r_G} U'_{\rm BB,s} \frac{N_s}{\Omega_G} \quad 4\pi r^2 dr \frac{r_s^2}{r^2}, \tag{A.16}$$

where $r_G$ is the galaxy radius, $U'_{\rm BB,s}$ refers to the Black Body at the temperature of the stellar sources[3], $\Omega_G$ is the volume of the whole galaxy, and the factor $U'_{\rm BB,s} \times N_s/\Omega_G$ the mean Black Body radiation inside the galaxy. Although the integrand of Equation A.16 is not strictly correct for evaluating the variation of the Black Body energy as a function of the galacto-centric distance, it is adequate to our purposes. The quantity $U'_{\rm BB,s}$ is given by:

$$U'_{\rm BB,s} = \frac{8\pi}{h^3c^3}\frac{\pi^4}{15}(kT)^4 \simeq 8.02 \text{ erg cm}^{-3} \tag{A.17}$$

so that for $U_{\rm BB,G}$ of Equation A.16 we estimate:

$$U_{\rm BB,G} \simeq 1.29 \times 10^{-12} \text{ erg cm}^{-3}, \tag{A.18}$$

where we assumed $N_s \simeq 10^{12}$ stars, $r_s \simeq 6.94 \times 10^{10}$ cm (roughly the solar radius), $\Omega_G \simeq 1.13 \times 10^{71}$ cm$^3$ for a galactic radius of about 100 kpc.

The mean density of kinetic energy of the stars turns out to be of the order of $3.52 \times 10^{-12}$ erg cm$^{-3}$ for a mean velocity dispersion of about 200 km s$^{-1}$.

The mean gravitational energy density for the galaxy (limited to the volume occupied by the BM) is:

$$E_{g,G} = G\frac{\mathcal{M}_G^2}{r_G^4}\frac{3}{4\pi} \simeq 7.79 \times 10^{-12} \text{ erg cm}^{-3}. \tag{A.19}$$

The gravitational energy is surely underestimated because we have neglected the presence of Dark Matter.

Therefore, also in this case there is an approximate relationship between the gravitational and the sum of electromagnetic and kinetic energy densities. We can then write the equation:

[3]In relation to this, we remind the reader that in most nearby galaxies the detected light is due to stars from the main sequence turnoff (or slightly fainter than that) to the tip of the RGB. In sufficiently old galaxies the corresponding mass range is rather small. In other words, the stellar population responsible for the observed light can be reduced to a single population of a certain age and mean chemical composition.

$$L_G = \alpha_G \mathcal{M}_G \sigma^2 = \alpha_G \overline{U_G} r_G^3. \tag{A.20}$$

Thanks to the assumption of uniform distribution of stars and stellar types most contributing to the light in our model galaxy, also the photon energy distribution inside is uniform and always equal to that of many Black Bodies of similar temperature. Furthermore, owing to the very large number of stars in a galaxy the light emitted by a certain region (e.g., within the effective radius) can be assimilated to that of Black Body at a certain mean temperature and very large surface. Therefore, we may write:

$$L_G = \overline{U_{\mathrm{BB},G}} 4\pi c r_G^2, \tag{A.21}$$

so that for solar-type stars $\alpha_G \simeq c/r_G \simeq 10^{-13}$ s$^{-1}$ $\simeq \alpha_s$. It is worth emphasizing here that $\alpha_G$ is nearly identical to $\alpha_s$ and for each galaxy there is a star with similar $\alpha$.

In conclusion, the classical Faber-Jackson relationship $L = L_0 \sigma^2$ can be understood as a sort of translation of the Stefan-Boltzmann law for BBs to the case of galaxies that can be viewed as the sum of many BBs.

Figure A.1 shows the range of values for the parameter $\alpha_G$ of galaxies and compares them with those for stars. Note that low-mass galaxies have in general higher $\alpha$ values (closer to the values for intermediate-mass stars), whereas the big galaxies are preferentially populated by low-mass stars. What matters here is the exsistence for every galaxy of a combination of $L_0$ ($\sim \alpha_s \mathcal{M}_G$) and $\sigma_G$ able to reproduce the total galaxy luminosity. The lower panel of Figure A.1 shows that $L_0 = \alpha_s \mathcal{M}_G$ is approximately constant for a wide range of galaxy masses.

We calculated $U_{\mathrm{BB},G}$ and $E_g$ for a small sample of nearby ETGs from (Moretti et al. 2014) for which all the basic data are available and estimated the $\alpha_G$ parameter for all of them. The results are shown in the two panels of Figure A.2.

One might argue whether this is true also for spiral galaxies. We believe that the origin of the Tully-Fisher relation for late-type systems can be likely reported to the same context. Here the mean characteristic velocity of the stellar system is no longer the velocity dispersion, but the circular rotation. For more complex systems, where rotation and velocity dispersion are significant, a combination of the two is required to characterize the total kinetic energy. This issue, however, is left to a future investigation.

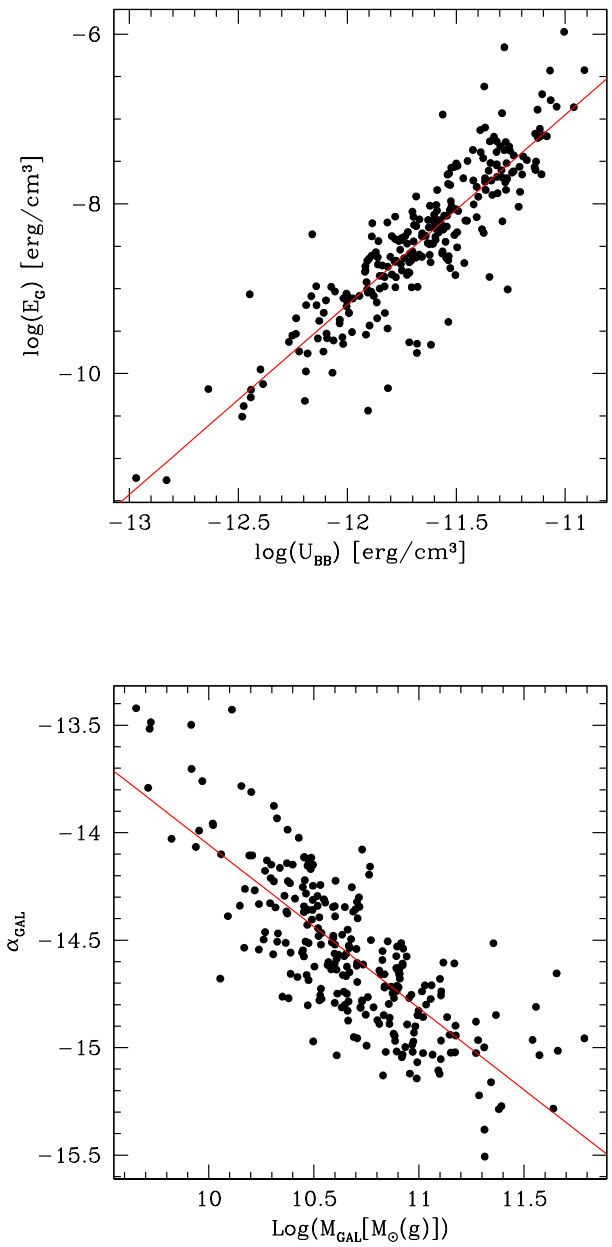


Figure A.2: Upper panel: the mean gravitational energy density as a function of the mean Black Body energy for a sample of ETGs. Bottom panel: the quantity $\alpha_G$ as a function of the stellar mass of the galaxy in solar units for the object of the same sample.

# Bibliography


Abdelsalam, H. M., Saha, P., and Williams, L. L. R. (1998). Nonparametric Reconstruction of Abell 2218 from Combined Weak and Strong Lensing. *AJ*, 116:1541–1552.

Abell, G. O. (1958). The Distribution of Rich Clusters of Galaxies. *ApJS*, 3:211.

Adami, C., Mazure, A., Katgert, P., and Biviano, A. (1998). The ESO nearby Abell cluster survey. VII. Galaxy density profiles of rich clusters of galaxies. *A&A*, 336:63–82.

Agulli, I., Aguerri, J. A. L., Diaferio, A., Dominguez Palmero, L., and Sánchez-Janssen, R. (2017). Deep spectroscopy of nearby galaxy clusters - II. The Hercules cluster. *MNRAS*, 467:4410–4423.

Agulli, I., Aguerri, J. A. L., Sánchez-Janssen, R., Dalla Vecchia, C., Diaferio, A., Barrena, R., Dominguez Palmero, L., and Yu, H. (2016). Deep spectroscopy of nearby galaxy clusters - I. Spectroscopic luminosity function of Abell 85. *MNRAS*, 458:1590–1603.

Akaike, H. (1973). Information theory and an extension of the maximum likelihood principle. In Petrov, B. N. and Ksáki, F., editors, *2nd International Symposium on Information Theory, Tsahkadsor, Armenia, USSR, September 2-8, 1971*, pages 267–281. The organization, Budapest: Akadémiai Kiadó.

Allen, S. W., Evrard, A. E., and Mantz, A. B. (2011). Cosmological Parameters from Observations of Galaxy Clusters. *ARA&A*, 49:409–470.

Allen, S. W., Schmidt, R. W., Fabian, A. C., and Ebeling, H. (2003). Cosmological constraints from the local X-ray luminosity function of the most X-ray-luminous galaxy clusters. *MNRAS*, 342:287–298.

Anderson, M. E., Bregman, J. N., Butler, S. C., and Mullis, C. R. (2009). Redshift Evolution in the Iron Abundance of the Intracluster Medium. *ApJ*, 698:317–323.

Andredakis, Y. C., Peletier, R. F., and Balcells, M. (1995). The Shape of the Luminosity Profiles of Bulges of Spiral Galaxies. *MNRAS*, 275:874.

Andreon, S. (2002). K-band luminosity (mass) segregation in AC 118 at z = 0.31. *A&A*, 382:821–828.

Andreon, S. (2015). Relative distribution of dark matter and stellar mass in three massive galaxy clusters. *A&A*, 575:A108.

Bahcall, N. A. and Fan, X. (1998). The Most Massive Distant Clusters: Determining $\Omega$ and $\sigma_8$. *ApJ*, 504:1–6.

Bahcall, N. A. and Soneira, R. M. (1983). The spatial correlation function of rich clusters of galaxies. *ApJ*, 270:20–38.

Baldry, I. K., Balogh, M. L., Bower, R. G., Glazebrook, K., Nichol, R. C., Bamford, S. P., and Budavari, T. (2006). Galaxy bimodality versus stellar mass and environment. *MNRAS*, 373:469–483.

Baldry, I. K., Glazebrook, K., Brinkmann, J., Ivezić, Ž., Lupton, R. H., Nichol, R. C., and Szalay, A. S. (2004). Quantifying the Bimodal Color-Magnitude Distribution of Galaxies. *ApJ*, 600:681–694.

Bamford, S. P., Nichol, R. C., Baldry, I. K., Land, K., Lintott, C. J., Schawinski, K., Slosar, A., Szalay, A. S., Thomas, D., Torki, M., Andreescu, D., Edmondson, E. M., Miller, C. J., Murray, P., Raddick, M. J., and Vandenberg, J. (2009). Galaxy Zoo: the dependence of morphology and colour on environment*. *MNRAS*, 393:1324–1352.

Bartelmann, M. and Steinmetz, M. (1996). A Comparison of X-ray and Strong Lensing Properties of Simulated X-ray Clusters. *MNRAS*, 283:431–446.

Baum, W. A. (1959). The Hertzsprung-Russell diagrams of old stellar Populations. In Greenstein, J. L., editor, *The Hertzsprung-Russell Diagram*, volume 10 of *IAU Symposium*, page 23.

Bender, R., Burstein, D., and Faber, S. M. (1992). Dynamically hot galaxies. I - Structural properties. *ApJ*, 399:462–477.

Bernardi, M., Sheth, R. K., Annis, J., Burles, S., Eisenstein, D. J., Finkbeiner, D. P., Hogg, D. W., Lupton, R. H., Schlegel, D. J., SubbaRao, M., Bahcall, N. A., Blakeslee, J. P., Brinkmann, J., Castander, F. J., Connolly, A. J., Csabai, I., Doi, M., Fukugita, M., Frieman, J., Heckman, T., Hennessy, G. S., Ivezić, Ž., Knapp, G. R., Lamb, D. Q., McKay, T., Munn, J. A., Nichol, R., Okamura, S., Schneider, D. P., Thakar, A. R., and York, D. G. (2003). Early-Type Galaxies in the Sloan Digital Sky Survey. III. The Fundamental Plane. *AJ*, 125:1866–1881.

Berta, S., Rubele, S., Franceschini, A., Held, E. V., Rizzi, L., Lonsdale, C. J., Jarrett, T. H., Rodighiero, G., Oliver, S. J., Dias, J. E., Buttery, H. J., Fiore, F., La Franca, F., Puccetti, S., Fang, F., Shupe, D., Surace, J., and Gruppioni, C. (2006). The ESO-Spitzer Imaging extragalactic Survey (ESIS). I. WFIB, V, R deep observations of ELAIS-S1 and comparison to Spitzer and GALEX data. *A&A*, 451:881–900.

Bertin, E. and Arnouts, S. (1996). SExtractor: Software for source extraction. *A&AS*, 117:393–404.

Bertin, G., Ciotti, L., and Del Principe, M. (2002). Weak homology of elliptical galaxies. *A&A*, 386:149–168.

Bertin, G., Saglia, R. P., and Stiavelli, M. (1992). Elliptical galaxies with dark matter. I - Self-consistent models. II - Optimal luminous-dark matter decomposition for a sample of bright objects. *ApJ*, 384:423–447.

Bettoni, D., Kjærgaard, P., Milvang-Jensen, B., D'Onofrio, M., Moretti, A., Poggianti, B. M., Fasano, G., and Moles, M. (2011). Studying the diverse nature of faint galaxies in nearby clusters of the WINGS sample. *Astronomische Nachrichten*, 332:299.

Biviano, A. and Girardi, M. (2003). The Mass Profile of Galaxy Clusters out to ˜$2r_{200}$. *ApJ*, 585:205–214.

Biviano, A., Moretti, A., Paccagnella, A., Poggianti, B. M., Bettoni, D., Gullieuszik, M., Vulcani, B., Fasano, G., D'Onofrio, M., Fritz, J., and Cava, A. (2017). The concentration-mass relation of clusters of galaxies from the OmegaWINGS survey. *ArXiv e-prints*.

Bolton, A. S., Treu, T., Koopmans, L. V. E., Gavazzi, R., Moustakas, L. A., Burles, S., Schlegel, D. J., and Wayth, R. (2008). The Sloan Lens ACS Survey. VII. Elliptical Galaxy Scaling Laws from Direct Observational Mass Measurements. *ApJ*, 684:248–259.

Borgani, S., Rosati, P., Tozzi, P., Stanford, S. A., Eisenhardt, P. R., Lidman, C., Holden, B., Della Ceca, R., Norman, C., and Squires, G. (2001). Measuring $\Omega_m$ with the ROSAT Deep Cluster Survey. *ApJ*, 561:13–21.

Borriello, A., Salucci, P., and Danese, L. (2003). The fundamental plane of ellipticals - I. The dark matter connection. *MNRAS*, 341:1109–1120.

Brinchmann, J., Charlot, S., White, S. D. M., Tremonti, C., Kauffmann, G., Heckman, T., and Brinkmann, J. (2004). The physical properties of star-forming galaxies in the low-redshift Universe. *MNRAS*, 351:1151–1179.

Burkert, A. (1993). Do elliptical galaxies have $r^{1/4}$ brightness profiles? *A&A*, 278:23–28.

Burnham, K. P. and Anderson, D. R. (2002). *Model Selection and Multimodel Inference*. Springer-Verlag, 2 edition.

Burstein, D., Bender, R., Faber, S., and Nolthenius, R. (1997). Global Relationships Among the Physical Properties of Stellar Systems. *AJ*, 114:1365.

Busarello, G., Capaccioli, M., Longo, G., and Puddu, E. (1997). Dynamical Non-Homology and the Tilt of the Fundamental Plane. In Arnaboldi, M., Da Costa, G. S., and Saha, P., editors, *The Nature of Elliptical Galaxies; 2nd Stromlo Symposium*, volume 116 of *Astronomical Society of the Pacific Conference Series*, page 184.

Caon, N., Capaccioli, M., and D'Onofrio, M. (1993). On the Shape of the Light Profiles of Early Type Galaxies. *MNRAS*, 265:1013.

Capaccioli, M. (1987). Distribution of light - Outer regions. In de Zeeuw, P. T., editor, *Structure and Dynamics of Elliptical Galaxies*, volume 127 of *IAU Symposium*, pages 47–60.

Capaccioli, M. (1989). The World of Galaxies. Berlin: Springer-Verlag.

Capaccioli, M., Caon, N., and D'Onofrio, M. (1992). Families of galaxies in the mu(e)-R(e) plane. *MNRAS*, 259:323–327.

Capelato, H. V., de Carvalho, R. R., and Carlberg, R. G. (1995). Mergers of Dissipationless Systems: Clues about the Fundamental Plane. *ApJ*, 451:525.

Cappellari, M. (2008). Measuring the inclination and mass-to-light ratio of axisymmetric galaxies via anisotropic Jeans models of stellar kinematics. *MNRAS*, 390:71–86.

Cappellari, M., Bacon, R., Bureau, M., Damen, M. C., Davies, R. L., de Zeeuw, P. T., Emsellem, E., Falcón-Barroso, J., Krajnović, D., Kuntschner, H., McDermid, R. M., Peletier, R. F., Sarzi, M., van den Bosch, R. C. E., and van de Ven, G. (2006). The SAURON project - IV. The mass-to-light ratio, the virial mass estimator and the Fundamental Plane of elliptical and lenticular galaxies. *MNRAS*, 366:1126–1150.

Cappellari, M., McDermid, R. M., Alatalo, K., Blitz, L., Bois, M., Bournaud, F., Bureau, M., Crocker, A. F., Davies, R. L., Davis, T. A., de Zeeuw, P. T., Duc, P.-A., Emsellem, E., Khochfar, S., Krajnović, D., Kuntschner, H., Morganti, R., Naab, T., Oosterloo, T., Sarzi, M., Scott, N., Serra, P., Weijmans, A.-M., and Young, L. M. (2013). The ATLAS$^{3D}$ project - XX. Mass-size and mass-$\sigma$ distributions of early-type galaxies: bulge fraction drives kinematics, mass-to-light ratio, molecular gas fraction and stellar initial mass function. *MNRAS*, 432:1862–1893.

Carlberg, R. G., Yee, H. K. C., Ellingson, E., Abraham, R., Gravel, P., Morris, S., and Pritchet, C. J. (1996). Galaxy Cluster Virial Masses and Omega. *ApJ*, 462:32.

Cava, A., Bettoni, D., Poggianti, B. M., Couch, W. J., Moles, M., Varela, J., Biviano, A., D'Onofrio, M., Dressler, A., Fasano, G., Fritz, J., Kjærgaard, P., Ramella, M., and Valentinuzzi, T. (2009). WINGS-SPE Spectroscopy in the WIde-field Nearby Galaxy-cluster Survey. *A&A*, 495:707–719.

Cavaliere, A. and Fusco-Femiano, R. (1976). X-rays from hot plasma in clusters of galaxies. *A&A*, 49:137–144.

Cenarro, A. J., Cardiel, N., Gorgas, J., Peletier, R. F., Vazdekis, A., and Prada, F. (2001). Empirical calibration of the near-infrared Ca ii triplet - I. The stellar library and index definition. *MNRAS*, 326:959–980.

Chiosi, C., Bressan, A., Portinari, L., and Tantalo, R. (1998). A new scenario of galaxy evolution under a universal Initial Mass Function. *A&A*, 339:355–381.

Ciotti, L., D'Ercole, A., Pellegrini, S., and Renzini, A. (1991). Winds, outflows, and inflows in X-ray elliptical galaxies. *ApJ*, 376:380–403.

Ciotti, L., Lanzoni, B., and Renzini, A. (1996). The tilt of the fundamental plane of elliptical galaxies - I. Exploring dynamical and structural effects. *MNRAS*, 282:1–12.

Cole, S. and Lacey, C. (1996). The structure of dark matter haloes in hierarchical clustering models. *MNRAS*, 281:716.

Dantas, C. C., Ribeiro, A. L. B., Capelato, H. V., and de Carvalho, R. R. (2000). The Two-Component Virial Theorem and the Physical Properties of Stellar Systems. *ApJ*, 528:L5–L8.

de Carvalho, R. R. and da Costa, L. N. (1988). Surface photometry of southern elliptical galaxies. *ApJS*, 68:173–227.

De Lucia, G. and Blaizot, J. (2007). The hierarchical formation of the brightest cluster galaxies. *MNRAS*, 375:2–14.

de Vaucouleurs, G. (1948). Recherches sur les Nebuleuses Extragalactiques. *Annales d'Astrophysique*, 11:247.

Dekel, A. and Cox, T. J. (2006). The dissipative merger progenitors of elliptical galaxies. *MNRAS*, 370:1445–1453.

Desmond, H. and Wechsler, R. H. (2017). The Faber-Jackson relation and Fundamental Plane from halo abundance matching. *MNRAS*, 465:820–833.

Djorgovski, S. and Davis, M. (1987). Fundamental properties of elliptical galaxies. *ApJ*, 313:59–68.

Donahue, M., Voit, G. M., Gioia, I., Luppino, G., Hughes, J. P., and Stocke, J. T. (1998). A Very Hot High-Redshift Cluster of Galaxies: More Trouble for $\Omega_0 = 1$. *ApJ*, 502:550–557.

D'Onofrio, M., Bindoni, D., Fasano, G., Bettoni, D., Cava, A., Fritz, J., Gullieuszik, M., Kjærgaard, P., Moretti, A., Moles, M., Omizzolo, A., Poggianti, B. M., Valentinuzzi, T., and Varela, J. (2014). Surface photometry of WINGS galaxies with GASPHOT. *A&A*, 572:A87.

D'Onofrio, M., Capaccioli, M., and Caon, N. (1994). On the Shape of the Light Profiles of Early Type Galaxies - Part Two - the - Diagram. *MNRAS*, 271:523.

D'Onofrio, M., Cariddi, S., Chiosi, C., Chiosi, E., and Marziani, P. (2017). On the Origin of the Fundamental Plane and Faber-Jackson Relations: Implications for the Star Formation Problem. *ApJ*, 838:163.

D'Onofrio, M., Fasano, G., Moretti, A., Marziani, P., Bindoni, D., Fritz, J., Varela, J., Bettoni, D., Cava, A., Poggianti, B., Gullieuszik, M., Kjærgaard, P., Moles, M., Vulcani, B., Omizzolo, A., Couch, W. J., and

Dressler, A. (2013). The hybrid solution for the Fundamental Plane. *MNRAS*, 435:45–63.

D'Onofrio, M., Fasano, G., Varela, J., Bettoni, D., Moles, M., Kjærgaard, P., Pignatelli, E., Poggianti, B., Dressler, A., Cava, A., Fritz, J., Couch, W. J., and Omizzolo, A. (2008). The Fundamental Plane of Early-Type Galaxies in Nearby Clusters from the WINGS Database. *ApJ*, 685:875–896.

D'Onofrio, M., Valentinuzzi, T., Fasano, G., Moretti, A., Bettoni, D., Poggianti, B., Vulcani, B., Varela, J., Fritz, J., Cava, A., Kjærgaard, P., Moles, M., Couch, W. J., and Dressler, A. (2011). On the Connection Between Shape and Stellar Population in Early-type Galaxies. *ApJ*, 727:L6.

Dressler, A. (1978). A comprehensive study of 12 very rich clusters of galaxies. I - Photometric technique and analysis of the luminosity function. *ApJ*, 223:765–775.

Dressler, A. (1980). Galaxy morphology in rich clusters - Implications for the formation and evolution of galaxies. *ApJ*, 236:351–365.

Dressler, A., Lynden-Bell, D., Burstein, D., Davies, R. L., Faber, S. M., Terlevich, R., and Wegner, G. (1987). Spectroscopy and photometry of elliptical galaxies. I - A new distance estimator. *ApJ*, 313:42–58.

Driver, S. P., Allen, P. D., Graham, A. W., Cameron, E., Liske, J., Ellis, S. C., Cross, N. J. G., De Propris, R., Phillipps, S., and Couch, W. J. (2006). The Millennium Galaxy Catalogue: morphological classification and bimodality in the colour-concentration plane. *MNRAS*, 368:414–434.

Durret, F., Adami, C., and Lobo, C. (2002). Environmental effects on the galaxy luminosity function in the cluster of galaxies Abell 496. *A&A*, 393:439–444.

Ebeling, H., Edge, A. C., Allen, S. W., Crawford, C. S., Fabian, A. C., and Huchra, J. P. (2000). The ROSAT Brightest Cluster Sample - IV. The extended sample. *MNRAS*, 318:333–340.

Ebeling, H., Edge, A. C., Bohringer, H., Allen, S. W., Crawford, C. S., Fabian, A. C., Voges, W., and Huchra, J. P. (1998). The ROSAT Brightest Cluster Sample - I. The compilation of the sample and the cluster log N-log S distribution. *MNRAS*, 301:881–914.

Ebeling, H., Edge, A. C., and Henry, J. P. (2001). MACS: A Quest for the Most Massive Galaxy Clusters in the Universe. *ApJ*, 553:668–676.

Ebeling, H., Voges, W., Bohringer, H., Edge, A. C., Huchra, J. P., and Briel, U. G. (1996). Erratum: Properties of the X-ray-brightest Abell-type clusters of galaxies (XBACs) from ROSAT All-SKy Survey data - I. The sample. *MNRAS*, 283:1103.

Einasto, J. (1965). On the Construction of a Composite Model for the Galaxy and on the Determination of the System of Galactic Parameters. *Trudy Astrofizicheskogo Instituta Alma-Ata*, 5:87–100.

Ettori, S. (2000). $\beta$-model and cooling flows in X-ray clusters of galaxies. *MNRAS*, 318:1041–1046.

Ettori, S., Donnarumma, A., Pointecouteau, E., Reiprich, T. H., Giodini, S., Lovisari, L., and Schmidt, R. W. (2013). Mass Profiles of Galaxy Clusters from X-ray Analysis. *Space Sci. Rev.*, 177:119–154.

Faber, S. M., Dressler, A., Davies, R. L., Burstein, D., and Lynden-Bell, D. (1987). Global scaling relations for elliptical galaxies and implications for formation. In Faber, S. M., editor, *Nearly Normal Galaxies. From the Planck Time to the Present*, pages 175–183.

Faber, S. M. and Jackson, R. E. (1976). Velocity dispersions and mass-to-light ratios for elliptical galaxies. *ApJ*, 204:668–683.

Fabricant, D., Beers, T. C., Geller, M. J., Gorenstein, P., Huchra, J. P., and Kurtz, M. J. (1986). An X-ray and optical study of the cluster of galaxies Abell 754. *ApJ*, 308:530–539.

Fasano, G., Bettoni, D., Ascaso, B., Tormen, G., Poggianti, B. M., Valentinuzzi, T., D'Onofrio, M., Fritz, J., Moretti, A., Omizzolo, A., Cava, A., Moles, M., Dressler, A., Couch, W. J., Kjærgaard, P., and Varela, J. (2010). The shapes of BCGs and normal ellipticals in nearby clusters. *MNRAS*, 404:1490–1504.

Fasano, G., Marmo, C., Varela, J., D'Onofrio, M., Poggianti, B. M., Moles, M., Pignatelli, E., Bettoni, D., Kjærgaard, P., Rizzi, L., Couch, W. J., and Dressler, A. (2006). WINGS: a WIde-field Nearby Galaxy-cluster Survey. I. Optical imaging. *A&A*, 445:805–817.

Fasano, G., Poggianti, B. M., Bettoni, D., D'Onofrio, M., Dressler, A., Vulcani, B., Moretti, A., Gullieuszik, M., Fritz, J., Omizzolo, A., Cava, A., Couch, W. J., Ramella, M., and Biviano, A. (2015). Morphological fractions of galaxies in WINGS clusters: revisiting the morphology-density paradigm. *MNRAS*, 449:3927–3944.

Fasano, G., Vanzella, E., Dressler, A., Poggianti, B. M., Moles, M., Bettoni, D., Valentinuzzi, T., Moretti, A., D'Onofrio, M., Varela, J., Couch, W. J., Kjærgaard, P., Fritz, J., Omizzolo, A., and Cava, A. (2012). Morphology of galaxies in the WINGS clusters. *MNRAS*, 420:926–948.

Feigelson, E. D. and Babu, G. J. (1992). Linear regression in astronomy. II. *ApJ*, 397:55–67.

Forbes, D. A., Ponman, T. J., and Brown, R. J. N. (1998). Dependence of the Fundamental Plane Scatter on Galaxy Age. *ApJ*, 508:L43–L46.

Freeman, K. C. (1970). On the Disks of Spiral and S0 Galaxies. *ApJ*, 160:811.

Fritz, J., Poggianti, B. M., Bettoni, D., Cava, A., Couch, W. J., D'Onofrio, M., Dressler, A., Fasano, G., Kjærgaard, P., Moles, M., and Varela, J. (2007). A spectrophotometric model applied to cluster galaxies: the WINGS dataset. *A&A*, 470:137–152.

Fritz, J., Poggianti, B. M., Cava, A., Moretti, A., and WINGS Collaboration (2011). Equivalent Width Measurements in Optical Spectra of Galaxies in Local Clusters: Hints on the Star Formation History in Clusters. *Baltic Astronomy*, 20:435–441.

Gargiulo, A., Haines, C. P., Merluzzi, P., Smith, R. J., La Barbera, F., Busarello, G., Lucey, J. R., Mercurio, A., and Capaccioli, M. (2009). On the origin of the scatter around the Fundamental Plane: correlations with stellar population parameters. *MNRAS*, 397:75–89.

Gerhard, O., Kronawitter, A., Saglia, R. P., and Bender, R. (2001). Dynamical Family Properties and Dark Halo Scaling Relations of Giant Elliptical Galaxies. *AJ*, 121:1936–1951.

Girardi, M., Borgani, S., Giuricin, G., Mardirossian, F., and Mezzetti, M. (2000). Optical Luminosities and Mass-to-Light Ratios of Nearby Galaxy Clusters. *ApJ*, 530:62–79.

Gómez, P. L., Nichol, R. C., Miller, C. J., Balogh, M. L., Goto, T., Zabludoff, A. I., Romer, A. K., Bernardi, M., Sheth, R., Hopkins, A. M., Castander, F. J., Connolly, A. J., Schneider, D. P., Brinkmann, J., Lamb, D. Q., SubbaRao, M., and York, D. G. (2003). Galaxy Star Formation as a Function of Environment in the Early Data Release of the Sloan Digital Sky Survey. *ApJ*, 584:210–227.

Gonzalez, A. H., Sivanandam, S., Zabludoff, A. I., and Zaritsky, D. (2013). Galaxy Cluster Baryon Fractions Revisited. *ApJ*, 778:14.

Graham, A. and Colless, M. (1997). Some effects of galaxy structure and dynamics on the Fundamental Plane. *MNRAS*, 287:221–239.

Graham, A. W., Merritt, D., Moore, B., Diemand, J., and Terzić, B. (2006). Empirical Models for Dark Matter Halos. II. Inner Profile Slopes, Dynamical Profiles, and $\rho/\sigma^3$. *AJ*, 132:2701–2710.

Graves, G. J., Faber, S. M., and Schiavon, R. P. (2009). Dissecting the Red Sequence. II. Star Formation Histories of Early-Type Galaxies Throughout the Fundamental Plane. *ApJ*, 698:1590–1608.

Grillo, C., Suyu, S. H., Rosati, P., Mercurio, A., Balestra, I., Munari, E., Nonino, M., Caminha, G. B., Lombardi, M., De Lucia, G., Borgani, S., Gobat, R., Biviano, A., Girardi, M., Umetsu, K., Coe, D., Koekemoer, A. M., Postman, M., Zitrin, A., Halkola, A., Broadhurst, T., Sartoris, B., Presotto, V., Annunziatella, M., Maier, C., Fritz, A., Vanzella, E., and Frye, B. (2015). CLASH-VLT: Insights on the Mass Substructures in the Frontier Fields Cluster MACS J0416.1-2403 through Accurate Strong Lens Modeling. *ApJ*, 800:38.

Gullieuszik, M., Poggianti, B., Fasano, G., Zaggia, S., Paccagnella, A., Moretti, A., Bettoni, D., D'Onofrio, M., Couch, W. J., Vulcani, B., Fritz, J., Omizzolo, A., Baruffolo, A., Schipani, P., Capaccioli, M., and Varela, J. (2015). OmegaWINGS: OmegaCAM-VST observations of WINGS galaxy clusters. *A&A*, 581:A41.

Hamabe, M. and Kormendy, J. (1987). Correlations Between R/1/4 - Law Parameters for Bulges and Elliptical Galaxies. In de Zeeuw, P. T., editor, *Structure and Dynamics of Elliptical Galaxies*, volume 127 of *IAU Symposium*, page 379.

Henning, J. W., Gantner, B., Burns, J. O., and Hallman, E. J. (2009). On the Origin of Cool Core Galaxy Clusters: Comparing X-ray Observations with Numerical Simulations. *ApJ*, 697:1597–1620.

Hjorth, J. and Madsen, J. (1995). Small deviations from the $R^{1/4}$ law, the fundamental plane, and phase densities of elliptical galaxies. *ApJ*, 445:55–61.

Hoekstra, H., Bartelmann, M., Dahle, H., Israel, H., Limousin, M., and Meneghetti, M. (2013). Masses of Galaxy Clusters from Gravitational Lensing. *Space Sci. Rev.*, 177:75–118.

Hoessel, J. G., Gunn, J. E., and Thuan, T. X. (1980). The photometric properties of brightest cluster galaxies. I - Absolute magnitudes in 116 nearby Abell clusters. *ApJ*, 241:486–492.

Hopkins, P. F., Cox, T. J., and Hernquist, L. (2008). Dissipation and the Fundamental Plane: Observational Tests. *ApJ*, 689:17–48.

Hyde, J. B. and Bernardi, M. (2009). The luminosity and stellar mass Fundamental Plane of early-type galaxies. *MNRAS*, 396:1171–1185.

Ishimaru, Y. and Arimoto, N. (1997). Roles of SN IA and SN II in ICM Enrichment. *PASJ*, 49:1–8.

Jones, C. and Forman, W. (1984). The structure of clusters of galaxies observed with Einstein. *ApJ*, 276:38–55.

Jones, C., Stern, C., Forman, W., David, L., Tucker, W., Tananbaum, H., Breen, J., Franx, M., and Fabian, A. (1992). ROSAT X-Ray Observations of Galaxies in the Fornax Cluster. In *American Astronomical Society Meeting Abstracts #180*, volume 24 of *Bulletin of the American Astronomical Society*, page 810.

Kass, R. E. and Raftery, A. E. (1995). Bayes Factors. *Annals of Statistics*, 90:773–795.

Kauffmann, G., Heckman, T. M., Tremonti, C., Brinchmann, J., Charlot, S., White, S. D. M., Ridgway, S. E., Brinkmann, J., Fukugita, M., Hall, P. B., Ivezić, Ž., Richards, G. T., and Schneider, D. P. (2003). The host galaxies of active galactic nuclei. *MNRAS*, 346:1055–1077.

King, I. (1962). The structure of star clusters. I. an empirical density law. *AJ*, 67:471.

Kneib, J.-P., Hudelot, P., Ellis, R. S., Treu, T., Smith, G. P., Marshall, P., Czoske, O., Smail, I., and Natarajan, P. (2003). A Wide-Field Hubble Space Telescope Study of the Cluster Cl 0024+1654 at z=0.4. II. The Cluster Mass Distribution. *ApJ*, 598:804–817.

Kormendy, J. (1977). Brightness distributions in compact and normal galaxies. II - Structure parameters of the spheroidal component. *ApJ*, 218:333–346.

La Barbera, F., De Carvalho, R. R., De La Rosa, I. G., Gal, R. R., Swindle, R., and Lopes, P. A. A. (2010). Spider. IV. Optical and Near-infrared Color Gradients in Early-type Galaxies: New Insight into Correlations with Galaxy Properties. *AJ*, 140:1528–1556.

La Barbera, F., Ferreras, I., Vazdekis, A., de la Rosa, I. G., de Carvalho, R. R., Trevisan, M., Falcón-Barroso, J., and Ricciardelli, E. (2013). SPIDER VIII - constraints on the stellar initial mass function of early-type galaxies from a variety of spectral features. *MNRAS*, 433:3017–3047.

La Barbera, F., Pasquali, A., Ferreras, I., Gallazzi, A., de Carvalho, R. R., and de la Rosa, I. G. (2014). SPIDER - X. Environmental effects in central and satellite early-type galaxies through the stellar fossil record. *MNRAS*, 445:1977–1996.

Lewis, I., Balogh, M., De Propris, R., Couch, W., Bower, R., Offer, A., Bland-Hawthorn, J., Baldry, I. K., Baugh, C., Bridges, T., Cannon, R., Cole, S., Colless, M., Collins, C., Cross, N., Dalton, G., Driver, S. P., Efstathiou, G., Ellis, R. S., Frenk, C. S., Glazebrook, K., Hawkins, E., Jackson, C., Lahav, O., Lumsden, S., Maddox, S., Madgwick, D., Norberg, P., Peacock, J. A., Percival, W., Peterson, B. A., Sutherland, W., and Taylor, K. (2002). The 2dF Galaxy Redshift Survey: the environmental dependence of galaxy star formation rates near clusters. *MNRAS*, 334:673–683.

Lubin, L. M. and Bahcall, N. A. (1993). The relation between velocity dispersion and temperature in clusters - Limiting the velocity bias. *ApJ*, 415:L17–L20.

MacArthur, L. A., Courteau, S., and Holtzman, J. A. (2003). Structure of Disk-dominated Galaxies. I. Bulge/Disk Parameters, Simulations, and Secular Evolution. *ApJ*, 582:689–722.

Macciò, A. V., Dutton, A. A., van den Bosch, F. C., Moore, B., Potter, D., and Stadel, J. (2007). Concentration, spin and shape of dark matter haloes: scatter and the dependence on mass and environment. *MNRAS*, 378:55–71.

Magoulas, C., Springob, C. M., Colless, M., Jones, D. H., Campbell, L. A., Lucey, J. R., Mould, J., Jarrett, T., Merson, A., and Brough, S. (2012). The 6dF Galaxy Survey: the near-infrared Fundamental Plane of early-type galaxies. *MNRAS*, 427:245–273.

Marmo, C., Fasano, G., Pignatelli, E., Poggianti, B., Bettoni, D., Halliday, C., Varela, J., Moles, M., Kjærgaard, P., Couch, W., and Dressler, A.

(2004). Scaling relations for galaxy clusters. In Diaferio, A., editor, *IAU Colloq. 195: Outskirts of Galaxy Clusters: Intense Life in the Suburbs*, pages 242–244.

Maughan, B. J., Giles, P. A., Rines, K. J., Diaferio, A., Geller, M. J., Van Der Pyl, N., and Bonamente, M. (2016). Hydrostatic and caustic mass profiles of galaxy clusters. *MNRAS*, 461:4182–4191.

Medezinski, E., Umetsu, K., Nonino, M., Merten, J., Zitrin, A., Broadhurst, T., Donahue, M., Sayers, J., Waizmann, J.-C., Koekemoer, A., Coe, D., Molino, A., Melchior, P., Mroczkowski, T., Czakon, N., Postman, M., Meneghetti, M., Lemze, D., Ford, H., Grillo, C., Kelson, D., Bradley, L., Moustakas, J., Bartelmann, M., Benítez, N., Biviano, A., Bouwens, R., Golwala, S., Graves, G., Infante, L., Jiménez-Teja, Y., Jouvel, S., Lahav, O., Moustakas, L., Ogaz, S., Rosati, P., Seitz, S., and Zheng, W. (2013). CLASH: Complete Lensing Analysis of the Largest Cosmic Lens MACS J0717.5+3745 and Surrounding Structures. *ApJ*, 777:43.

Mei, S., Holden, B. P., Blakeslee, J. P., Rosati, P., Postman, M., Jee, M. J., Rettura, A., Sirianni, M., Demarco, R., Ford, H. C., Franx, M., Homeier, N., and Illingworth, G. D. (2006). Evolution of the Color-Magnitude Relation in High-Redshift Clusters: Early-Type Galaxies in the Lynx Supercluster at z ˜ 1.26. *ApJ*, 644:759–768.

Merritt, D., Graham, A. W., Moore, B., Diemand, J., and Terzić, B. (2006). Empirical Models for Dark Matter Halos. I. Nonparametric Construction of Density Profiles and Comparison with Parametric Models. *AJ*, 132:2685–2700.

Merten, J., Meneghetti, M., Postman, M., Umetsu, K., Zitrin, A., Medezinski, E., Nonino, M., Koekemoer, A., Melchior, P., Gruen, D., Moustakas, L. A., Bartelmann, M., Host, O., Donahue, M., Coe, D., Molino, A., Jouvel, S., Monna, A., Seitz, S., Czakon, N., Lemze, D., Sayers, J., Balestra, I., Rosati, P., Benítez, N., Biviano, A., Bouwens, R., Bradley, L., Broadhurst, T., Carrasco, M., Ford, H., Grillo, C., Infante, L., Kelson, D., Lahav, O., Massey, R., Moustakas, J., Rasia, E., Rhodes, J., Vega, J., and Zheng, W. (2015). CLASH: The Concentration-Mass Relation of Galaxy Clusters. *ApJ*, 806:4.

Michard, R. (1985). Detailed surface photometry of 36 E-SO galaxies. *A&AS*, 59:205–228.

Mohr, J. J., Mathiesen, B., and Evrard, A. E. (1999). Properties of the Intracluster Medium in an Ensemble of Nearby Galaxy Clusters. *ApJ*, 517:627–649.

Moretti, A., Bettoni, D., Poggianti, B. M., Fasano, G., Varela, J., D'Onofrio, M., Vulcani, B., Cava, A., Fritz, J., Couch, W. J., Moles, M., and Kjærgaard, P. (2015). Galaxy luminosity functions in WINGS clusters. *A&A*, 581:A11.

Moretti, A., Gullieuszik, M., Poggianti, B., Paccagnella, A., Couch, W. J., Vulcani, B., Bettoni, D., Fritz, J., Cava, A., Fasano, G., D'Onofrio, M., and Omizzolo, A. (2017). OmegaWINGS: spectroscopy in the outskirts of local clusters of galaxies. *A&A*, 599:A81.

Moretti, A., Poggianti, B. M., Fasano, G., Bettoni, D., D'Onofrio, M., Fritz, J., Cava, A., Varela, J., Vulcani, B., Gullieuszik, M., Couch, W. J., Omizzolo, A., Valentinuzzi, T., Dressler, A., Moles, M., Kjærgaard, P., Smareglia, R., and Molinaro, M. (2014). WINGS Data Release: a database of galaxies in nearby clusters. *A&A*, 564:A138.

Mulchaey, J. S. and Zabludoff, A. I. (1998). The Properties of Poor Groups of Galaxies. II. X-Ray and Optical Comparisons. *ApJ*, 496:73–92.

Natarajan, P., Chadayammuri, U., Jauzac, M., Richard, J., Kneib, J.-P., Ebeling, H., Jiang, F., van den Bosch, F., Limousin, M., Jullo, E., Atek, H., Pillepich, A., Popa, C., Marinacci, F., Hernquist, L., Meneghetti, M., and Vogelsberger, M. (2017). Mapping substructure in the HST Frontier Fields cluster lenses and in cosmological simulations. *MNRAS*, 468:1962–1980.

Navarro, J. F., Eke, V. R., and Frenk, C. S. (1996). The cores of dwarf galaxy haloes. *MNRAS*, 283:L72–L78.

Navarro, J. F., Frenk, C. S., and White, S. D. M. (1995). Simulations of X-ray clusters. *MNRAS*, 275:720–740.

Navarro, J. F., Frenk, C. S., and White, S. D. M. (1997). A Universal Density Profile from Hierarchical Clustering. *ApJ*, 490:493–508.

Navarro, J. F., Hayashi, E., Power, C., Jenkins, A. R., Frenk, C. S., White, S. D. M., Springel, V., Stadel, J., and Quinn, T. R. (2004). The inner structure of ΛCDM haloes - III. Universality and asymptotic slopes. *MNRAS*, 349:1039–1051.

Newman, A. B., Treu, T., Ellis, R. S., and Sand, D. J. (2013). The Density Profiles of Massive, Relaxed Galaxy Clusters. II. Separating Luminous and Dark Matter in Cluster Cores. *ApJ*, 765:25.

Nigoche-Netro, A., Aguerri, J. A. L., Lagos, P., Ruelas-Mayorga, A., Sánchez, L. J., and Machado, A. (2010). The Faber-Jackson relation for early-type galaxies: dependence on the magnitude range. *A&A*, 516:A96.

Nigoche-Netro, A., Ruelas-Mayorga, A., and Franco-Balderas, A. (2008). The Kormendy relation for early-type galaxies. Dependence on the magnitude range. *A&A*, 491:731–738.

Nipoti, C., Londrillo, P., and Ciotti, L. (2006). Dissipationless collapse, weak homology and central cores of elliptical galaxies. *MNRAS*, 370:681–690.

Oñorbe, J., Domínguez-Tenreiro, R., Sáiz, A., Serna, A., and Artal, H. (2005). Clues on the Physical Origin of the Fundamental Plane from Self-Consistent Hydrodynamical Simulations. *ApJ*, 632:L57–L60.

Oemler, Jr., A. (1974). The Systematic Properties of Clusters of Galaxies. Photometry of 15 Clusters. *ApJ*, 194:1–20.

Omizzolo, A., Fasano, G., Reverte Paya, D., De Santis, C., Grado, A., Bettoni, D., Poggianti, B., D'Onofrio, M., Moretti, A., Varela, J., Fritz, J., Gullieuszik, M., Cava, A., Grazian, A., and Moles, M. (2014). U-band photometry of 17 WINGS clusters. *A&A*, 561:A111.

Paccagnella, A., Vulcani, B., Poggianti, B. M., Moretti, A., Fritz, J., Gullieuszik, M., Couch, W., Bettoni, D., Cava, A., D'Onofrio, M., and Fasano, G. (2016). Slow Quenching of Star Formation in OMEGAWINGS Clusters: Galaxies in Transition in the Local Universe. *ApJ*, 816:L25.

Pahre, M. A., de Carvalho, R. R., and Djorgovski, S. G. (1998). Near-Infrared Imaging of Early-Type Galaxies. IV. The Physical Origins of the Fundamental Plane Scaling Relations. *AJ*, 116:1606–1625.

Pasquato, M. and Bertin, G. (2008). On the Fundamental Plane of the Galactic globular cluster system. *A&A*, 489:1079–1089.

Peletier, R. F. and Balcells, M. (1996). Ages of Galaxies Bulges and Disks From Optical and Near-Infrared Colors. *AJ*, 111:2238.

Perlmutter, S., Aldering, G., della Valle, M., Deustua, S., Ellis, R. S., Fabbro, S., Fruchter, A., Goldhaber, G., Groom, D. E., Hook, I. M., Kim, A. G.,

Kim, M. Y., Knop, R. A., Lidman, C., McMahon, R. G., Nugent, P., Pain, R., Panagia, N., Pennypacker, C. R., Ruiz-Lapuente, P., Schaefer, B., and Walton, N. (1998). Discovery of a supernova explosion at half the age of the universe. *Nature*, 391:51.

Pierpaoli, E., Borgani, S., Scott, D., and White, M. (2003). On determining the cluster abundance normalization. *MNRAS*, 342:163–175.

Poggianti, B. M. (1997). K and evolutionary corrections from UV to IR. *A&AS*, 122:399–407.

Poggianti, B. M., Calvi, R., Bindoni, D., D'Onofrio, M., Moretti, A., Valentinuzzi, T., Fasano, G., Fritz, J., De Lucia, G., Vulcani, B., Bettoni, D., Gullieuszik, M., and Omizzolo, A. (2013). Superdense Galaxies and the Mass-Size Relation at Low Redshift. *ApJ*, 762:77.

Poggianti, B. M., Fasano, G., Bettoni, D., Cava, A., Dressler, A., Vanzella, E., Varela, J., Couch, W. J., D'Onofrio, M., Fritz, J., Kjaergaard, P., Moles, M., and Valentinuzzi, T. (2009). The Evolution of Spiral, S0, and Elliptical Galaxies in Clusters. *ApJ*, 697:L137–L140.

Poggianti, B. M., von der Linden, A., De Lucia, G., Desai, V., Simard, L., Halliday, C., Aragón-Salamanca, A., Bower, R., Varela, J., Best, P., Clowe, D. I., Dalcanton, J., Jablonka, P., Milvang-Jensen, B., Pello, R., Rudnick, G., Saglia, R., White, S. D. M., and Zaritsky, D. (2006). The Evolution of the Star Formation Activity in Galaxies and Its Dependence on Environment. *ApJ*, 642:188–215.

Ponman, T. J. and Bertram, D. (1993). Hot gas and dark matter in a compact galaxy group. *Nature*, 363:51–54.

Postman, M., Coe, D., Ford, H., Riess, A., Zheng, W., Donahue, M., Moustakas, L., and CLASH Team (2011). CLASH: Cluster Lensing and Supernova survey with Hubble. In *American Astronomical Society Meeting Abstracts #217*, volume 43 of *Bulletin of the American Astronomical Society*, page 227.06.

Prugniel, P. and Simien, F. (1997). The fundamental plane of early-type galaxies: non-homology of the spatial structure. *A&A*, 321:111–122.

Ramella, M., Biviano, A., Pisani, A., Varela, J., Bettoni, D., Couch, W. J., D'Onofrio, M., Dressler, A., Fasano, G., Kjørgaard, P., Moles, M., Pignatelli, E., and Poggianti, B. M. (2007). Substructures in WINGS clusters. *A&A*, 470:39–51.

Reiprich, T. H. and Böhringer, H. (2002). The Mass Function of an X-Ray Flux-limited Sample of Galaxy Clusters. *ApJ*, 567:716–740.

Riess, A. G., Filippenko, A. V., Challis, P., Clocchiatti, A., Diercks, A., Garnavich, P. M., Gilliland, R. L., Hogan, C. J., Jha, S., Kirshner, R. P., Leibundgut, B., Phillips, M. M., Reiss, D., Schmidt, B. P., Schommer, R. A., Smith, R. C., Spyromilio, J., Stubbs, C., Suntzeff, N. B., and Tonry, J. (1998). Observational Evidence from Supernovae for an Accelerating Universe and a Cosmological Constant. *AJ*, 116:1009–1038.

Rines, K., Geller, M. J., Diaferio, A., Kurtz, M. J., and Jarrett, T. H. (2004). CAIRNS: The Cluster and Infall Region Nearby Survey. II. Environmental Dependence of Infrared Mass-to-Light Ratios. *AJ*, 128:1078–1111.

Rines, K., Geller, M. J., Diaferio, A., Mohr, J. J., and Wegner, G. A. (2000). The Infall Region of Abell 576: Independent Mass and Light Profiles. *AJ*, 120:2338–2354.

Rines, K., Geller, M. J., Kurtz, M. J., Diaferio, A., Jarrett, T. H., and Huchra, J. P. (2001). Infrared Mass-to-Light Profile throughout the Infall Region of the Coma Cluster. *ApJ*, 561:L41–L44.

Robertson, B., Cox, T. J., Hernquist, L., Franx, M., Hopkins, P. F., Martini, P., and Springel, V. (2006). The Fundamental Scaling Relations of Elliptical Galaxies. *ApJ*, 641:21–40.

Sadat, R. (1995). Influence of the Non-Luminous Component on Dynamical and Structural Properties of Galaxy Clusters. Does X-Ray Gas Mimic the Missing Mass? *Ap&SS*, 234:303–323.

Saglia, R. P., Bertin, G., and Stiavelli, M. (1992). Elliptical Galaxies with Dark Matter. II. Optimal Luminous–Dark Matter Decomposition for a Sample of Bright Objects. *ApJ*, 384:433.

Sanderson, A. J. R., Ponman, T. J., Finoguenov, A., Lloyd-Davies, E. J., and Markevitch, M. (2003). The Birmingham-CfA cluster scaling project - I. Gas fraction and the M-$T_X$ relation. *MNRAS*, 340:989–1010.

Schombert, J. M. (1986). The structure of brightest cluster members. I - Surface photometry. *ApJS*, 60:603–693.

Schuecker, P., Böhringer, H., Collins, C. A., and Guzzo, L. (2003). The REFLEX galaxy cluster survey. VII. Omega$_m$ and sigma$_8$ from cluster abundance and large-scale clustering. *A&A*, 398:867–877.

Schwarz, G. E. (1978). Estimating the dimension of a model. *Annals of Statistics*, 6:461–464.

Scodeggio, M., Gavazzi, G., Belsole, E., Pierini, D., and Boselli, A. (1998). The tilt of the Fundamental Plane of early-type galaxies: wavelength dependence. *MNRAS*, 301:1001–1018.

Secco, L. (2001). The Fundamental Plane as a consequence of Clausius' virial minimum. *New Astronomy*, 6:339–357.

Secco, L. and Bindoni, D. (2009). On the tilt of fundamental plane by Clausius' Virial maximum theory. *New Astronomy*, 14:567–578.

Seitz, S., Saglia, R. P., Bender, R., Hopp, U., Belloni, P., and Ziegler, B. (1998). The z=2.72 galaxy cB58: a gravitational fold arc lensed by the cluster MS1512+36. *MNRAS*, 298:945–965.

Seljak, U. (2002). Cluster number density normalization from the observed mass-temperature relation. *MNRAS*, 337:769–773.

Sérsic, J. L. (1963). Influence of the atmospheric and instrumental dispersion on the brightness distribution in a galaxy. *Boletin de la Asociacion Argentina de Astronomia La Plata Argentina*, 6:41.

Sersic, J. L. (1968). *Atlas de Galaxias Australes*.

Sheth, R. K. and Bernardi, M. (2012). Plain fundamentals of Fundamental Planes: analytics and algorithms. *MNRAS*, 422:1825–1834.

Skrutskie, M. F., Cutri, R. M., Stiening, R., Weinberg, M. D., Schneider, S., Carpenter, J. M., Beichman, C., Capps, R., Chester, T., Elias, J., Huchra, J., Liebert, J., Lonsdale, C., Monet, D. G., Price, S., Seitzer, P., Jarrett, T., Kirkpatrick, J. D., Gizis, J. E., Howard, E., Evans, T., Fowler, J., Fullmer, L., Hurt, R., Light, R., Kopan, E. L., Marsh, K. A., McCallon, H. L., Tam, R., Van Dyk, S., and Wheelock, S. (2006). The Two Micron All Sky Survey (2MASS). *AJ*, 131:1163–1183.

Smail, I., Ellis, R. S., Fitchett, M. J., and Edge, A. C. (1995). Gravitational lensing of distant field galaxies by rich clusters - II. Cluster mass distributions. *MNRAS*, 273:277–294.

Smith, R. J., Hudson, M. J., Nelan, J. E., Moore, S. A. W., Quinney, S. J., Wegner, G. A., Lucey, J. R., Davies, R. L., Malecki, J. J., Schade, D., and Suntzeff, N. B. (2004). NOAO Fundamental Plane Survey. I. Survey Design, Redshifts, and Velocity Dispersion Data. *AJ*, 128:1558–1569.

Songaila, A., Cowie, L. L., and Lilly, S. J. (1990). Galaxy formation and the origin of the ionizing flux at large redshift. *ApJ*, 348:371–377.

Springel, V., White, S. D. M., Jenkins, A., Frenk, C. S., Yoshida, N., Gao, L., Navarro, J., Thacker, R., Croton, D., Helly, J., Peacock, J. A., Cole, S., Thomas, P., Couchman, H., Evrard, A., Colberg, J., and Pearce, F. (2005). Simulations of the formation, evolution and clustering of galaxies and quasars. *Nature*, 435:629–636.

Strateva, I., Ivezić, Ž., Knapp, G. R., Narayanan, V. K., Strauss, M. A., Gunn, J. E., Lupton, R. H., Schlegel, D., Bahcall, N. A., Brinkmann, J., Brunner, R. J., Budavári, T., Csabai, I., Castander, F. J., Doi, M., Fukugita, M., Győry, Z., Hamabe, M., Hennessy, G., Ichikawa, T., Kunszt, P. Z., Lamb, D. Q., McKay, T. A., Okamura, S., Racusin, J., Sekiguchi, M., Schneider, D. P., Shimasaku, K., and York, D. (2001). Color Separation of Galaxy Types in the Sloan Digital Sky Survey Imaging Data. *AJ*, 122:1861–1874.

Terlevich, A. I. and Forbes, D. A. (2002). A catalogue and analysis of local galaxy ages and metallicities. *MNRAS*, 330:547–562.

Tortora, C., Napolitano, N. R., Romanowsky, A. J., Capaccioli, M., and Covone, G. (2009). Central mass-to-light ratios and dark matter fractions in early-type galaxies. *MNRAS*, 396:1132–1150.

Treu, T., Ellis, R. S., Liao, T. X., and van Dokkum, P. G. (2005). Keck Spectroscopy of Distant GOODS Spheroidal Galaxies: Downsizing in a Hierarchical Universe. *ApJ*, 622:L5–L8.

Trujillo, I., Erwin, P., Asensio Ramos, A., and Graham, A. W. (2004). Evidence for a New Elliptical-Galaxy Paradigm: Sérsic and Core Galaxies. *AJ*, 127:1917–1942.

Umetsu, K., Medezinski, E., Broadhurst, T., Zitrin, A., Okabe, N., Hsieh, B.-C., and Molnar, S. M. (2010). The Mass Structure of the Galaxy Cluster Cl0024+1654 from a Full Lensing Analysis of Joint Subaru and ACS/NIC3 Observations. *ApJ*, 714:1470–1496.

Umetsu, K., Medezinski, E., Nonino, M., Merten, J., Postman, M., Meneghetti, M., Donahue, M., Czakon, N., Molino, A., Seitz, S., Gruen, D., Lemze, D., Balestra, I., Benítez, N., Biviano, A., Broadhurst, T., Ford, H., Grillo, C., Koekemoer, A., Melchior, P., Mercurio, A., Moustakas, J., Rosati, P., and Zitrin, A. (2014). CLASH: Weak-lensing Shear-and-magnification Analysis of 20 Galaxy Clusters. *ApJ*, 795:163.

Valentinuzzi, T., Poggianti, B. M., Fasano, G., D'Onofrio, M., Moretti, A., Ramella, M., Biviano, A., Fritz, J., Varela, J., Bettoni, D., Vulcani, B., Moles, M., Couch, W. J., Dressler, A., Kjærgaard, P., Omizzolo, A., and Cava, A. (2011). The red-sequence of 72 WINGS local galaxy clusters. *A&A*, 536:A34.

Valentinuzzi, T., Poggianti, B. M., Saglia, R. P., Aragón-Salamanca, A., Simard, L., Sánchez-Blázquez, P., D'onofrio, M., Cava, A., Couch, W. J., Fritz, J., Moretti, A., and Vulcani, B. (2010). Superdense Massive Galaxies in the ESO Distant Cluster Survey (EDisCS). *ApJ*, 721:L19–L23.

Valentinuzzi, T., Woods, D., Fasano, G., Riello, M., D'Onofrio, M., Varela, J., Bettoni, D., Cava, A., Couch, W. J., Dressler, A., Fritz, J., Moles, M., Omizzolo, A., Poggianti, B. M., and Kjærgaard, P. (2009). WINGS: a WIde-field nearby Galaxy-cluster survey. III. Deep near-infrared photometry of 28 nearby clusters. *A&A*, 501:851–864.

van Dokkum, P. G. and Conroy, C. (2010). A substantial population of low-mass stars in luminous elliptical galaxies. *Nature*, 468:940–942.

van Dokkum, P. G., Franx, M., Fabricant, D., Illingworth, G. D., and Kelson, D. D. (2000). Hubble Space Telescope Photometry and Keck Spectroscopy of the Rich Cluster MS 1054-03: Morphologies, Butcher-Oemler Effect, and the Color-Magnitude Relation at Z = 0.83. *ApJ*, 541:95–111.

Varela, J., D'Onofrio, M., Marmo, C., Fasano, G., Bettoni, D., Cava, A., Couch, W. J., Dressler, A., Kjærgaard, P., Moles, M., Pignatelli, E., Poggianti, B. M., and Valentinuzzi, T. (2009). WINGS: A WIde-field Nearby Galaxy-cluster Survey. II. Deep optical photometry of 77 nearby clusters. *A&A*, 497:667–676.

Vogelsberger, M., Genel, S., Springel, V., Torrey, P., Sijacki, D., Xu, D., Snyder, G., Nelson, D., and Hernquist, L. (2014). Introducing the Illustris Project: simulating the coevolution of dark and visible matter in the Universe. *MNRAS*, 444:1518–1547.

Vulcani, B., Poggianti, B. M., Aragón-Salamanca, A., Fasano, G., Rudnick, G., Valentinuzzi, T., Dressler, A., Bettoni, D., Cava, A., D'Onofrio, M., Fritz, J., Moretti, A., Omizzolo, A., and Varela, J. (2011a). Galaxy stellar mass functions of different morphological types in clusters, and their evolution between z= 0.8 and 0. *MNRAS*, 412:246–268.

Vulcani, B., Poggianti, B. M., Dressler, A., Fasano, G., Valentinuzzi, T., Couch, W., Moretti, A., Simard, L., Desai, V., Bettoni, D., D'Onofrio,

M., Cava, A., and Varela, J. (2011b). The evolution of early-type galaxies in clusters from z˜ 0.8 to z ˜ 0: the ellipticity distribution and the morphological mix. *MNRAS*, 413:921–941.

Vulcani, B., Poggianti, B. M., Fasano, G., Desai, V., Dressler, A., Oemler, A., Calvi, R., D'Onofrio, M., and Moretti, A. (2012). The importance of the local density in shaping the galaxy stellar mass functions. *MNRAS*, 420:1481–1494.

White, S. D. M., Navarro, J. F., Evrard, A. E., and Frenk, C. S. (1993). The baryon content of galaxy clusters: a challenge to cosmological orthodoxy. *Nature*, 366:429–433.

Wu, X.-P. and Fang, L.-Z. (1997). A Statistical Comparison of Cluster Mass Estimates from Optical/X-Ray Observations and Gravitational Lensing. *ApJ*, 483:62–67.

Young, C. K. and Currie, M. J. (1994). A New Extragalactic Distance Indicator Based on the Surface Brightness Profiles of Dwarf Elliptical Galaxies. *MNRAS*, 268:L11.

Zaritsky, D. (2012). Implications and Applications of Kinematic Galaxy Scaling Relations. *ISRN Astronomy and Astrophysics*, 2012:189625.

Zhao, D. H., Jing, Y. P., Mo, H. J., and Börner, G. (2009). Accurate Universal Models for the Mass Accretion Histories and Concentrations of Dark Matter Halos. *ApJ*, 707:354–369.

Zwicky, F. (1933). Die Rotverschiebung von extragalaktischen Nebeln. *Helvetica Physica Acta*, 6:110–127.

# Acknowledgements

"If you want to go fast, go alone. If you want to go far, go together."
- African proverb.

It is the end of the journey and I wish to thank everyone who walked by my side because, even though there is my name on the thesis, this is actually a team work. And the team that contributed to obtainig these amazing results is made of all the people who walked by my side in good and bed times, even for a single day, during the past 28 years.

It would be too long to mention them all, and after 200 pages of thesis I guess that nobody is really prone to reading another 200 pages of thanksgivings, so I will mention more or less only those people who had a direct and measurable impact on my PhD work.

First of all, I want to thank all the friends that, during the last three years, endured an uncountable number of hours of delirium, during lunches and coffe-breaks, and still have the strength to speak to me. According to the length of our relationship, they are: Sara, Matteo, Francesco, Azadeh, Gemma, Vanessa, Francesca, Soccorsa, Edoardo, Rosaria, Giada, Valeria, Giovanni, Alessandro, Maria Laura, Francesca, Devid, Chiara, Erica, Lorenzo, Alessandra and Maria.

I want to thank my mother for all the times I got back home past midnight and yet I found the table set and something edible on it. (I know the temptation of strangling me was strong, mom, so thank you for enduring it!)

I want to thank the WINGS group (and, in particular, my supervisor: Prof. Mauro D'Onofrio) for "adopting" me in this beautiful family. Thank you for everything Giovanni, Bianca, Marco, Alessia, and Daniela.

I want to thank Mario for the sushi and the tobacco, Giovanni for the chilly peppers, Andrea for the flat bread and the drinks, Giorgio for the cultural discussions (and, more recently, the alcohol as well) and Francesco for the sushi, the chilli peppers and the cigars that had a very positive impact on my mood.

I want to thank Davide again for his invaluable help in the statistical analysis. (You made me save so much time, buddy, that you cannot possibly imagine it!)

I want to thank Lýdia, Liana, Vanessa and Sara for more reasons than those I could reasonably summarize here. I love you, girls, thank you for being there!

I want to thank all the friends with which I spent my social moments, and in particular everyone who had a good word for me, everyone who encouraged me, everyone who believed in me, and everyone who helped or supported me. You are too many for me to mention you one by one, so please accept a global thank you!

I want to thank Daniela, Luca, Adriano, Roberto, Michele, Marco and everyone else for being still there, despite my fluctuating presence.

I want to thank Prof. Ortolani, Prof. Piotto, Prof. Ciroi, Prof. Rodighiero, Prof. D'Onofrio, and all the others I do not know about for standing by my side in my darkest hour.

Finally, I want to thank those who hampered me, who tried to stop me and who spread negative rumors about me. You do not know it, but you have been my second strongest reason for succeeding.

I am grateful to you all, people. May you all have enough ambition for turning your greatest dreams into goals, and may you also find the strength for achieving them!

"The fact that the price must be paid is proof it is worth paying."

- Robert Jordan, The Wheel of Time.